Data-driven exact model order reduction for computational multiscale methods to predict high-cycle fatigue-damage in short-fiber reinforced plastics

Zur Erlangung des akademischen Grades eines

Doktors der Ingenieurwissenschaften (Dr.-Ing.)

von der KIT-Fakultät für Maschinenbau des
Karlsruher Instituts für Technologie (KIT)
angenommene

Dissertation

von

M. Sc. Nicola Henkelmann geb. Magino

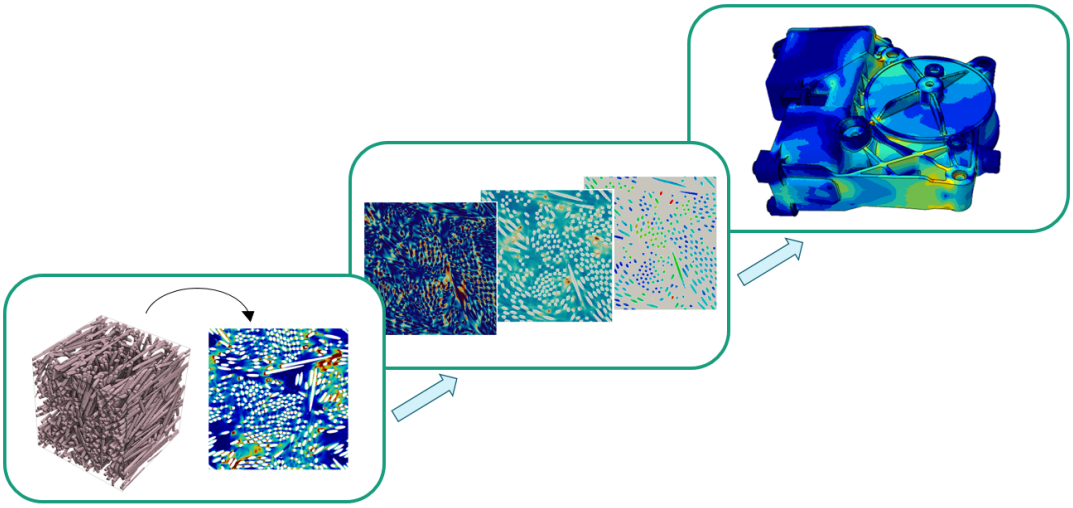

Tag der mündlichen Prüfung: 20. März 2023

Hauptreferent	JP. Dr. Matti Schneider
Korreferent	PD. Dr. Heiko Andrä
Korreferent	Prof. Dr.-Ing. Ralf Müller

Zusammenfassung

Motiviert durch die Entwicklung energieeffizienterer Maschinen und Transportmittel hat der Leichtbau in den letzten Jahren enorm an Wichtigkeit gewonnen. Eine wichtige Klasse der Leichtbaumaterialien sind die faserverstärkten Kunststoffe. In der vorliegenden Arbeit liegt der Fokus auf der Entwicklung und Bereitstellung von Materialmodellen zur Vorhersage des Ermüdungsverhaltens kurzglasfaserverstärkter Thermoplaste. Diese Materialien unterscheiden sich dabei durch ihre Aufschmelzbarkeit und ihrer damit einhergehenden besseren Recyclebarkeit von thermosetbasierten Materialien. Außerdem erlauben die Kurzglasfasern im Gegensatz zu Langfasern eine einfache und zeiteffiziente Herstellung komplexer Komponenten.
Ermüdung ist ein wichtiger Versagensmechanismus in solchen Komponenten, insbesondere für Bauteile z.B. in Fahrzeugen, die vibrationsartigen Belastungen ausgesetzt sind. Durch die inherente Anisotropie des Materials sind die experimentelle Charakterisierung und Vorhersage dieses Versagensmechanismus jedoch äußerst zeitintensiv und stellen somit eine wesentliche Herausforderung im Entwicklungsprozess und für die breitere Anwendung solcher Bauteile dar. Daher ist die Entwicklung komplementärer simulativer Methoden von großem Interesse. Im Rahmen dieser Arbeit werden Methoden zur Vorhersage der Ermüdungsschädigung kurzglasfaserverstärkter Werkstoffe im Rahmen einer Multiskalenmethode entwickelt. Die in der Arbeit betrachteten Multiskalenmodelle bieten die Möglichkeit, allein anhand der experimentellen Charakterisierungen der Materialparameter der Konstituenten, d.h. Faser und Matrix, komplexe anisotrope Effekte des Verbundmaterials vorherzusagen. Der experimentelle Aufwand kann dadurch enorm reduziert werden. Dazu werden zunächst Materialmodelle für die Konstituenten des Komposits entwickelt. Mithilfe FFT-basierter rechnergestützter Homogenisierung wird daraus das Materialverhalten des Komposits für verschiedene Mikrostrukturen und Lastfälle vorhergesagt. Die vorberechneten Lastfälle auf Mikrostrukturebene werden mit datengetriebenen Methoden auf die Makroskala übertragen. Das ermöglicht eine effiziente Berechnung von Bauteilen in wenigen Stunden, wohingegen eine entsprechende Berechnung mit geometrischer Auflösung aller einzelnen Fasern der Mikrostruktur auf heutigen Computern viele Jahre dauern würden.

Für die Matrix werden unterschiedliche Schädigungsmodelle untersucht. Ihre Vor- und Nachteile werden analysiert. Die Mikrostruktursimulationen geben einen Einblick in den Einfluss verschiedener statistischer Parameter wie Faserlängen und Faservolumengehalt auf das Kompositverhalten. Ein neues Modellordnungsreduktionsverfahren wird entwickelt und zur Simulation des Ermüdungsschädigungsverhaltens auf Bauteilebene angewandt. Weiter werden Modellerweiterungen zur Berücksichtigung des R-Wert-Verhältnisses und viskoelastischer Effekte in der Evolution der Ermüdungsschädigung entwickelt und mit experimentellen Ergebnissen validiert.
Das entstandene Simulationsframework erlaubt nach Vorrechnungen auf einer geringen Menge von Mikrostrukturen und Lastfällen eine effiziente Makrosimulation eines Bauteils vorzunehmen. Dabei können Effekte wie Viskoelastizität und R-Wert-Abhängigkeit je nach gewünschter Modellierungstiefe berücksichtigt oder vernachlässigt werden, um immer das effizientste Modell, das alle relevanten Effekte abbildet, nutzen zu können.

Summary

Motivated by, amongst others, the development of more energy-efficient machines and means of transport, lightweight construction has gained enormous importance in recent years. One important class of lightweight materials comprises fiber-reinforced plastics. The present work focuses on the development of material models for the fatigue behavior of short glass-fiber reinforced thermoplastics. These materials differ from thermoset-based materials in their meltability and, thus, their better recyclability. Additionally, in contrast to long fibers, short glass-fibers allow for a simple and time-efficient production of complex components.

Fatigue is an important failure mechanism in these materials for components subjected to vibration-like loads, e.g., in the transport domain. However, the characterization and prediction of this failure mechanism are experimentally extremely time-consuming. Thus, fatigue assessment represents a significant challenge in the development process and for the broader application of short-fiber reinforced components. Therefore, the development of complementary simulative methods is of great interest.

In the present work, methods to predict fatigue damage of short-fiber reinforced materials are developed within the framework of a multiscale method. Multiscale models offer the possibility to predict complex, anisotropic effects of the composite material based solely on the experimental characterizations of the material parameters of the constituents, i.e., fiber and matrix. The experimental effort can thus be reduced significantly. For this purpose, first, material models for the constituents are developed on the microscale. Then, using FFT-based computational homogenization, the material behavior of the composite is predicted for different microstructures and load cases. The precomputed load cases at the microstructure level are transferred to the macroscale using data-driven methods. This enables efficient computations of engineering components, which would not be predictable by methods resolving the fiber structure on state of the art computers in years of computational time.

Various damage models for the matrix are investigated and advantages as well as disadvantages are analyzed. The microstructure simulations provide insight into the influence

of various statistical parameters such as fiber length and fiber volume content on the composite behavior. A new model order reduction procedure is developed and successfully applied to the simulation of fatigue damage. Further, model extensions are developed to account for the stress ratio and viscoelastic effects in the evolution of fatigue damage. Both extensions are validated with experimental results. The resulting simulation framework allows the engineer to perform an efficient macrosimulation of the component after precomputations on a set of microstructures. Effects such as viscoelasticity and stress ratio dependence can be taken into account or excluded depending on the desired modeling depth in order to always use the simplest possible model that captures all relevant effects.

Acknowledgments

This thesis is the result of my time at the Fraunhofer Institute of Industrial Mathematics (ITWM) and the Institute of Engineering Mechanics (ITM) of the Karlsruhe Institute of Technology (KIT) between 2019 and 2022.
It would have not been possible without the support of Matti Schneider, whom I owe deepest gratitude. His willingness to share his extensive knowledge through countless discussions enabled me to learn so much, and his humorous view on things carried me through both my Ph.D. time and a pandemic. Similarly, I would like to express special thanks to Heiko Andrä for his guidance and many fruitful conversations. His deep understanding of the topic and on-point questions have contributed substantially to the quality of this work. A big thank you goes to Ralf Müller as well for the countless hours given and for the sharing of his rich knowledge of damage and engineering mechanics. I also thank Fabian Welschinger for many discussions and for his support with experimental data.
Furthermore I am very grateful to all of my colleagues at the Fraunhofer Institute for Industrial Mathematics as well as the Institute of Engineering Mechanics (KIT); they helped make this whole journey an enjoyable one. Thank you for every shared coffee break, for joint memories of conferences and workshop events, for new hints provided at the right time, for introducing me to Palatinate culture. A special thanks goes to Jonathan Köbler.
Last but not least, I would like to thank my husband, Felix Henkelmann, for his loving support and for encouraging me to pursue my chosen path. I thank my parents, Hiltrud and Lutz Magino, for being the best I could have wished for. I thank my family and friends for being there for me at all times.

Contents

1. Introduction

1.1. Motivation

The increasing demand for energy efficient mechanical systems, especially in the transport industry, fostered the development of lightweight construction and materials. Fiber-reinforced materials offer a high stiffness to weight ratio [1] and thus have the potential add to a development towards more energy efficient transportation. In contrast to their continuous fiber reinforced counterparts, the production of complex components using short-fiber reinforced thermoplastics (SFRT) is rather simple and cost-effective. Continuous fiber reinforced parts are typically produced by firstly manufacturing a fiber preform, e.g., by waving or braiding, and secondly a forming process. This takes a significant amount of time. SFRTs are typically manufactured via injection molding. While the casting mold may be complex and difficult to produce, once the mold is manufactured the injection molding process allows for time-efficient production of large quantities of components. While this is a advantage in the manufacturing stage of the product life cycle, the complexity of manufacturing prototypes is a challenge in the development stage. In SFRTs, typical fiber length to diameter ratios are in the order of ten and fibers are stirred into the molten matrix prior to the injection process. The thermoplastic matrix typically used is meltable and thus easier to recycle than composite materials based on thermosets. These advantages make them interesting for various applications in the transportation sector, for consumer goods and for electrical components. Some of the most commonly used materials are carbon and glass for the fiber and polypropylene (PP), polyamide (PA) and polybutylene terephthalate (PBT) for the matrix. Due to their favorable properties, the market size of short-fiber reinforced polymers is expected to grow significantly [2].
The orientation of the fibers in the component and thus the macroscopic anisotropic material behavior depend on the injection molding process. Consequently, a large number of experiments is necessary to understand a multitude of fiber orientations and their material behavior to fully characterize a component's behavior. This leads to a rather complex characterization process.

Fatigue is one of the most prevalent failure mechanisms of components subjected to prolonged vibrations, e.g, in the transportation sector. The material response under cyclic loading conditions can be quite different from the response under static loading conditions. In contrast to metals, fatigue degradation in SFRTs leads to a significant decrease of the stiffness properties of the material [3–6], leading to stress redistribution inside the component. The critical spot inside the component is thus dependent on the loading history. Fatigue degradation in SFRTs is a complex process, comprising mean stress effects, thermal effects and viscoelastic effects. Experimental investigation of the long time behavior of these materials is a time and cost intensive task, especially in combination with the fiber orientation dependence that needs to be understood. With increasing demands for rapid development of new designs, long lasting experimental characterization processes are a challenge to a broader application of the materials. Optimization of the life time of components as well as the reduction of material usage are key aspects in the development towards a more sustainable economy. Therefore, the demand for complementary computational prediction methods for fatigue degradation in SFRTs is high.

The aim of this work is to significantly speed up the development process of SFRT-components as well as providing a tool for optimization of material usage and life time duration by developing computational prediction methods. The overall goal is a more sustainable product life cycle. State-of-the-art development processes for SFRTs need material and time intensive experimental programs: dependent on local fiber orientation, the stiffness degradation of the material needs to be fully characterized for a multitude of load cases, e.g., considering stress amplitude, stress ratio and frequency. Based on tests on standard specimens, the stiffness degradation in actual components is still unclear. Production of prototypes is time and cost intensive and a change in the design of the component or the manufacturing process leads to a need for a renewed characterization. To overcome the necessity of studying the macroscopic material behavior for every possible microstructure separately, a multiscale approach is developed in this work. Here, after a characterization of the material behavior of the constituents, i.e., fiber and matrix, the behavior of the composite can be derived via homogenization methods. Existing analytical homogenization [7–9] approaches are limited to particular inclusion geometries and interactions between them are only captured to a certain degree. Thus, we make use of computational homogenization techniques in the work at hand. FFT-solvers based on a Lippman-Schwinger formulation of the elasticity problem enable an efficient computation of complex micro-structures [10, 11], both in terms of computational time and memory usage. The development of suitable model order reduction techniques (MOR) enables the application of an effective, microstructure-informed material law on the macroscale.

Having the developed computational methods at hand, the goal of this work is a signifi-

cantly simplified development process for SFRT components: Based on the material laws of the *constituents* which are dependent on only few parameters and thus comparatively to characterize, the stiffness degradation of an *arbitrary* component can be predicted. Advanced computational methods (micromechanics, data-driven exact model order reduction) help to overcome the *computational* complexity of the problem and enable the prediction of engineering components in a very time efficient manner. The computational effort in the online-phase, i.e., the macroscale computation after performing precomputations on a set of microstructures, is comparable to that of phenomenological fatigue damage models for the composite material while, on the same time, keeping the advantage in accuracy of microscale models. Monitoring of the local stiffness degradation inside the component is enabled and ensures its reliability.

1.2. Objectives

The main goal of the work at hand is the accurate prediction of the fatigue degradation of short-fiber reinforced thermoplastics under high-cycle loading and a reduction of the number of necessary experiments to fully characterize the material behavior. To keep the experimental effort at a minimum, we decided to develop a multiscale model. Here, only the material parameters for the material laws of the constituents have to identified experimentally. Then, we subdivide the goal of the thesis into several objectives:

1. development of a material model for fiber a matrix that incorporates the most relevant effects of fatigue degradation,
2. transfer of the microscale equations into an effective macroscopic material model,
3. validation of the developed material model with experimental data.

This work partially builds upon the Ph.D. thesis of Jonathan Köbler [12]. The result of his work was a multiscale simulation framework for SFRTs. From his thesis, in particular, several open questions remained to be adressed:

1. What does the correct fatigue damage model look like?
2. How can the damage model be integrated within the database-approach proposed?
3. How does the volume element size on the microscale influence macroscopic failure (size effect)?

4. How can wave form effects be simulated efficiently (stress ratio dependence)?

5. How do viscoelastic effects influence the material behavior (frequency dependence, creep)?

With the development of the fatigue damage models within this thesis, the above questions are adressed. The outline in section 1.3 gives an overview of the following chapters. A summarizing discussion of the above questions and outlook is given in the conclusion section 7.

1.3. Outline

This work presents research done in the course of the author's time as a doctoral candidate. It has been published in scientific journals. This thesis aims to set the results in context.
First, the fundamentals of this work are discussed in chapter 2. A main challenge in the prediction of these materials is their complex fiber structure, as shown in Fig. 1.1(a). Thus, we choose to develop a prediction method within a computational multiscale framework. This enables the derivation of the macroscopic material behavior for every fiber orientation of the SFRT based on a database concept and precomputations on the microscale.
In particular, we are interested in modeling the stiffness degradation of the material prior to failure. As shown in Fig. 1.1(b), the stiffness degradation in SFRTs under fatigue loading at constant stress amplitudes can be subdivided into three stages. With increasing cycle number N, the measured dynamic modulus E of the specimen decreases. Here, E denotes the elastic modulus of the specimen in the respective direction. The first stage is characterized by a rapid decrease of the stiffness properties, followed by a second stage of moderate degeneration which covers most of the life time of the component. In the third stage, the stiffness degradation rapidly increases and ultimately leads to final failure of the specimen.
In chapter 3, we chose a localizing fatigue damage model for the thermoplastic matrix to model this stiffness degradation. The fiber inclusions are modeled as linear elastic. Based on the chosen material models, the influence of the microstructure on the composite material behavior is thoroughly studied. The effect of a varying fiber aspect ratio, fiber volume content and fiber orientation is demonstrated. A model order reduction approach using the non-uniform transformation field analysis (NTFA) enables an efficient computation

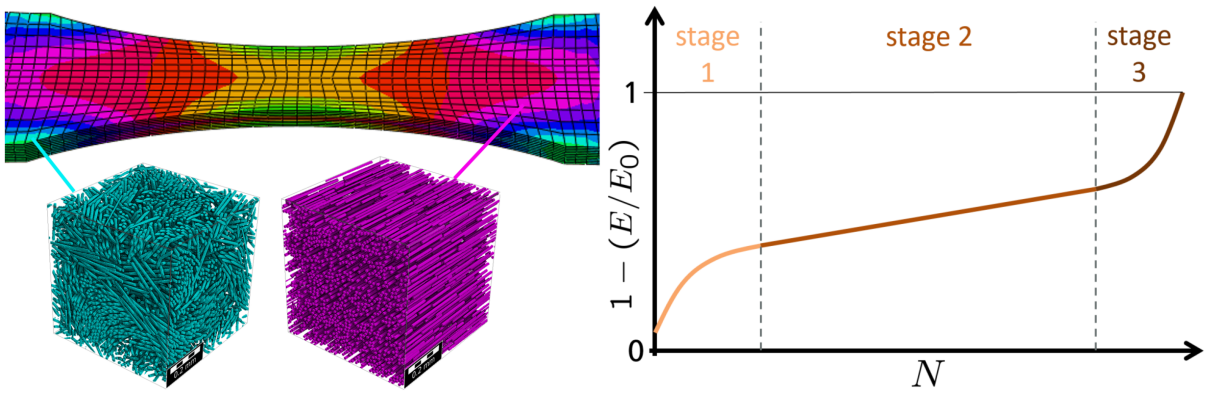

(a) Fiber orientation in a SFRT-component (b) Stiffness degradation

Figure 1.1.: Fatigue degradation in SFRT-component

of the stiffness degradation within an engineering component.

The damage model chosen in chapter 3 permits for localization of the damage field. This comes with several disadvantages. Firstly, localization of damage leads to a loss of representativity of the precomputed structures. Secondly, the damage field needs to be regularized by gradient terms due to the non-convex nature of the equations to obtain a mesh-independent numerical solution. These gradient terms add to the compexity and consequently the run time of the micro- and macroscale model. Thirdly, a large number of snapshots is necessary to capture the localized cracks. We are interested in the fatigue damage degradation prior to failure. Thus, there is no need for a model that captures the localization of cracks at the microstructure level. To overcome the mentioned disadvantages, we propose to use a non-localizing damage model for the matrix material in chapter 4. It proves to be sufficient to capture experimental measurements of the stiffness degradation of short-fiber reinforced polybutylene terephthalate (PBT). A new model order reduction approach based on a reformulation of the model in terms of stress and damage fields is proposed. The reduced order model is demonstrated to be 17 times faster than the model presented in chapter 3 and more memory efficient.

The material models in chapter 3 and 4 are directly formulated in (logarithmic) cycle scale, and consequently enable an efficient computation of the material's degeneration up to a large number of cycles. However, the model does not account for a change in the loading path within a cycle, e.g., a different stress ratio $R = \sigma_{\min}/\sigma_{\max}$. Thus, in chapter 5, the material equations are formulated in time space. For this model, a change in the loading path within one cycle directly affects the damage evolution. For sinusoidal loading at different stress ratios, a damage evolution equation in (logarithmic) cycle space is obtained via an approximation of the time evolution equations. In combination with

the model order reduction approach discussed in section 4, a space-time upscaling scheme is obtained for the fatigue damage evolution of SFRTs under sinusoidal fatigue loading at different stress ratios. The predicted stiffness degradation is compared to experimental data of reinforced polyamide at different stress amplitudes and stress ratios for specimens with different notch geometries and fiber orientations.
In the above described chapters, the thermoplastic matrix is modeled by an elastic damage material. In chapter 5, the capability of this model to capture the relative stiffness decrease under fatigue loading is demonstrated. However, thermoplastic materials are well-known to be rate-dependent. Thus, the absolute value of the measured dynamic stiffness is frequency-dependent. In chapter 6, the influence of a linear viscoelastic matrix material on the predicted dynamic stiffness is thoroughly studied. At high cycle numbers, viscoelastic materials under fatigue loading with constant stress or strain amplitudes reach a steady state. This fact is exploited to approximate the dynamic stiffness of SFRTs at high cycle numbers by an elastic computation. Based on the obtained stiffness, a viscoelastic fatigue damage model is proposed. The model is suitable for the MOR described in chapter 4.
The developments presented in each chapter can be seen as a flexible framework for fatigue damage modeling in SFRTs. Based on the application, features like mean stress dependence, see chapter 5, or frequency dependence, see chapter 6, may be added or left out to find the most simple and at the same time accurate model for the purpose at need.

1.4. Notation

In the work at hand we use non-bold letters for scalars, bold letters for vectors and second-order tensors and double-stroke symbols for fourth-order tensors, e.g., the fouth-oder stiffness tensor $\mathbb{C}$.
We use tensor notation and denote contraction and double contraction by $\cdot$ and :, respectively. A list of frequently used operators can be found in table 1.1 below.

div	Divergence
det	Determinant
$\langle . \rangle_Y$	mean value over volume Y
∇	Gradient
∇^{s}	Symmetrized gradient

Table 1.1.: Operators

2. Fundamental concepts

2.1. Continuum mechanics

The section aims to discuss the fundamental concepts of continuum mechanics relevant for further discussion in a nutshell and is by no means complete or original, as is none of chapter 2. For further reading, we refer to, e.g., the textbooks [13–15].

2.1.1. Kinematics

To describe the motion of a material body $\mathcal{B}$, it is convenient to chose a reference configuration of the body $\mathcal{B}_0$. As shown in Fig. 2.1, this initial configuration of the body can be described by reference or material coordinates. A description of the body in terms of the reference coordinates $\mathbf{X}$ is called Lagrangian description.
Under motion, the path of a typical particle $\mathbf{X}$ is given parametrically by

$$\mathbf{x} = \chi(\mathbf{X}, t). \tag{2.1.1}$$

A description of a field quantity in terms of the coordinates of the current configuration $\mathbf{x}$ is called Eulerian description. The displacement vector $\mathbf{u}$ is defined by

$$\mathbf{u} = \mathbf{x} - \mathbf{X}, \tag{2.1.2}$$

which indicates the difference between current and reference placement. Based on the coordinates in reference and current configuration, the deformation gradient $\mathbf{F}$ and the displacement gradient $\mathbf{H}$ are defined as

$$\mathbf{F} = \frac{\partial \chi(\mathbf{X}, t)}{\partial \mathbf{X}} = \frac{\partial \mathbf{x}}{\partial \mathbf{X}} \tag{2.1.3}$$

and, closely related,

$$\mathbf{H} = \frac{\partial \mathbf{u}}{\partial \mathbf{X}} = \mathbf{F} - \mathbf{I}, \tag{2.1.4}$$

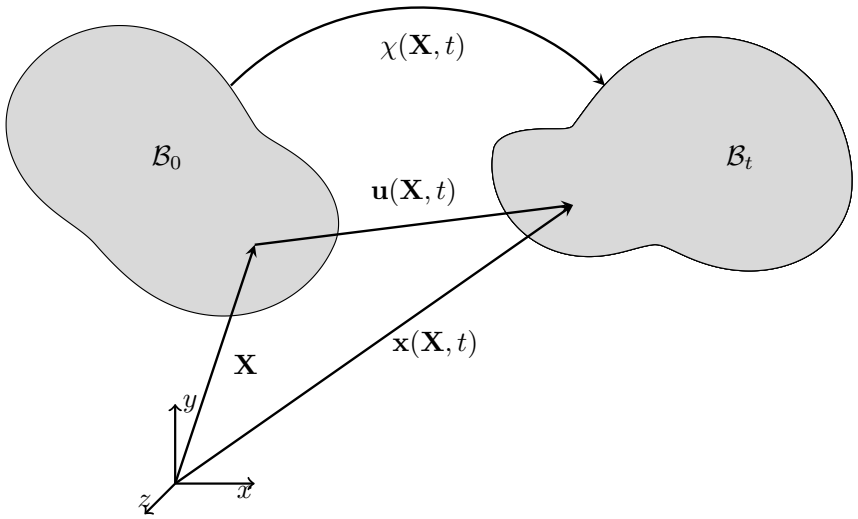

Figure 2.1.: Motion of the material body $\mathcal{B}$

where $\mathbf{I}$ denotes the second-order identity tensor.
Based on the deformation gradient, an infinitesimal material line element $\mathrm{d}\mathbf{X}$, area element $\mathrm{d}\mathbf{A} = \mathrm{d}A \cdot \mathbf{N}$ and volume element $\mathrm{d}V = \mathrm{d}\mathbf{A}^T \cdot \mathrm{d}\mathbf{L}$ in the reference configuration can be expressed in the current configuration

$$\mathrm{d}\mathbf{x} = \mathbf{F} \cdot \mathrm{d}\mathbf{X}, \tag{2.1.5}$$

$$\mathrm{d}\mathbf{a} = \det \mathbf{F}\, \mathbf{F}^{-T} \cdot \mathrm{d}\mathbf{A}, \tag{2.1.6}$$

$$\mathrm{d}v = \det \mathbf{F}\, \mathrm{d}V, \tag{2.1.7}$$

using Nanson's relation. A commonly used strain measure is the Green-Lagrange strain tensor $\mathbf{E}_G$

$$\mathbf{E}_G = \frac{1}{2}\left(\mathbf{F}^T\mathbf{F} - \mathbf{I}\right) = \frac{1}{2}\left(\mathbf{H} + \mathbf{H}^T + \mathbf{H}^T\mathbf{H}\right), \tag{2.1.8}$$

which describes the change of length and angles in an infinitesimal neighborhood of a material point $\mathbf{X}$.
If the deformations are small, i.e.,

$$\|\mathbf{H}\| \ll 1, \tag{2.1.9}$$

where $\|.\|$ denotes the Frobenius norm, linearizing the Green-Lagrange tensor $\mathbf{E}_G$ around the reference state yields

$$\mathbf{E}_G \approx \frac{1}{2}\left(\mathbf{H} + \mathbf{H}^T\right) \tag{2.1.10}$$

and it is no longer necessary to distinguish between current and reference configuration

$$\mathbf{x} \approx \mathbf{X}. \tag{2.1.11}$$

The linearized (infinitesimal) strain tensor $\boldsymbol{\varepsilon}$ is thus defined as

$$\boldsymbol{\varepsilon} = \frac{1}{2}\left(\mathbf{H} + \mathbf{H}^T\right). \tag{2.1.12}$$

In the thesis at hand, we restrict all further discussion to small deformations, where linear deformation theory can be applied.

2.1.2. Balance equations

In this section, the balance equations of continuum mechanics are discussed. The description is based on the textbook of Liu [16, Chapter 2]. To discuss the conservation equations of continuum mechanics in a generalized form, first, the *general balance equation* of a quantity ψ in any bounded regular subregion $\mathcal{V}_t \in \mathcal{B}$ of a body $\mathcal{B}$

$$\frac{\mathrm{d}}{\mathrm{d}t}\int_{\mathcal{V}_t} \psi \,\mathrm{d}v = \int_{\partial\mathcal{V}_t} \boldsymbol{\Phi}_\psi \cdot \mathbf{n} \,\mathrm{d}a + \int_{\mathcal{V}_t} s_\psi \,\mathrm{d}v \tag{2.1.13}$$

is postulated, where $\boldsymbol{\Phi}_\psi$ denotes the flux of ψ and s_ψ the source term of ψ.
In a regular point $\mathbf{x}$, using the Gaussian divergence theorem, its local form

$$\frac{\partial \psi}{\partial t} + \operatorname{div}\left(\psi\,\dot{\mathbf{x}}\right) = s_\psi + \operatorname{div}\,\boldsymbol{\Phi}_\psi \tag{2.1.14}$$

is obtained.

Conservation of mass

To discuss the *balance equation of mass*, the quantity of interest is the mass density ρ, i.e., $\psi \equiv \rho$.
In classical (non-relativistic) mechanics, mass source term $s_\rho = 0$ is postulated to be zero. Additionally, in most solid materials, there is no mass flux $\boldsymbol{\Phi}_\rho = 0$. Thus, the balance equation reads

$$\frac{\mathrm{d}}{\mathrm{d}t}\int_{\mathcal{V}_t} \rho \,\mathrm{d}v = 0 \quad \text{or} \quad \frac{\partial \rho}{\partial t} + \operatorname{div}\left(\rho\,\dot{\mathbf{x}}\right) = 0 \tag{2.1.15}$$

in its integral and local form, respectively.

Balance of linear momentum

To discuss the *balance equation of linear momentum*, the quantity of interest is the linear momentum density $\rho\,\dot{\mathbf{x}}$, i.e., $\psi \equiv \rho\,\dot{\mathbf{x}}$.
According to Euler's laws of motion, the source term depends on the external body force density $\mathbf{b}$ acting on the point $\mathbf{x}$, e.g., a gravitational force, $\mathbf{s}_\psi = \rho\,\mathbf{b}$. The flux of linear momentum is given by the Cauchy stress tensor $\boldsymbol{\sigma}$ which relates the stress vector $\mathbf{t}$ on an inner surface to its normal vector $\mathbf{n}$

$$\mathbf{t} = \boldsymbol{\sigma}^T \cdot \mathbf{n} \qquad \text{(Cauchy's stress theorem).} \tag{2.1.16}$$

As discussed in the next section, the stress tensor $\boldsymbol{\sigma}$ is symmetric. Thus, the *balance of linear momentum* reads

$$\frac{\mathrm{d}}{\mathrm{d}t}\int_{\mathcal{V}_t} \rho\,\dot{\mathbf{x}}\,\mathrm{d}v = \int_{\mathcal{V}_t} \rho\,\mathbf{b}\,\mathrm{d}v + \int_{\partial\mathcal{V}_t} \boldsymbol{\sigma}\cdot\mathbf{n}\,\mathrm{d}a \quad \text{or} \quad \rho\,\ddot{\mathbf{x}} = \rho\,\mathbf{b} + \operatorname{div}\boldsymbol{\sigma} \tag{2.1.17}$$

in its integral and local form, respectively.

Balance of angular momentum

To discuss the *balance equation of angular momentum*, the quantity of interest is the angular momentum density $\rho\,(\mathbf{x}-\mathbf{x}_0)\times\dot{\mathbf{x}}$ w.r.t. some reference point $\mathbf{x}_0$, i.e., $\psi \equiv \rho\,(\mathbf{x}-\mathbf{x}_0)\times\dot{\mathbf{x}}$. Here, $\times$ denotes the vector product.
According to Euler's laws of motion, the source term depends on the external body force density $\mathbf{b}$, i.e., $\mathbf{s}_\psi = \rho\,(\mathbf{x}-\mathbf{x}_0)\times\mathbf{b}$. The flux of angular momentum depends on Cauchy stress tensor $\boldsymbol{\sigma}$, i.e., $\boldsymbol{\Phi}_\psi = (\mathbf{x}-\mathbf{x}_0)\times\boldsymbol{\sigma}$.
Thus, the *balance of angular momentum* reads

$$\frac{\mathrm{d}}{\mathrm{d}t}\int_{\mathcal{V}_t} \rho\,(\mathbf{x}-\mathbf{x}_0)\times\dot{\mathbf{x}}\,\mathrm{d}v = \int_{\mathcal{V}_t} \rho\,(\mathbf{x}-\mathbf{x}_0)\times\mathbf{b}\,\mathrm{d}v + \int_{\partial\mathcal{V}_t} (\mathbf{x}-\mathbf{x}_0)\times(\boldsymbol{\sigma}\cdot\mathbf{n})\,\mathrm{d}a \tag{2.1.18}$$

in its integral form. If the balance of linear momentum holds, then the local form of the balance of angular momentum reduces to a symmetry condition for Cauchy's stress tensor

$$\boldsymbol{\sigma}^T = \boldsymbol{\sigma}. \tag{2.1.19}$$

Conservation of energy

To discuss the *balance equation of energy*, the quantity of interest is the total energy, i.e., the sum of the internal energy $\rho\, e$ and the kinetic energy $\rho\, \dot{\mathbf{x}}\cdot\dot{\mathbf{x}}/2$. We set $\psi \equiv \rho\, e + \rho\, \dot{\mathbf{x}}\cdot\dot{\mathbf{x}}/2$. The flux of the total energy consists of a mechanical part $\boldsymbol{\sigma} : \nabla\dot{\mathbf{x}}$ and the heat flux $\mathbf{q}$, i.e., $\Phi_\psi = \boldsymbol{\sigma} : \nabla\dot{\mathbf{x}} - \mathbf{q}$. The source term s_ψ in the balance of energy is given by the power of the external body forces $\rho\dot{\mathbf{x}}\cdot\mathbf{b}$ and the heat source term r. Thus, the conservation of energy reads

$$\frac{\mathrm{d}}{\mathrm{d}t}\int_{\mathcal{V}_t}\left(\rho e + \frac{\rho}{2}\dot{\mathbf{x}}\cdot\dot{\mathbf{x}}\right)\,\mathrm{d}v = \int_{\partial\mathcal{V}_t}(\dot{\mathbf{x}}\cdot\boldsymbol{\sigma}\cdot\mathbf{n} - \mathbf{q}\cdot\mathbf{n})\,\mathrm{d}a + \int_{\mathcal{V}_t}(\rho\dot{\mathbf{x}}\cdot\mathbf{b} + \rho r)\,\mathrm{d}v \tag{2.1.20}$$

in its integral or, by inserting the balance of linear moment, in its local form

$$\rho\dot{e} + \operatorname{div}\,\mathbf{q} = \boldsymbol{\sigma} : \nabla\dot{\mathbf{x}} + \rho r. \tag{2.1.21}$$

2.1.3. Material equations

With the kinematic equations (section 2.1.1) and the balance equations (section 2.1.2) at hand, the system is not yet solvable. The missing piece is the material equations or constitutive laws, which are, in contrast to the balance equations and the kinematics, material dependent.

The design and validation of material models is a challenging task. There are few restrictions on the design of constitutive laws, comprising thermodynamic consistency. One class of material models introduced by Nguyen and coworkers [17,18] are the *Generalized Standard Materials* (GSM) described by the Helmholtz free energy potential

$$w : \operatorname{sym}(3)\times\mathbb{R}^M \to \mathbb{R},\ \ (\boldsymbol{\varepsilon},\mathbf{q}) \mapsto w(\boldsymbol{\varepsilon},\mathbf{q}) \tag{2.1.22}$$

and a convex dissipation potential

$$\phi : \mathbb{R}^M \to \mathbb{R},\ \ \dot{\mathbf{q}} \mapsto \phi(\dot{\mathbf{q}}). \tag{2.1.23}$$

Here, $\mathbf{q}$ denotes the vector of internal state variables. Then, the stress $\boldsymbol{\sigma}$ and the generalized driving forces $\mathbf{f}_\mathbf{q}$ of the internal variables $\mathbf{q}$ are given by

$$\boldsymbol{\sigma} = \frac{\partial w}{\partial\boldsymbol{\varepsilon}}, \tag{2.1.24}$$

$$\mathbf{f}_\mathbf{q} = -\frac{\partial w}{\partial\mathbf{q}}. \tag{2.1.25}$$

For the potentials holds

$$w(\mathbf{0},\mathbf{0}) = 0, \;\; \phi(\mathbf{0}) = 0 \;\text{ and }\; \frac{\partial \phi}{\partial \dot{q}}(0) = 0. \tag{2.1.26}$$

The evolution of the internal variables is governed by the complementary law

$$\mathbf{f_q} = \frac{\partial \phi}{\partial \dot{\mathbf{q}}}. \tag{2.1.27}$$

This yields the Biot equation

$$\frac{\partial w}{\partial \mathbf{q}} + \frac{\partial \phi}{\partial \dot{\mathbf{q}}} = 0 \tag{2.1.28}$$

for the evolution of the internal variables. In the isothermal case, the second law of thermodynamics is given by the Clausius-Duhem inequality

$$\mathcal{D} = \boldsymbol{\sigma} : \dot{\boldsymbol{\varepsilon}} - \dot{w} \geq 0, \tag{2.1.29}$$

where $\mathcal{D}$ denotes the dissipation. For a GSM, the inequality reduces to

$$\frac{\partial \phi}{\partial \dot{\mathbf{q}}} \cdot \dot{\mathbf{q}} \geq 0, \tag{2.1.30}$$

which holds by construction of the dissipation potential (convex and demands 2.1.26).

2.2. Homogenization

We are interested in the material modeling of a composite material, i.e., a material comprising multiple constituents. Typically, the microstructure of the composite material and the constitutive equations of both constituents are assumed to be known. In multiscale models the aim is to find appropriate constitutive equations for the composite material.

2.2.1. Introduction to homogenization

The goal of homogenization techniques is to replace a heterogeneous (possibly complex) material by a homogeneous one, which has the same material response. The foundations of analytic homogenization methods in solid mechanics were laid by Voigt [19] and Reuss [20], who proposed bounds for the composite stiffness using the harmonic and the

arithmetic average of its constituents. Hashin and Shtrikman [21] improved these bounds for isotropically distributed inclusions, where both matrix and inclusion are assumed to have isotropic material properties.

To obtain macroscopic effective properties of the microstructure, suitable averaging techniques are applied to a representative sample of the microstructure, i.e., a *representative volume element* (RVE). There exist different definitions on what it means for a volume element to be considered representative [22, 23]. One possible definition is that the stiffness tensor of an elastic composite needs to be close to independent of the imposed boundary condition (uniform stress or uniform strain) [24]. Another possible definition is that the effective properties of it must be close to that of an infinitely large volume with macroscopic homogeneous properties. In any case, the characteristic length ℓ_{char}, e.g., the diameter of an inclusion, must be much smaller than the characteristic length ℓ_{RVE} of the representative volume element

$$\ell_{\text{char}} \ll \ell_{\text{RVE}} \tag{2.2.1}$$

to capture the behavior of the infinite microstructure. On the contrary, for the scale separation to be valid, the characteristic length of the microstructure ℓ_{RVE} needs to be much smaller than the characteristic length of the macroscopic component L

$$\ell_{\text{RVE}} \ll L. \tag{2.2.2}$$

The different length scales are illustrated in Fig. 2.2.

Consider a representative volume element Y on which a stress field $\boldsymbol{\sigma}(\mathbf{x})$ and a strain field $\boldsymbol{\varepsilon}(\mathbf{x})$ are given. Then, the macroscopic stress $\langle\boldsymbol{\sigma}\rangle_Y$ and strain $\langle\boldsymbol{\varepsilon}\rangle_Y$ are defined as

$$\langle\boldsymbol{\sigma}\rangle_Y = \frac{1}{|Y|}\int_Y \boldsymbol{\sigma}(\mathbf{x})\,\mathrm{d}Y, \tag{2.2.3}$$

$$\langle\boldsymbol{\varepsilon}\rangle_Y = \frac{1}{|Y|}\int_Y \boldsymbol{\varepsilon}(\mathbf{x})\,\mathrm{d}Y, \tag{2.2.4}$$

where

$$|Y| = \int_Y \mathrm{d}Y \tag{2.2.5}$$

denotes the volume of the body Y. The Hill-Mandel condition [25]

$$\langle\boldsymbol{\sigma}(\mathbf{x}) : \dot{\boldsymbol{\varepsilon}}(\mathbf{x})\rangle_Y = \langle\boldsymbol{\sigma}(\mathbf{x})\rangle_Y : \langle\dot{\boldsymbol{\varepsilon}}(\mathbf{x})\rangle_Y \tag{2.2.6}$$

links the macroscopic and the microscopic scale, i.e., if the averaged stress and strain rate are considered as macroscopic variables, then the virtual power on the macroscale equals the power on the microscale. For linear displacement boundary conditions, uniform stress boundary conditions as well as periodic boundary conditions, the Hill-Mandel condition is satisfied.

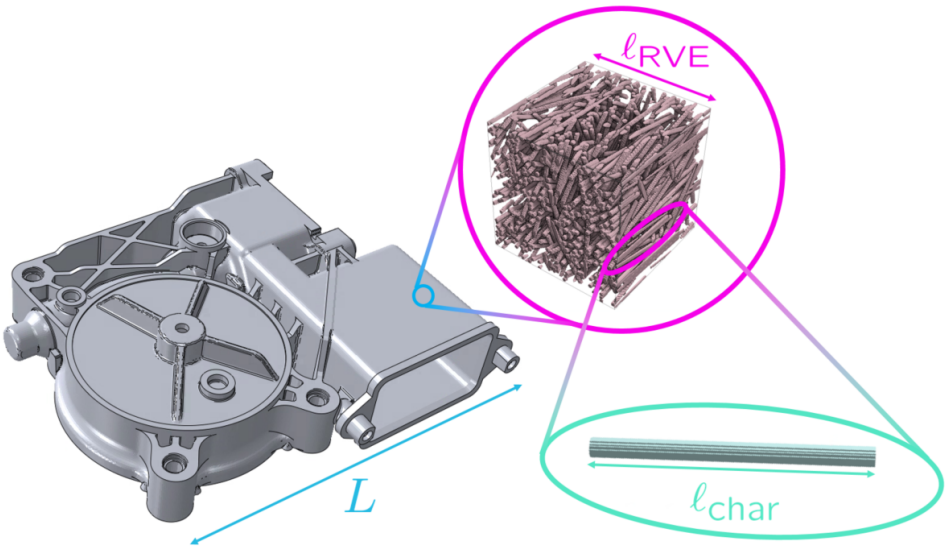

Figure 2.2.: Length scales in homogenization

2.2.2. Problem Setting

We are interested in the effective constitutive equation of a composite component. We assume the microstructure to be known and the material laws of the constituents to be given. Furthermore, the constitutive equations of the material are assumed to fall into the class of Generalized Standard Materials (GSM) as described in section 2.1.3. Then, Suquet [24,26] shows that the composite material can be expressed in terms of a GSM as well. Thus, there exists a macroscopic potential of the free energy W

$$\left(\langle \boldsymbol{\varepsilon} \rangle_Y, \mathrm{Q}\right) \mapsto W\left(\langle \boldsymbol{\varepsilon} \rangle_Y, \mathrm{Q}\right) \tag{2.2.7}$$

and a macroscopic dissipation potential Φ

$$\dot{\mathbf{Q}} \mapsto \Phi(\dot{\mathbf{Q}}) \tag{2.2.8}$$

based on which the macroscopic stress-strain relation

$$\langle \boldsymbol{\sigma} \rangle_Y = \frac{\partial W}{\partial \langle \boldsymbol{\varepsilon} \rangle_Y} \tag{2.2.9}$$

and the Biot equation defining the evolution of the state variables

$$\frac{\partial W}{\partial \mathbf{Q}} + \frac{\partial \Phi}{\partial \dot{\mathbf{Q}}} = 0$$

are given. However, the number N of state variables in the macroscopic material model can become infinite. Furthermore, the macroscopic material model strongly depends on the microstructure of the composite. In general, there is no explicit representation of the macroscopic constitutive equations. Instead, approximate models or computational methods have been developed to derive effective material equations. The following sections 2.2.3 and 2.2.4 are devoted to a short overview.

2.2.3. From analytical to computational approaches

Since Eshelby [27] found a solution to the elliptic inclusion problem, analytical methods to estimate the effective stiffness of a complex microstructure have been continuously developed and are commonly-known as mean-field approaches, see e.g. the review of Zaoui [28] for an overview. The popular approaches include the self-consistent scheme [29–31], the Mori-Tanaka scheme [32, 33] or the differential scheme [34, 35]. For an overview, the interest reader may be referred to Gross and Seelig [36, chapter 8].
Mean-field approaches are restricted to simple inclusions [37] of uniform distribution and fail to accurately capture interactions between inclusions. Thus, with increasing availability of computational power, computational homogenization methods have been developed. These methods have been used in both hierarchical and concurrent approaches [38]. In the concurrent approach, the material is divided into different subdomains with possibly different length and time scales. In the hierarchical approach on the other hand, different scales are resolved in the same region. Another possible classification of homogenization methods is their coupling. In decoupled methods, the information is passed from the microscale to the macroscale and has been applied to, e.g., viscoelastic materials [39, 40]. For material laws with high nonlinearities, a coupled approach is advisable. The FE^2-approach is an example of a fully-coupled micro-macro simulation. Originally developed by Feyel [41–43], it has been successfully applied to many materials, e.g., elasto-viscoplasticity [44] and damage [45,46]. Disadvantages of FE-based methods are their high demand for computational resources and storage [47]. To improve on these, Moulinec and Suquet [10, 48] proposed a FFT-based computational method to efficiently compute the response of a complex microstructure. This method has since then seen rapid development, see, e.g., Schneider [11] for a recent overview. Fully-coupled simulations, i.e., FFT-FE-approaches [49, 50] have been applied. In the thesis at hand, an FFT-based scheme is used to solve the boundary value problem at the microscale. Thus, the method is discussed in more detail in the upcoming section 2.2.4. Instead of a direct coupling,

in this work, the scale-transition is achieved via a model order strategy, fundamentals of which are discussed in section 2.4.

2.2.4. FFT-based computational homogenization

We consider a heterogeneous material made of constituents that are modeled by generalized standard materials. First, we derive the microscopic boundary value problem by asymptotic homogenization. We introduce a scalar parameter $\kappa > 0$, which represents the quotient between macroscopic and microscopic length scale. Then, considering a body $Y \subseteq \mathbb{R}^3$, the field equations derived in section 2.1, are given with

$$\operatorname{div} \boldsymbol{\sigma}^{\kappa}(\mathbf{x}) = -\mathbf{b}(\mathbf{x}), \text{ in } Y, \tag{2.2.10}$$

$$\boldsymbol{\sigma}^{\kappa}(\mathbf{x}) = \frac{\partial w}{\partial \boldsymbol{\varepsilon}} \left(\frac{\mathbf{x}}{\kappa}, \boldsymbol{\varepsilon}^{\kappa}, \mathbf{q}^{\kappa} \right), \text{ in } Y, \tag{2.2.11}$$

$$\boldsymbol{\varepsilon}^{\kappa}(\mathbf{x}) = \nabla^{\mathrm{s}} \mathbf{u}^{\kappa}(\mathbf{x}), \text{ in } Y, \tag{2.2.12}$$

for every field $\boldsymbol{\sigma}^{\kappa}$, $\boldsymbol{\varepsilon}^{\kappa}$ and $\mathbf{u}^{\kappa}$.
Subsequently, the asymptotic ansatz

$$\mathbf{u}^{\kappa}(\mathbf{x}) = \mathbf{u}^{0}\left(\mathbf{x}, \frac{\mathbf{x}}{\kappa}\right) + \kappa \mathbf{u}^{1}\left(\mathbf{x}, \frac{\mathbf{x}}{\kappa}\right) + \kappa^{2} \mathbf{u}^{2}\left(\mathbf{x}, \frac{\mathbf{x}}{\kappa}\right) + \mathcal{O}\left(\kappa^{3}\right), \tag{2.2.13}$$

$$\boldsymbol{\varepsilon}^{\kappa}(\mathbf{x}) = \boldsymbol{\varepsilon}^{0}\left(\mathbf{x}, \frac{\mathbf{x}}{\kappa}\right) + \kappa \boldsymbol{\varepsilon}^{1}\left(\mathbf{x}, \frac{\mathbf{x}}{\kappa}\right) + \mathcal{O}\left(\kappa^{2}\right), \tag{2.2.14}$$

$$\boldsymbol{\sigma}^{\kappa}(\mathbf{x}) = \boldsymbol{\sigma}^{0}\left(\mathbf{x}, \frac{\mathbf{x}}{\kappa}\right) + \kappa \boldsymbol{\sigma}^{1}\left(\mathbf{x}, \frac{\mathbf{x}}{\kappa}\right) + \mathcal{O}\left(\kappa^{2}\right), \tag{2.2.15}$$

$$\mathbf{q}^{\kappa}(\mathbf{x}) = \mathbf{q}^{0}\left(\mathbf{x}, \frac{\mathbf{x}}{\kappa}\right) + \kappa \mathbf{q}^{1}\left(\mathbf{x}, \frac{\mathbf{x}}{\kappa}\right) + \mathcal{O}\left(\kappa^{2}\right) \tag{2.2.16}$$

is made. We define the microscopic variable $\mathbf{y} = \mathbf{x}/\kappa$ to proceed. Inserting the asymptotic ansatz into the equations (2.2.10)-(2.2.12) and as $\kappa \to 0$, we obtain the relation

$$\nabla^{s}_{\mathbf{y}} \mathbf{u}^{0}(\mathbf{x}, \mathbf{y}) = 0 \tag{2.2.17}$$

from which follows that $\mathbf{u}^0$ is independent of the microscopic variable $\mathbf{y}$ via the Korn-Poincaré inequality [51] and the equations

$$\boldsymbol{\varepsilon}^{0}(\mathbf{x}, \mathbf{y}) = \nabla^{\mathrm{s}}_{\mathbf{x}} \mathbf{u}^{0}(\mathbf{x}) + \nabla^{\mathrm{s}}_{\mathbf{y}} \mathbf{u}^{1}(\mathbf{x}, \mathbf{y}), \text{ microscopic compatibility condition} \tag{2.2.18}$$

$$\boldsymbol{\sigma}^{0}(\mathbf{x}, \mathbf{y}) = \frac{\partial w}{\partial \boldsymbol{\varepsilon}^{0}} \left(\boldsymbol{\varepsilon}^{0}, \mathbf{q}^{0} \right)(\mathbf{x}, \mathbf{y}), \text{ microscopic constitutive equation} \tag{2.2.19}$$

$$\operatorname{div}_{\mathbf{y}} \boldsymbol{\sigma}^{0}(\mathbf{x}, \mathbf{y}) = 0, \text{ microscopic balance of linear momentum} \tag{2.2.20}$$

$$\operatorname{div}_{\mathbf{x}} \left\langle \boldsymbol{\sigma}^{0}(\mathbf{x}, \mathbf{y}) \right\rangle_{Y} = -\mathbf{b}, \text{ macroscopic balance of linear momentum.} \tag{2.2.21}$$

Inserting equation (2.2.18) and (2.2.19) into equation (2.2.20) and using the short-hand notation $\mathbf{E} = \nabla^{\mathrm{s}}_{\mathbf{x}} \mathbf{u}^0(\mathbf{x})$ for the macroscopic strain, we obtain

$$\operatorname{div}_{\mathbf{y}} \left(\frac{\partial w}{\partial \boldsymbol{\varepsilon}^0} \left(\mathbf{E} + \nabla^{\mathrm{s}}_{\mathbf{y}} \mathbf{u}^1, \mathbf{q}^0 \right) \right) = 0 \tag{2.2.22}$$

for the microscopic balance of linear momentum. In the context of FFT-based micromechanics, it is convenient to reformulate the microscopic balance of linear momentum (2.2.22) in the Fourier space. For the displacement fluctuation $\mathbf{u}^1$, we make the ansatz

$$\mathbf{u}^1 = \sum_{\eta \in \mathbb{Z}^d} \hat{\mathbf{u}}(\eta) \exp\left(\frac{2\pi i}{L} \mathbf{y} \cdot \eta \right), \tag{2.2.23}$$

where $\mathbb{Z}^d$ denotes the space of d-dimensional integers, i is the complex unit and $\hat{\mathbf{u}}$ are the complex valued Fourier coefficients. We introduce the auxiliary problem

$$\operatorname{div}_{\mathbf{y}} \left(\mathbb{C}_0 : \nabla^s \mathbf{u} \right) = \mathbf{f} \tag{2.2.24}$$

with the isotropic reference stiffness $\mathbb{C}_0$ with the Lamé constants λ_0 and μ_0. The Green's operator $\mathbf{G}_0$ defined as

$$\hat{\mathbf{G}}_0(\eta) = \begin{cases} -\frac{1}{\mu_0 \|\eta\|^2} \mathbf{I} + \frac{\mu_0 + \lambda_0}{(2\mu_0 + \lambda_0)\, \mu_0\, \|\eta\|^2} \eta \otimes \eta, & \text{if } \eta \neq 0, \\ 0, & \text{otherwise.} \end{cases} \tag{2.2.25}$$

Then, we obtain the solution

$$\hat{\mathbf{u}}\left(\eta\right) = \hat{\mathbf{G}_0}\left(\eta\right) \cdot \hat{\mathbf{f}}\left(\eta\right) \quad \text{or} \quad \mathbf{u}(\mathbf{x}) = \left(\mathbf{G}_0 * \mathbf{f}\right)(\mathbf{x}) = \int_Y \mathbf{G}_0(\mathbf{x} - \mathbf{y}) \cdot \mathbf{f}(\mathbf{y}) \mathrm{d}\mathbf{y}. \tag{2.2.26}$$

With the auxiliary solution at hand, we turn our attention back to the microscopic boundary value problem (2.2.22) and subtract the term $\operatorname{div}\left(\mathbb{C}_0 : \left(\mathbf{E} + \nabla^{\mathrm{s}} \mathbf{u}^1\right)\right)$ on both sides of the equation

$$\operatorname{div}\ \left(\frac{\partial w}{\partial \boldsymbol{\varepsilon}^0} \left(\mathbf{E} + \nabla^{\mathrm{s}}_{\mathbf{y}} \mathbf{u}^1, \mathbf{q}^0 \right) - \mathbb{C}_0 : \left(\mathbf{E} + \nabla^{\mathrm{s}} \mathbf{u}^1 \right) \right) = -\operatorname{div}\ \left(\mathbb{C}_0 : \left(\mathbf{E} + \nabla^{\mathrm{s}} \mathbf{u}^1 \right) \right), \tag{2.2.27}$$

where we dropped the dependence of the variables on the microscopic variable $\mathbf{y}$ for simplicity of notation. Since $\mathbb{C}_0 : \mathbf{E}$ is constant, the term $\operatorname{div}\left(\mathbb{C}_0 : \mathbf{E}\right)$ vanishes, and we obtain

$$-\operatorname{div}\ \left(\frac{\partial w}{\partial \boldsymbol{\varepsilon}^0} \left(\mathbf{E} + \nabla^{\mathrm{s}}_{\mathbf{y}} \mathbf{u}^1, \mathbf{q}^0 \right) - \mathbb{C}_0 : \left(\mathbf{E} + \nabla^{\mathrm{s}} \mathbf{u}^1 \right) \right) = \operatorname{div}\ \left(\mathbb{C}_0 : \left(\nabla^{\mathrm{s}} \mathbf{u}^1 \right) \right). \tag{2.2.28}$$

We define the polarization stress τ by

$$\tau\left(\mathbf{u}^1, \mathbf{q}^0\right) = \frac{\partial w}{\partial \boldsymbol{\varepsilon}^0}\left(\mathbf{E} + \nabla_{\mathbf{y}}^{\mathrm{s}}\mathbf{u}^1, \mathbf{q}^0\right) - \mathbb{C}_0 : \left(\mathbf{E} + \nabla^{\mathrm{s}}\mathbf{u}^1\right) \tag{2.2.29}$$

and finally derive

$$-\mathrm{div}\ \tau = \mathrm{div}\left(\mathbb{C}_0 : \left(\nabla^{\mathrm{s}}\mathbf{u}^1\right)\right), \tag{2.2.30}$$

which is of the same form as the auxiliary problem (2.2.24) for which we know the solution. We obtain the equation

$$\mathbf{u}^1 = -\mathbf{G}_0\,\mathrm{div}\left[\tau\left(\mathbf{u}^1, \mathbf{q}^0\right)\right] \tag{2.2.31}$$

or

$$\boldsymbol{\varepsilon}^0 = \mathbf{E} - \nabla^{\mathrm{s}}\mathbf{G}_0\,\mathrm{div}\left[\tau\left(\mathbf{u}^1, \mathbf{q}^0\right)\right]. \tag{2.2.32}$$

The latter is the well-known Lippmann-Schwinger equation in elasticity. The operator $\boldsymbol{\Gamma}^0 = \nabla^s\mathbf{G}_0\mathrm{div}$ is called Eshelby-Green operator. We derived the Lippmann-Schwinger equation from the microscopic boundary value problem (2.2.18)-(2.2.20). Both formulations are equivalent.
Moulinec and Suquet [10] proposed an algorithm to solve the Lippmann-Schwinger equation by using the Fast Fourier Transform (FFT). For fixed $\mathbf{q}^0$, the equation (2.2.32) is a fixed point equation. With the definition of an operator $\mathbb{B}$ via

$$\mathbb{B} : \boldsymbol{\varepsilon}^0 = \boldsymbol{\Gamma}^0 * \left(\frac{\partial w}{\partial \boldsymbol{\varepsilon}^0}\left(\boldsymbol{\varepsilon}^0, \mathbf{q}^0\right) - \mathbb{C}_0 : \boldsymbol{\varepsilon}^0\right) \tag{2.2.33}$$

the Lippmann-Schwinger equation (2.2.32) can be rearranged to

$$\boldsymbol{\varepsilon}^0 = (\mathbf{I} + \mathbb{B})^{-1} : \mathbf{E}. \tag{2.2.34}$$

For the linear case, a representation of the above equation as Neumann series

$$(\mathbf{I} + \mathbb{B})^{-1} : \mathbf{E} = \mathbf{E} + \sum_{i=1}^{\infty}(-\mathbb{B})^j : \mathbf{E} \tag{2.2.35}$$

gives rise to the iterative scheme known as the continuous algorithm [10]. To be able to compute a microstructure on a computer, we discretize the continuous problem to obtain an approximate problem with finite degrees of freedom. Suppose we have a cubic body Y_N subdivided into $N \times N \times N$ cubic elements called voxels. Then, instead of evaluating the microscopic fields on all $\mathbf{y} \in Y$ as in the continuous algorithm, the microscopic fields are only evaluated at $n = 1 \ldots N^3$ points and the Fourier transform $\mathcal{FT}$ is

Algorithm 1 Discrete algorithm [10]

// Initialization
$\boldsymbol{\varepsilon}_N = E$
while no convergence **do**
  $\tau_N = \boldsymbol{\sigma}_N(\boldsymbol{\varepsilon}_N) - \mathbb{C}_0 : \boldsymbol{\varepsilon}_N$
  $\hat{\tau}_N = \mathcal{DFT}(\tau_N)$
  check convergence
  $\hat{\boldsymbol{\varepsilon}}_N(\eta) = -\hat{\Gamma}^0_N : \hat{\tau}_N(\eta)$
  $\hat{\boldsymbol{\varepsilon}}_N(0) = \mathbf{E}$
  $\boldsymbol{\varepsilon}_N = \mathcal{DFT}^{-1}(\hat{\boldsymbol{\varepsilon}}_N)$
end while

replaced by the discrete Fourier transform $\mathcal{DFT}$. Moulinec and Suquet [10, 48] proposed to evaluate the strain fluctuations at the voxel centers and use the approximated strain field $\boldsymbol{\varepsilon}_N$

$$\boldsymbol{\varepsilon}_N(\mathbf{y}) = \sum_{\eta \in \mathbb{Z}^3_N} \hat{\boldsymbol{\varepsilon}}_N(\eta) \exp\left(\frac{2\pi i}{N} \eta \cdot \mathbf{y}\right) \tag{2.2.36}$$

with

$$\mathbb{Z}^3_N = \left\{ \eta \in \mathbb{Z}^3 \,\middle|\, -(N/2) + 1 \leq \eta_j \leq (N/2) \text{ for all } j = 1, \ldots, 3 \right\}. \tag{2.2.37}$$

The obtained algorithm is summarized in algorithm 1. The Eshelby-Green operator Γ^0 has an explicit representation in Fourier space and is thus applied in the Fourier space. The development of the *Fast Fourier Transform* (FFT) algorithm and its efficient and parallelized execution using the *Fastest Fourier Tranform in the West* (FFTW) [52] implementation significantly contributes to the performance of the scheme.
This original discretization with trigonometric functions has some disadvantages such as ringing artifacts in the solution fields. It has triggered further development of different discretization schemes for FFT-based solvers, such as the Willot discretization [53] and the staggered grid scheme [54]. At the same time, solution methods have also been developed further. We refer to the review article of Schneider [11] for a recent overview.

2.3. Galerkin method

To solve boundary value problems of classical continuum mechanics discussed in chapter 2.1 or other partial differential equations numerically, the next step is a discretization of the equations.
In solid mechanics, a popular discretization method is the Galerkin discretization. It is used both in finite element methods (FEM) and model order reduction techniques and approximates the variational equation (weak form) of the boundary value problem in a finite dimensional space.

2.3.1. Galerkin discretization

For the sake of simplicity, we restrict the discussion to the isothermal case with linear-elastic materials in this section. For non-linear problems, typically the linearized system is solved. First, we present the Galerkin discretization starting from the classical formulation of the equations. Subsequently, its application in the finite element method (section 2.4) and model order reduction techniques (section 2.3.2) is discussed.
For a conservative mechanical systems, its potential energy Π is given by the sum of its inner potential

$$\Pi_i(\mathbf{u}) = \int_{\mathcal{B}} w(\boldsymbol{\varepsilon}(\mathbf{u}))\,\mathrm{d}V \tag{2.3.1}$$

and the potential of external forces

$$\Pi_a(\mathbf{u}) = -\int_{\mathcal{B}} \mathbf{u}\cdot\mathbf{b}\,\mathrm{d}V - \int_{\partial\mathcal{B}_n} \mathbf{t}_0\cdot\mathbf{u}\,\mathrm{d}A. \tag{2.3.2}$$

via

$$\Pi(\mathbf{u}) = \Pi_i(\mathbf{u}) + \Pi_a(\mathbf{u}). \tag{2.3.3}$$

Using the principle of minimum total potential energy, the first variation $\delta\Pi$ must be zero, i.e.,

$$\delta\Pi = 0. \tag{2.3.4}$$

For linear-elastic materials, the free energy potential $w(\boldsymbol{\varepsilon})$ is given by

$$w(\boldsymbol{\varepsilon}) = \frac{1}{2}\boldsymbol{\varepsilon} : \mathbb{C} : \boldsymbol{\varepsilon} \tag{2.3.5}$$

Then, the first variation of the potential energy Π in the direction of a test function $\mathbf{w}$ is

$$\delta\Pi = \int_{\mathcal{B}} [(\mathbb{C} : \nabla^s \mathbf{u}) : \nabla^s \mathbf{w} - b \cdot \mathbf{w}] \, \mathrm{d}V - \int_{\partial\mathcal{B}_n} \mathbf{t}_0 \cdot \mathbf{w} \, \mathrm{d}A. \tag{2.3.6}$$

The displacement $\mathbf{u}$ is equal to prescribed values $\mathbf{u}_0$ on the Dirichlet boundary $\mathcal{B}_\mathbf{u}$ and lives in the space of solution functions

$$\mathcal{V}^* = \left\{ \mathbf{u} \in \mathcal{H}^1 \, : \, \mathbf{u}\big|_{\mathcal{B}_u} = \mathbf{u}_0 \right\}, \tag{2.3.7}$$

with the Sobolev space $\mathcal{H}^1$. A function $\mathbf{u}$ is an element of the Sobolev space $\mathcal{H}^1$ if the components of $\mathbf{u}$, denoted by u_α, and their partial derivatives $\partial u_\alpha / \partial x_\alpha$ are elements of the Lebesgue space $\mathcal{L}_2$ on which the scaler product

$$(f, g)_{\mathcal{L}_2} := \int_{\mathcal{B}} f \, g \, \mathrm{d}V \tag{2.3.8}$$

is defined. We introduce the short-hand notations

$$a(\mathbf{u}, \mathbf{w}) = \int_{\mathcal{B}} (\mathbb{C} : \nabla^s \mathbf{u}) : \nabla^s \mathbf{w} \, \mathrm{d}V, \tag{2.3.9}$$

$$f(\mathbf{w}) = \int_{\mathcal{B}} \mathbf{w} \cdot \mathbf{b} \, \mathrm{d}V + \int_{\partial\mathcal{B}_n} \mathbf{t}_0 \cdot \mathbf{w} \, \mathrm{d}A. \tag{2.3.10}$$

Then, the variational equation can be expressed in a compact manner via the bilinear form a and the linear form f:

$$\mathbf{u} \in \mathcal{V}^* \, : \, a(\mathbf{u}, \mathbf{w}) = f(\mathbf{w}) \;\; \text{for all } \mathbf{w} \in \mathcal{V}. \tag{2.3.11}$$

In Galerkin methods, the discretized problem is obtained by projection of the continuous formulation onto a finite dimensional subspace $\mathcal{V}_h^* \subset \mathcal{V}^*$ and $\mathcal{V}_h \subset \mathcal{V}$. The discretized form reads

$$\mathbf{u}_h \in \mathcal{V}_h^* \, : \, a(\mathbf{u}_h, \mathbf{w}_h) = f(\mathbf{w}_h) \;\; \text{for all } \mathbf{w}_h \in \mathcal{V}_h. \tag{2.3.12}$$

2.3.2. Finite element method

As shown in Fig. 2.3, in finite element methods the material body $\mathcal{B}$ is approximated by a decomposition

$$\mathcal{B} \approx \mathcal{B}_h = \bigcup_{e=1}^{n_e} \mathcal{B}_e \tag{2.3.13}$$

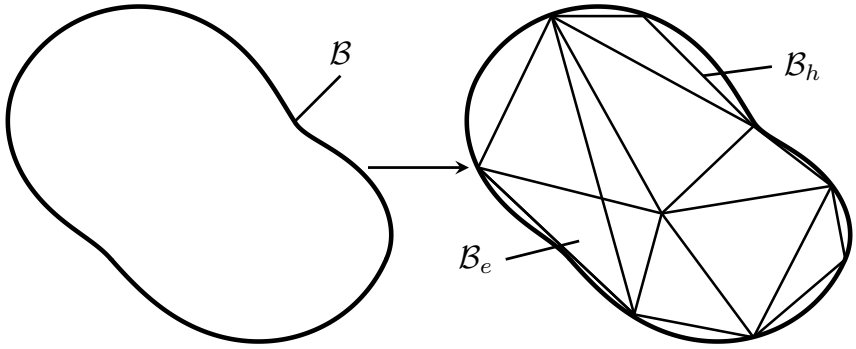

Figure 2.3.: Discretization with triangular finite elements

into a finite number of elements $\mathcal{B}_e$. The displacement is determined by a finite number of nodes x_i on the element with the nodal displacements $\mathbf{u}_i$. Using shape functions $N_i(\mathbf{x})$, the ansatz

$$\mathbf{u}_h = \sum_{i=1}^{N} N_i(\mathbf{x})\mathbf{u}_i \quad \text{for all} \quad \mathbf{x} \in \mathcal{B}_e \tag{2.3.14}$$

is made for the discretized displacement $\mathbf{u}_h$. For the test functions $\mathbf{w}_h$ the same shape functions are chosen. From the obtained discretized system, a linear system of equations can be assembled and the solved computationally. The finite element method is widely used in continuum mechanics simulation. We refer to Zienkiewicz et al. [55] and Fish and Belytschko [56] for an overview.

2.4. Model order reduction

Model order reduction approaches may be subdivided into system theoretical approaches and numerical analysis of partial differential equations [57, Chapter 1]. We are focus on a discussion of the latter in this section.

In most practical applications, a direct coupling of micro- and macroscale, e.g., via the FE^2-method or an FFT-FE-scheme, is limited to rather small macroscale components or two-dimensional simulations. To predict the macroscopic behavior of complex components with limited computational resources and in a limited amount of time, reduced models have been developed.

In reduced basis methods, an M-dimensional projection space $\mathcal{V}_H$ is identified. The reduced order model seeks a solution

$$a(\mathbf{u}_H, \mathbf{w}_H) = f(\mathbf{w}_H) \quad \text{for all } \mathbf{w}_H \in \mathcal{V}_H.$$

where the full-field solution $\mathbf{u}_h$ is approximated by

$$\mathbf{u}_h \approx \sum_{i=0}^{M} \mathbf{u}_H^i V_H^i \tag{2.4.1}$$

and V_H^i are the modes spanning $\mathcal{V}_H$. Here, the dimension of the full order model (FOM) N needs to be much larger than the dimension of the ROM M to gain computational efficiency. For the identification of the projection space, multiple methods have been applied in literature. One of the most common is the proper orthogonal decomposition (POD) [58, 59]. Here, the point of departure is some N-dimensional solution fields $\mathbf{u}_h$ obtained by the FOM, e.g. a finite element computation (section 2.3.2) or a FFT-computation (section 2.2), often called snapshots. Subsequently, the the principal components of the fields and their associated eigenvalues are computed. A set of principal components with the largest corresponding eigenvalues is then chosen as reduced basis. It is easy to implement and approximation is optimal in the $\mathcal{L}^2$-norm. Reduced basis methods (RB) [60], in contrast, need fewer FOM-realizations and uses of a greedy sampling approach. In contrast to POD and RB, Proper Generalized Decomposition (PGD) [61,62] methods not only decompose the solution in time and spatial domain, but decompose the solution into a functional representation of each spatial variable and parameter. This makes the method very general and can be viewed as an extension of the classical POD. In the context of micromechanics and for nonlinear materials with constitutive equations that admit a split into elastic and inelastic components, Dvorak and coworkers [63,64] developed the Transformation Field Analysis (TFA). Here, the basis functions are piece-wise constant. This approach later sparked the development of the Nonuniform Transformation Field Analysis (NTFA) [65] using POD to identify mode fields [66]. On the question of suitable evolution equations for the macroscopic state variables within this framework, Fritzen [67] proposed a derivation of the evolution laws based on an incremental variational formulation, which is applicable to arbitrary generalized standard materials (GSM). Another approach, first proposed by Liu and coworkers [68] is the self consistent clustering analysis directly derived from a Lippmann-Schwinger formulation for microstructures with piece-wise constant fields. It has been shown to be closely related to th TFA [69]. Recent developments include an adaptive clustering [70] and extension to the macroscale [71].
A problem remaining in projection-based reduced order models is the efficient evaluation of models with non-affine parameter dependence. Then, an integration of a mode-dependent function over the microsopic domain is necessary at the online-stage. Thus, the computational effort of the reduced order model still depends on the size of the microscopic volume element. Common methods to overcome this issue are the empirical interpolation method, where the forcing term is projected on to a collateral basis [72, 73], and quadra-

ture approaches [74, 75] to get a fast approximation of the integral in the online phase. For comparison of the latter two methods, see, e.g., von Tuijl et al. [76]. Other approaches rely on Taylor approximations [77–80].
Instead of using linear projection techniques like the POD, nonlinear low-dimensional representations of the space may be used, e.g., exploiting neural network architectures [81, 82] (NN). Other NN-based methods directly construct a purely data-driven macroscopic model [83,84] or approximate the forcing term of the equations via NNs [85].
A different route to efficient macroscale models is based on the approximation of the microstructure (instead of the material law). Recent developments in this direction comprise the method of statistical similar volume elements [86, 87] and deep material networks [88–90].

2.5. Short-fiber reinforced thermoplastics

After having discussed the fundamentals of mechanics and discretization schemes as well as computational homogenization in the previous sections, we now turn our attention to a discussion of the material class of SFRT.
Due to their comparatively large stiffness to weight ratio, the usage of fiber reinforced polymers in light-weight engineering applications increased significantly in recent years. Available fiber reinforced polymers can be classified by their fiber length or their matrix material. In the work at hand, we are interested in *short*-fiber reinforced polymers. Typical fiber aspect ratios, i.e., the fiber length to fiber diameter ratios are in the order of ten. In contrast to other polymeric materials such as thermosets, thermoplastic materials can be melted and welded, which improves their recycability in comparison to thermoset materials.
The material behavior of thermoplastic materials is rather complex. Its properties depend on a multitude of conditions, such as their crystallinity, in some cases humidity [91, 92] and temperature [93–95]. Additionally, they exhibit rate dependency. The root cause of their rate dependent material behavior can be found on the molecular scale of the material: time-dependent chain oscillations and grain boundary relaxation [96]. These chain oscillations can be thermally activated. Thus, an increase in temperature leads to a shift of the mechanical properties of the material. Williams, Landel and Ferry [97] proposed a widely used model to represent this temperature-rate superposition. The (rate dependent) properties of thermoplastics are not only dependent on temperature, but may also be changed by fillers [98, 99] or the blending of different thermoplastics [100].

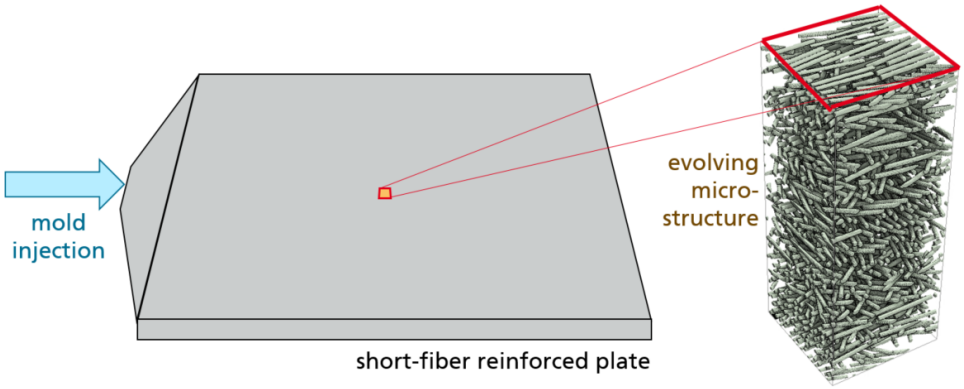

Figure 2.4.: Evolving microstructure in injection molded short-fiber reinforced component

The complex material behavior of neat thermoplastics is transferred to the effective behavior of (short-)fiber reinforced composites, e.g., the rate dependency observed in neat materials translates to a rate dependency of the composite materials [101–103]. As shown in Fig. 2.4, short-fiber reinforced thermoplastic components are typically produced by injection molding. Even for simple component geometries, e.g. the plate shown in Fig. 2.4, the process leads to a locally varying fiber structure within the engineering component. The fiber orientation evolving depends on the plate thickness. For a 2mm thick plate, Andrä et al. [104] analyzed the fiber orientation over the plate thickness. In the shell layer of the plate most fibers point in flow direction, while in the inner layers a more planar isotropic structure evolves. In more sophisticated engineering components, the microstructure is rather complex and process dependent. Thus, a different (anisotropic) macroscopic material behavior at possibly every point of the component has to be understood, when predicting the mechanical behavior of the component. Additional to the fiber orientation, the macroscopic material behavior depends on its fiber volume content and the geometry of the inclusions [105, 106].

2.6. Fatigue

Mechanical fatigue is the process of slow degeneration and final failure of a material under cyclic loading with rather low amplitudes. In the following section, firstly, the material scientific origin of fatigue degradation in SFRT is briefly reviewed (section 2.6.1). Secondly, material modeling of fatigue is discussed in section 2.6.2.

2.6.1. Material science of fatigue

The fatigue degradation of metallic material has been an area of extensive research during the last century. Fatigue in metallic materials is caused by dislocation motion [107]. In contrast to that, polymer materials are rather new. Here, molecular rearrangements and the formation of microvoids are the root cause of fatigue degradation. Thus, the cristallinity of the material affects its fatigue strength [108]. In semi-crystalline materials, the elementary process from which a damage process starts, is nucleation [109]. In the first stage of fatigue of neat thermoplastics, the number of cavities increases whereas their size remains constant [110]. In this regime of uncorrelated nucleation, the dynamic modulus of the material decreases linear over the logarithmic cycle space [111]. Later, dependent on the disorder and the stress level in the material, either an accumulation of the defects or growth of a single cavity lead up to third and final stage of fatigue: microcrack propagation and failure of the material [111]. The dynamics of this process have been modeled by Fusco et al. [112]. Careful analysis suggests, that in creep and fatigue fracture intraspherulitic fracture develops ahead of the microcrack, which propagates in charcteristic increments that correspond to the size of spherulits in size [113,114]. However, the precise mechanism is still under research as detection of microvoids and thus understanding the physically processes involved is still rather challenging [114, 115].
In SFRT, local fatigue mechanisms leading to this macroscopically observable degradation are fiber failure, fiber debonding and damage within the matrix material [116]. The contribution of the fatigue damage evolving within the matrix is rather significant for the degradation process [110, 117–119]. As in the neat material, the root cause of fatigue damage is microvoid formation [110] that triggers all other damage mechanisms. The introduction of fibers into the matrix leads to a complex stress distribution and the local fatigue processes strongly depend on fiber orientation [120, 121], fiber volume fraction, fiber aspect ratio [122] and fiber-matrix adhesion [117]. For an overview of the most relevant effects, see Mortazavian et al. [123].

2.6.2. Fatigue modelling

Fatigue was first studied by Wöhler [124] for metallic materials. He observed an logarithmic dependence of the bearable stress amplitude on the cycle number. A Wöhler curve gives the expected failure cylce for a specific component. Later, based on Griffith's theory of brittle fracture [125], Paris [126] first described the evolution of a crack under fatigue loading, linking fracture mechanics and fatigue prediction.

To understand mechanisms at molecular level, molecular dynamics simulations can be applied to amorphous polymers [127, 128]. At a coarser level, polymer-based materials subjected to fatigue loading typically show three stages of fatigue [3–6]: an initial rapid decrease of the stiffness properties, a secondary stable and moderate stiffness degradation and a final failure corresponding to a rapid decay of the material stiffness, see Fig. 1.1(b). On this coarser level, the material can be modeled as a continuum. Based on continuum damage mechanics [129] or the closely related phase-field fracture approach [130–133], constitutive models indirectly account for the physical processes like crazing on the microscale. The damage models of Lemaitre [134, 135] and Gurson [136] regard fatigue damage as a reduction of the effective cross section, i.e., a reduction of the stiffness of the material. This reduction is parameterized by a damage variable, which evolves under certain loading conditions. The phase-field fracture approach [132, 133] is motivated by the regularization of a sharp crack to a diffuse approximation. Originally developed for fracture under static loading conditions, it has also been applied to fatigue fracture [137–139].

To predict fatigue *failure* of fiber-reinforced materials, one of the first developed approaches was the Through Processes Modeling (TPM). It is based on an elastic computation on the component, the identification of critical spots based on the stress field in the elastic computation and a prediction of the fatigue failure based on a suitable fatigue criterion [140–144]. The approach enables a simple and efficient estimation of the fatigue failure. However, due to the stiffness degradation of SFRT prior to failure, a redistribution of stresses may occur on component level. TPM methods are not able to account for this effect.

To predict the gradual degradation of the material, fatigue *damage* models have been developed. They can be subdivided into phenomenological, analytical and computational methods. Phenomenological models are formulated directly on the macroscopic scale [5, 145–148]. Their demand for experimental investigations is comparatively high, as a multitude of load cases needs to be investigated prior to the formulation of a meaningful material model for the composite. However, once identified, they are computationally efficient and rather simple to implement. On the other hand, multiscale methods formulate material models for each constituent and derive the composite behavior from homogenization techniques. The necessary experimental effort is thus significantly decreased. Mean field methods for fatigue damage [7–9] are based on analytic homogenization and are thus limited to rather simple inclusion shapes. Their main advantage is their computational efficiency. Another multiscale approach is computational homogenization. It is advantageous in its accuracy of the prediction and more flexible in comparison to mean-field approaches. FFT-based computational methods are discussed in section 2.2 in more detail.

3. A computational multi-scale model for the stiffness degradation of short-fiber reinforced plastics subjected to fatigue loading[1]

3.1. Introduction

In this chapter, we introduce a multi-scale model for fatigue-induced stiffness degradation of short-fiber reinforced composites which, on the one hand, accounts for the microscopic geometry of fiber-reinforced composites, and, on the other hand, is capable of performing industrial-scale component simulations.
A continuum damage model for the matrix material serves as our point of departure. The model which is discussed within the setting of the two-potential framework of dissipative materials introduced by Halphen & Nguyen [17]. We chose to work directly in cycle space, such that we may ignore viscous effects, on the one hand, and profit from a discretization in "time" that permits skipping several orders of cycles at once. The model is presented in section 3.2, and is based on a quadratic degradation function.
We assume that fatigue effects are rooted on the micro-scale, and that the inclusions

[1] Reproduced from: J. Köbler, N. Magino, H. Andrä, F. Welschinger, R. Müller, M. Schneider, "A computational multi-scale model for the stiffness degradation of short-fiber reinforced plastics subjected to fatigue loading," *Computer Methods in Applied Mechanics and Engineering*, vol. 373, pp. 113522, 2021.

serve as "defects" where cracks originate from. The scale-transition procedure within the two-potential framework is discussed in section 3.2. By this homogenization process, the anisotropic degradation of the effective stiffness is naturally accounted for.
Subsequently, see section 3.3, we thoroughly investigate the multi-scale model on volume-element level, both in terms of the numerical parameters, cf. section 3.3.2 and by varying both the loading and the composition of the fiber-filled volume elements, see section 3.3.3.
We discuss the model-order reduction strategy in section 3.4, including the necessary fiber-orientation interpolation procedure, and present numerical investigations on the necessary modes and on the accuracy of the model. The matrix fatigue-damage model was chosen essentially *because* it permits straightforward model-order reduction while, at the same time, maintaining several properties of a fatigue-damage model that we consider attractive. For instance, it naturally accounts for irreversibility of damage, and forces the damage variables to attain values in the interval $[0, 1]$ automatically.
Finally, in section 3.5.4, we demonstrate that the fully identified multi-scale model permits conducting industrial-scale finite element simulations on component level by analyzing an automotive application, i.e., a plastic housing component of an electric window-lift drive.
The presented model contrasts strongly to the approach to fatigue damage in the phase-field context proposed by Carrara et al. [137] and Alessi et al. [138], as the mentioned references are primarily concerned with metallic materials and model the growth of fatigue cracks (on component scale). This is achieved by adding an evolution equation for the crack resistance.
The model presented in this work targets the stiffness degradation observed in polymeric materials under fatigue loading – an effect that is negligible for most metallic components – and is explicitly settled in a multi-scale context. Also, we do not model crack growth on the macroscopic scale.
Of course, that does not mean that both models could not be combined. However, the intrinsic anisotropy of short-fiber reinforced materials necessitates also modeling the crack resistance in an anisotropic way [149, 150].

3.2. A gradient-enhanced fatigue-damage model for the matrix

We use the two-potential framework [17] for describing our fatigue-damage model. However, we shall work in the cycle domain instead of the time domain. Notice that, for fatigue experiments, a large number of cycles N, typically on the order of a few thousands or

millions at least, has to be considered. Within each cycle, a periodic or quasi-periodic loading is applied. As each individual cycle again needs to be discretized by a number of time steps, resolving fatigue-type experiments in the time domain may be computationally demanding or even infeasible.

As a workaround, time-homogenization approaches may be used [151, 152] for realizing an upscaling in time. For the article at hand, we chose to start with a model defined in the cycle domain right away, i.e., the temporal evolution of the fields and quantities of interested is described in terms of a continuous parameter $N \geq 0$ with dimension 1 instead of the more familiar time variable.

Clearly, the two-potential framework [17] carries over viz-a-viz to this setting, with terminological modifications. For instance, $\boldsymbol{\varepsilon}$ and $\boldsymbol{\sigma}$ refer to (tensorial) strain and stress *amplitudes*, respectively. Also, the dimensions of the dissipation potential ϕ change - in the cycle domain, the total dissipation of the cycle is measured, and not per unit of time. Despite these changes, we shall retain the terminology dissipation potential. We indicate the derivative of any quantity q w.r.t. the cycle N by $q' \equiv \mathrm{d}q/\mathrm{d}N$ for notational convenience.

For the homogeneous model, we work with a single scalar damage variable d. As free energy density, we use

$$w(\boldsymbol{\varepsilon}, d) = \tfrac{1}{2}[\eta + (1-d)^2]\, \boldsymbol{\varepsilon} : \mathbb{C} : \boldsymbol{\varepsilon} \tag{3.2.1}$$

involving a given stiffness tensor $\mathbb{C}$ and a positive constant η. The latter constant is typically small, and introduced for avoiding ill-posedness of the resulting field equations. Indeed, the constant η determines the residual stiffness $\eta\,\mathbb{C}$ in a fully damaged state, i.e., for $D = 1$. The corresponding stress computes as

$$\boldsymbol{\sigma} \equiv \frac{\partial w}{\partial \boldsymbol{\varepsilon}}(\boldsymbol{\varepsilon}, d) = [\eta + (1-d)^2]\, \mathbb{C} : \boldsymbol{\varepsilon}, \tag{3.2.2}$$

i.e. the variable $d \in (0, 1]$ decreases the stiffness in a homothetic fashion.

The two-potential framework is complemented by the quadratic dissipation potential

$$\phi(d') = \frac{1}{2\alpha_{\mathrm{d}}}(d')^2, \tag{3.2.3}$$

involving a phenomenological parameter α_{d} of dimension 1/stress, i.e., 1/MPa. The resulting Biot's equation

$$0 = \frac{\partial w}{\partial d}(\boldsymbol{\varepsilon}, d) + \frac{\partial \phi}{\partial d'}(d') \equiv -(1-d)\, \boldsymbol{\varepsilon} : \mathbb{C} : \boldsymbol{\varepsilon} + \frac{1}{\alpha_{\mathrm{d}}}\, d'$$

may be re-arranged into the ordinary differential equation

$$d' = \alpha_{\mathrm{d}}\, (1-d)\, \boldsymbol{\varepsilon} : \mathbb{C} : \boldsymbol{\varepsilon}, \tag{3.2.4}$$

i.e., the evolution of D is governed by (a scaled version of) the stored elastic energy $\frac{1}{2}\boldsymbol{\varepsilon} : \mathbb{C} : \boldsymbol{\varepsilon}$ corresponding to the undamaged medium. We see that the parameter α_{d} controls the speed of evolution of the ordinary differential equation (3.2.4).
For a free energy of the form (4.2.1) we see that, as long as $d \leq 1$, d is non-decreasing. Thus, the irreversibility of damage is a direct consequence of the evolution (3.2.4). Also, for $d = 1$, the right hand side of (3.2.4) vanishes. Thus, provided $d(0) = 0$ is used as the initial condition, d will remain in the interval $[0, 1]$ for all time, in accordance with physical reasoning.
As α_{d} enters linearly in the right-hand side of the evolution equation (3.2.4), the latter equation may be re-arranged in the form

$$\frac{\mathrm{d}d}{\mathrm{d}(\lambda N)} = \frac{\alpha_{\mathrm{d}}}{\lambda}\,(1-d)\,\boldsymbol{\varepsilon} : \mathbb{C} : \boldsymbol{\varepsilon} \quad \text{for any} \quad \lambda > 0.$$

Thus, scaling α_{d} essentially changes the time scale on which effects take place. Put differently, on a normalized cycle scale, the behavior of the model (3.2.4) is *independent* of α_{d}.

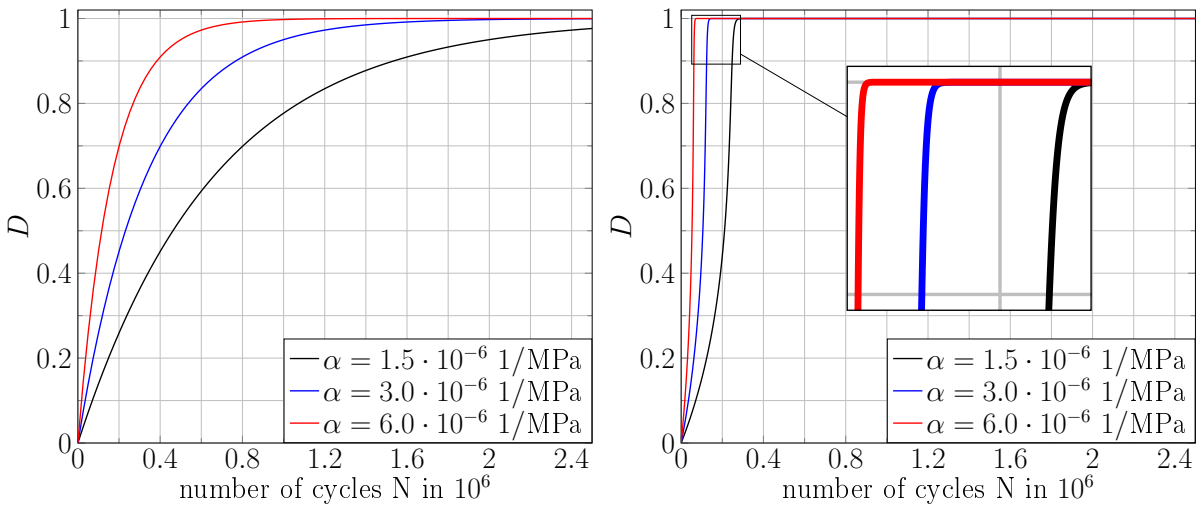

(a) Constant strain (amplitude)

(b) Constant stress (amplitude)

Figure 3.1.: One-dimensional solution for different α_{d} subjected to constant strain (left) and stress (right) amplitudes

To gain intuition concerning this model, we shall investigate uni-axial extension in one spatial dimension. For prescribed uni-axial strain (amplitude) ε_0 and initial condition $d(0) = 0$, the solution computes as

$$d(N) = 1 - \exp\left(-\alpha_{\mathrm{d}} E \varepsilon_0^2 N\right), \tag{3.2.5}$$

where E denotes Young's modulus. For $\varepsilon_0 = 2\ \%$ and $E = 2500\,\mathrm{MPa}$, the solution is shown in figure 3.1(a). For constant strain (amplitude), the damage variable converges asymptotically to the fully broken state.
For constant stress amplitude σ_0, the solution D at cycle N satisfies the equation

$$(1-d)^4 + 4\eta\,(1-d)^2 + 4\eta^2 \ln(1-D) = 1 + 4\eta - \alpha_\mathrm{d}\frac{4\sigma_0^2}{E}N. \tag{3.2.6}$$

Solutions for $\sigma_0 = 50$ MPa, $\eta = 0.1$ and $E = 2500\,\mathrm{MPa}$ and different values for α_d are shown in figure 3.1(b). The damage variables increases with increasing slope until it reaches a plateau close to 1. Due to the residual stiffness η, a smooth transition from the highly damaged to the fully broken state is ensured.
We complete the discussion of the material model with several remarks.

1. As the damage leads to a reduction in stiffness, higher strains occur in the stress-controlled simulation (see figure 3.1(b)) than in the strain-controlled variant (see figure 3.1(a)). These higher strains lead to a faster growth of the damage d in the stress-controlled simulation.

2. The presented fatigue-damage model is deliberately simple. We only model a homothetic decrease of the stiffness, do not account for irreversibility and choose both a quadratic damage-degradation function and a quadratic dissipation potential. The reasons behind these choices are two-fold. Firstly, we would like to have a model that is as simple as possible and to have a minimum number of parameters. Indeed, our principal goal is to study the influence of the microstructure on the fatigue behavior. Thus, we regard homogenization as an operation acting on material models, see Gajek et al. [90] for details on this point of view.
   Secondly, we wish to ensure applicability of the ensuing model on component scale. We realize this by an order-reduction framework, see section 3.4. Thus, we chose a model which permits straightforward model-order reduction. Notice that this choice is purely by comfort, and is not based on any physical reasons. Still, we target obtaining insights on the way microstructural characteristics manifest in the effective stiffness degradation of composites subjected to fatigue loading, see section 3.3.

3. Localization effects prevent using the presented model in simulations directly. However, adding a non-local term cures these problems, see section 3.2.

The two-potential framework offers a convenient framework for first-order homogenization in mechanics. Suquet [24] showed that the class of generalized standard materials is closed upon periodic homogenization, provided an infinite number of internal variables is

permitted. In this spirit, we shall use the fatigue-damage model of the previous section for obtaining an effective model on component scale. Suppose a periodic cuboid cell $Q \subseteq \mathbb{R}^d$ is given, together with a decomposition into two regions determined by a characteristic function $\chi : Q \to \{0,1\}$. We assume that the "matrix", $\chi^{-1}(1)$, is governed by the fatigue-damage model of section (3.2), with parameters $\mathbb{C}^{\mathrm{M}}$, η and α_{d} , whereas the complement, $\chi^{-1}(0)$, behaves elastically with elasticity tensor $\mathbb{C}^{\mathrm{F}}$. Furthermore, to avoid damage localization [153], we introduce a non-local term in the free energy whose effect is determined by two parameters γ and ℓ, the former an intensity factor with dimensions of stress, and the latter a length scale responsible for the regularization width.
The effective free energy is given by

$$\begin{aligned} W: \ \mathrm{Sym}(d) \times \mathcal{U} \times \mathcal{D} &\to \mathbb{R} \\ (\overline{\boldsymbol{\varepsilon}}, u, d) &\mapsto \frac{1}{2|Q|} \int_Q \chi(\eta + (1-d)^2)\boldsymbol{\varepsilon} : \mathbb{C}^{\mathrm{M}} : \boldsymbol{\varepsilon} + (1-\chi)\boldsymbol{\varepsilon} : \mathbb{C}^{\mathrm{F}} : \boldsymbol{\varepsilon} \\ &\qquad + \gamma\, \ell^2\, \chi \|\nabla d\|^2 \,\mathrm{d}\mathbf{x}, \end{aligned} \tag{3.2.7}$$

whereas the dissipation potential reads

$$\Phi : \mathcal{U} \times \mathcal{D} \to \mathbb{R}, \quad (\mathbf{u}, d') \mapsto \frac{1}{2|Q|} \int_Q \chi \frac{(d')^2}{\alpha_{\mathrm{d}}} \,\mathrm{d}\mathbf{x}. \tag{3.2.8}$$

For fixed $d \in \mathcal{D}$, the effective stiffness tensor $\mathbb{C}^{\mathrm{eff}}$ is given by linearly homogenizing the heterogeneous stiffness tensor

$$\chi(\eta + (1-d)^2)\mathbb{C}^{\mathrm{M}} + (1-\chi)\mathbb{C}^{\mathrm{F}}$$

on Q, i.e., for fixed $E \in \mathrm{Sym}(()d)$, we have

$$\mathbb{C}^{\mathrm{eff}}(d) : E = \frac{1}{Q} \int_Q \left[\chi(\eta + (1-d)^2)\mathbb{C}^{\mathrm{M}} + (1-\chi)\mathbb{C}^{\mathrm{F}}\right] : (E + \nabla^s v_E) \,\mathrm{d}\mathbf{x}, \tag{3.2.9}$$

where the periodic displacement fluctuation field $v_E : Q \to \mathbb{R}$ solves the balance of linear momentum on the micro-scale

$$\mathrm{div} \ \left\{\left[\chi(\eta + (1-d)^2)\mathbb{C}^{\mathrm{M}} + (1-\chi)\mathbb{C}^{\mathrm{F}}\right] : (E + \nabla^s v_E)\right\} = 0. \tag{3.2.10}$$

Clearly, for $E = \overline{\boldsymbol{\varepsilon}}$, equation (3.2.9) just computes the effective stress. However, as the microscopic free energy entering (3.2.7) is quadratic in the strain, we may even define the complete effective stiffness.
We conclude with a few comments.

1. The model (3.2.7) and (3.2.8) may be considered as a gradient-extended continuum, see Svendsen [154]. We shall not dwell upon the continuum-mechanical interpretations. The gradient term was merely introduced for numerical reasons. Indeed,

without the gradient-extension, the material behavior led to strong localizations which prevented further analysis of the model.

2. Alternatively, the model (3.2.7) and (3.2.8) may be considered as a special phase-field damage model [131, 155]. Although the incremental potential (3.2.15) will be remarkably similar to phase-field models for fracture [132, 156], there are some differences. On the one hand, no additional damage term enters the free energy. On the other hand, the dissipation potential (3.2.8) is quadratic and finite-valued.
   In contrast to Carrara et al. [137], who model emerging fatigue cracks in metallic and brittle materials, we model a stiffness degradation. In particular, Carrara et al. [137] do not account for a degradation of stiffness, but rather a degradation of the crack resistance. Also, Carrara et al. [137] work in the time domain, whereas we chose to work in cycle space right from the beginning.

3. The Biot's equation for u of the model reduces to the quasi-static balance of linear momentum (3.2.10) on the micro-scale for $E = \overline{\boldsymbol{\varepsilon}}$, i.e.,

$$\operatorname{div} \frac{\partial w}{\partial \boldsymbol{\varepsilon}}(\mathbf{x}, \overline{\boldsymbol{\varepsilon}} + \nabla^s u, \mathbf{z}) = 0. \tag{3.2.11}$$

   On the other hand, Biot's equation for d leads to

$$d' = \alpha_{\mathrm{d}} \left[(1-d)\boldsymbol{\varepsilon} : \mathbb{C}^M : \boldsymbol{\varepsilon} - \gamma \ell^2 \Delta d \right] \tag{3.2.12}$$

   in the matrix material $\chi^{-1}(1)$, where $\Delta = \operatorname{div} \nabla$ denotes the Laplace operator, and with Neumann boundary conditions

$$\frac{\partial d}{\partial n}(x) = 0 \quad \text{on} \quad \overline{\partial \chi^{-1}(0)} \cap \overline{\partial \chi^{-1}(1)}, \tag{3.2.13}$$

   i.e., the interface. Hence, we recover the evolution equation (3.2.4), augmented by a non-local term. The equation (3.2.12) only evolves d in the matrix. The latter approach requires a special numerical treatment, as FFT-based methods, as in Ernesti et al. [157] are not directly applicable.

4. Due to the gradient enhancement, we can no longer conclude a growth of d pointwise. However, upon backward Euler-discretization, we may conclude $d^n(\mathbf{x}) \in [\min_{\mathbf{x} \in Q} d_{n-1}(\mathbf{x}), 1]$ for almost every $\mathbf{x} \in Q$, with arguments similar to section 3.4 in Ernesti et al. [157]. In particular, using the initial condition $d_0 \equiv 0$, we obtain $d(\mathbf{x}) \in [0, 1]$ for almost every $\mathbf{x} \in Q$.

5. Wulfinghoff et al. [158] introduced a criterion for tensorial damage models based on continuum micromechanics. Suppose an irreversible damage process is taking place

described by some scalar parameter s, with corresponding stiffness $\overline{\mathbb{C}}(s)$. Then, the identity $\overline{\mathbb{C}}(s_1) \geq \overline{\mathbb{C}}(s_2)$ should hold provided $s_1 \leq s_2$, where the latter inequality should be understood in terms of quadratic forms, i.e., $\xi : \overline{\mathbb{C}}(s_1) : \xi \geq \xi : \overline{\mathbb{C}(s_2)} : \xi$ for all $\xi \in \mathrm{Sym}(()d)$.

The reasoning behind the criterion is as follows. Suppose $\overline{\mathbb{C}}(s)$ arises as the effective stiffness of a microscopic stiffness distribution $\mathbb{C}$ on Q, depending also on s. Then, for $s_2 \geq s_1$ the inequalities $\mathbb{C}(s_1, \mathbf{x}) \geq \mathbb{C}(s_2, \mathbf{x})$ valid for $x \in Q$ imply $\mathbb{C}^{\mathrm{eff}}(s_1) \geq \mathbb{C}^{\mathrm{eff}}(s_2)$, see Appendix B in Ponte Castañeda & Suquet [159].

For the local model, cf. equation (3.2.4), we established a point-wise decrease of the elastic stiffness. Thus, for $\ell \equiv 0$, by the arguments of Ponte-Castañeda & Suquet, the effective stiffness decreases as well. By a continuity argument, for small values of $\gamma\ell^2$, the elastic stiffness will decrease, as well. For the numerical experiments considered, see section 3.3, we did not observe an increase of the elastic stiffness.

We could have added a point-wise growth of d to the model, i.e., encoded by the dissipation potential. However, the latter condition is difficult to realize in a model-order reduced setting.

Upon an implicit Euler discretization in cycles, the balance of linear momentum (3.2.10) and the cycle-discrete variant of the evolution equation (3.2.12),

$$\frac{d - d^n}{\Delta N_n} = \alpha_{\mathrm{d}} \left[\chi(1-d)\boldsymbol{\varepsilon} : \mathbb{C}^M : \boldsymbol{\varepsilon} - \gamma\ell^2 \Delta d \right], \tag{3.2.14}$$

may be written as critical points of an incremental energy, i.e.,

$$\mathcal{I}_n : \mathrm{Sym}(()d) \times \mathcal{U} \times \mathcal{D} \to \mathbb{R}, \quad (\overline{\boldsymbol{\varepsilon}}, \mathbf{u}, d) \mapsto W(\overline{\boldsymbol{\varepsilon}}, \mathbf{u}, d) + \Delta N_n \, \Phi\left(\frac{d - d^n}{\Delta N_n} \right), \tag{3.2.15}$$

where, for brevity of notation, considered Φ as a function of d only. We refer to section 3.3.1 for implementation details. As a final remark for this section, notice that the incremental energy (3.2.15) is convex in the variables $\mathbf{u}$ and d separately, but not in the combined variable $(\mathbf{u}, d)$.

3.3. Model predictions for short-fiber reinforced microstructures

This section is devoted to discussing the predictions of the multiscale fatigue-damage model introduced in section 4.2. After exposing our setup in section 3.3.1, we thoroughly

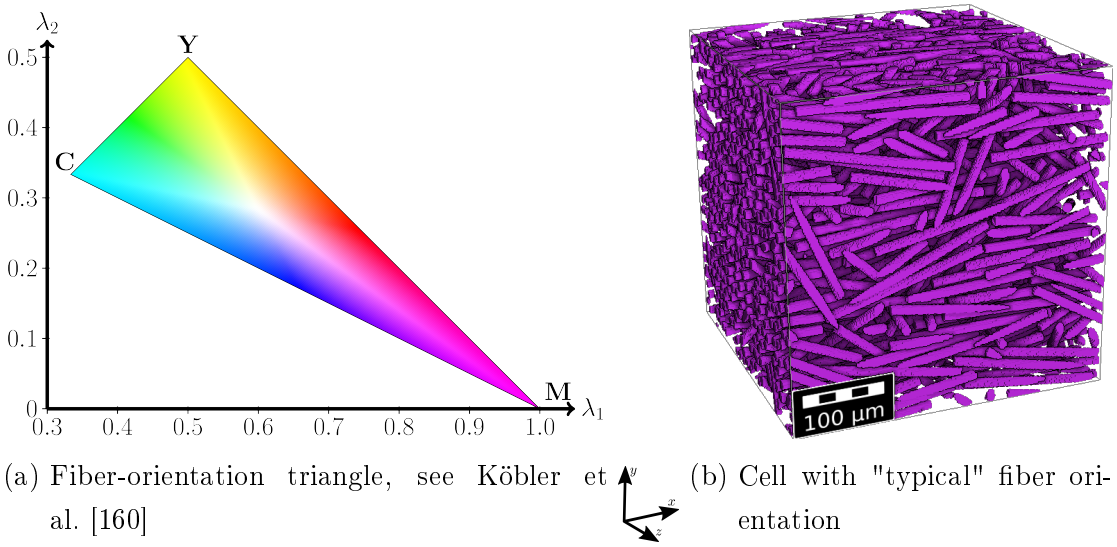

(a) Fiber-orientation triangle, see Köbler et al. [160]

(b) Cell with "typical" fiber orientation

Figure 3.2.: Fiber-orientation triangle and "typical" fiber orientation with $A = \mathrm{diag}(0.81, 0.15, 0.04)$

discuss the selection of necessary numerical and model parameters to ensure representative simulation results in section 3.3.2. Once this is accomplished, we study the model predictions in section 3.3.3.

3.3.1. Implementation, hardware and setup

The multi-scale model (3.2.7) and (3.2.8) was discretized in space on a regular voxel grid by finite-difference discretizations both for the displacement (via the staggered-grid approach [54]) and the fatigue-damage variable (via the standard 7-point star used for the Laplacian [161]). As discretizations in time we used an implicit Euler method, both with fixed time-step sizes and by an adaptive approach, and a Crank-Nicolson scheme, see section 3.3.2 for a thorough discussion. For these discretizations, the equation (3.2.10) may be solved by alternating minimization [155, 162], i.e., we alternatively solve equation (3.2.10) for fixed damage variable d and solve equation (3.2.14) for fixed displacement field $\mathbf{u}$. Due to the specific form of the energy (3.2.15), both subproblems (for d and $\mathbf{u}$) separately constitute quadratic optimization problems, and may be solved by dedicated techniques. For solving the balance of linear momentum (3.2.10), we use the conjugate gradient method in the context of FFT-based computational micromechanics, see Zeman et al. [163] and Brisard & Dormieux [164, 165], and use mixed boundary conditions [166]. The equation (3.2.14) for the damage variable with zero-outflux boundary condition (3.2.13) was solved

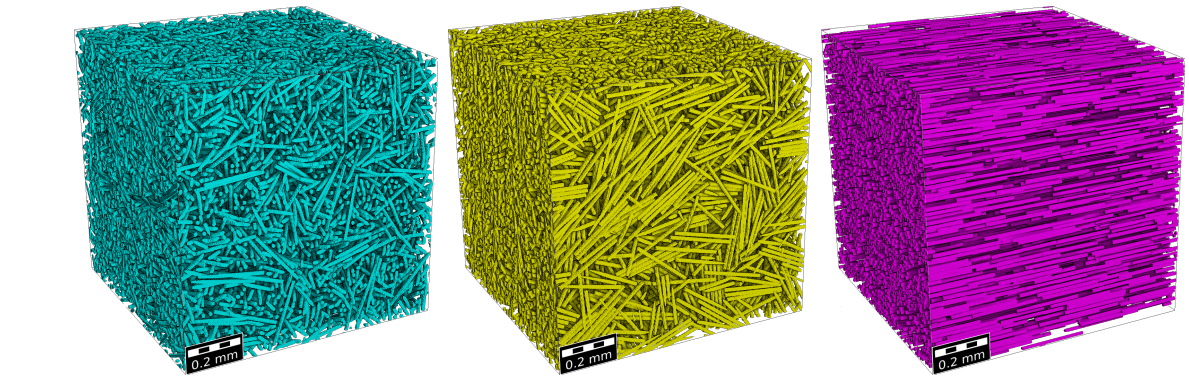

(a) Isotropic orientation, $\lambda_1 = \lambda_2 = \frac{1}{3}$

(b) Planar isotropic orientation, $\lambda_1 = \lambda_2 = \frac{1}{2}$

(c) Uni-directional orientation, $\lambda_1 = 1$, $\lambda_2 = 0$

Figure 3.3.: Considered extreme fiber orientations

by a textbook Gauss-Seidel method [167]. For further details on the computational resolution for a closely related problem, we refer to Ernesti et al. [157]. As the programming language of choice we used Julia [168].
The computations were performed on a Linux cluster where the typical nodes have either 64 GB RAM or 192 GB RAM.
Our investigations in section 3.3 are divided into two parts. In the first part, we study the sensitivity of the presented computational results w.r.t. the numerical and geometrical parameters involved, for instance the mesh resolution and the size of the investigated unit cells. This step enables us to clearly separate errors that result from the computational results from intrinsic modeling errors. In the second part, we thoroughly investigate the model predictions by varying both the physical parameters entering the model and the morphological parameters that determine the fiber-filled microstructure we are interested in, cf. section 3.3.3.

material	E	ν	further parameters
E-glass	72 GPa	0.22	–
Polymer	3.35 GPa	0.38	$\alpha_\mathrm{d} = 1.5 \cdot 10^{-7}$ 1/MPa, $\gamma = 1.0$ MPa, $\ell = 7.8125$ μm

Table 3.1.: Model parameters used for this article, see section 3.3.2 for the choice of ℓ

We define a specific set of material parameters and, also, numerical and morphological parameters that serve as our point of departure for the subsequent variations. The used

material parameters are collected in table 3.1. Also, we choose a reference set of morphological parameters for the investigated fiber-filled unit cells. We will consider short (glass) fibers with a fiber length of 200 μm and a diameter of 10 μm that are in typical commercial use. These fibers have an aspect ratio (fiber diameter/fiber length) of 20. The considered unit cells have a fiber-volume fraction of 19.5 % which corresponds to a mass fraction of 35 % for glass-fiber reinforced polyamide PA66.

We will use the second-order fiber-orientation tensor [169], a symmetric and positive semi-definite 3×3-matrix that we will typically denote as A, as our primary descriptor of the fiber-orientation state. Although it is known that A does not fully characterize the fiber-orientation distribution, see Müller & Böhlke [170], it is "the" common output of most injection-molding software packages, see Kennedy & Zheng [171]. As A is symmetric and positive semi-definite, we may use an eigenvalue decomposition

$$A = U \operatorname{diag}(\lambda_1, \lambda_2, \lambda_3)\, U^T$$

in terms of ordered eigenvalues $\lambda_1 \geq \lambda_2 \geq \lambda_3 \geq 0$ and an orthogonal matrix U for reducing the space of considered fiber orientations further. Indeed, the mechanical response of a fiber composite should transform covariantly w.r.t. Euclidean motions, see Köbler et al. [160] for a detailed discussion. Accounting for the trace constraint $\lambda_1 + \lambda_2 + \lambda_3 = 1$ permits us to eliminate the smallest eigenvalue λ_3, and we are left with investigating only a two-dimensional phase space of fiber orientations that takes the form of a triangle in λ_1-λ_2-space, see figure 3.2(a). For this fiber-orientation triangle, we use a specific coloring scheme [160], such that the extreme orientations are cyan (isotropic, $\lambda_1 = \lambda_2 = \frac{1}{3}$), yellow (planar isotropic, $\lambda_1 = \lambda_2 = \frac{1}{2}$) and magenta (uni-directional, $\lambda_1 = 1$, $\lambda_2 = 0$), see also[2] figure 3.3. The fiber-filled unit cells that are shown in this article were generated by the Sequential Addition and Migration method [173] that takes the fiber length, the fiber diameter, the minimum fiber distance, the desired volume fraction ϕ and the second-order fiber-orientation tensor A as input. For the minimum fiber distance, we use 4.6875 μm, which is about half a fiber diameter. (This somewhat odd number arises as follows. We typically use cells with $2 \times L = 400\,\mu$m edge length, discretized by 256^3 voxels. Then, we enforce that a fiber diameter is discretized by about six voxels [174] and at least three voxels must lie between the fibers.) Apart from the extreme orientation states, we also consider a "typical" diagonal orientation with eigenvalues $\lambda_1 = 0.81$, $\lambda_2 = 0.15$ and $\lambda_3 = 0.04$, see figure 3.2(b), that was the most frequently encountered fiber-orientation state in the fiber-filled component considered in Köbler et al. [160].

Last but not least, we consider a loading in x-direction with an amplitude of 40 MPa unless stated otherwise.

[2] The microstructure images in this work were rendered with GeoDict [172].

3.3.2. Verification

For the verification, we investigate the necessary size of the considered volume elements for ensuring representative results and the influence of the chosen resolution in space and time, the effect of the residual stiffness η and the dependence of the length-scale parameter ℓ, always for the extreme fiber orientations that appear as vertices of the fiber-orientation triangle 3.2(a). Typically, one of these extreme fiber orientations serves as the worst-case scenario for the investigations compared to all the intermediate fiber-orientation states in the fiber-orientation triangle, cf. figure 3.2(a).

On the necessary size of volume elements

We start our series of investigations with taking a look at the dependence of the computed stiffness degradation on the size of the volume element. We consider cubic cells with an edge length proportional to the fiber length L, starting with $1 \times L$ up to $5 \times L$. In turn, these unit cells correspond to a discretization with 128^3 up to 640^3 voxels. We consider the three extreme fiber-orientation states cf. Fig. (3.3), for a *single* generated unit cell, and subject the microstructures to uni-axial stress (amplitude) loading. For reasons of symmetry, we consider only loading in x-direction for the isotropic structures, and comply with loading in the x- and the y-direction, respectively, for the planar isotropic and the uni-directional structures. The latter correspond to an in-plane/out-of-plane loading and loading in fiber direction/transverse to the fiber direction for the two latter orientation states.
To reduce the full complexity of the stiffness degradation, our primary quantity of interest is the direction-dependent Young's modulus, which is defined, for any stiffness tensor $\mathbb{C}$ and any unit vector $p \in \mathbb{R}^3$ implicitly via

$$\frac{1}{E(\mathbb{C}, p)} = p \otimes p : \mathbb{C}^{-1} : p \otimes p, \tag{3.3.1}$$

see Böhlke & Brüggemann [175]. If it is clear from the context, we will drop the explicit dependence on $\mathbb{C}$, and write $E_x^{\text{eff}} = E(\mathbb{C}^{\text{eff}}, \mathbf{e_1})$ (and similarly for E_y^{eff} and E_z^{eff}).
In figure 3.4, the evolution of the effective Young's moduli E^{eff} in x-, y- and z-direction is shown vs. the number of cycles N, for all five considered scenarios. Notice that the considered cycle interval depends on the different loading cases and investigated fiber orientations, consistent to the physical intuition that these scenarios also lead to a different fatigue life, in general. The simulation results computed on the cell with edge length $5 \times L$ are shown in black, and serve as the reference for simulations on the smaller elements.

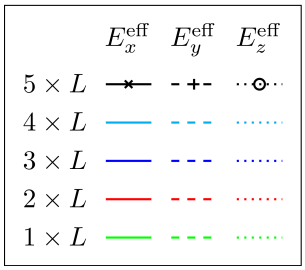

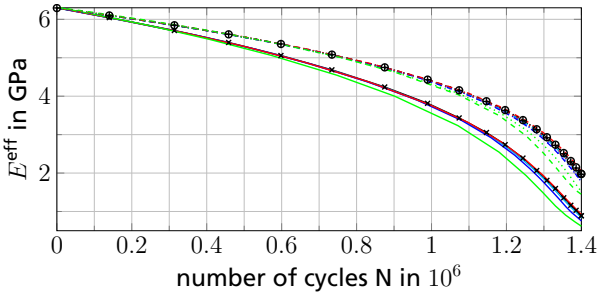

(a) Isotropic orientation, loading in x-direction

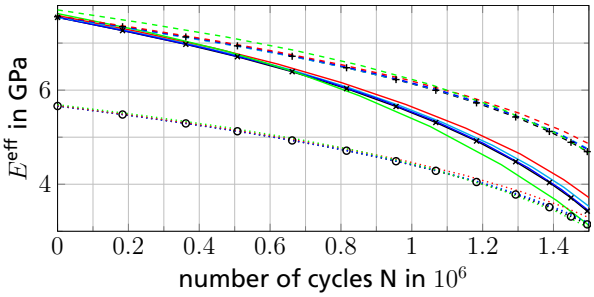

(b) Planar isotropic orientation, loading in x-direction

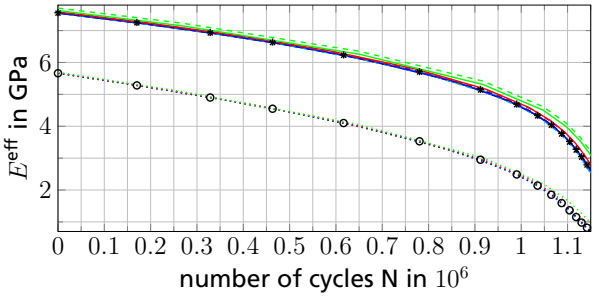

(c) Planar isotropic orientation, loading in z-direction

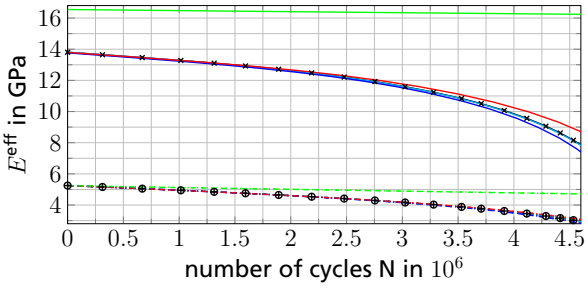

(d) Uni-directional orientation, loading in x-direction

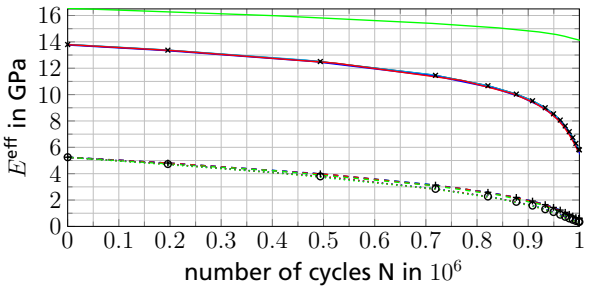

(e) Uni-directional orientation, loading in z-direction

Figure 3.4.: Directional Young's modulus (3.3.1) vs. number of cycles for different orientations and loading directions. We investigate the influence of the volume-element size, measured in units of fiber length L

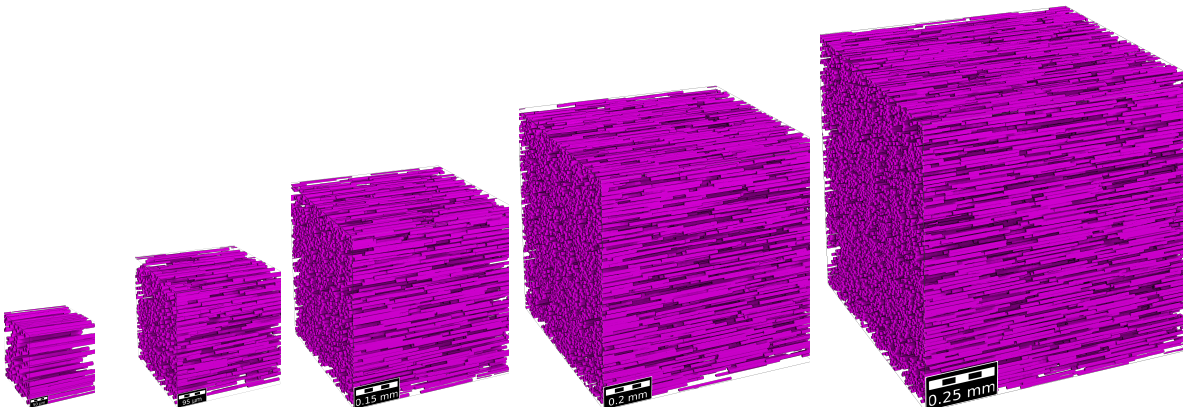

(a) $1 \times L$ (b) $2 \times L$ (c) $3 \times L$ (d) $4 \times L$ (e) $5 \times L$

Figure 3.5.: Generated volume elements with with different edge lengths and unidirectional orientation

For the isotropic case, shown in figure 3.4(a), the Young's moduli curves start at the same value of about 6.3 GPa. Then, E_x^{eff} decreases faster than the Young's moduli in the perpendicular directions. In general, the relative errors in the Young's moduli for the smaller elements compared to the $5 \times L$-element are on a low level compared to the other investigated cases. Even for the $1 \times L$-cell, where the decrease of the Young's moduli is overestimated, the relative error is below 5 % up to 0.9×10^6 cycles. For the $2 \times L$-cell, the relative error lies below the error of the $3 \times L$-cell (which is a *stochastic* effect that we will look into more detail shortly), and exceeds 5 % only after 1.3×10^6 cycles.
For the planar-isotropic orientation loaded in x-direction, shown in figure 3.4(b), we observe that, initially, the two in-plane Young's moduli are identical and lie above the out-of-plane Young's modulus. For increasing cycles, all Young's moduli are decreasing. Among the in-plane Young's moduli, the Young's modulus in loading direction decreases significantly faster then the transverse in-plane Young's modulus. This decrease is so strong that at the end of the considered cycle window, the Young's modulus in loading direction lies only slightly above the (decreased) out-of-plane Young's modulus. For the $1 \times L$-cell, the relative errors stay below 5 % for less than 1.15×10^6 cycles, whereas the $2 \times L$-cell remains below that level up to 1.3×10^6 cycles. Thus, the approximation properties are qualitatively similar to the isotropic orientation.
For the planar isotropic structure and out-of plane loading, the decrease of Young's modulus in all three directions is qualitatively similar. Consistent to intuition, the in-plane Young's moduli decrease in an identical way. For the $1 \times L$-structure, the relative error in the Young's moduli remains below 5 % up to 8.5×10^5 cycles, whereas the $2 \times L$-structure

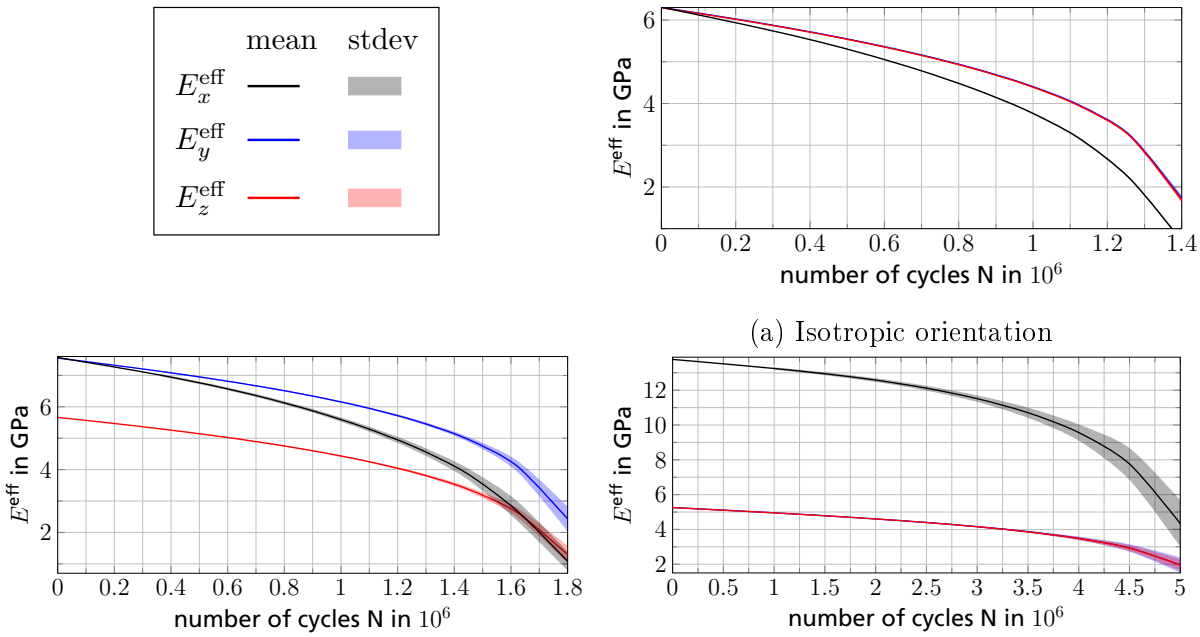

(a) Isotropic orientation

(b) Planar isotropic orientation

(c) Uni-directional orientation

Figure 3.6.: Mean value (mean) and standard deviation (stdev) of the directional Young's moduli upon loading in x-direction, based on five different volume-element SAM-realizations per orientations with a cell-edge length of $2 \times L$

retains this level of accuracy up to 1.05×10^6 cycles.

When loading the uni-directional structure in fiber direction, cf. figure 3.4(d), the Young's modulus in fiber direction decreases significantly. Also the transverse Young's moduli decrease, but less significantly. Comparing the different cell sizes, we observe strong differences in the predicted Young's moduli. For the $1 \times L$-cell, the fibers are as long as the cell edges. As the fibers are uni-directional, they actually represent a *continuous* configuration. For the latter scenario, it would have been possible to rely upon a two-dimensional cell, in fact, as the structure does not depend on the x-coordinate. Comparing the results for the continuously reinforced cell and the discontinuously reinforced cells, we become aware of the differences in terms of stiffness degradation between these two fiber-reinforced composites, cf. figure 3.5. Indeed, the transverse Young's modulus does not decrease significantly for the continuous reinforcement, whereas the Young's modulus in fiber direction is captured accurately.

Concerning the accuracy, the minimum relative error for the $1 \times L$-cell exceeds 10 %, even for the first cycle. The $3 \times L$-cell is accurate up 6 % for the entire considered cycle interval. This is a result of our assumption that the fibers behave elastically, and a loading in fiber direction is primarily governed by this elastic behavior.

In figure 3.4(e), transverse loading is considered for the uni-directional structure. For the $1 \times L$-cell, i.e., for the continuously reinforced cell, the predictions are not even close to the discontinuously reinforced cells. Both the Young's modulus in fiber direction and the two transverse Young's moduli decrease significantly during loading. The difference in the two transverse Young's moduli appears to be small, mostly as a result of the scale in the figure. Concerning the accuracy, 5 % relative error is not exceeded up to 0.9×10^6 cycles for the $2 \times L$-cell.

Due to the localization permitted by the non-local fatigue-damage model presented in section 3.2, and also as a result of the inherent non-convexity, we cannot expect to find a representative volume element [176, 177]. Instead, we need to be content with a specific window of parameters that we "trust" the model to be representative. For the situation at hand, this parameter window concerns the number of cycles that we "trust" the model prior to complete localization.

To gain more insight into the factors involved, we investigate, for a fixed cell size, the remaining *stochastic* influence. For the preceding analysis, we considered a single realization of the microstructure in question, but with different sizes. For the simulations conducted and the data that was analyzed, we consider an edge length of $2 \times L$ sufficient for our purposes. Still, we would like to quantify the remaining stochastic fluctuations inherent to the results. For that purpose, we consider five different randomly generated microstructures for the three extreme orientations, each with an edge-cell length of $2 \times L$, and investigate the predicted Young's moduli - or, rather, the expectation and the standard deviation, cf. figure 3.6. We only show the loading in x-direction, as the other cases lead to similar results.

We see that the variance is almost non-existent for the isotropic cell, whereas the standard deviation is increasing for increasing loading, and highest for the Young's modulus in loading direction. Apparently, the standard deviation only becomes comparatively large when localization occurs.

Resolution study

In this section, we vary the mesh size to see the influence of the resolution. Of course, the mesh size of this section was chosen iteratively accounting for the results of the previous section. Otherwise, the reported results would not be meaningful.

We modify our basic resolution of $h = 2 \times L/256 = 1.5625\,\mu\text{m}$ by factors of 2 and 0.5, respectively. We wish to show that the resolution we chose is fine enough, but not unnecessarily so in order to keep the simulation time as short as possible.

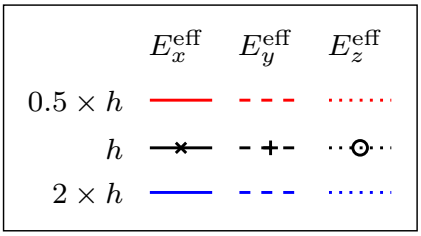

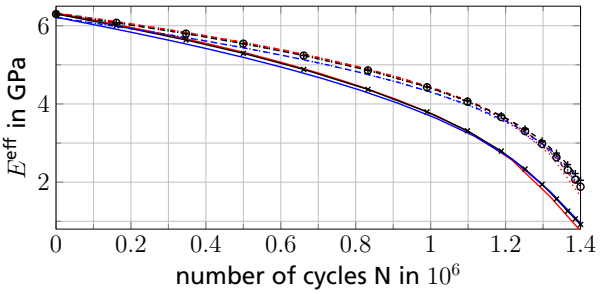

(a) Isotropic orientation, loading in x-direction

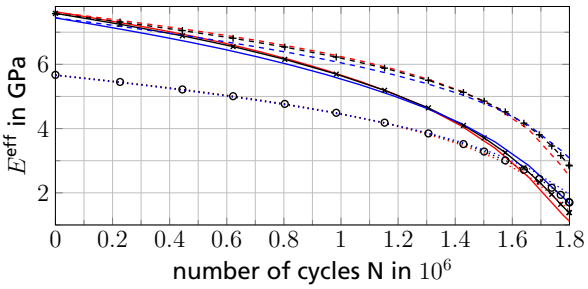

(b) Planar isotropic orientation, loading in x-direction

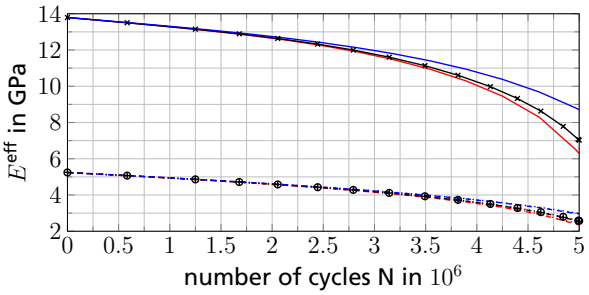

(c) Uni-directional orientation, loading in x-direction

Figure 3.7.: Directional Young's modulus (3.3.1) vs. number of cycles for different orientations. We investigate the influence of the resolution for the volume-element size determined in section 3.3.2

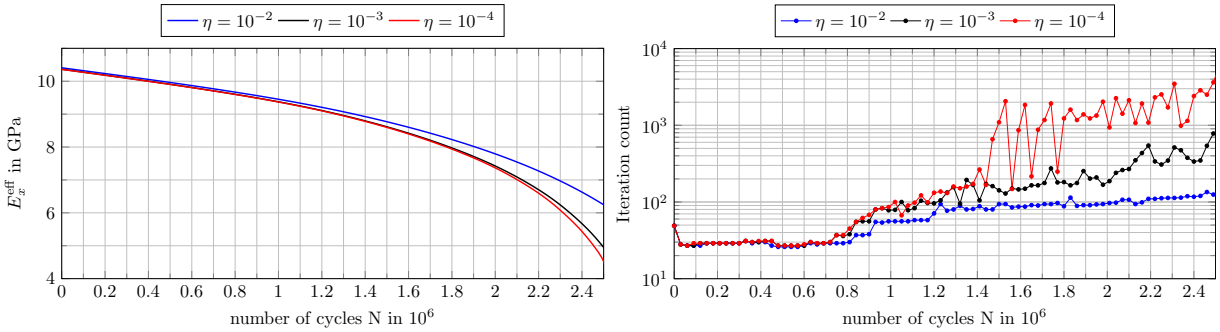

(a) Predicted E_x^{eff}-curves (b) Number of iterations for the elasticity solver

Figure 3.8.: Influence of relative residual stiffness η for loading in x-direction of the reference structure, see figure 3.2(b)

Simulations were conducted for the three extreme micro-structures, a unit-cell length of $2 \times L = 400\,\mu$m and the three discussed mesh spacings, resolving the same microstructure by different voxel counts, cf. figure 3.3.
The isotropic structure in figure 3.7(a) is largely insensitive to a change in mesh width. Only for N exceeding 1.2×10^6 cycles, a slight overestimation of E_x^{eff} is seen for $1 \times h$ and $2 \times h$. For the planar isotropic orientation, cf. figure 3.7(b), and for the uni-directional structure in figure 3.7(c), strong deviations may be observed when going below 60 % of the initial Young's moduli.
We observe that, for higher resolution, the final decrease of the Young's modulus is faster, probably due to the localization present on the micro-scale that requires a more accurate resolution to be captured accurately. However, the deviation between $1 \times h$ and $0.5 \times h$ is still reasonable for all cycles. Therefore, the resolution of 6.4 voxels per fiber diameter is considered sufficient, and chosen for the succeeding analyses.

Influence of the relative residual stiffness

According to the free energy density (4.2.1), the relative residual stiffness η determines the remaining stiffness of the material when $d = 1$. In this section, we investigate the dependence of both the predicted stiffness degradation and the required number of *elastic* iterations on the quantity η. The latter are chosen because they represent the major computational effort involved in solving the system of coupled partial differential equations (3.2.10) and (3.2.10).
For that purpose, we consider the reference structure in figure 3.2(b) with parameters as before, and vary η. The relative residual stiffness used before was set to $\eta = 10^{-3}$,

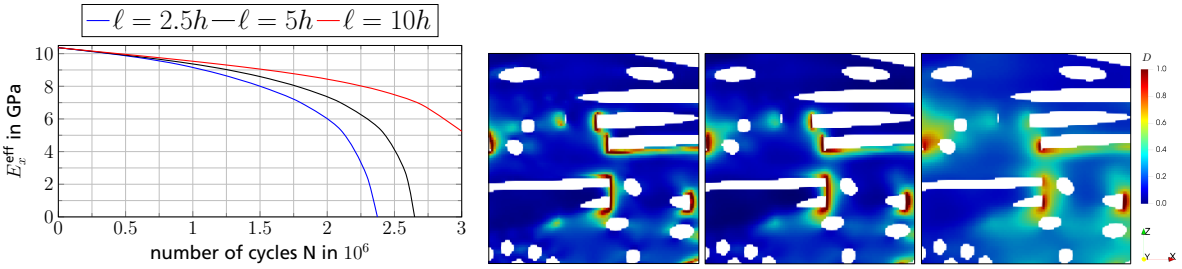

(a) Degradation of the effective Young's modulus in fiber direction

(b) Zoomed local fields for $\ell = 2.5h$ (left), $\ell = 5h$ (middle) and $\ell = 10h$ (right) at $E_x^{\text{eff}} = 7\,\text{GPa}$

Figure 3.9.: Influence of varying the length-scale parameter ℓ on the directional Young's modulus of the reference structure figure 3.2(b) subjected to loading in x-direction, both on the macroscopic response and locally, at the fiber tips

i.e., upon complete damage, only 0.1 % of the original stiffness remains. We also consider $\eta = 10^{-2}$ and $\eta = 10^{-4}$, corresponding to 1 % and 0.01 % remaining stiffness, respectively. Taking a look at the predicted E_x^{eff}-curves, cf. figure 3.8(a), we see that for $\eta = 10^{-2}$, the predicted Young's modulus is consistently overestimated. Both $\eta = 10^{-3}$ and $\eta = 10^{-4}$ lead to a similar stiffness degradation, and the associated degradation curves differ only for more than 2.2×10^6 cycles.
Lower values of η increase the computational burden, as the elastic contrast is increased, and the elastic contrast is mainly responsible for the convergence behavior of the conjugate-gradient solver [178]. A closer look at figure 3.8(b) confirms these theoretical predictions. Upon activated fatigue-damage, at about $1.4{\times}10^6$ cycles, the elastic iterations for $\eta = 10^{-4}$ are about an order of magnitude higher than for $\eta = 10^{-3}$.
As a practical compromise between accuracy and computational speed, we choose a relative residual stiffness of 10^{-3} for the ensuing investigations.

Dependence on the length-scale parameter

In this section the effects of varying the length-scale parameter ℓ are studied. For that purpose, we change the length-scale parameter ℓ, that we typically set to $\ell = 5h \equiv 7.8125\,\mu\text{m}$ by factors of 0.5 and 2, respectively. As in the previous section, we investigate loading in x-direction for the reference structure figure 3.2(b).
The evolution of the effective Young's modulus in fiber direction for the three investigated length-scale parameters is shown in figure 3.9(a). We see that ℓ has a strong influence, and that a smaller length-scale parameter leads to an earlier decrease of the stiffness,

whereas the larger length-scale parameter slows down the stiffness decrease significantly. To understand the strong influence of ℓ, we investigate the local fatigue-damage fields. As our reference, we consider the simulation with $\ell = 5h$ and take a look at the fatigue-damage field at cycle $N = 2.4 \times 10^6$, more precisely a zoomed cutout, which is shown in the center of figure 3.9(b). To ensure comparability, taking into account that, for this cycle and for $\ell = 5h$, the effective in-fiber Young's modulus E_x^{eff} is about 7 GPa, we investigate those cycles where E_x^{eff} is about 7 GPa for the two other ℓ-values as well. The corresponding images are shown on the left and on the right in figure 3.9(b), respectively. We see that the smallest ℓ-value considered leads to very thin "cracks", mostly located at the fiber tips, which are highly localized. For the highest ℓ-value considered, the fatigue-damage field is much more diffuse, although the general locations, where damage occurs, are identical. These diffuse patterns also emphasize the damage character of the model, as, for most of the volume, the fatigue-damage field attains values not even close to unity. The stiffness degradation associated to the fatigue-damage reflects potential cracks on a sub-micron scale within our model.

The ℓ-value $\ell = 5h$ lies in between the two extreme cases, showing both cracks (but not as localized as for $\ell = 2.5h$) and a diffuse fatigue-damage pattern in the matrix.

These observations shed further light on our observations made in figure 3.9(a), as a stronger localization behavior also induces an earlier failure.

Last but not least, let us take a look in figure 3.10 at the evolution of both the fatigue-damage field and the stress field upon cyclic loading for the reference structure, cf. figure 3.2(b). For the first image, at cycle 1.8×10^6, the fatigue-damage field is still mostly zero. Only at the fiber tips of those fibers pointing in loading direction high fatigue-damage values emerge. These fiber-tip localizations of the fatigue-damage field are also reflected in the stress fields, as the fibers in loading direction do *not* carry the highest stresses, as would be expected, for instance, in a purely linear elastic analysis.

In the second image, at cycle $N = 2.4 \times 10^6$, the fatigue-damage field has evolved to a more heterogeneous state, and the defects at the fiber tips have coalesced and combined to individual cracks. Also, we see an example where the fatigue-damage field has enclosed half of a specific fiber, reflecting a fiber pull-out scenario. These changes also reflect in the stress fields. Indeed, the peak level of stress within the fibers is greatly reduced compared to the previously considered cycle.

In the final image, at cycle $N = 2.58 \times 10^6$, we observe a crack that runs through approximately half of the structure, and relying upon homogenization schemes for such a situation is highly questionable. In particular, we see the limits of the continuum-mechanical multiscale modeling. At this point, insights from fracture mechanics are required. The stress field corresponding to this last cycle clearly reflects the change in loading conditions, as

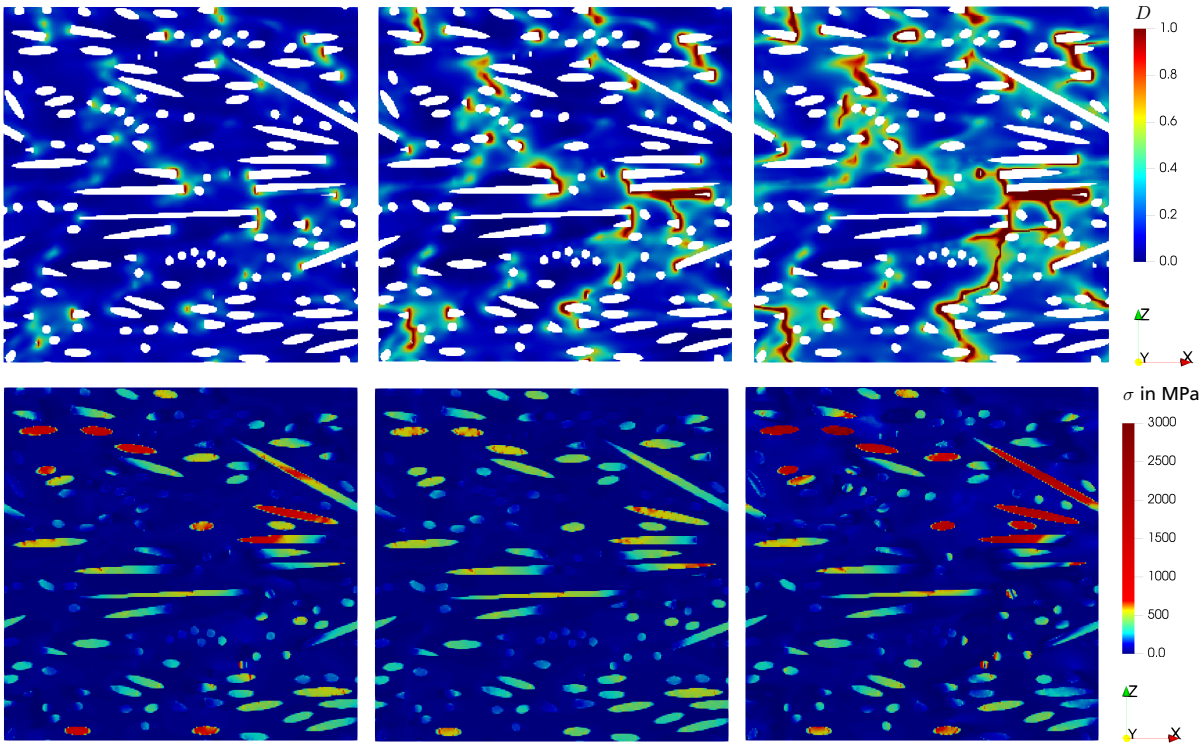

Figure 3.10.: Fatigue-damage field D (top) and von Mises equivalent stress $\boldsymbol{\sigma}_{\mathrm{vM}}$ (bottom) for $\ell = 5h$ and at cycles $N = 1.8 \times 10^6$ (left), $N = 2.4 \times 10^6$ (middle) and $N = 2.58 \times 10^6$ (right)

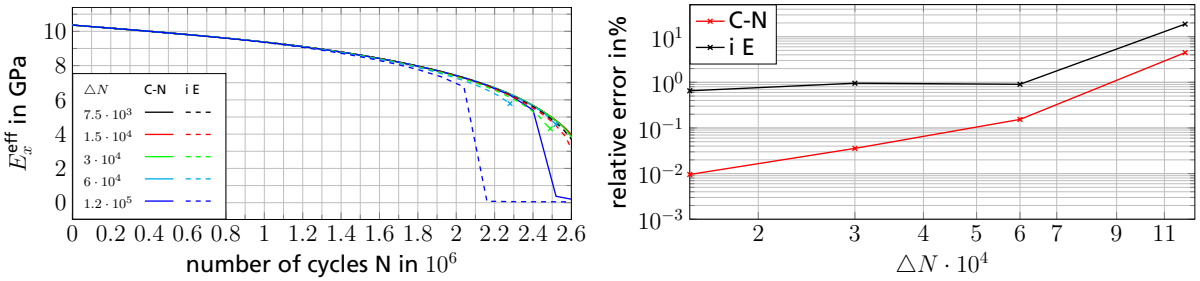

(a) E_x^{eff}-N-plot; a cross marks the last converged step

(b) Maximum relative error of E_x^{eff} vs. cycle step-size

Figure 3.11.: Comparing different cycle step-sizes and integration schemes for the reference structure, cf. figure 3.2(b), (C-N): Crank-Nicolson, (i E): implicit Euler

the lower part of the structure does not possess any remaining load-bearing capacity. As a consequence the stress levels on the upper part of the microstructure are increased.
For the experimental determination of the internal length-scale and other fatigue-damage model parameters, indirect identification methods have to be used [179]. Methods similar to those used to determine length scale parameters in gradient damage or phase-field fracture models can be applied. To determine the length-scale parameter for a gradient damage model experimentally, Geers et al. [180] proposed to carry out Compact-Tension tests (CT-tests) on a short glass-fiber reinforced polypropylene. As for phase-field fracture models, the length-scale parameter may also be related to experimental results via the maximum stress reached for problems with analytical solutions [181, 182].

Discretization in cycle space and cycle-step size

Both for the accuracy of the predicted results and for keeping the overall run-time of the simulations reasonable, a proper discretization in cycle space is essential in terms of the integration scheme and in terms of the used cycle step-size. In addition to the classical implicit Euler scheme, we also investigate the Crank-Nicolson scheme [183], as its effort is comparable to the implicit Euler scheme, but promises higher-order accuracy.
For the reference structure, see figure 3.2(b), loaded in x-direction by a constant stress amplitude of 40MPa up to $2.6 \cdot 10^6$ cycles, the decrease in Young's modulus is shown in figure 3.11(a). Whereas both considered integration schemes and all step-sizes lead to comparable results, for larger cycles, strong differences emerge. As a general trend, for larger step-sizes, the alternating-minimization scheme did not converge anymore within

the prescribed 200 iterations.
Qualitative results may be read off figure 3.11(b), where the maximum relative error of the computed effective Young's modulus in x-direction is shown, where the error is computed relative to the Crank-Nicolson prediction with $\Delta N = 7.5 \cdot 10^3$, and the maximum is computed over all cycles.
We see that the error increases, for both schemes, with increasing step size, i.e., a smaller step size *consistently* leads to a smaller error. In general, the Crank-Nicolson scheme is an order of magnitude more accurate than the implicit Euler scheme, consistently for any step size. For the implicit Euler scheme, if the step size is below 6×10^4, the error remains below 1 %. This is also true for the Crank-Nicolson scheme, but, unfortunately, for the step size 1.2×10^5, the error exceeds 1 %. Thus, although the Crank-Nicolson scheme improves the accuracy, it does not help us in reducing the necessary step size to ensure *engineering* accuracy.
To still gain an improvement in computation time, we rely upon an automatic cycle-size control for the implicit Euler scheme. This might be helpful because a scheme with constant increments may be too fine initially, but too coarse later on (when the change in stiffness is strong). The basic idea of our simple automatic stepping is to limit the local change in fatigue-damage to a specific value κ. Suppose that the last converged fatigue-damage value $D^n(x)$ is known at $x \in Q$. Then, we would like to have

$$d(\mathbf{x}) \leq d^n(\mathbf{x}) + \kappa, \quad \text{i.e.,} \quad d(\mathbf{x}) - d^n(\mathbf{x}) \leq \kappa.$$

By equation (3.2.14) we know that

$$\frac{d(\mathbf{x}) - d^n(\mathbf{x})}{\Delta N_n} = \alpha_{\mathrm{d}} \left[(1 - d(\mathbf{x}))\boldsymbol{\varepsilon}(\mathbf{x}) : \mathbb{C}^M : \boldsymbol{\varepsilon}(\mathbf{x}) - \gamma \ell^2 \Delta d(\mathbf{x}) \right]$$

holds for the matrix material. Replacing the right-hand side by the values of the *last converged* cycle, we obtain the requirement

$$\alpha_{\mathrm{d}} \left[(1 - d^n(\mathbf{x}))\boldsymbol{\varepsilon}^n(\mathbf{x}) : \mathbb{C}^M : \boldsymbol{\varepsilon}^n(\mathbf{x}) - \gamma \ell^2 \Delta d^n(\mathbf{x}) \right] \overset{!}{\leq} \frac{\kappa}{\Delta N_n}.$$

With this explicit and cheap estimate, we are led to define

$$\Delta N_n = \min_{\mathbf{x}} \frac{\kappa / \alpha_{\mathrm{d}}}{(1 - d^n(\mathbf{x}))\boldsymbol{\varepsilon}^n(\mathbf{x}) : \mathbb{C}^M : \boldsymbol{\varepsilon}^n(\mathbf{x}) - \gamma \ell^2 \Delta d^n(\mathbf{x})}, \tag{3.3.2}$$

where the minimum is evaluated only over the matrix material. In figure 3.12(a) we compare the finest step-size considered previously to the automatic approach (3.3.2) for damage limitation numbers $\kappa = 0.15$, $\kappa = 0.3$ and $\kappa = 0.45$, respectively, in terms of the predicted effective Young's modulus in x-direction for the reference structure, cf.

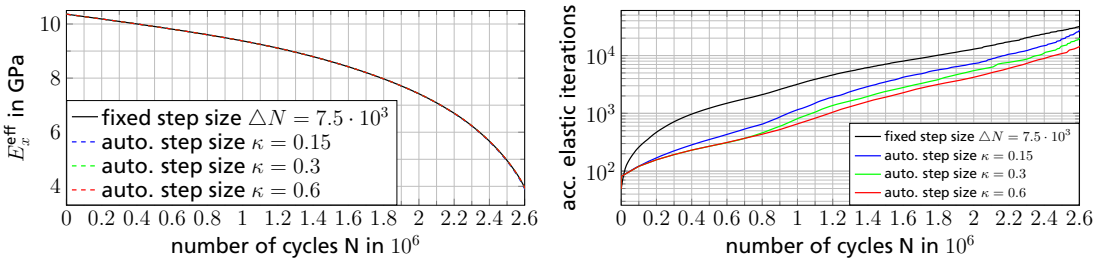

(a) Young's modulus in x-direction (b) Accumulated elastic iteration count

Figure 3.12.: Investigating the effect of κ on the automatic step-size control for the implicit Euler discretization

figure 3.2(b). Recall that, for instance, $\kappa = 0.15$ estimates that the increase in fatigue-damage does not exceed 0.15 from one cycle to the next (for all voxels). figure 3.12(a) demonstrates that all three considered κ-values lead to accurate predictions and do not suffer from a lack of convergence of the alternating-minimization scheme, as we observed for large cycle increments, cf. figure 3.11(a).

The qualitative gain in computational performance is assessed in figure 3.12(b) by tracking the accumulated iterations of the elasticity solver up to a specific cycle. We see that, initially, the automatic cycle-stepping leads to a tremendous decrease in computational expense, as the constant cycle-steps are chosen much too fine. Later on during the loading, this advantage becomes smaller, essentially because the automatic step-size control forces the step-size to account for the strong changes in the local fatigue-damage field. Increasing the permitted damage increase κ decreases the required iteration count, and $\kappa = 0.15$ appears to be too cautious. For the succeeding analysis, we rely upon $\kappa = 0.3$, and we see from figure 3.12(b) that we reduce the iteration count roughly by half an order of magnitude, which translates into a factor of about 3 in the overall runtime.

3.3.3. Material-scientific studies

After studying the influence of the numerical parameters entering the proposed multi-scale fatigue-damage model (3.3.2), we devote our attention to the predictions when varying the loading, both in terms of the overall level and when changing the direction of loading, and the characteristics of the fiber-reinforced composites, like volume fraction, fiber length and fiber orientation. As a consequence of the high dimension of the parameter space, we focus on varying each parameter separately relative to a reference configuration, see

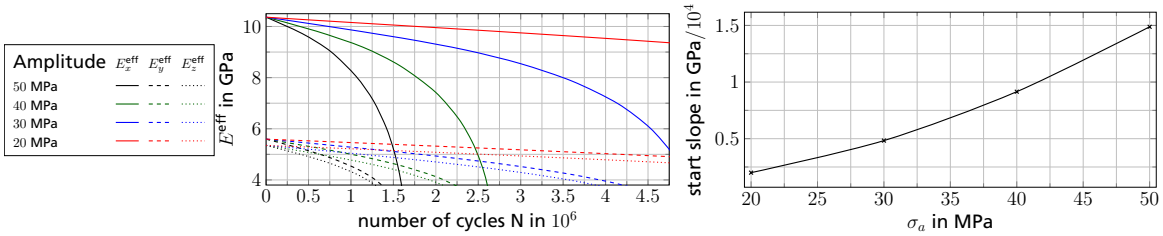

(a) Decrease of the directional Young's moduli (b) Negative slope $-\mathrm{d}E_x^{\text{eff}}/\mathrm{d}N$ at $N = 0$

Figure 3.13.: Effects of varying the applied stress amplitude σ_a for the microstructure shown in figure 3.2(b)

section 3.3.1. In particular, the "typical" fiber-orientation state shown in figure 3.2(b) and an applied stress amplitude of 40MPa in x-direction serve as the point of departure.

Consequences of varying loading amplitude

Figure 3.13 illustrates the impact of varying the applied stress amplitude σ_a on the composite response for the reference microstructure, see figure 3.2(b). For the investigated loading amplitudes $\sigma_a \in \{20\,\text{MPa}, 30\,\text{MPa}, 40\,\text{MPa}, 50\,\text{MPa}\}$, the evolution of the directional Young's moduli, cf. equation (3.3.1), in the three coordinate directions is shown in figure 3.13(a). We see that an increase in loading level also leads to a stronger decrease of all three considered directional Young's moduli. We also notice that the decrease in x-direction is stronger than for the perpendicular directions.
Figure 3.13(b) illustrates the dependence of the initial slope (or, rather, furnished with a minus sign) of E_x^{eff} on the loading amplitude σ_a. We observe a slightly nonlinear behavior which is a consequence of the superlinear dependence of the fatigue-damage variable on the stress amplitude σ_a in the evolution equation (3.2.6). In contrast, the cycle when E_x^{eff} drops below 4 GPa depends on σ_a in a strongly nonlinear fashion. The latter observation might be a consequence of the strong interaction of the strain and the fatigue-damage fields within the complex microstructure when subjected to fatigue loading.

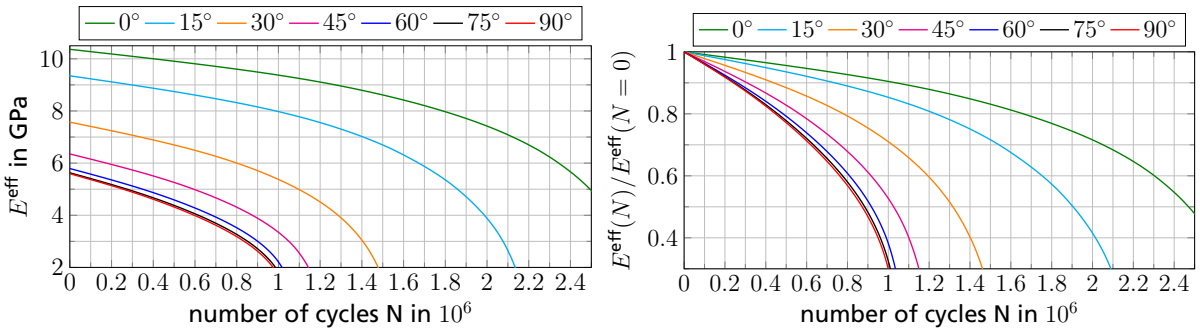

(a) Absolute values

(b) Relative values

Figure 3.14.: Influence of the loading angle in the x-y-plane on the effective Young's modulus in loading direction, cf. equation (3.3.3)

Outcomes of varying loading direction

Fixing the applied stress amplitude to 40MPa, we vary the direction of loading via

$$\overline{\boldsymbol{\sigma}} = \sigma_a \, \mathbf{p} \otimes \mathbf{p} \quad \text{with} \quad \mathbf{p} = (\cos\theta, \sin\theta, 0) \quad \text{and} \quad \theta \in \left[0, \frac{\pi}{2}\right], \tag{3.3.3}$$

i.e., we consider loading in x-direction for $\theta = 0°$ and loading in y-direction for $\theta = 90°$, for the microstructure shown in figure 3.2(b). The computed Young's moduli in the respective directions $\mathbf{p}$ are shown in figure 3.14, where we consider 15°-increments. The absolute values for the directional Young's moduli are shown in figure 3.14(a). Even initially, there are strong differences in the directional Young's moduli, varying between slightly less than 6 GPa in y-direction up to slightly above 10 GPa in x-direction. To gain deeper insight, we investigate the relative stiffness loss in figure 3.14(b), i.e., we normalize the directional Young's modulus at a specific cycle by the initial directional Young's modulus. We see that, with increasing loading angle θ, also the speed of decrease of the relative Young's modulus is increasing.
Notice that for θ exceeding 60°, the predicted curves are very close, in both absolute and relative terms, which is typical for a strongly oriented fiber-reinforced microstructure.

Influence of the fiber-volume fraction

After discussing the impact of the direction and level of the applied stress amplitude, we turn our attention to the influence of the composition of the fiber-reinforced unit cells that we are concerned with, in the first place. It is well-known, see for instance

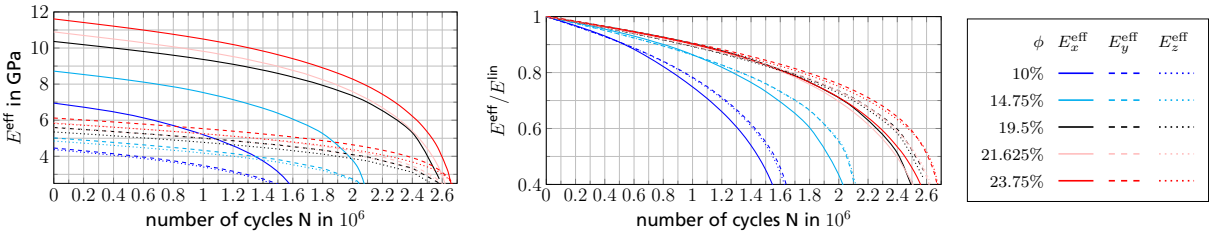

(a) Absolute decrease (b) Relative decrease

Figure 3.15.: Influence of the fiber-volume fraction ϕ on the axial Young's moduli for the fiber orientation shown in figure 3.2(b) upon loading in x-direction

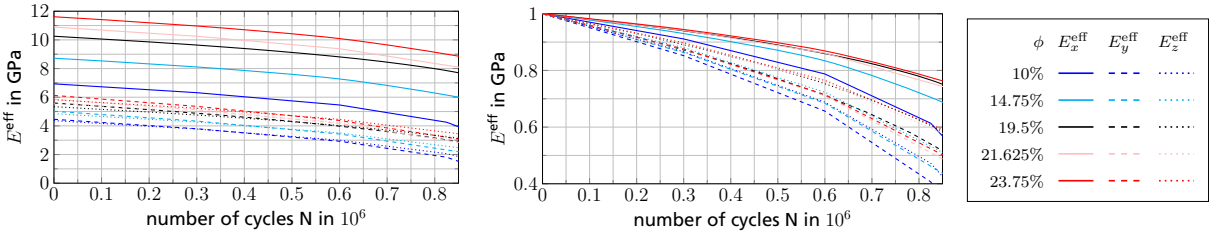

(a) Absolute decrease (b) Relative decrease

Figure 3.16.: Influence of the fiber-volume fraction ϕ on the axial Young's moduli for the fiber orientation shown in figure 3.2(b) upon loading in y-direction

Milton's monograph [184], that the volume fractions of a composite have a significant effect on its effective material response. For instance, in the case of elastic phases, series expansions of the effective stiffness tensor, cf. section 14.1 in Milton [184], reveal that the volume fraction completely determines the linear term in the expansion. The latter observation manifests the fiber-volume fraction as the "most important" characteristic of a fiber-reinforced composite.

For that purpose we study the influence of the fiber-volume fraction on the stiffness degradation upon cyclic loading for the reference fiber-orientation tensor. We varied the fiber-volume fraction around a reference value of $\phi = 19.5\,\%$, going down to $\phi = 10\,\%$ and up to $23.5\,\%$. The latter value is already quite high for most short-fiber reinforced plastics relevant for industrial applications. Furthermore, we added the intermediate value between $\phi = 19.5\,\%$ and the extreme fiber-volume values considered. The results for loading in x-direction are shown in figure 3.15. Taking a look at the absolute values, cf. figure 3.15(a), we see that the rate of decrease of the directional Young's moduli is comparable for the different volume fractions considered. In relative terms, see figure 3.15(b), the latter observation translates into a faster relative decrease for the cells with lower fiber content. However, for each fixed volume fraction, the relative decrease of the Young's

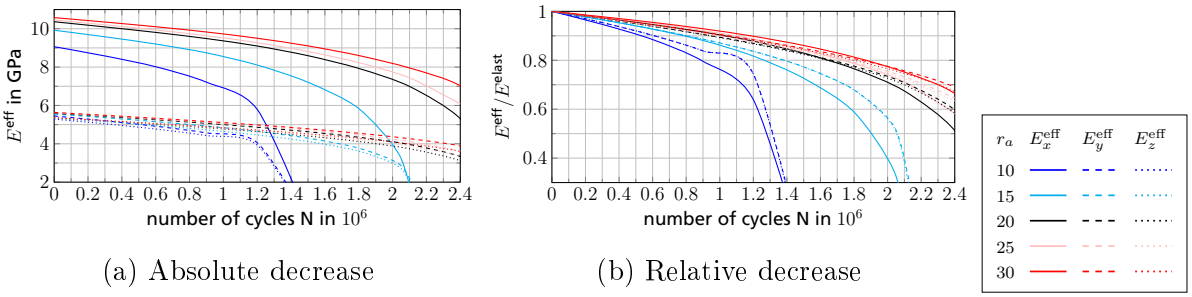

(a) Absolute decrease (b) Relative decrease

Figure 3.17.: Influence of the fiber aspect-ratio r_a on the axial Young's moduli for the fiber orientation shown in figure 3.2(b) upon loading in x-direction

moduli in the different coordinate directions is rather similar.
For comparison we also investigated a loading in y-direction, see figure 3.16. Again, we observe a similar slope of decrease for the absolute values, cf. figure 3.16(a). For the relative values, cf. figure 3.16(b), the spread of the different degradation curves is smaller than for the loading in x-direction, cf. figure 3.15(b). This observation, consistent to the experimental results of Pietrogrande [185] may result from the lower heterogeneity in the stress field upon transverse loading, or from a stronger influence of the matrix behavior.

Dependence on the fiber aspect-ratio

Next, we fix the fiber-volume fraction to 19.5 %, but vary the original fiber aspect-ratio (the quotient of fiber length and fiber diameter) of 20 from 10 to 30 by increments of 5 to see the influence of the stiffness-degradation behavior of our typical structure. Please keep in mind that we fix the unit-cell size to $2 \times L$, where L denotes the fiber length, but keep the resolution fixed. Therefore, the necessary simulations were conducted on cells of different voxel counts, from 128^3 for $r_a = 10$ up to 384^3 voxels for $r_a = 30$.
The resulting directional Young's moduli are recorded in figure 3.17.
The strong dependence of the Young's modulus in principal fiber direction E_x^{eff} on the fiber aspect-ratio is reflected by the differences visible at $N = 0$, whereas the transverse Young's moduli are almost unaffected by changes in the fiber aspect-ratio, cf. figure 3.17(a). For increasing cycles, the decrease of E_x^{eff} depends significantly on the aspect ratio, also in absolute terms. Recall that we found that the absolute decrease did not depend much on the volume fraction. More significantly, we also observe strong differences in the transverse Young's moduli, which is particular surprising when taking into account their close proximity at $N = 0$. These observations are also visible in the normalized Young's moduli, cf.

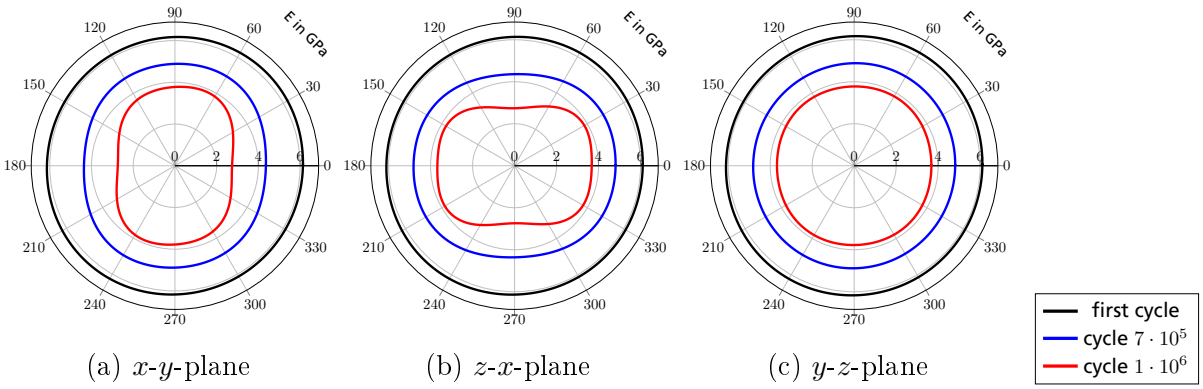

(a) x-y-plane (b) z-x-plane (c) y-z-plane

Figure 3.18.: Evolution of the Young's modulus body, cf. equation (3.3.4), in terms of planar cuts, for a microstructure with isotropic fiber-orientation tensor

figure 3.17(b). However, we see that, for fixed aspect ratio, the decrease of the normalized Young's modulus is similar for the different axial directions.

Fiber-orientation dependence

In this section, we gain insights into the effect of changing the fiber orientation of the composites under consideration, and also the evolving anisotropy induced by the propagation of fatigue damage. For that purpose, we investigate a microstructure with isotropic second-order fiber-orientation tensor, $A = \frac{1}{3}\,\mathrm{Id}$. Due to symmetry considerations, the used microstructure-generation method [173] ensures that the effective elasticity tensor of such a structure is also isotropic. Thus, we may take a deeper look at an emergent anisotropy of the effective stiffness tensor predicted by our multi-scale model described by equations (3.2.7) and (3.2.8). For that purpose, we take a look at the Young's modulus body, defined for a fixed stiffness tensor $\mathbb{C}$ as the surface

$$\left\{ E(\mathbb{C}, \mathbf{p})\, \mathbf{p} \;\middle|\; \mathbf{p} \in \mathbb{R}^3,\ \|\mathbf{p}\| = 1 \right\} \subseteq \mathbb{R}^3, \tag{3.3.4}$$

and subject a microstructure with isotropic fiber-orientation tensor to uni-axial stress-amplitude loading in x-direction. The resulting cuts through the coordinate planes of the Young's modulus body for different cycles are shown in figure 3.18. In all three coordinate planes, the initial directional Young's moduli coincide, i.e., the stiffness in all directions is identical. Subsequently, the Young's moduli decrease differently for different directions, inducing an anisotropy in the x-y- and the z-x-plane, cf. figure 3.18(a) and figure 3.18(b), respectively. The Young's moduli in the y-z-plane also decrease, cf. figure 3.18(c), but in an isotropic fashion. This may be expected when loading an initially isotropic structure

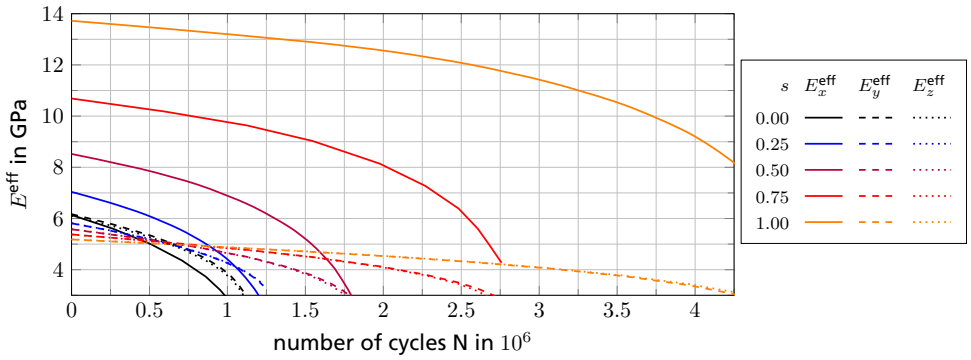

Figure 3.19.: Evolution of the directional Young's modulus for structures with fiber-orientation tensors given by equation (3.3.5), subjected to loading in x-direction

in a specific direction. Still, it is interesting to see that these expectations are fulfilled also in practical simulations. We also conducted similar simulations for planar isotropic and uni-directional fiber-orientation tensors. However, as the results did not add anything significantly new, and for reasons of brevity, we decided to skip these cases.
Rather, we turn our attention to a *continuous* deformation of the fiber-orientation state. For that purpose, we continuously deform one vertex of the fiber-orientation triangle, cf. figure 3.2(a), into another via prescribing

$$A(s) = \frac{s}{3}\,\mathrm{Id} + (1-s)\,\mathbf{e_1} \otimes \mathbf{e_1}, \tag{3.3.5}$$

i.e., we linearly deform the isotropic state for $s = 0$ to the uni-directional fiber orientation at $s = 1$. For three equidistantly spaced s-values between 0 and 1, the emerging axial Young's moduli for loading in x-direction are shown in figure 3.19. At the first cycle, the three axial Young's moduli for the isotropic structure ($s = 0$) are identical, whereas a strong contrast between the in-fiber Young's modulus and the transverse Young's moduli are visible for the uni-axial fiber-orientation state ($s = 1$). Changing the parameter s leads to a continuous deformation between these two states, also in terms of the predicted Young's-moduli evolutions. Notice that the interpolation (3.3.5) produces only transversely isotropic fiber-orientation states (w.r.t. the $\mathbf{e_1}$-axis), and the loading in x-direction preserves this symmetry. That is why, for any fixed value of the interpolation parameter s, we actually only see *two* curves, corresponding to E_x^{eff} and $E_y^{\text{eff}} = E_z^{\text{eff}}$. We observe a continuous dependence of the predicted E^{eff}-curves on the interpolation parameter s. Similar computations may be carried out based on interpolating the isotropic and the transversely isotropic state and deforming the uni-directional fiber-orientation state to the transversely isotropic state. Again, for reasons of brevity, we did not include them.

The state space of second-order fiber-orientation tensors is two-dimensional, and we would like to cover essentially *all* fiber-orientation states present in the fiber-orientation triangle in our multi-scale model. Indeed, for injection-molded components, the predicted fiber-orientation states vary continuously, or, at least, from element to element in the (finite volume) discretization. Unfortunately, we can only compute a finite number of microstructures. Due to the observed continuity of the effective predictions when varying the fiber orientation we opt for an interpolation approach, pioneered by Köbler et al. [160], for constructing an effective model that is capable of covering essentially all possible fiber-orientation tensors of second order. As a preliminary step, we shall discuss a model-order reduction technique necessary for transferring our multi-scale model to component scale.

3.4. A model-order reduction strategy for fatigue damage

To enable computations on component scale, in this section, a model-order reduction framework for the fatigue-damage model of section 3.2 is introduced, loosely based on the non-uniform transformation field analysis [65,67,80,186,187]. The discussion is split into two parts. First, the model-order reduction for a single fiber-reinforced volume element is treated, see section 3.4.1. Subsequently, the extension to varying fiber orientation is discussed, based on fiber-orientation interpolation [160], see section 3.4.2.

3.4.1. Galerkin-type model-order reduction for the polynomial free energy

The starting point for our discussion is the model described by equations (3.2.10) and (3.2.12) of section 3.2, which we assume to be discretized in cycle space by a backward Euler method (see equation (3.2.15)). Recall that the equations of interest may be obtained as critical points of the incremental energy (3.2.15)

$$\mathcal{I}_n : \mathrm{Sym}(()d) \times \mathcal{U} \times \mathcal{D} \to \mathbb{R}, \quad (\overline{\boldsymbol{\varepsilon}}, u, D) \mapsto W(\overline{\boldsymbol{\varepsilon}}, \mathbf{u}, d) + \Delta N_n \, \Phi\left(\frac{d - d^n}{\Delta N_n}\right).$$

This functional may also be written in full detail,

$$\mathcal{I}_n(\overline{\boldsymbol{\varepsilon}}, \mathbf{u}, d) = \frac{1}{2|Q|}\int_Q \chi(\eta + (1-d)^2)\boldsymbol{\varepsilon} : \mathbb{C}^{\mathrm{M}} : \boldsymbol{\varepsilon} + (1-\chi)\boldsymbol{\varepsilon} : \mathbb{C}^{\mathrm{F}} : \boldsymbol{\varepsilon} + \frac{(d-d^n)^2}{\alpha_{\mathrm{d}}\Delta N_n} + \gamma\,\ell^2\,\chi\|\nabla d\|^2\,dx, \tag{3.4.1}$$

where the local strain field is the sum of the applied macroscopic strain and the strain fluctuation $\boldsymbol{\varepsilon} = \overline{\boldsymbol{\varepsilon}} + \nabla^s \mathbf{u}$. We include the macroscopic strain $\overline{\boldsymbol{\varepsilon}}$ as an input variable to $\mathcal{I}_n$, although it is more natural to regarded it as a parameter. We do this for a reason, to be discussed below.

Notice that, in contrast to the general two-potential framework, the dissipation potential (3.2.8) is finite-valued. Thus, the incremental energy (3.4.1) is finite-valued, as well. Furthermore, we draw the reader's attention to the fact that the incremental potential is a *polynomial* in the variables $\mathbf{u}$ and d, see Mujica [188], chapter I, for the background on polynomials in the general Banach-space setting. More precisely, the highest powers of $\mathbf{u}$ and d that appear are quadratic, and the highest power of the combined variable $(\mathbf{u}, d)$ is four.

We employ a straightforward Galerkin-type model-order reduction procedure for the incremental potential (3.4.1), i.e., suppose linearly independent elements $u_1, \dots, u_M$ of $\mathcal{U}$ and $D_1, \dots, D_P$ of $\mathcal{D}$ are given. For fixed cycle step, define the model-order reduced incremental potential

$$\widetilde{\mathcal{I}}_n : \mathrm{Sym}(()d) \times \mathbb{R}^M \times \mathbb{R}^P \to \mathbb{R}, \quad (\overline{\boldsymbol{\varepsilon}}, \xi, \delta) \mapsto \mathcal{I}_n\left(\overline{\boldsymbol{\varepsilon}}, \sum_{i=1}^M \xi_i \mathbf{u}_i, \sum_{\beta=1}^P \delta_\beta d_\beta\right), \tag{3.4.2}$$

where $d^n = \sum_{\beta=1}^P \delta_\beta^n d_\beta$ entering the incremental energy (3.2.15) is the reduced fatigue-damage state of the last cycle step.

Several remarks are in order.

1. Showing the existence of minimizers for the reduced incremental potential (3.4.1) and prescribed strain $\overline{\boldsymbol{\varepsilon}}$ is straightforward. Indeed, the problem is finite-dimensional, and the functional is continuous w.r.t. ξ as well as δ and satisfies a growth condition.

2. Our approach is slightly different from more classical NTFA-approaches for elasto-viscoplasticity, where the displacement fluctuation variable is not chosen in a reduced space. This is a result of the Hookean part of the elasto-viscoplastic free energy, which typically reads
$$\frac{1}{2}(\boldsymbol{\varepsilon} - \boldsymbol{\varepsilon}_{\mathrm{vp}}) : \mathbb{C} : (\boldsymbol{\varepsilon} - \varepsilon_{\mathrm{vp}})$$
in terms of a viscoplastic strain $\boldsymbol{\varepsilon}_{\mathrm{vp}}$, and ensures that the associated balance of linear momentum leads to a linear equation for the displacement fluctuation for prescribed

viscoplastic strain. We are not aware of any comparable simplification strategy for our potential (3.4.1).

3. For fixed $\overline{\boldsymbol{\varepsilon}}$, critical points (ξ, δ) of the reduced incremental potential (3.4.2) satisfy a reduced version of the balance of linear momentum (3.2.10)

$$\int_Q \left[\chi(\eta + (1-d)^2)\mathbb{C}^{\mathrm{M}} : \boldsymbol{\varepsilon} + (1-\chi)\mathbb{C}^{\mathrm{F}} : \boldsymbol{\varepsilon}\right] : \nabla^s \mathbf{u}_i \, dx = 0 \text{ for all } i = 1, \dots M, \tag{3.4.3}$$

and, of the cycle-discrete evolution equation for the fatigue damage (3.2.12)

$$\int_Q d_\beta \left[\chi(1-d)\boldsymbol{\varepsilon} : \mathbb{C}^{\mathrm{M}} : \boldsymbol{\varepsilon} + \frac{d - d^n}{\alpha_{\mathrm{d}} \Delta N_n}\right] - \chi\gamma\ell^2 \nabla d \cdot \nabla d_\beta \, \mathrm{d}\mathbf{x} = 0 \text{ for all } \beta = 1, \dots P, \tag{3.4.4}$$

where

$$\boldsymbol{\varepsilon} = \overline{\boldsymbol{\varepsilon}} + \sum_{i=1}^{M} \xi_i \nabla^s \mathbf{u}_i, \quad d = \sum_{\beta=1}^{P} \delta_\beta d_\beta \quad \text{and} \quad d^n = \sum_{\beta=1}^{P} \delta_\beta^n d_\beta.$$

The current effective stress may be computed as for any two-potential material,

$$\tilde{\boldsymbol{\sigma}}^{\mathrm{eff}} = \frac{\partial \widetilde{\mathcal{I}}}{\partial \overline{\boldsymbol{\varepsilon}}}(\overline{\boldsymbol{\varepsilon}}, \xi, \delta).$$

In formulas, we recover the usual strain-equivalence relation

$$\tilde{\boldsymbol{\sigma}}^{\mathrm{eff}} = \frac{1}{|Q|} \int_Q [\eta + (1-d)^2]\mathbb{C} : \boldsymbol{\varepsilon} \, \mathrm{d}\mathbf{x}.$$

More generally, for any fixed state of reduced fatigue damage, $\delta \in \mathbb{R}^P$, we may compute the associated effective stiffness matrix by equation (3.2.9), where the associated periodic displacement fluctuation field $v_E) : Q \to \mathbb{R}$ solves a reduced version of linear momentum-balance on the micro-scale (3.2.10), compare equation (3.4.3). In terms of effort, in three spatial dimensions, 6 linear problems with M variables need to be solved.

4. For any cycle increment, for solving the equations (3.4.3) and (3.4.4) we rely upon Newton's method with backtracking. As the reduced incremental potential (3.4.1) is a polynomial, equations (3.4.3) and (3.4.4) may also be regarded as polynomial equations in the variable (ξ, δ). In particular, all coefficients of this polynomial can be precomputed once and for all. Due to the specific form of the incremental potential, the cost of storing the coefficients (and assembling the residuals and system matrices for Newton's method) scales as $M^2 \times P^2$. Thus, if M and P are on the order of 10, the effort is on the order of $10^2 \times 10^2 = 10000$. If M and P are on the

order of 100, the effort is on the order of $10^4 \times 10^4 = 10^8$, which may already be too much for practical use, compare Michel & Suquet [189]. We refer to section 3.5.2 for further details.
As a side remark, we tried to work with incremental energies which are linear in d to reduce computational effort. Then, however, no intrinsic bounds on the fatigue-damage variable D may be established for the continuous model, and the resulting model led to non-sense prediction without an explicit constraint on D (which interferes with simple model-order reduction). Also, the non-local term is crucial, as the strong localization otherwise necessitates a large number of modes in the reduced model in order to capture the effective response of the un-reduced model reasonably well.

5. The approximation quality of the reduced-order model (3.4.2) strongly depends on how the "modes" $\{\mathbf{u}_i\}$ and $\{d_\beta\}$ are chosen. We use snapshot-POD, as exposed in Carlberg & Farhat [190], for instance, see section 3.5.2 for further details.

3.4.2. Fiber-orientation interpolation of effective models

Injection-molded short-fiber reinforced thermoplastic parts are characterized by a spatially varying fiber orientation. If described in terms of the second-order Advani-Tucker fiber-orientation tensor [169], the fiber-orientation interpolation-technique introduced by Köbler et al. [160] may be used to cover all possible fiber orientations (which may be described by second-order fiber-orientation tensors) without computing them all.
The basic idea is to realize that the phase space of all possible second-order fiber-orientation tensors, up to rotations, corresponds to a triangle, cf. figure 3.2(a). Thus, a finite-element discretization by linear triangular elements of this triangle may be used, furnishing every node of the triangulation with a material model. Any desired fiber-orientation state is located in some element. Its stress response to a specific loading history is determined by computing the stress response to this loading for the nodes of the triangular element in question, and interpolating the resulting stress values accordingly. Finally, the stress tensor is rotated into the proper frame, recovering the information lost during projection onto the fiber-orientation triangle. This approach circumvents the difficulty that, in general, internal variables on different microstructural elements may not be interpolated in a sensible fashion. Interpolating the stress tensors, however, is possible (even at finite strains for the first Piola-Kirchhoff stress tensor).
The approach just described was shown to preserve the two-potential structure [160]. Concerning the computational effort, for every Gauss point on component level, three

material models need to be evaluated - one per node of the orientation-triangle mesh. Also, the internal variables corresponding to these three nodal models need to be stored. If the computational efforts and the number of internal variables are on a similar level for all nodal models, on average, both the storage requirements and the computational effort are tripled compared to using only a single material model of the same type on component scale.
For the reduced-order model at hand, see section 3.4.1, the fiber-orientation interpolation-procedure may be applied as a special case. We refer to section 3.5 for a computational investigation.

3.5. Numerical demonstrations for the reduced-order model

3.5.1. Setup and used hardware

For selecting the bases $\{\mathbf{u}_i\}$ and $\{d_\beta\}$, sometimes also called *modes*, we performed computations for pre-selected load cases with the discretizations in space and time as well as the solution techniques discussed in section 3.3.1. Details on the mode-selection process and an assessment of the accuracy of the ensuing fiber-orientation interpolation process are described in section 3.5.2 and section 3.5.3 below, respectively.
The presented order-reduced model, cf. section 3.4.1, was integrated into a user-defined material routine (UMAT) in the commercial software ABAQUS [192]. The precomputed data is stored in a common data file, which is accessed by the individual elements separately during their UMAT calls when assembling the algorithmic tangent necessary for applying Newton's method.
We investigate a short-fiber reinforced component in section 3.5.4, and conduct a mold-filling simulation with the software FLUID [191, 193, 194], which solves the Folgar-Tucker equation [195] and relies upon the smooth-orthotropic closure approximation [196], assuming the fiber-volume fraction to be fixed at $\phi = 18.5\,\%$. We used the parameters listed in table 3.2. They correspond to the Carreau-Arrhenius law [171]

$$\mu(T, \dot{\gamma}) = \mu_0 \frac{e^{-A_2(T-T_{ref})}}{(1 + (A_0\dot{\gamma})^2)^{\frac{1-A_1}{2}}}. \tag{3.5.1}$$

In particular, due to the finite-volume discretization, we obtain a second-order fiber-orientation tensor per element of the finite-volume mesh. Subsequently, this data is

Parameter	Value
Density	1100 kg/m^3
Injection temperature	275°C
Wall temperature	50°C
Specific heat	linear interpolation
	719 J/K ($T = 31$°C) - 1635 J/K ($T = 243$°C)
Thermal conductivity	linear interpolation
	0.224 W/(m·K) ($T = 50$°C) - 0.266 ($T = 250$°C)
Initial fiber orientation	$A = \mathrm{diag}(0.8, 0.1, 0.1)$
Fiber-aspect ratio	$r_a = 25$
Folgar-Tucker diffusivity	$C_i = 0.0035$
Glass-transition temperature	$T_{ref} = 240$°C
A_0	0.00051s
A_1	0.395
A_2	0.0077 1/K
μ_0	73Pa·s

Table 3.2.: Material parameters [191] used for the injection-molding simulation, cf. equation (3.5.1)

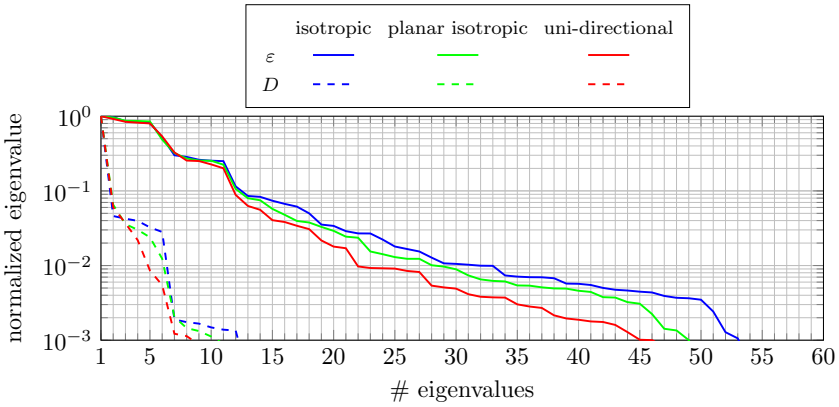

Figure 3.20.: Sorted normalized eigenvalues of the correlation matrices for the strain and fatigue-damage field and the three extreme orientations

mapped to the finite-element mesh which might be different from the original finite-volume mesh.
We conduct a component-scale finite-element simulation with the material and model parameters listed in section 3.3.1, using 2.892.934 linear tetrahedron elements. The computations were performed on a Linux cluster and ran on 256 CPUs distributed on 16 cluster nodes for approximately 1923 hours.

3.5.2. Selecting the reduced bases

For the mode-selection process, we use the proper orthogonal decomposition (POD), see Carlberg & Farhat [190], accounting for the non-equidistant cycle increments by a proper re-weighting of the components of the POD correlation matrices. We rely upon the L^2 inner product for the fatigue-damage variable and the L^2-norm for the strains, which corresponds to an inner product of Korn type for the displacement fields.
As precomputations, we compute three uni-axial loading scenarios corresponding to the three coordinate axes with a stress amplitude of 40MPa and three shear load cases in the coordinate planes with a stress amplitude of 20MPa, see figure 3.21 for an illustration. All load cases were computed up to a stiffness reduction of 50 % using the automatic step-size control introduced in section 3.3.2. We selected 10 snapshots per load case, and used those to build up the POD correlation matrices for the fatigue damage and the displacement field, respectively.
For the three extreme orientations and both the strain and the fatigue-damage fields, we computed the eigenvalues of the POD correlation matrices, sorted them in descending

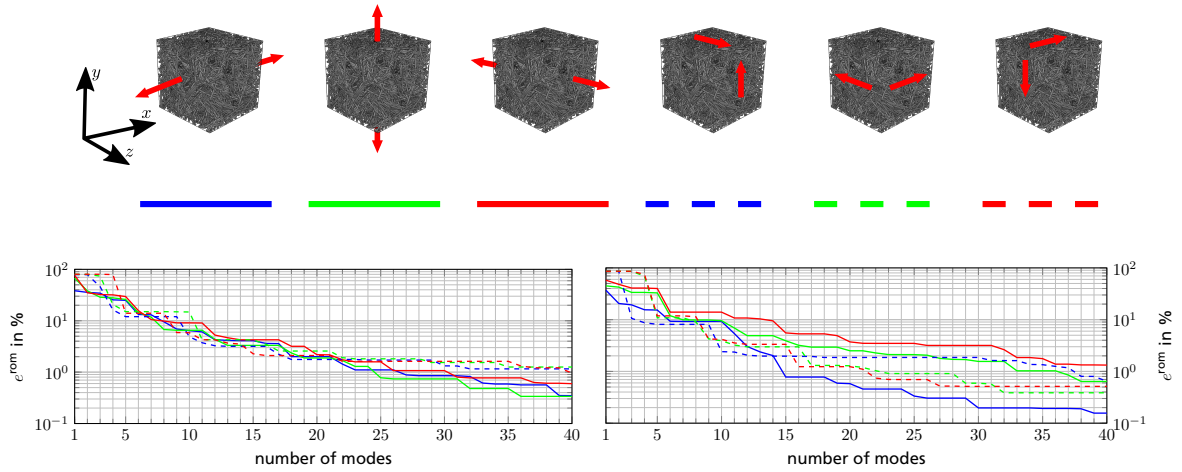

(a) isotropic orientation (b) uni-directional orientation

Figure 3.21.: Average relative error (3.5.2) depending on the number of modes used for two of the three extreme orientations and for the six load cases considered

order and normalized them by the largest eigenvalue, cf. figure 3.20. We see that only a few modes, on the order of 10, are necessary for describing the damage field, whereas a much larger number of modes is necessary for the strain modes. Choosing our threshold to be 0.1 % of the largest eigenvalue, on the order of 50 strain modes are necessary for describing the strain fields for all six load cases to the mentioned accuracy. Notice the uni-directional structure may be described by fewer modes than the planar isotropic structure, which in turn requires fewer modes than the isotropic structure.

Of course, we are not only interested in approximating the fields but also in the predicted effective properties of the reduced model. For that purpose, we integrated the reduced-order models, as described in section 3.4.1, corresponding to the extreme fiber orientations and subjected to the six mentioned load cases for an increasing number of modes (up to 40), cf. figure 3.21. We always use the same number of strain and fatigue-damage modes, and measure the error

$$e^{\text{rom}} = \frac{1}{K} \sum_{i=1}^{K} \frac{\|\overline{\boldsymbol{\varepsilon}}(N_i) - \overline{\boldsymbol{\varepsilon}}^{\text{rom}}(N_i)\|}{\|\overline{\boldsymbol{\varepsilon}}(N_i)\|} \tag{3.5.2}$$

by averaging over all of the K cycle steps, where the cycles N_i are determined, for each loading case and every considered orientation, by the adaptive technique described in section 3.3.2 for the full-field simulation. In equation (3.5.2), $\overline{\boldsymbol{\varepsilon}}(N_i)$ stands for the effective strain amplitude at cycle N_i, and $\overline{\boldsymbol{\varepsilon}}^{\text{rom}}(N_i)$ refers to the effective strain amplitude of the reduced model with a specific number of modes.

The results are collected in figure 3.21 for the isotropic and the uni-directional fiber orien-

tation. We also conducted the simulations for the transversely isotropic orientation, but the results lie in between the two shown cases.
For the isotropic orientation and a low number of modes (below six), cf. figure 3.21(a), in particular the shear cases are not captured. This is a result of not including the corresponding mode. For higher number of included modes, the error e^{rom} decreases in a linear fashion (in the log-plot) until about 25 modes, where the shear-load cases stagnate at about 2 % error. It is interesting to see that, although we saw in section 3.3.2 that the predicted Young's moduli in the direction of loading decreases independently of the loading direction for the isotropic structure, the error reported in figure 3.21(a), *does* depend on the axial direction. This phenomenon cannot be avoided, as we do not account for such a type of symmetry. Rather, we have to live with the fact that the errors for the different axial load cases converge in a similar way on average, i.e., upon increasing the number of modes the specific axis which is the most accurate is also changing in a roughly alternating fashion.
The errors corresponding to the uni-directional fiber-orientation state are reported in figure 3.21(b). We see that the loading in fiber direction is captured most accurately among the considered cases. This is probably rooted in the fact that loading in fiber direction leads to the most pronounced effects, and the POD procedure favors such dominant effects. Interestingly, the shear cases lead to similar error levels as for the isotropic orientation, cf. figure 3.21(a). In contrast to the isotropic case, for the uni-directional microstructure, axial loading in transverse direction is captured with least accuracy, and almost 40 modes are required to maintain an overall accuracy of 2 %. As previously mentioned, this is a consequence of the POD-selection procedure and that the change in the Young's moduli in transverse direction is quite small compared to the tremendous changes experienced by the in-fiber Young's modulus.

We conducted an analysis similar to figure 3.21 for all 15 edges of a triangulation of the fiber-orientation triangle, already considered by Köbler et al. [160], and were led to a relative error not exceeding 2 % for all 15 orientations and all six load cases used as precomputations when using all 40 strain and fatigue-damage modes.

3.5.3. Fiber-orientation interpolation

We identified reduced-order models for all vertices of the fiber-orientation triangulation shown in figure 3.22, using 40 strain and fatigue-damage modes each, and relied upon a piece-wise linear fiber-orientation interpolation scheme, as presented in Köbler et al. [160]. To assess the introduced errors, we compute the error (3.5.2) at the centroids of the fiber-

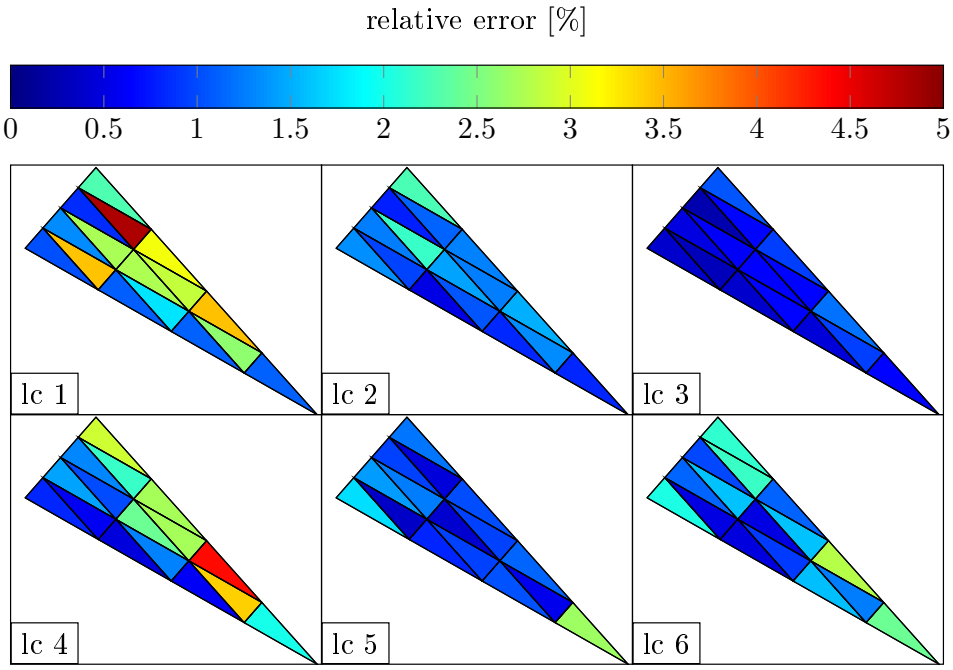

Figure 3.22.: Relative errors (3.5.2) computed at the *centroids* of the triangular elements of the fiber-orientation triangle, evaluated for the six load cases shown from left to right in figure 3.21

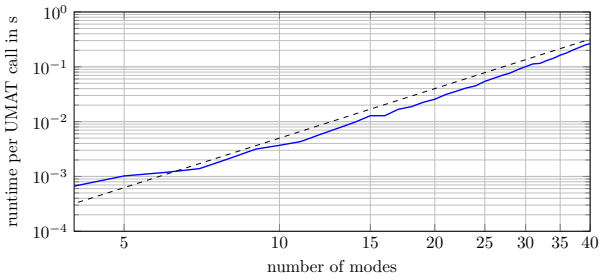

Figure 3.23.: Average run-time for computing the effective response of the reference structure in figure 3.2(b), loaded in x-direction by a constant stress amplitude of 40MPa up to $2.6 \cdot 10^6$ cycles, using the reduced-order model and fiber-orientation interpolation (solid line). For comparison, the dashed line shows a slope of $(\#\text{modes})^3$.

orientation mesh for the three axial and the three shear cases, cf. figure 3.22.
We see that the errors for the individual triangles lie mostly below 2.5 % and do not exceed 5 %. The largest errors are reached for uni-axial extension in x-direction (load case 1) close to the planar isotropic fiber orientation and for shearing in the y-z-plane in between the uni-directional and the planar isotropic fiber-orientation state.
With this final verification step at hand, we are finally in a position to conduct component-scale simulations.
To assess the computational complexity of the model-order reduction procedure, we computed the effective response of the reference structure in figure 3.2(b), loaded in x-direction by a constant stress amplitude of 40MPa up to $2.6 \cdot 10^6$ using the reduced-order model for different number of modes. The results are shown in figure 3.23. The overall computation time for this load case using 40 modes was approximately 70 s. The run-time of our implementation scales like $(\#\text{modes})^3$, as shown in figure 3.23. Indeed, the computational complexity of direct solvers scales cubically in the degrees of freedom.

3.5.4. Application on component scale

To demonstrate the applicability of the presented multi-scale model on component scale, we conducted a finite-element computation of an industrial scale structure. More precisely, we consider an automotive application, i.e., a housing component of an electric window lifter, cf. figure 3.25(a). Such fiber-reinforced components occur frequently in automotive applications, and are typically manufactured by an injection-molding process. In service, such kind of components are typically subjected to cyclic vibrational loads.

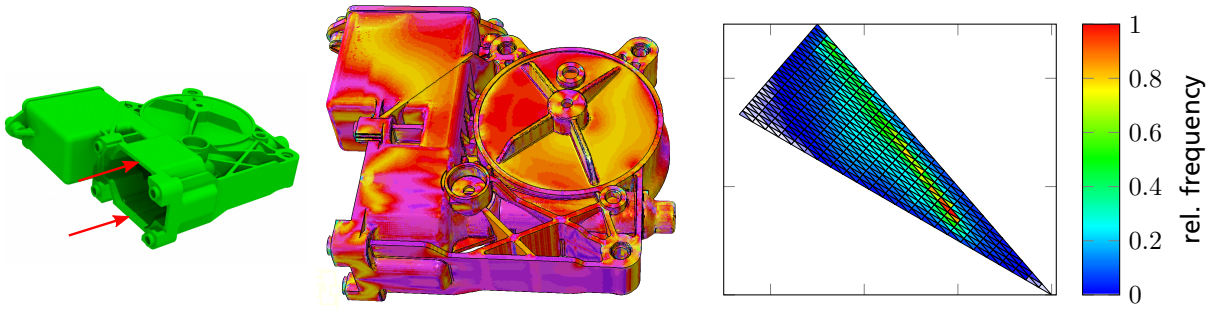

(a) Injection points (b) Fiber-orientation distribution using coloring scheme of Fig. 3.2(a) (c) Relative frequency of fiber orientations in motor housing

Figure 3.24.: Housing component of an electric window-lift drive

For gate positions on the left, cf. figure 3.24(a), the distribution of the fiber orientation was computed by the software FLUID [191, 193, 194] and the parameters listed in table 3.2. The resulting distribution of second-order fiber-orientation tensors is shown in figure 3.24(b), where we use the coloring scheme introduced in figure 3.2(a). Large parts of the structure are either magenta, corresponding to a uni-directional orientation induced by mostly convective flow, and red, which is close to planar isotropic as a consequence of comparatively small thickness of the component in these areas.

The occurring fiber orientations were binned according to a fine triangulation of the fiber-orientation triangle, cf. figure 3.24(c). We see that the isotropic case and the uni-directional fiber orientation do not occur. Also, most areas within the fiber-orientation triangle are only infrequently occurring, cf. figure 3.24(c), and the fiber orientations are concentrated in a green-to-red strip connecting an almost uni-directional and an almost planar isotropic fiber-orientation state. The most frequent fiber-orientation state has eigenvalues $\lambda_1 = 0.8$, $\lambda_2 = 0.12$ and $\lambda_3 = 0.08$. Such a fiber-orientation distribution within a component is typical, see, for instance, Köbler et al. [160]. The component is subjected to a loading whose schematic is shown in figure 3.25(a). In more detail, the component is clamped on the insides of the drilling holes, and a constant stress amplitude $\boldsymbol{\sigma}_a$ =0.5MPa is applied to the area on the left-hand side of figure 3.25(a) that is marked in orange (and by blue arrows).

The material parameters are chosen as specified in section 3.3.1. For the model-order reduction 40 modes are chosen both for the strain and the fatigue-damage field.

To assess the changes in the local stress field and to investigate the subsequent ramifications for ensuing fatigue-crack growth, the principal stress field is shown in figure 3.28 in the virgin state and after 2.6×10^6 cycles. The principal stress, the maximum eigenvalue

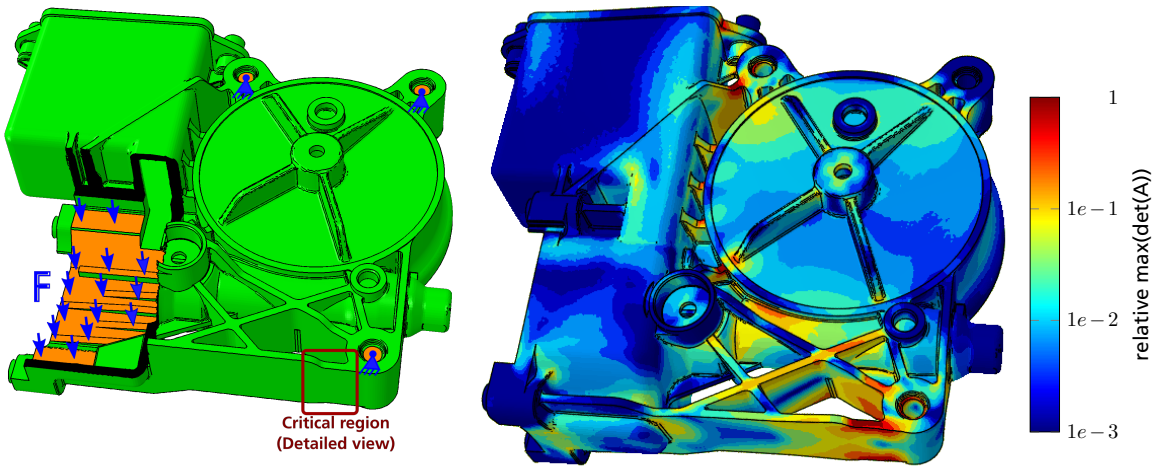

(a) Loading conditions (b) $\Lambda(N)$-field (3.5.4) at $N = 2.6 \times 10^6$

Figure 3.25.: Schematic of the applied loading conditions and relative degradation of the acoustic tensor $\Lambda(N)$ (3.5.4) at $N = 2.6 \times 10^6$ cycles

of the stress tensor, serves as the most basic failure hypothesis for brittle and quasi-brittle materials, see section 2.2.1 in Gross & Seelig [36]. In Fig. 3.28, a considerable redistribution of the principal stresses upon fatigue loading is apparent. Indeed, the peak at the lower right of the structure is significantly reduced. In turn, those regions experiencing a significantly lower stress level remain almost unaffected by the fatigue-damage evolution. To gain deeper insight, we investigate two specific finite elements within a ciritical region of the component, highlighted in red in Fig. 3.25(a), more closely. Element A is chosen because its elastic energy is maximum at the first cycle, whereas Element B maximizes the elastic energy density at cycle 2.6×10^6. The respective elements are marked in Fig. 3.28. In Fig. 3.29(a), the evolution of the principal stress and the von Mises equivalent stress are shown. For the chosen elements, we observe a monotonic decrease of both considered stress measures. The maximal principal stress of element A drops below the maximal principal stress of element B at about 1.75×10^6 cycles, while the von Mises stress of element A is higher as the von Mises stress of element B at all cycles. These observations already indicate a complex redistribution of the experienced loading within the fiber-reinforced structure upon fatigue loading.

For the two respective finite elements, the evolving Young's modulus bodies, cf. equation (3.3.4), in the z-x-plane are shown in figure 3.29(b). Initially, the Young's modulus bodies of the two elements are very similar. Indeed, the predominant fiber orientation may be read from figure 3.24(c). However, the local loading conditions differ, which is reflected in the maximum principal stress. Their absolute values and directions projected to the

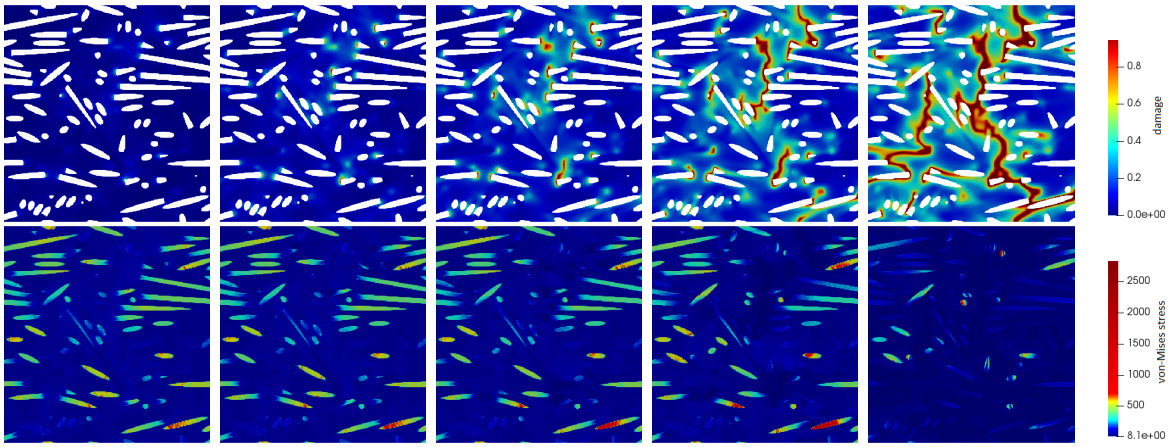

Figure 3.26.: Local fields in the corresponding micro-simulation for element A at time instances 1-5 (left to right): damage (top) and von Mises stress (bottom)

z-x-plane are plotted along the Young's modulus bodies in figure 3.29(b). Due to these different conditions, a change in the local stiffness tensor is induced. The emerging differences are significant at the final cycle considered, as is readily apparent from inspecting figure 3.29(b).

To gain deeper insight into the different behavior of the elements A and B, respectively, we investigate the evolution of the corresponding micromechanical fields during the loading procedure. For this purpose, we extracted the loading history from the macroscopic simulation and conducted strain-amplitude driven microscopic simulations on microstructures with proper fiber orientations. The resulting local damage and stress fields are shown in figure 3.26 and figure 3.27 at specific time instances, specifically marked in figure 3.26. We observe an evolving damage field, starting at the fiber tips and eventually coalescing into a crack that leads to a complete failure of the entire volume element. Comparing the two elements, the damage level in element B significantly exceeds element A. Correspondingly, the stresses are redistributed as, due to damage in the surrounding matrix, the fibers lose their load-bearing capacity.

To complement the previous investigations, we turn our attention to the evolution of the acoustic tensor. Whenever the strain field is discontinuous in a direction $\mathbf{g}$ across a discontinuity with normal vector $\mathbf{n}$, necessarily $\mathbf{g}$ is an element of the null space of the acoustic tensor $A(\mathbf{n}, \mathbb{C})$, i.e.,

$$A(\mathbf{n}, \mathbb{C}) \cdot \mathbf{g} = 0 \tag{3.5.3}$$

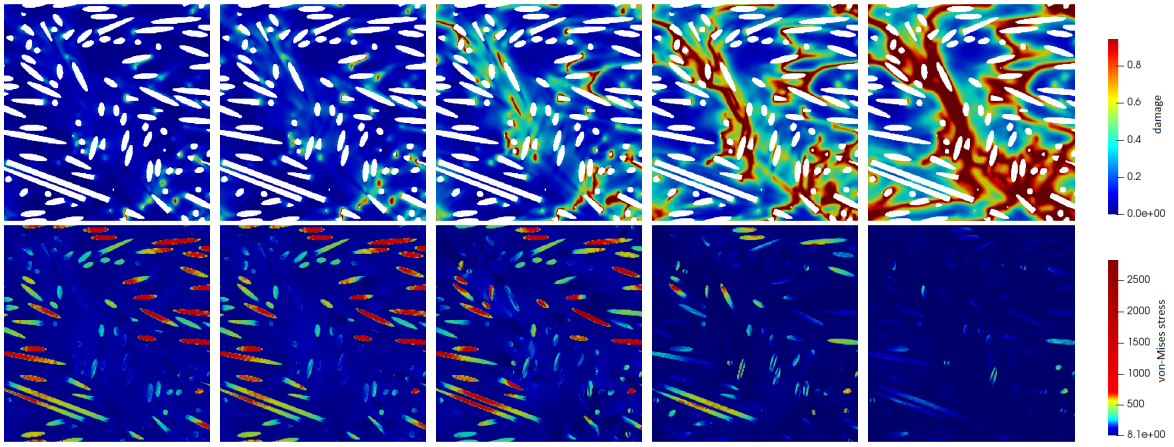

Figure 3.27.: Local fields in the corresponding micro-simulation for element B at time instants 1-5 (left to right): damage (top) and von Mises stress (bottom)

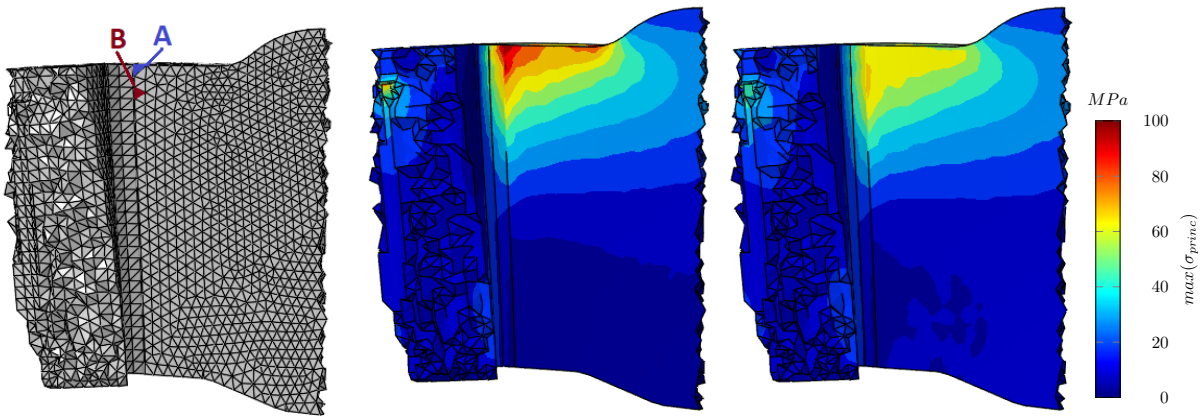

Figure 3.28.: FE mesh and closely examined elements A and B (left) and principal stress $\boldsymbol{\sigma}_{\max}$ in a bottom view for the undamaged state (middle) and after 2.6×10^6 cycles (right)

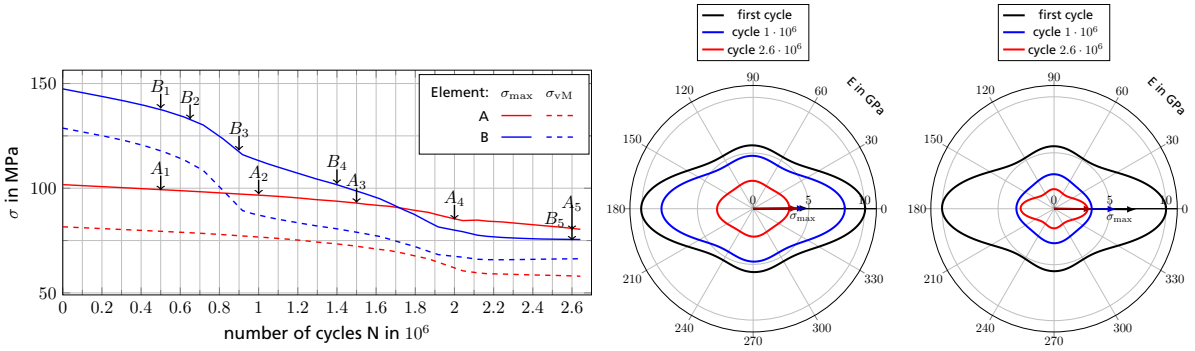

(a) Evolution of principal and von Mises stress (b) Evolving Young's modulus body in the z-x-plane for element A (left) and B (right)

Figure 3.29.: Investigations for the finite elements A (highest elastic energy at cycle 0) and B (highest elastic energy at cycle 2.6×10^6)

holds for the acoustic tensor, implicitly defined as the symmetric order-two tensor satisfying

$$\mathbf{u} \cdot A(\mathbf{n}, \mathbb{C}) \cdot \mathbf{v} = \mathbf{u} \otimes_s \mathbf{n} : \mathbb{C} : \mathbf{u} \otimes_s \mathbf{n} \quad \text{for all} \quad \mathbf{u}, \mathbf{v} \in \mathbb{R}^3,$$

where $\otimes_s$ denotes the symmetrized tensor product and $\mathbb{C}$ stands for the current stiffness tensor. In particular, the condition (3.5.3) is necessary for a damage model to exhibit localization in terms of crack initiation or grack growth. We refer to section 9.5 in Gross & Seelig [36] for background and discussion.
For a stiffness tensor evolving in cycle space, the quantity

$$\Lambda(N) = \max_{\|\mathbf{n}\|=1} \left[1 - \frac{\det A(\mathbf{n}, \mathbb{C}(N))}{\det A(\mathbf{n}, \mathbb{C}(0))} \right] \tag{3.5.4}$$

measures the change in the determinant of the acoustic tensor in a quantitative manner. Indeed, $\Lambda(0) = 0$ and $\Lambda(N) = 1$ implies that the localization condition (3.5.3) holds for some normal $\mathbf{n}$ and a non-zero direction $\mathbf{g}$.
The $\Lambda(N)$-field for the investigated component and at the final cycle $N = 2.6 \times 10^6$ is shown in figure 3.25(b) on a logarithmic scale. There are large parts of the structure where no localization is imminent. However, in particular at the ribs of the component, fatigue cracks are expected to nucleate, confirming engineering intuition.

3.6. Conclusion

This chapter was concerned with simulating the stiffness-degradation behavior of short-fiber reinforced plastics subjected to high-cycle fatigue loading. The multiple scales in-

volved, both in space and time, make the problem challenging, together with the inherent anisotropy of fiber-reinforced materials and the variations in the composition of the phases (both in terms of volume fraction and fiber orientation) inherent to injection-molded short-fiber reinforced components.

We put special emphasis on the multi-scale structure of the problem *in space*, because the fibers induce heterogeneous stress fields on the microscopic scale, essentially playing the role of "notches". Our intention was to show the effect of the reinforcements on the stiffness degradation. To do so, we relied upon a series of simplifications. To start, we decided to ignore the growth of fatigue cracks on the macroscopic scale and focused on macroscopic stiffness degradation induced by fatigue-crack growth on the microscopic scale. Also, we skipped the time domain entirely, and started our modeling directly in cycle space. It would be interesting to see how cycle-jump techniques [197,198] or homogenization approaches in time [199, 200] may either be combined to the presented model, or serve as a verification of the approach.

The model we chose was kept deliberately simple to ensure that the resulting multi-scale problem admits a model order reduction. We guarantee this property by using only polynomials in the incremental potential. In this way, a straightforward Galerkin-type model-order reduction is ensured. This choice, in turn, has consequences for the physical assumptions that are taken into account. For instance, we disregard tension-compression asymmetry [132, 201]. Also, we cannot ensure point-wise irreversibility of damage in the reduced model.

The assumption of being order-reducible needs to be critically reviewed, because such an assumption is not supported by physical reasoning. Rather, it is merely convenient from a computational point of view. Despite the strong simplifications, we were able to complete a full multi-scale simulation chain, starting from the matrix modeling up to the component-scale simulations.

Augmented by a non-local term in the damage evolution, we studied both the sensitivity on numerical parameters and the model predictions on fiber-reinforced volume elements. We were able to vary essentially all parameters entering the multi-scale model, both physical parameters and morphological parameters of the composite, and could also change the loading. In doing so, we were able to give detailed predictions of the degradation of the *entire* stiffness tensor, i.e., for each component individually, and the influence of the various parameters. These investigations give rise to a wealth of data (much more than we could show), and are expected to complement experimental results, thereby reducing the emerging costs.

As a downside, our presented model does not admit representative volume elements, as a consequence of the localization permitted by the model [177]. When modeling failure

processes, localization cannot be avoided. However, as we wanted to model the stiffness degradation, in the first place, it would be interesting to find a stiffness-degradation model that admits representative volume elements. As a byproduct, we could eliminate the strong dependence of our model on the length-scale parameter, which is often difficult to estimate in practice [202].

We presented a model-order reduction strategy, that was furthermore integrated into the fiber-orientation interpolation technique of Köbler et al. [160]. It is only in this work that we realize the full potential of the fiber-orientation interpolation technique, as the latter applies to arbitrary material behavior and appears to be a promising tool for multi-scale modeling of short-fiber reinforced materials.

It might be wise to exploit alternatives, such the recently proposed self-consistent clustering analysis [68, 69] or approaches based on artificial intelligence [90, 203]. Last but not least let us mention that this work is devoted to stiffness degradation upon fatigue loading, but does not explicitly model fatigue-crack growth. The model we presented may be supplemented by a conventional fracture criterion [135] to additionally provide a lifetime estimate for a specific component.

As a next step, it would be interesting to extend the presented model to a (at least quasi-static) fatigue-crack growth model.

4. A multiscale high-cycle fatigue-damage model for the stiffness degradation of fiber-reinforced materials based on a mixed variational framework[1]

4.1. Introduction

This chapter builds upon the approach introduced by Jain et al. [9] and refined in chapter 3 in terms of a suitable multiscale fatigue-damage model of short-fiber polymer composites. Following their strategy, we are interested in modeling the progressive stiffness degradation in the stable phase prior to failure, serving as the basis of a subsequent failure assessment via an appropriate criterion. To be more precise, we introduce a scalar fatigue-damage model for the polymer matrix, and the stiffness degradation of the composite arises from a suitable MOR strategy in a computational homogenization framework.
In chapter 3, we used a fatigue-damage model that is quite similar to classical phase-field fracture models [133, 204, 205] and exploited the fact that the corresponding incremental potential is a fourth-order polynomial in the involved fields, which permits to express the incremental potential in a MOR framework *exactly* in terms of suitable precomputed quantities. In particular, no special quadrature [189] is necessary in the NTFA procedure. Taking a closer look at the typical stiffness degradation of polymer composites upon fatigue loading [3, 5], see Fig. 4.1, we notice that the first and the second phase of the

[1] N. Magino, J. Köbler, H. Andrä, F. Welschinger, R. Müller, M. Schneider, "A multiscale high-cycle fatigue-damage model for the stiffness degradation of fiber-reinforced materials based on a mixed variational framework," *Computer Methods in Applied Mechanics and Engineering*, vol. 388, pp. 114198, 2022.

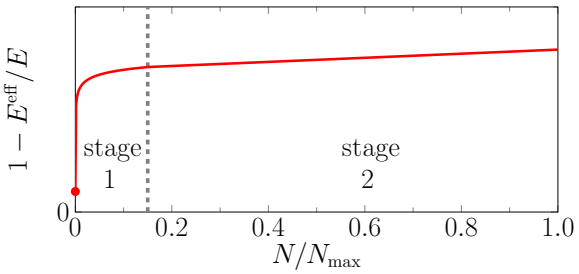

(a) Constant strain amplitude

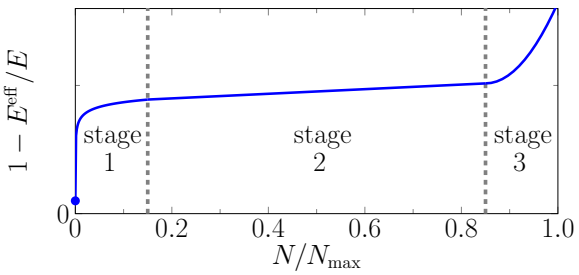

(b) Constant stress amplitude

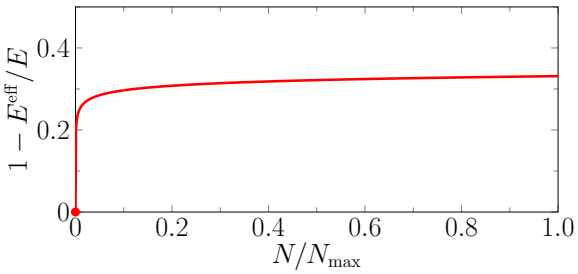

(c) Constant strain amplitude

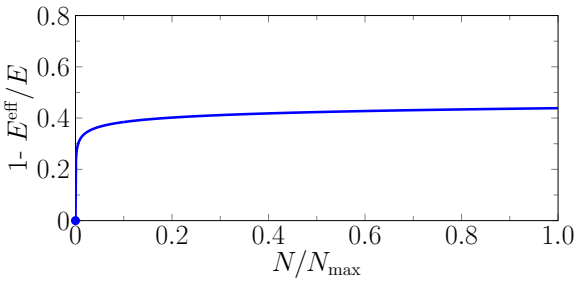

(d) Constant stress amplitude

Figure 4.1.: Comparison of the effective fatigue damage reported in the literature [5] (left) and predicted by the proposed model (right), distinguishing constant strain amplitude (top) and constant stress amplitude (bottom) for reversible loading (i.e., $R = 0$)

fatigue-damage evolution on the macroscale are characterized by a steady and stable damage evolution. Only for prescribed stress amplitude and in the third, final phase, localization occurs. As the models of Jain et al. [9] and chapter 3 only require modeling the first and the second phase of the fatigue-damage evolution to assess the lifetime of the component, we sought an alternative damage model which permits a more efficient numerical treatment. Indeed, to model this stable phase, it appears sufficient to employ fatigue-damage model which avoids the negative side effects of softening damage models, like the inherently high number of modes necessary to capture the evolution in the strain softening regime appropriately, see Fig 3.21, and the loss of representativity upon softening [177].

For this purpose, we build upon the convex, rate-independent damage model [135, 206] of Görthofer et al. [207]. Inspired by the work of Govindjee [208], Görthofer et al. [207] proposed a framework for damage models that directly operates on the compliance matrix as an internal variable and satisfies Wulfinghoff's damage criterion [209]. The resulting strain energy is jointly convex in the strain and internal variables and thus precludes strain softening [210], leading to mesh-independent results without the necessity of introducing a gradient term of the damage variable [132,134,137,211–214]. In contrast to elastoplastic models, which may be used for modeling a shift in the "secant stiffness", our approach permits to predict the degradation of the full stiffness tensor, accounting for anisotropy effects.

To reproduce the characteristic behavior of the fatigue-damage evolution in the first two stages, see Fig. 4.1, we formulate the model in the *logarithmic cycle* space. In addition to closely matching what is observed in experiments, see Fig. 4.1, this formulation leads to a high computational efficiency, as a large number of cycles can be simulated quickly. Endowing the thermoplastic matrix with this model leads to a naturally emerging multiscale model, see section 4.2.2, which we demonstrate to be appropriate to capture the loss of stiffness upon fatigue loading for a glass-fiber reinforced polybutylene terephthalate (PBT), see section 4.2.3, at least if the stiffness reduction introduced in the initial phase, which can be determined experimentally with little effort, is considered.

Unfortunately, in its original form, the introduced fatigue-damage model is not directly suitable for efficient model-order reduction. In contrast to the model of chapter 3, the class of models introduced by Görthofer et al. [207] leads to an incremental potential whose integrand is no longer a polynomial in the fields. In particular, the precomputing strategy of chapter 3 does not apply. Of course, approximation procedures [79,80], Gauss quadrature [189] or polynomialization [215] could be applied. To avoid the resulting decrease in accuracy or increase in computational effort, we follow a different route. More precisely, we exploit a reformulation of the fatigue-damage evolution in terms of the stress

amplitude. Mathematically speaking, we apply a partial Legendre transform in the strain amplitude. By this nonlinear transformation, the underlying saddle-point problem has an incremental potential which is a third-order polynomial in the involved stress-amplitude and fatigue-damage field. In particular, the precomputation strategy of chapter 3 applies. However, this reformulation comes at a cost. The original, primal minimization principle is replaced by a mixed variational principle, and its structure needs to be studied anew, in particular concerning model-order reduction. Fortunately, see section 4.3 for details, the corresponding mixed variational principle turns out to be well-posed, even upon model-order reduction, as long as suitable (physically sound) conditions hold. We thoroughly investigate the sensitivity of the multiscale model and its reduced-order model w.r.t. the involved parameters in section 4.4, and demonstrate the capabilities of the ensuing model on component scale, see section 4.5.

4.2. A fatigue-damage model for the stiffness degradation

In section 4.2.1, we introduce a (homogeneous) material model for the polymer matrix which models the stiffness degradation upon fatigue loading. The material model may appear simple, but was selected with its favorable properties concerning model-order reduction in mind.
In chapter 3, we work directly in cycle space for reasons of efficiency. In a similar direction, we consider a time-like variable directly in *logarithmic* cycle space. We investigate the material behavior in a one-dimensional stress- and strain-driven load case and compare the material behavior to fatigue degradation of short-fiber reinforced polymers reported in the literature [4, 5, 142]. Subsequently, in section (4.2.2), the described model enters as a constituent in a composite, mathematically encoded by an appropriate first-order homogenization framework. Upon discretization in cycle space and for prescribed stress (amplitude), we also discuss the naturally associated variational principle. We close this section by showing that the introduced model captures the phase of second, stable stiffness degradation of fiber-reinforced composite microstructures quite accurately, at least if the initial stiffness degradation is considered.

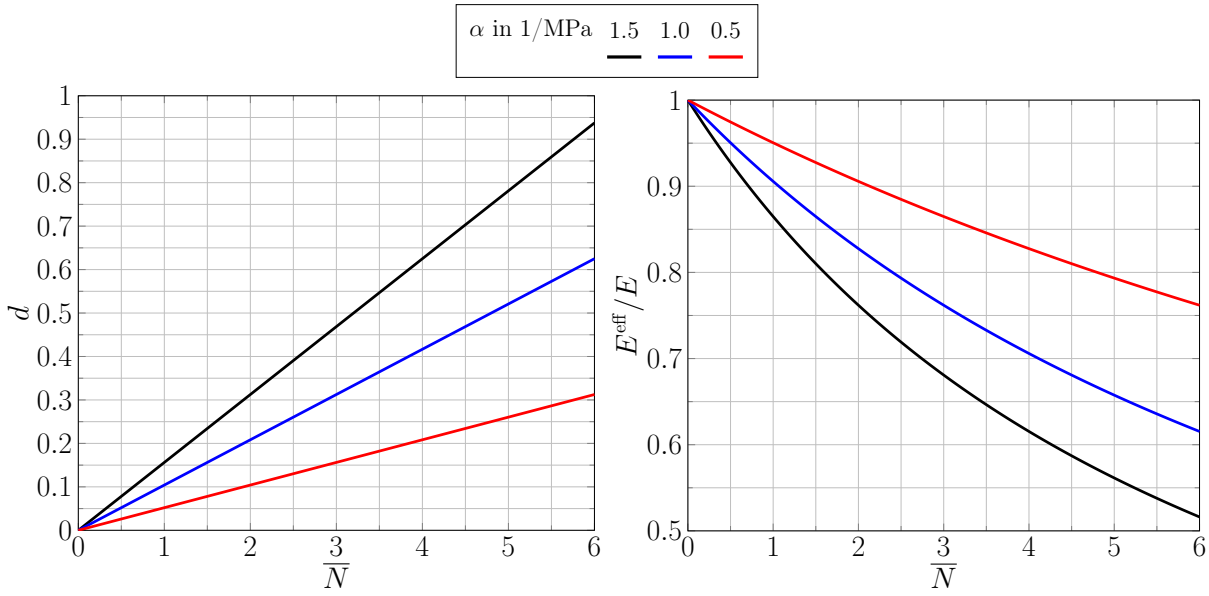

(a) Evolution of fatigue damage

(b) Evolution of effective Young's modulus

Figure 4.2.: Effect of changing the parameter α on the model for constant stress amplitude $\sigma_{\max} = 25$ MPa

4.2.1. Matrix modeling

We introduce a fatigue-damage material model at small strains using the framework of generalized standard materials (GSMs) of dissipative solids [17, 216]. We formulate our model in logarithmic cycle space, described by a continuous variable $\overline{N} \geq 0$, instead of the more standard *time* framework. To be precise, we use the rescaling $\overline{N} = \log_{10}(N)$ throughout this work, where N refers to the current cycle, and introduce a time like derivative $q' \equiv \mathrm{d}q/\mathrm{d}\overline{N}$. This choice permits taking large steps $\triangle\overline{N}$ in logarithmic cycle space, necessary for treating high-cycle fatigue problems, instead of small time steps $\triangle t$. The GSM framework is carried over to the cycle setting, by simply relabeling the time t by the cycle $\overline{N}$ (some care has to be taken with the dimensions, as the time-like scale $\overline{N}$ is dimensionless).

The proposed model involves a scalar damage variable $D \geq 0$ as the only internal variable. We consider the free energy

$$w(\boldsymbol{\varepsilon}, d) = \frac{1}{2(1+D)}\, \boldsymbol{\varepsilon} : \mathbb{C} : \boldsymbol{\varepsilon}, \tag{4.2.1}$$

where $\boldsymbol{\varepsilon}$ refers to the elastic (small) strain tensor and $\mathbb{C}$ denotes the (undamaged) fourth-order stiffness tensor. The model is completed by the dissipation potential

$$\phi(D') = \frac{1}{2\alpha}(D')^2, \tag{4.2.2}$$

where $\alpha > 0$ determines the speed of evolution and D' denotes the derivative of the fatigue-damage variable D w.r.t. the continuous logarithmic cycle variable $\overline{N}$. The associated Cauchy stress-tensor $\boldsymbol{\sigma}$ is defined by

$$\boldsymbol{\sigma} \equiv \frac{\partial w}{\partial \boldsymbol{\varepsilon}} (\boldsymbol{\varepsilon}, D) = \frac{1}{(1+D)} \mathbb{C} : \boldsymbol{\varepsilon}, \tag{4.2.3}$$

i.e., the stiffness tensor is reduced by a factor $1/(1+D)$ for growing fatigue-damage variable d. Biot's equation associated to the described model reads

$$0 \stackrel{!}{=} \frac{\partial w}{\partial D} (\boldsymbol{\varepsilon}, D) + \frac{\partial \phi}{\partial D'} (D') = -\frac{1}{2(1+D)^2} \boldsymbol{\varepsilon} : \mathbb{C} : \boldsymbol{\varepsilon} + \frac{D'}{\alpha}, \tag{4.2.4}$$

i.e., in explicit form

$$D' = \frac{\alpha}{2(1+D)^2} \boldsymbol{\varepsilon} : \mathbb{C} : \boldsymbol{\varepsilon}. \tag{4.2.5}$$

As the right-hand side is always non-negative, the damage variable is non-decreasing for increasing cycles $\overline{N}$.

An implicit Euler discretization of equation (4.2.5) in logarithmic cycle space leads to the equation

$$\frac{D^{n+1} - D^n}{\triangle \overline{N}} = \frac{\alpha}{2(1+D^{n+1})^2} \boldsymbol{\varepsilon} : \mathbb{C} : \boldsymbol{\varepsilon}, \tag{4.2.6}$$

where D^n refers to the damage value at the previous and D^{n+1} to the damage value at the current state.

To gain some understanding of the predictions made by the model, we shall discuss uniaxial extension for the one-dimensional case in more detail. In this context, we denote the Young's modulus by E.

For a constant peak stress $\sigma_{\max}$, the differential equation (4.2.5) with initial condition $D(0) = 0$ may be integrated exactly,

$$D\left(\overline{N}\right) = \frac{\alpha}{2} \frac{\sigma_{\max}^2}{E} \overline{N}. \tag{4.2.7}$$

Thus, the damage variable D grows linearly in the variable $\overline{N}$. In Fig. 4.2(a), the solution is plotted for a stress amplitude of $\sigma_{\max} = 25$ MPa and the Young's modulus $E = 3$ GPa. The fatigue-damage variable depends linearly on the parameter parameter α, resulting in a faster evolution of the damage variable D with increasing α. The damage variable has no upper bound and evolves towards $+\infty$ under fatigue loading. This corresponds to an asymptotic degradation of the effective stiffness $E^{\text{eff}} = \frac{1}{1+D} E$ towards zero,

$$E^{\text{eff}} = \frac{1}{1 + \frac{1}{2}\alpha\sigma_{\max}^2 \overline{N}/E} E, \tag{4.2.8}$$

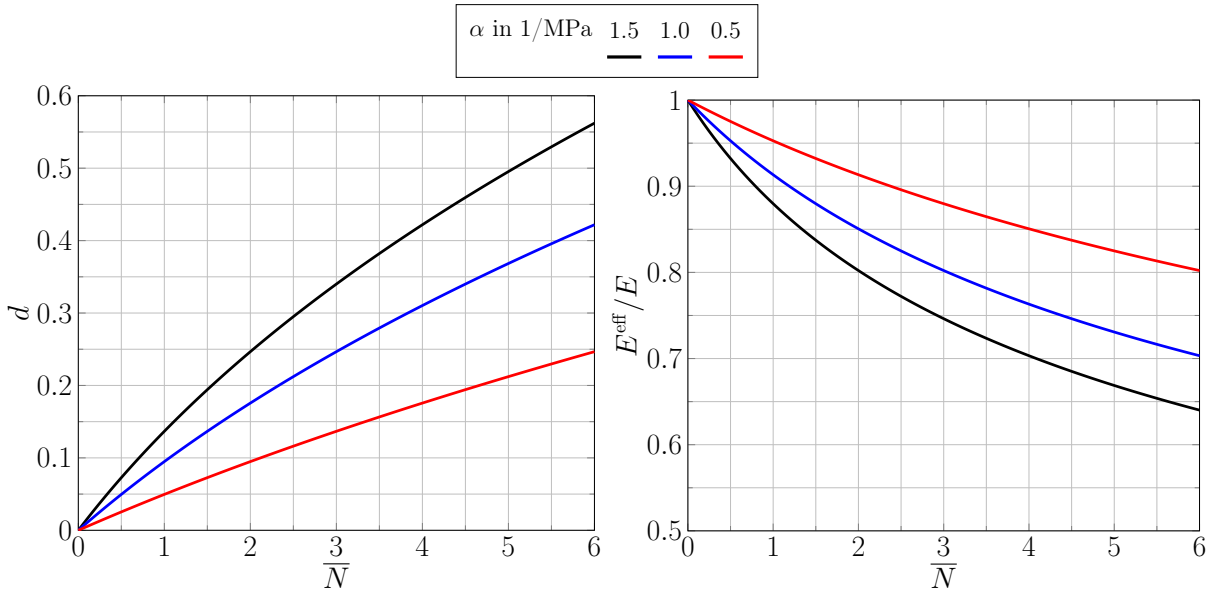

(a) Evolution of fatigue damage

(b) Evolution of effective Young's modulus

Figure 4.3.: Effect of the parameter α on the model for constant strain amplitude $\varepsilon_{\max} = 8.33 \times 10^{-3}$

as shown in Fig. 4.2(b). At the undamaged state $D = 0$, the current effective Young's modulus E^{eff} equals the elastic modulus E. Under fatigue loading, the effective Young's modulus decreases. The slope of the E-$\overline{N}$-curve decreases with increasing $\overline{N}$. Thus, for high number of cycles, the degradation of the effective Young's modulus is slowed down. Indeed, since the damage variable D never reaches $+\infty$, the state $E = 0$ of the material is not reached.

For a constant peak strain $\varepsilon_{\max}$ and the initial condition $D(0) = 0$, the damage evolution integrates to the expression

$$D\left(\overline{N}\right) = \left(1 + \frac{3\alpha}{2} E \varepsilon_{\max}^2 \overline{N}\right)^{\frac{1}{3}} - 1. \tag{4.2.9}$$

The solution is plotted for a strain amplitude of $\varepsilon_{\max} = 8.33 \times 10^{-3}$ and a Young's modulus of $E = 3$ GPa in Fig. 4.3(a). The corresponding evolution of the effective Young's modulus

$$E^{\text{eff}} = \frac{1}{\left(1 + \frac{3}{2}\alpha E \varepsilon_{\max}^2 \overline{N}\right)^{\frac{1}{3}}} E \tag{4.2.10}$$

is shown in Fig. 4.3(b). The exponent in the evolution of the damage variable of 1/3 is smaller than under constant stress, where the exponent is one. Still, as for stress loading, the fatigue damage evolution grows to $+\infty$ as $\overline{N} \to +\infty$. Under constant strain

amplitude, the evolution of the effective Young's modulus asymptotically goes to zero, as well. However, due to the cubic root-type evolution of the damage variable under constant strain amplitude compared to the linear evolution under constant stress amplitude, the degradation of the material progresses at a slower rate.
Both under constant stress and constant strain amplitude, the model does not feature a fatigue limit. Instead, the model predicts a stable stiffness degradation to zero, due to fatigue damage. To predict the complete failure upon fatigue loading, an additional failure criterion needs to be supplemented.
In Fig. 4.1, the introduced fatigue-damage model is compared to typical experimental results from the literature. The stiffness evolution of the proposed model is given for $\alpha = 1.5$ 1/MPa and a Young's modulus of $E = 3$ GPa. The loadings are chosen with a stress amplitude of $\sigma_\mathrm{a} = 25$ MPa and a strain amplitude of $\varepsilon_\mathrm{max} = 8.33 \times 10^{-3}$. In strain-controlled fatigue experiments of short-fiber reinforced polymers, two distinct stages emerge in cycle space. Starting from an initial damage value evoked by the preloading step (and whose magnitude depends on the applied displacement [5]), the stiffness decreases rapidly in the first stage of fatigue loading. The proposed fatigue-damage model may reproduce the initial loss in stiffness by considering a positive initial value $D_0 > 0$. If $D_0 = 0$ is used, the stiffness degradation experienced in the first cycle will not be accounted for. The model at hand qualitatively reproduces the rapid degradation of the material in stage-1 fatigue. Subsequently, in experimental stage-2 fatigue, the material degradation enters a stable phase of stiffness degradation. The effective Young's modulus of the material decreases gradually. The model at hand may reproduce this fatigue-loading regime quite accurately.
Under constant stress-amplitude loading, the stiffness degradation is also characterized by these two phases, but enters a third stage, which was not observed for displacement-driven experiments. In this third stage, a critical damage state forms which leads to a complete fracture of the test specimen. This stage-3 fatigue is not accounted for by the proposed fatigue model on the microscale. Rather, the onset of macroscopic failure can be determined via a suitable failure criterion, like a prescribed amount of stiffness lost [9, 217, 218].

4.2.2. Model on the microscale

Consider a cubic cell $Y \subseteq \mathbb{R}^m$, and suppose that a microscopic stiffness distribution $Y \ni \mathbf{x} \mapsto \mathbb{C}(\mathbf{x})$, associating a (non-degenerate) linear elastic stiffness tensor to each microscopic point, and a (bounded) field $\alpha : Y \to [0, \infty)$, are given. For a prescribed path

of macroscopic stress amplitudes

$$\overline{\boldsymbol{\varepsilon}} : [0, \overline{N}_{\max}] \to \mathrm{Sym}(m), \tag{4.2.11}$$

mapping into the space $\mathrm{Sym}(m)$ of symmetric $m \times m$ tensors, we seek a displacement fluctuation field u, a strain field $\boldsymbol{\varepsilon}$, a stress field $\boldsymbol{\sigma}$ and a damage field D, all defined on the microscopic scale, satisfying kinematic compatibility

$$\boldsymbol{\varepsilon}\left(\overline{N}, \mathbf{x}\right) = \left\langle \boldsymbol{\varepsilon}\left(\overline{N}, \cdot\right)\right\rangle_Y + \nabla^s \mathbf{u}\left(\overline{N}, \mathbf{x}\right), \tag{4.2.12}$$

where $\langle . \rangle_Y$ stands for averaging over the cell Y, the constitutive equation

$$\boldsymbol{\sigma}\left(\overline{N}, \mathbf{x}\right) = \frac{1}{\left(1 + D\left(\overline{N}, \mathbf{x}\right)\right)} \mathbb{C}\left(\mathbf{x}\right) : \boldsymbol{\varepsilon}\left(\overline{N}, \mathbf{x}\right), \tag{4.2.13}$$

the (quasi-static) balance of linear momentum

$$\mathrm{div}\ \boldsymbol{\sigma}\left(\overline{N}, \mathbf{x}\right) = 0 \tag{4.2.14}$$

and Biot's equation

$$D'\left(\overline{N}, \mathbf{x}\right) = \frac{\alpha\left(\mathbf{x}\right)}{2\left(1 + D\left(\overline{N}, \mathbf{x}\right)\right)^2} \boldsymbol{\varepsilon}\left(\overline{N}, \mathbf{x}\right) : \mathbb{C}\left(\mathbf{x}\right) : \boldsymbol{\varepsilon}\left(\overline{N}, \mathbf{x}\right), \tag{4.2.15}$$

together with the prescribed stress amplitude $\overline{\boldsymbol{\sigma}}\left(\overline{N}\right)$

$$\left\langle \boldsymbol{\sigma}\left(\overline{N}, \cdot\right)\right\rangle_Y = \overline{\boldsymbol{\sigma}}\left(\overline{N}\right) \tag{4.2.16}$$

and the initial condition

$$D\left(0, \mathbf{x}\right) = 0 \tag{4.2.17}$$

for all $\mathbf{x} \in Y$. Upon an implicit discretization in time and eliminating all fields except for $\overline{\boldsymbol{\varepsilon}}^n$, $\mathbf{u}^n$ and D^n, where the macroscopic strain $\overline{\boldsymbol{\varepsilon}}^n$ at cycle $\overline{N}^n$ is defined as

$$\overline{\boldsymbol{\varepsilon}}^n = \left\langle \boldsymbol{\varepsilon}\left(\overline{N}^n, \cdot\right)\right\rangle_Y, \tag{4.2.18}$$

the latter set of equations, at the current cycle step, corresponds to a critical point of the variational principle

$$F^{n+1}\left(\overline{\boldsymbol{\varepsilon}}, \mathbf{u}, D\right) \longrightarrow \min \tag{4.2.19}$$

for the Ortiz-Stainier functional [219, 220]

$$F^{n+1}\left(\overline{\boldsymbol{\varepsilon}}, \mathbf{u}, D\right) = \left\langle \frac{1}{2\left(1 + D\right)} \left(\overline{\boldsymbol{\varepsilon}} + \nabla^s \mathbf{u}\right) : \mathbb{C} : \left(\overline{\boldsymbol{\varepsilon}} + \nabla^s \mathbf{u}\right) + \frac{1}{2\alpha \triangle \overline{N}} \left(D - D^n\right)^2 \right\rangle_Y - \overline{\boldsymbol{\varepsilon}} : \overline{\boldsymbol{\sigma}}^{n+1}. \tag{4.2.20}$$

Material	E in GPa	ν	Additional parameters
E-glass fibers	72	0.22	–
PBT matrix	2.69	0.4	$\alpha = 15$ 1/GPa

Table 4.1.: Model parameters adjusted to experimental data

For the latter definition, we use the convention that $F^{n+1}(\overline{\boldsymbol{\varepsilon}}, \mathbf{u}, D) = +\infty$ if $\alpha(\mathbf{x}) = 0$ and $D(\mathbf{x}) \neq D^n(\mathbf{x})$ for $\mathbf{x} \in Y$. Also, the short-hand notation $\overline{\boldsymbol{\sigma}}^n = \overline{\boldsymbol{\sigma}}\left(\overline{N}^n\right)$ is used.
For the article at hand, we are primarily interested in the evolution of the *effective* stiffness upon fatigue loading. The latter arises from the local stiffness tensor field $\mathbb{C}/(1+D)$ by linear elastic homogenization [221].
If $\mathbb{C}$ is uniformly positive and bounded and α is bounded as well, it is not difficult to see that the problem (4.2.20) admits a unique minimizer in a suitable Sobolev space [222]. Indeed, eliminating the damage variable D via Biot's equation (4.2.6) leads to a strictly convex optimization problem in the strain field, whose condensed energy grows with an exponent between 4/3 and 2 in the strain, depending on whether α vanishes or not. Once the strain field is obtained, the (square-integrable) damage field may be recovered via Biot's equation.
Thus, the presented model is well-defined for Sobolev spaces with exponents larger than one. In particular, by construction, no damage localization is permitted by the mathematical model. Indeed, such localization behavior is typically observed for energies with linear growth in the strain. The superlinear growth of the condensed energy precludes localization. Thus, focusing on the stable fatigue damage regime, see stage-1 and stage-2 fatigue in Fig. 4.1, the presented damage model comes with a beneficial numerical treatment, as it leads to mesh-independent results also without gradient enrichment. Physically speaking, the model at hand monitors the phase of stiffness decrease which does not (yet) have fracture mechanical ramifications. This contrasts with the model discussed in chapter 3.

4.2.3. Parameter identification

After discussing the ability of the model to reproduce the typical fatigue-damage behavior of short-fiber reinforced polymers in the one-dimensional case, see section 4.2.1, this section is devoted to identifying the single free parameter α, which governs the speed of fatigue-damage growth for the model at hand. We compare experimental results to simulations on representative volume elements (RVE) to determine this parameter. Moreover,

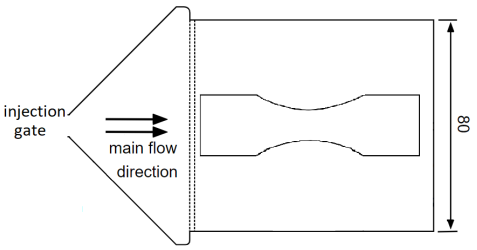

(a) Specimen manufacturing

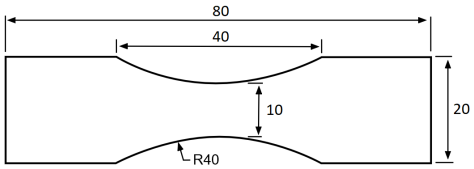

(b) Geometry of the specimens

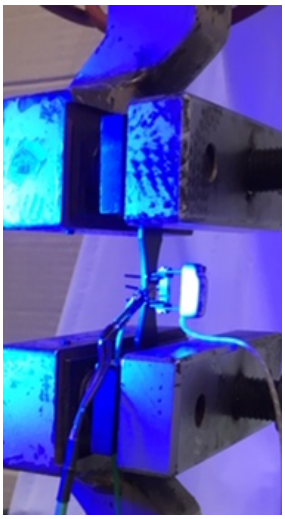

(c) Experimental setup

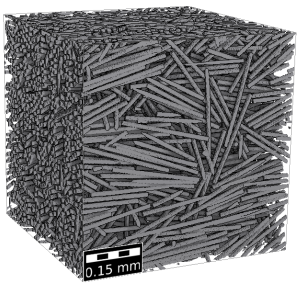

(d) Fiber structure for computational experiment

Figure 4.4.: Setup and geometries for experiments

the capability of the model to reproduce the stiffness decrease is further discussed.
We performed experiments on specimens made of polybutylene terephthalate (PBT) reinforced by E-glass fibers. The isotropic elastic moduli for these materials are given in Tab. 4.1. The elastic properties of the E-glass fibers are standard, whereas the elastic properties of the polymer matrix were identified via quasi-static testing of the pure matrix material using so-called Becker samples, see [223], on a Zwick universal testing machine. We restrict ourselves to stress ratios

$$R = \frac{\overline{\boldsymbol{\sigma}}_{\min}}{\overline{\boldsymbol{\sigma}}_{\max}} \tag{4.2.21}$$

of $R = 0$ throughout this work.
The specimens used for the fatigue tests were cut from an injection-molded plate as shown in Fig. 4.4(a). Each specimen has a thickness of 2 mm and the geometric properties of the specimens are shown in Fig. 4.4(b).
The fatigue tests were performed on a Schenk hydropulser as shown in in Fig. 4.4(c). With respect to a time-efficient testing, the frequencies of the experiments were chosen in the range from 2 Hz to 12 Hz depending on the loading amplitudes. Of course, induced self-heating of the samples limits the maximum frequency that can be applied. The chosen frequency ensures that the temperature increase during testing, measured at the sample surface, does not exceed 2 K. For the positioning of the temperature sensor on the sample, see Fig. 4.4(c). The local deformation in the middle of the sample is recorded using

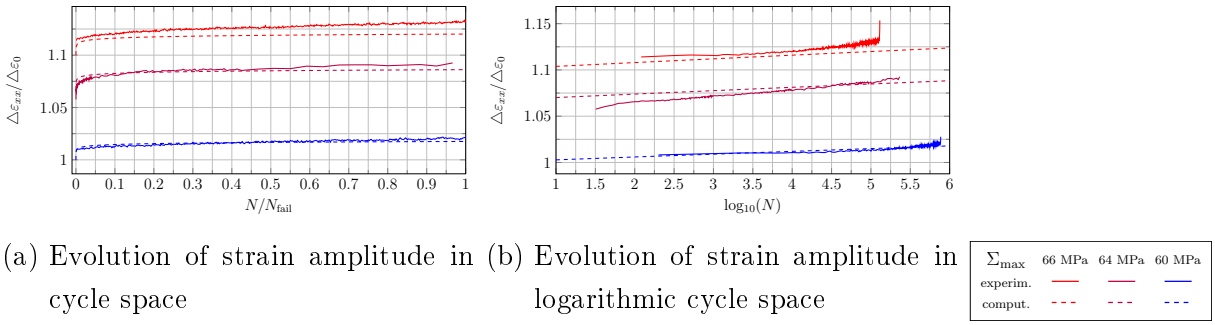

(a) Evolution of strain amplitude in cycle space

(b) Evolution of strain amplitude in logarithmic cycle space

Figure 4.5.: Comparison of experimental data and simulation results

extensometers with a gauge length $l_0 = 10\,\text{mm}$, see Fig. 4.4(c).
In accordance with the literature [5, 118, 142], the experiments show an initial rapid decrease of the stiffness for low cycles and a secondary steady regime in the linear cycle space, see Fig. 4.5(a). The strain results are normalized by a reference strain ε_0, more precisely $\varepsilon_0 = \varepsilon_{xx}(\overline{N} = 0)$ at a stress amplitude of 60 MPa. This decrease corresponds to a linear evolution when displayed in *logarithmic* cycle space, see Fig. 4.5(b).
For parameter identification using numerical computations on representative volume elements, it is necessary to characterize the fiber orientation state of the experimental specimens. Thus, the microstuctural properties of the specimens were examined via high-resolution X-ray microcomputed tomography (μCT) analysis. For details of the characterization process, we refer to Hessman et al. [224]. The fiber volume content was found to be 17.8%. The identified aspect ratio depends on the segmentation algorithm and the chosen batch. The algorithm proposed by Hessman et al. [224] predicts an aspect ratio of 26.1, whereas the aspect ratio obtained from the commercial Simpleware ScanIP software is 23.9. As such small changes in the fibers' aspect ratio have little influence on the effective material behavior, we use the aspect ratio of 25 for the numerical simulations throughout this work.
The fiber orientations in these specimens show a layered structure over the thickness. To keep the procedure simple, we consider a homogeneous, averaged fiber orientation and compute the second-order Advani-Tucker tensor from the scan over the complete specimen thickness. The second-order Advani-Tucker fiber-orientation tensor A [169] is computed from the fiber directions $p_i \in \mathcal{S} := \{p \in \mathbb{R}^3, \|p\| = 1\}$ via the formula

$$A = \frac{1}{N_{\text{fiber}}} \sum_{i=1}^{N_{\text{fiber}}} p_i \otimes p_i. \tag{4.2.22}$$

The obtained eigenvalues in the specimens are $\lambda_1 = 0.770, \lambda_2 = 0.213$ and $\lambda_3 = 0.017$. We use these parameters to generate the microstructure in Fig. 4.4(d) by the sequential

addition and migration algorithm [173].
Subsequently, the microstructure shown is subjected to uni-axial extension in the principal fiber direction at the same stress amplitudes that were used in the experiment. We identified the parameter $\alpha = 0.015$ 1/MPa. In Fig. 4.5, we compare the measurements to numerical experiments for using a log-cycle scale $\overline{N}$.
For the stress amplitudes at hand, the strain evolution curves are captured quite well by the model. Both the slopes of the strain evolution as well as the initial strain amplitude, corresponding to the strain amplitude at the first cycle, are captured. However, for computations at higher or lower stress amplitudes than shown here, the initial strain amplitudes at the first cycle deviate from the experimental results. This kind of initial stiffness decrease in the first few cycles prior to stage-1 fatigue shown in Fig. 4.1(b) is not accounted for by the proposed model. For the work at hand, we focus on the region between initial damage (or plastic deformation) and fracture, namely stage-1 and stage-2 fatigue. The prediction of the initial strain amplitude decrease is left for subsequent work.
The damage evolution in the fatigue damage region between initial loading and final fracture has been observed to be of logarithmic character. The formulation of the model at hand in log-cycle space $\overline{N}$ is thus reasonable.

4.3. A model-order reduction strategy based on a mixed formulation

4.3.1. A reformulation in terms of the stress

In the previous section we formulated our model based on the Ortiz-Stainier potential (4.2.20)

$$F\left(\overline{\boldsymbol{\varepsilon}}, \mathbf{u}, D\right) = \left\langle \frac{1}{2\left(1+D\right)} \left(\overline{\boldsymbol{\varepsilon}} + \nabla^s \mathbf{u}\right) : \mathbb{C} : \left(\overline{\boldsymbol{\varepsilon}} + \nabla^s \mathbf{u}\right) + \frac{1}{2\alpha \triangle \overline{N}} \left(D - D^n\right)^2 \right\rangle_Y - \overline{\boldsymbol{\varepsilon}} : \overline{\boldsymbol{\sigma}}, \tag{4.3.1}$$

where we drop the superscript $n+1$ for this section. This formulation is not ideally suited for model-order reduction. For a basis of preselected modes, we would like to express the functional to be minimized in terms of quantities that can be precomputed, avoiding any access to full fields. However, such a precomputation is not possible, as the damage variable D enters the denominator in the Ortiz-Stainier potential. Instead of relying upon an

approximation, for instance by a Taylor polynomial [79,80,189], we follow a different route. Let us invert the stress-strain relationship (4.2.3) of the matrix model,

$$\boldsymbol{\varepsilon} = (1+D)\ \mathbb{S} : \boldsymbol{\sigma} \tag{4.3.2}$$

in terms of the compliance tensor $\mathbb{S} = (\mathbb{C})^{-1}$. Similarly, we may recast Biot's equation (4.2.5) in the form

$$D' = \frac{\alpha}{2}\,\boldsymbol{\sigma} : \mathbb{S} : \boldsymbol{\sigma}, \quad \text{or,} \quad \frac{D - D^n}{\triangle \overline{N}} = \frac{\alpha}{2}\,\boldsymbol{\sigma} : \mathbb{S} : \boldsymbol{\sigma} \tag{4.3.3}$$

upon an implicit Euler discretization in logarithmic cycle space. With precomputations useful for model-order reduction in mind, this reformulation is very convenient. Indeed, the equations (4.3.2) and (4.3.3) involve only terms that are jointly quadratic in the internal variables $(\boldsymbol{\sigma}, D)$. A lower degree of homogeneity in the joint internal variables is favorable for precomputations, as this degree affects the number of the precomputed system matrices in the reduced order model, see section 4.3.2.

As for the primal model, see section equations (4.2.1) and (4.2.2), we may establish a (mixed) variational principle

$$S(\boldsymbol{\sigma}, D) \longrightarrow \min_{D} \max_{\substack{\operatorname{div} \boldsymbol{\sigma} = 0 \\ \langle \boldsymbol{\sigma} \rangle_Y = \overline{\boldsymbol{\sigma}}}} \tag{4.3.4}$$

in terms of the saddle-point function

$$S(\boldsymbol{\sigma}, D) = \left\langle -\frac{(1+D)}{2}\,\boldsymbol{\sigma} : \mathbb{S} : \boldsymbol{\sigma} + \frac{1}{2\alpha \triangle \overline{N}}\,(D - D^n)^2 \right\rangle_Y . \tag{4.3.5}$$

The equivalence of the strain- and the stress based formulations, (4.2.19) and (4.3.4), respectively, in terms of the relation (4.3.2) is shown in Appendix A.1. However, some care has to be taken with this formulation. Please notice that the function S is always convex in D, but concavity in $\boldsymbol{\sigma}$ is only ensured for $D \geq -1$. Thus, instead of the formal mixed variational principle (4.3.4), it is recommended to fix some $D_- \in (-1, 0]$ and to consider the constrained mixed variational principle

$$S(\boldsymbol{\sigma}, D) \longrightarrow \min_{D \geq D_-} \max_{\substack{\operatorname{div} \boldsymbol{\sigma} = 0 \\ \langle \sigma \rangle_Y = \overline{\boldsymbol{\sigma}}}} \tag{4.3.6}$$

instead. Please notice that the considered mixed variational principle differs from the mixed variational principle of Fritzen-Leuschner [67]. Indeed, we perform a partial Legendre transform in the strain, whereas Fritzen-Leuschner rely upon a partial Legendre transform in the internal variable.

Suppose that M_D damage modes

$$\delta_a : Y \to \mathbb{R}, \quad a = 1, \ldots, M_D, \tag{4.3.7}$$

and $M_{\boldsymbol{\sigma}}$ stress modes

$$s_i : Y \to \mathrm{Sym}(m), \quad i = 1, \ldots, M_{\boldsymbol{\sigma}}, \tag{4.3.8}$$

satisfying

$$\langle s_i \rangle_Y = 0 \quad \text{and} \quad \mathrm{div}\ s_i = 0, \quad i = 1, \ldots, M_{\boldsymbol{\sigma}}, \tag{4.3.9}$$

are given. Then, for $M = (M_\sigma, M_D)$, and coefficients

$$\vec{D} = (D_1, \ldots, D_{M_D}) \in \mathbb{R}^{M_D} \quad \text{and} \quad \vec{\sigma} = (\sigma_1, \ldots, \sigma_{M_\sigma}) \in \mathbb{R}^{M_\sigma}, \tag{4.3.10}$$

we consider the reduced-order model determined by the mixed variational principle (4.3.6)

$$S_M\left(\vec{\sigma}, \vec{D}\right) \longrightarrow \min_{\vec{D},\, D \geq D_-} \max_{\vec{\sigma}} \tag{4.3.11}$$

involving the function

$$S_M\left(\vec{\sigma}, \vec{D}\right) \equiv S\left(\boldsymbol{\sigma}, D\right) \quad \text{with} \quad \boldsymbol{\sigma} = \overline{\boldsymbol{\sigma}} + \sum_{i=1}^{M_\sigma} \sigma_i s_i \quad \text{and} \quad D = \sum_{a=1}^{M_D} D_a \delta_a, \tag{4.3.12}$$

and where the previous cycle step is represented in the form

$$D^n = \sum_{a=1}^{M_D} D_a^n \delta_a \quad \text{for a suitable} \quad \vec{D}^n \in \mathbb{R}^{M_D}. \tag{4.3.13}$$

Notice that, in the reduced-order setting, it is not readily apparent that the problem (4.3.11) is solvable, and that there is a unique solution. For this purpose, let us introduce the non-linear operator

$$\mathcal{A}_M : \mathbb{R}^{M_\sigma} \times \mathbb{R}^{M_D} \to \mathbb{R}^{M_\sigma} \times \mathbb{R}^{M_D}, \tag{4.3.14}$$

implicitly defined via

$$\left\langle \mathcal{A}_M\left(\vec{\sigma}^\beta, \vec{D}^\beta\right), \left(\vec{\sigma}^\gamma, \vec{D}^\gamma\right) \right\rangle_M =$$

$$\left\langle \left(1 + D^\beta\right)\left(\overline{\boldsymbol{\sigma}} + \sigma^\beta\right) : \mathbb{S} : \sigma^\gamma + \frac{1}{\alpha \triangle \overline{N}}\left(D^\beta - D^n\right) D^\gamma - \frac{1}{2} D^\gamma \left(\overline{\boldsymbol{\sigma}} + \sigma^\beta\right) : \mathbb{S} : \left(\overline{\boldsymbol{\sigma}} + \sigma^\beta\right) \right\rangle_Y,$$

for any $\left(\vec{\sigma}^\beta, \vec{D}^\beta\right), \left(\vec{\sigma}^\gamma, \vec{D}^\gamma\right) \in \mathbb{R}^{M_\sigma} \times \mathbb{R}^{M_D}$, where we use the abbreviations

$$\boldsymbol{\sigma}^\kappa = \sum_{i=1}^{M_\sigma} \sigma_i^\kappa s_i \quad \text{as well as} \quad D^\kappa = \sum_{a=1}^{M_D} D_a^\kappa \delta_a \quad \text{for} \quad \kappa \in \{\beta, \gamma\} \tag{4.3.15}$$

and the inner product

$$\left\langle \left(\vec{\sigma}^\beta, \vec{D}^\beta\right), \left(\vec{\sigma}^\gamma, \vec{D}^\gamma\right) \right\rangle_M = \left\langle \sum_{i,j=1}^{M_\sigma} \sigma_i^\beta \sigma_j^\gamma s_i : s_j + \sum_{a,b=1}^{M_D} D_a^\beta D_b^\gamma \delta_a \delta_b \right\rangle_Y \tag{4.3.16}$$

on the space $\mathbb{R}^{M_\sigma} \times \mathbb{R}^{M_D}$. The operator (4.3.14) is closely related to the mixed variational principle (4.3.11) and (4.3.12). Indeed, $\mathcal{A}_M$ may be written in the form

$$\mathcal{A}_M\left(\vec{\sigma}, \vec{D}\right) = \left(-\frac{\partial S_M}{\partial \vec{\sigma}}, \frac{\partial S_M}{\partial \vec{D}}\right). \tag{4.3.17}$$

Thus, any saddle point $\left(\vec{\sigma}, \vec{D}\right)$ of the mixed variational principle (4.3.11) which satisfies $D > D_-$ is a root of the operator $\mathcal{A}_M$. Conversely, any root $\left(\vec{\sigma}, \vec{D}\right)$ of the operator $\mathcal{A}_M$ is a saddle point of the variational principle (4.3.11). Of course, the same holds with the gradient of the function S_M in place of the operator $\mathcal{A}_M$. However, the simple sign reserval (4.3.17) in the first component provides the operator $\mathcal{A}_M$ with better properties. Indeed, with the abbreviations (4.3.15), the identity

$$\begin{aligned}&\left\langle \mathcal{A}_M\left(\vec{\sigma}^\beta, \vec{D}^\beta\right) - \mathcal{A}_M\left(\vec{\sigma}^\gamma, \vec{D}^\gamma\right), \left(\vec{\sigma}^\beta, \vec{D}^\beta\right) - \left(\vec{\sigma}^\gamma, \vec{D}^\gamma\right)\right\rangle_M = \\ &\left\langle \frac{2 + D^\beta + D^\gamma}{2}\left(\sigma^\beta - \sigma^\gamma\right) : \mathbb{S} : \left(\sigma^\beta - \sigma^\gamma\right) + \frac{1}{\alpha \triangle \overline{N}}\left(D^\beta - D^\gamma\right)^2\right\rangle_Y\end{aligned} \tag{4.3.18}$$

holds for any $\left(\vec{\sigma}^\beta, \vec{D}^\beta\right), \left(\vec{\sigma}^\gamma, \vec{D}^\gamma\right) \in \mathbb{R}^{M_\sigma} \times \mathbb{R}^{M_D}$. Suppose that the stiffness distribution $\mathbb{C}$ is uniformly bounded from above and from below

$$c_- \, \boldsymbol{\varepsilon} : \boldsymbol{\varepsilon} \leq \boldsymbol{\varepsilon} : \mathbb{C}(\mathbf{x}) : \boldsymbol{\varepsilon} \leq c_+ \, \boldsymbol{\varepsilon} : \boldsymbol{\varepsilon}, \quad \mathbf{x} \in Y, \quad \boldsymbol{\varepsilon} \in \mathrm{Sym}(m), \tag{4.3.19}$$

with positive constants $c_\pm$, and let α_+ be an upper bound for α. Then, under the condition $D^\kappa \geq D_-$ for $\kappa \in \{\beta, \gamma\}$, the identity (4.3.18) implies the estimate

$$\begin{aligned}&\left\langle \mathcal{A}_M\left(\vec{\sigma}^\beta, \vec{D}^\beta\right) - \mathcal{A}_M\left(\vec{\sigma}^\gamma, \vec{D}^\gamma\right), \left(\vec{\sigma}^\beta, \vec{D}^\beta\right) - \left(\vec{\sigma}^\gamma, \vec{D}^\gamma\right)\right\rangle_M \geq \\ &c_-\left(1 + D_-\right)\left\langle \left(\sigma^\beta - \sigma^\gamma\right) : \left(\sigma^\beta - \sigma^\gamma\right)\right\rangle_Y + \frac{1}{\triangle \overline{N} \alpha_+}\left\langle \left(D^\beta - D^\gamma\right)^2\right\rangle_Y.\end{aligned} \tag{4.3.20}$$

In particular, as $D_- > -1$, the operator $\mathcal{A}_M$ is strongly monotone, and the monotonicity constant does not depend on the chosen bases. We refer to Appendix A.2 for a derivation of the identity (4.3.18). By similar arguments, the identity

$$\left\langle \mathcal{A}_M\left(\vec{\sigma}, \vec{D}\right), \left(\vec{\sigma}, \vec{D}\right)\right\rangle_M = \left\langle \frac{2 + D}{2}\left(\overline{\boldsymbol{\sigma}} + \sigma\right) : \mathbb{S} : \sigma + \frac{1}{\alpha \triangle \overline{N}}\left(D - D^n\right) D\right\rangle_Y, \tag{4.3.21}$$

using the abbreviations (4.3.15), may be deduced. Hence, the operator $\mathcal{A}_M$ is also coercive. Moreover, due to its representation by a polynomial, the operator $\mathcal{A}_M$ is continuous. Thus, as long as the constraint $D \geq D_- > -1$ is satisfied, classical monotone operator theory [225] implies that there is a unique root of the operator $\mathcal{A}_M$.

For our computational experiments, it was not necessary to enforce the constraint $D \geq D_-$ explicitly, see section 4.4.3. Thus, the latter constraint may be regarded as a theoretical prerequisite that may not always be required in practice.

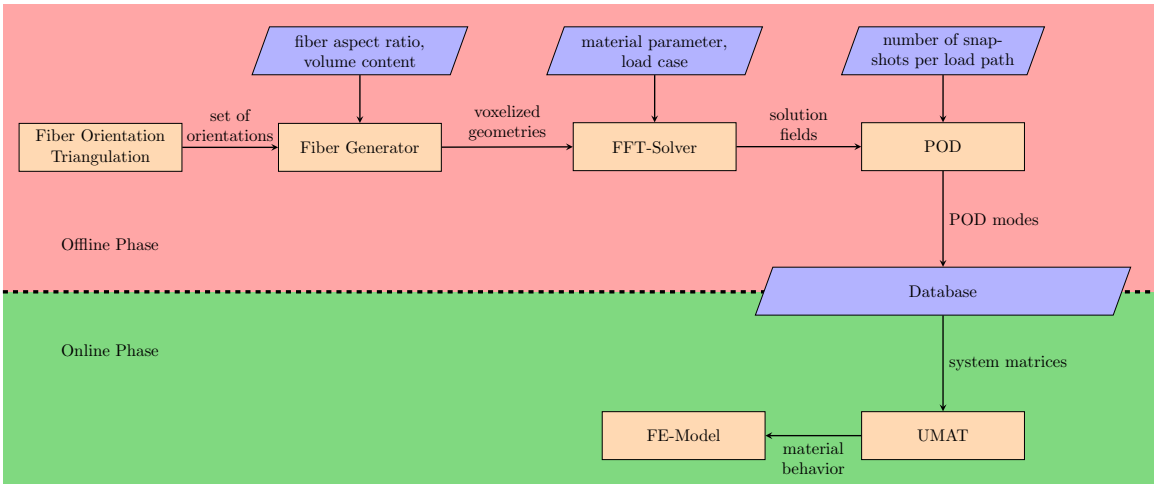

Figure 4.6.: Concept of precomputations and online phase

4.3.2. Implementation and solution of the discretized system

The proposed fatigue model permits a straightforward model-order reduction. Thus, precomputations on the microscale can be completed once and for all in an offline phase. The derivation of macroscopic equations and system matrices from the POD modes are discussed in this section.

The polynomial character of the saddle point functional (4.3.12) permits this saddle point functional, considered as a function of the mode coefficients, to be precomputed exactly (up to numerical precision). In particular, no access to the full fields is required during the online evaluation of the proposed multiscale fatigue-damage model. Let us first discuss why a polynomial potential enables a precomputation strategy. Suppose a function f of a vectorial variable $\vec{z}$ is given. We assume the variable $\vec{z}$ to be finite-dimensional with dimension M_z, and denote the components of $\vec{z}$ by z_i, reserving Latin indices i, j, k for this purpose. Suppose furthermore that a number of modes $\vec{z}^a$ $(a = 1, \ldots, M_m)$ were selected, and we seek an approximation

$$\vec{z} = \sum_{a=1}^{M_m} \xi_a \vec{z}^a \tag{4.3.22}$$

in terms of suitable mode coefficients ξ_a $(a = 1, \ldots, M_m)$. In particular, we are interested in the function

$$\tilde{f}(\xi_1, \ldots, \xi_{M_m}) = f\left(\sum_{a=1}^{M_m} \xi_a \vec{z}^a\right), \tag{4.3.23}$$

which only depends on the mode coefficients. For MOR to be effective, the number of mode coefficients M_m in the representation (4.3.23) should be much smaller than the

number of vector components M_z. For general functions f, little is gained by considering the function $\tilde{f}$ (4.3.23), as its definition follows the indirect way via the variable $\vec{z}$. For polynomial functions f, in contrast, a different strategy can be followed. For concreteness, let us assume the function f to be a polynomial of degree 3, i.e., it may be expressed in the form

$$f(\vec{z}) = C + \sum_{i=1}^{M_z} f_i\, z_i + \sum_{i,j=1}^{M_z} f_{ij}\, z_i z_j + \sum_{i,j,k=1}^{M_z} f_{ijk}\, z_i z_j z_k \tag{4.3.24}$$

in terms of suitable coefficients C, f_i, f_{ij} and f_{ijk}. Then, inserting the mode representation (4.3.23), we obtain the expression

$$\tilde{f}(\xi_1, \ldots, \xi_{M_m}) = C + \sum_{a=1}^{M_m} \tilde{f}_a\, \xi_a + \sum_{a,b=1}^{M_m} \tilde{f}_{ab}\, \xi_a \xi_b + \sum_{a,b,c=1}^{M_m} \tilde{f}_{abc}\, \xi_a \xi_b \xi_c, \tag{4.3.25}$$

which turns out to be a third-order polynomial in the *mode* coefficients and involves the precomputable coefficients

$$\begin{aligned} \tilde{f}_a &= \sum_{i=1}^{M_z} f_i\, z_i^a, \\ \tilde{f}_{ab} &= \sum_{i,j=1}^{M_z} f_{ij}\, z_i^a z_j^b, \\ \tilde{f}_{abc} &= \sum_{i,j,k=1}^{M_z} f_{ijk}\, z_i^a z_j^b z_k^c \end{aligned} \tag{4.3.26}$$

for $a, b, c = 1, \ldots, M_m$.

Let us return to the fatigue-damage model at hand. For fixed modes (4.3.8) and (4.3.7), we set $\vec{z} = (\vec{\sigma}, \vec{D})$, i.e., $M_z = M_\sigma + M_D$, and consider the objective function $f = S_M$ (4.3.12), which is a third-order polynomial in the unknowns. Similar to the representation (4.3.25) involving the quantities (4.3.26), we obtain an expression of the objective function S_M in the form

$$\begin{aligned} S_M\left(\vec{\sigma}, \vec{D}\right) = &-\frac{1}{2}\overline{\boldsymbol{\sigma}} : \langle \mathbb{S} \rangle_Y : \overline{\boldsymbol{\sigma}} - \overline{\boldsymbol{\sigma}} : \Pi_i \sigma_i - \frac{1}{2} S_{ij} \sigma_i \sigma_j \\ &- \frac{1}{2}\overline{\boldsymbol{\sigma}} : \mathbb{D}_a : \overline{\boldsymbol{\sigma}}\, D_a - \overline{\boldsymbol{\sigma}} : \Lambda_{ia} \sigma_i D_a - \frac{1}{2} T_{ija} \sigma_i \sigma_j D_a \\ &+ \frac{1}{2\alpha \triangle \overline{N}}\, D_{ab} D_a D_b - \frac{1}{\alpha \triangle \overline{N}} D_{ab} D_a D_b^n + \frac{1}{2\alpha \triangle \overline{N}}\, D_{ab} D_a^n D_b^n. \end{aligned} \tag{4.3.27}$$

From equation (4.3.27) onwards, we use Einstein's summation convention, i.e., we sum over pairs of appearing indices. For clarity, we reserve the indices a and b for damage modes, i.e., they sum from one to M_D, and use i as well as j for the stress modes,

summing from one to M_σ. In the expression (4.3.27), the following quantities are precomputed:

$$\begin{aligned}
\Pi_i &= \langle \mathbb{S} : s_i \rangle_Y \,, \\
S_{ij} &= \langle s_i : \mathbb{S} : s_j \rangle_Y \,, \\
\mathbb{D}_a &= \langle \delta_a \mathbb{S} \rangle_Y \,, \\
\Lambda_{ia} &= \langle \delta_a \mathbb{S} : s_i \rangle_Y \,, \\
T_{ija} &= \langle \delta_a s_i : \mathbb{S} : s_j \rangle_Y \,, \\
D_{ab} &= \langle \delta_a \delta_b \rangle_Y \,,
\end{aligned} \tag{4.3.28}$$

where the appearing indices have the same range as above. Notice also that all appearing quantities (4.3.28) are symmetric in the index pairs (a, b) and (i, j), respectively. To increase notational clarity, we use a Greek letter for $\mathrm{Sym}(m)$-valued objects, Roman letters for scalar-valued objects and double stroke letters for fourth order tensor objects. The memory consumption for precomputing the quantities (4.3.28) is $O\left(M_D M_\sigma^2\right)$. As already mentioned in section 4.3.1, the evolution equations of the proposed damage model (4.3.2), (4.3.3) are jointly quadratic in the internal variables. For a Galerkin-discretization using constant POD-modes the highest complexity in the precomputed matrices is thus in the order of three. Here, for $M_D = O\left(M_\sigma\right)$, the array T_{ija} has the highest complexity with $M_D \times M_\sigma \left(M_\sigma + 1\right)/2$ independent components.
Saddle points of the function S_M (4.3.27) satisfy the balance of linear momentum

$$S_{ij}\sigma_j + \overline{\boldsymbol{\sigma}} : \Lambda_{ia} D_a + T_{ija}\sigma_j D_a = -\boldsymbol{\sigma} : \Pi_i \quad (i = 1, \ldots, M_\sigma) \tag{4.3.29}$$

and Biot's equation

$$\frac{1}{\alpha \triangle \overline{N}} D_{ab} D_b - \frac{1}{\alpha \triangle \overline{N}} D_{ab} D_b^n = \frac{1}{2}\boldsymbol{\sigma} : \mathbb{D}_a : \boldsymbol{\sigma} + \boldsymbol{\sigma} : \Lambda_{ia}\sigma_i + \frac{1}{2} T_{ija}\sigma_i\sigma_j \quad (a = 1, \ldots, M_D)\,. \tag{4.3.30}$$

Please notice that, if the macroscopic strain $\overline{\boldsymbol{\varepsilon}}$ is specified instead of the macroscopic stress $\boldsymbol{\sigma}$, the equation

$$\langle \mathbb{S} \rangle_Y : \overline{\boldsymbol{\sigma}} + \Pi_i \sigma_i + \mathbb{D}_a : \overline{\boldsymbol{\sigma}}\, D_a + \Lambda_{ia}\sigma_i d_a = \overline{\boldsymbol{\varepsilon}} \tag{4.3.31}$$

needs to be added to the system in order to determine $\overline{\boldsymbol{\sigma}}$.
For the convenience of the reader, an overview of offline and online computation is given in Fig. 4.6: Based on the fiber orientation interpolation concept [160], a finite number of fiber orientations is chosen. For each of these orientations, a short-fiber microstructure is generated [173]. For specified material parameters of matrix and fiber, the fatigue-damage evolution is computed using an FFT-based solver and a number of load cases, see section 4.4.1 for details. Using the resulting solution fields, stress and damage modes

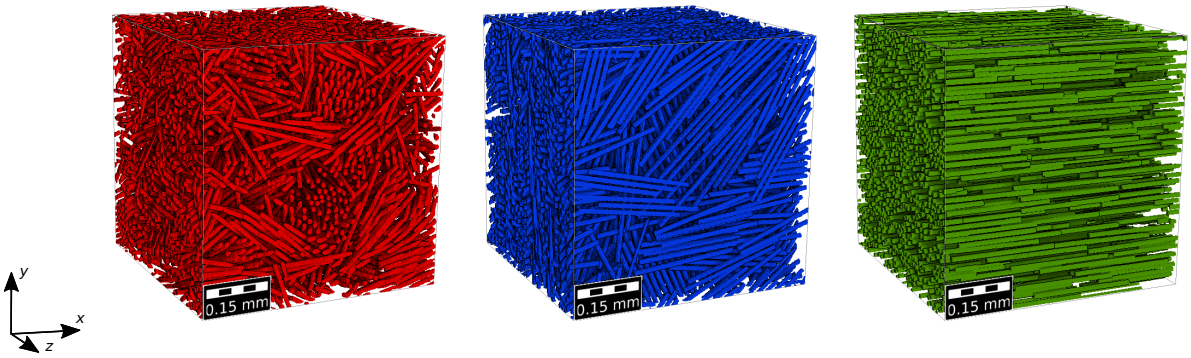

(a) Isotropic (b) Planar isotropic (c) Unidirectional

Figure 4.7.: Reference microstructures with different fiber orientations

are extracted via proper orthogonal decomposition (POD). More precisely, the damage and stress full-field solutions for all precomputed load cases and either all or a subset of cycle steps (see Section 4.4.3 for a study) are stored on disk. For a microstructure with N^3 voxels, this amounts to storing N^3 or $6 \times N^3$ double-precision floating-point numbers per (damage or stress) snapshot, corresponding to either one or six scalars per voxel. Then, the POD correlation matrices are set up based on the L^2 inner product both for the fatigue-damage variable and the stress field, and the damage and stress modes are extracted by the usual eigenvalue thresholding [190, 226], see Section 4.4.3 for a study. Eventually, the relevant system matrices (as discussed in this section) are precomputed, and the model is ready for application on the component scale.
For solving the equations (4.3.29), (4.3.30) and (4.3.31), we use Newton's method with backtracking. For strongly monotone operators, the latter scheme converges quadratically. As the termination condition for the scheme, we use

$$\|\nabla S\| \overset{!}{\leq} 10^{-8} \, \|\overline{\boldsymbol{\varepsilon}}\|, \tag{4.3.32}$$

where we chose the Frobenius norm for the strain-amplitude tensor.

4.4. Computational investigations

4.4.1. Setup

The multiscale fatigue model described in section 4.2.2 is discretized in time via an implicit Euler scheme and on a staggered grid in space [54]. For resolving the balance of linear

Parameter	Value	Unit
Fiber length	250	μm
Fiber diameter	10	μm
Aspect ratio	25	-
Fiber-volume content	17.8	%
Minimum fiber distance	5	μm
Average voxels per diameter	6.4	-
Cell length / fiber length	2.4	-

Table 4.2.: Properties of the generated microstructures and the spatial discretization

momentum, we rely upon a nonlinear conjugate gradient method [178] to reduce the strain-based residual suggested in Kabel et al. [227] below a tolerance of 10^{-5}.
The material model was implemented as a user subroutine in the FFT-based software FeelMath [228] and in Julia [168], which also served as the environment for the model-order reduction. For the computations, a Linux cluster equipped with Intel Xeon Gold 1648 processors was used.

4.4.2. Microscale studies

To study the material behavior on the microscale, we introduce three reference structures with different fiber orientations: an isotropic structure, a planar-isotropic structure and a unidirectional structure. The structures were generated by the sequential addition and migration algorithm [173] using the parameters listed in Tab. 4.2. The resulting reference structures are shown in Fig. 4.7, visualized with GeoDict[2]. The SAM algorithm permits achieving high accuracy for the second-order fiber-orientation tensors. For example, for the isotropic and the planar isotropic microstructures shown in Fig. 4.7, the realized second-order fiber-orientation tensors read

$$A_{\text{iso}}^{(2)} = \begin{bmatrix} 0.333334 & -9.65272 \times 10^{-8} & 4.43788 \times 10^{-7} \\ -9.65272 \times 10^{-8} & 0.333333 & 2.71964 \times 10^{-8} \\ 4.43788 \times 10^{-7} & 2.71964e \times 10^{-8} & 0.333333 \end{bmatrix} \tag{4.4.1}$$

[2]Math2Market GmbH, http://www.geodict.de

and

$$A^{(2)}_{\text{piso}} = \begin{bmatrix} 0.499739 & -0.000526419 & -4.66944 \times 10^{-6} \\ -0.000526419 & 0.499739 & 7.31379 \times 10^{-6} \\ -4.66944 \times 10^{-6} & 7.31379 \times 10^{-6} & 0.000521332 \end{bmatrix}, \tag{4.4.2}$$

respectively.

On the necessary spatial resolution

For a start, we investigate the resolution that is necessary to obtain mesh-insensitive results. As our reference, we use 6.4 voxels per fiber diameter to resolve a fiber and call the respective voxel size h, see Tab. 4.2. Subsequently, we increase and decrease the resolution by a factor of two and compare the effective properties obtained from simulations on these structures to simulations on the reference structure. In Fig. 4.8, the evolution of the effective Young's moduli [175] for the selected fiber orientations under uni-axial extension in x- and z-direction are shown. Due to the direction independence of the isotropic microstructure, only extension in x-direction is considered. For all three fiber orientations, the effective Young's moduli are plotted in x- and z-direction.
We introduce the error measure

$$e^{\text{Young}} = 2 \max_i \frac{\|E_1(\overline{N}_i) - E_2(\overline{N}_i)\|}{\|E_1(\overline{N}_i) + E_2(\overline{N}_i)\|} \tag{4.4.3}$$

to quantify the deviation between two Young's modulus evolutions E_1 and E_2. For the isotropic structure, the deviation between the $2 \times h$-discretization and the $0.5 \times h$-discretization is 1.01% in x-direction and 1.21% in z-direction in terms of the stiffness-based error measure (4.4.3). Comparing the h-discretization and the $0.5 \times h$-discretization, the errors are below 0.5%, i.e., 0.25% in x-direction and 0.32% in z-direction.
For the planar-isotropic orientation, the observations are similar. For the unidirectional structure, the deviations at the $2 \times h$ discretization are even less pronounced. Indeed, the unidirectional microstructure under loading in x-direction shows an error of 0.20% in x-direction and 0.01% in z-direction, when comparing the $2 \times h$ discretization to the $0.5 \times h$ discretization in terms of the stiffness-based error measure (4.4.3). Under loading in z-direction, the deviation is 0.20% in x-direction and 0.06% in z-direction.
Since the error measure (4.4.3) stays below 1% for all discussed load cases and directions, compared the h- to the $2 \times h$-discretization, we consider the deviation of the h discretization from the $2 \times h$ discretization acceptable, and fix the mesh spacing to h for all subsequent studies.

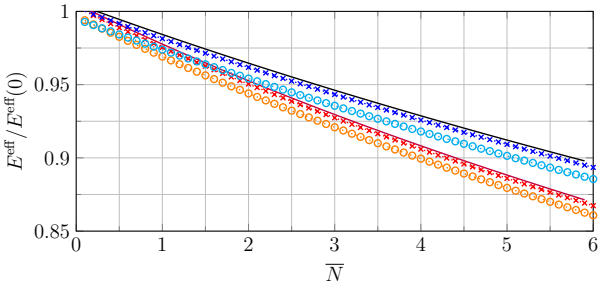

(a) Isotropic, loading in x

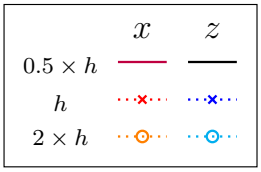

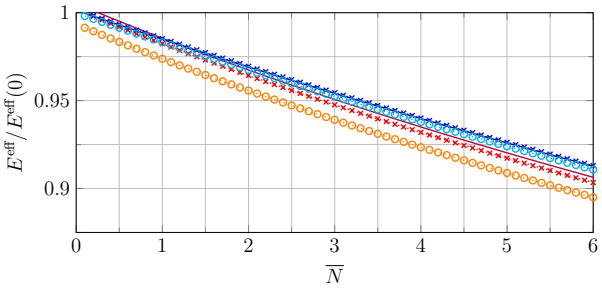

(b) Planar isotropic, loading in x

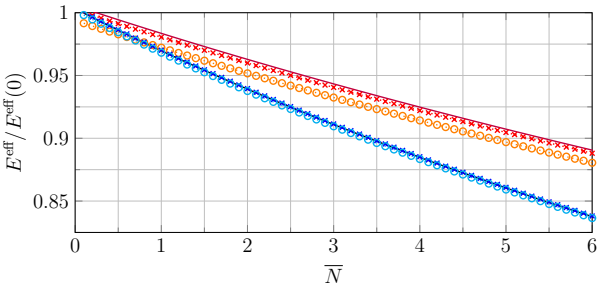

(c) Planar isotropic, loading in z

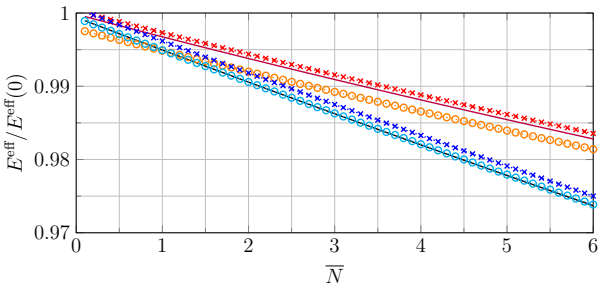

(d) Unidirectional, loading in x

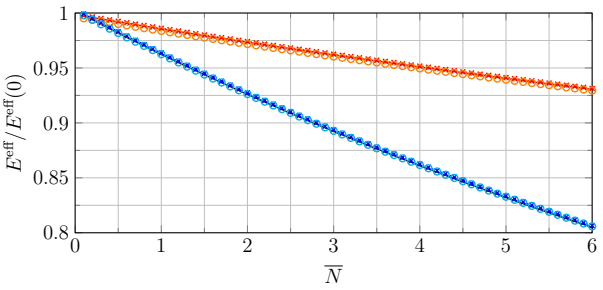

(e) Unidirectional, loading in z

Figure 4.8.: Influence of the mesh size on the computational results

On the necessary resolution in log-cycle space

As a second verification step on the microscale, we investigate the necessary step size $\triangle\overline{N}$ in logarithmic cycle space. For an implicit Euler discretization with uniform step sizes $\triangle\overline{N} \in \{0.05, 0.1, 0.2\}$, results are shown in Fig. 4.9. Please notice that the logarithmic cycle variable $\overline{N}$ is dimensionless.
The results show that the model turns out to be rather robust w.r.t. the chosen cycle step size. Even a step size of 0.2 produces only small errors. We fix a constant step size of 0.1 for the succeeding investigations.

On the necessary size of the unit cell

After studying the necessary resolution per fiber and the necessary step size, we turn our attention to the necessary size of the considered unit cell to produce representative results. Please keep in mind that the convexity of the model permits classical homogenization theory [221] to be applicable, see section 4.2.2. In particular, the emergence of an *effective* material response on representative volume elements [176, 177] is ensured, in contrast to the closely related model of chapter 3.
As our reference, we use volume elements with of 384^3 voxels, see Tab. 4.2. To study necessity and sufficiency of this fixed size, we increase and decrease the unit cell to comprise 256^3 and 512^3-voxels, respectively. The arising edge length of the unit cells are 3.2 fiber lengths and 1.6 fiber lengths.
The evolving effective Young's moduli are shown in Fig. 4.10, where we restrict to those cases with highest errors. We observe non-negligible deviations of the effective properties obtained from the 1.6 fiber length structures to those of the 3.2 fiber length structures for all considered loading scenarios. Comparing the Young's modulus evolution of the 256^3-voxel volume element to the 512^3-voxel volume element, the stiffness-based error measure (4.4.3) is of the order of several percent for the considered load cases, with the highest error observed in the evolution of the Young's modulus body of the planar-isotropic structure. For the planar-isotropic structure under loading in x-direction, the deviation reaches 3.0% in x-direction; for loading in z-direction, the deviation is 2.6% in x-direction. In particular, the volume element with 256^3 voxels fails to be representative.
Comparing the predictions for the 384^3-structure, encompassing 2.4 fibers per edge, to the predictions of the larger volume size with 512^3 voxels and an edge length of 3.2 fiber lengths, these deviations decrease. For the isotropic and unidirectional structures, the errors of the Young's modulus evolution under loading in x- and z-direction are smaller than

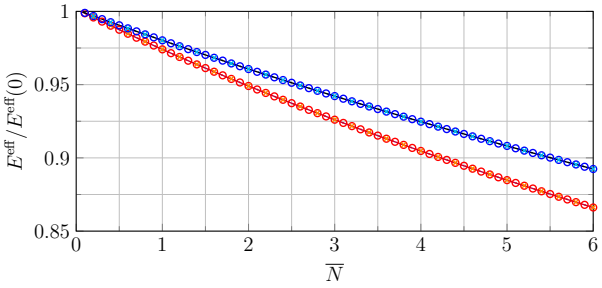

(a) Isotropic, loading in x

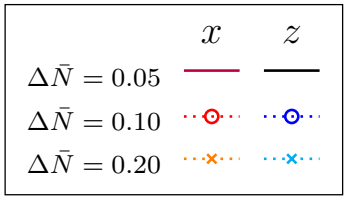

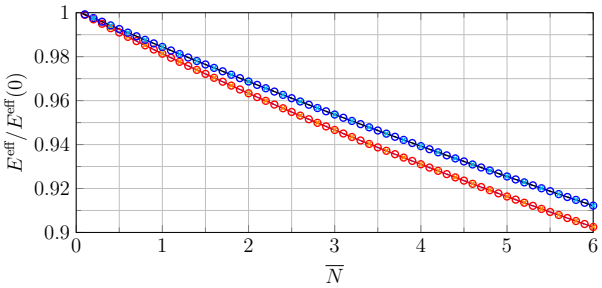

(b) Planar isotropic, loading in x

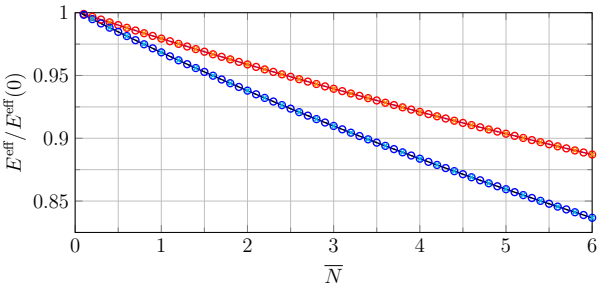

(c) Planar isotropic, loading in z

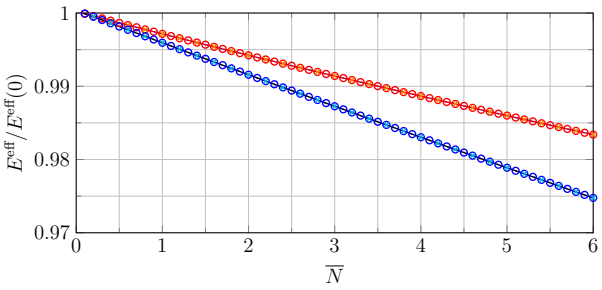

(d) Unidirectional, loading in x

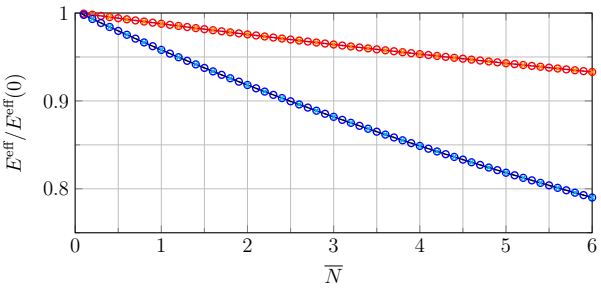

(e) Unidirectional, loading in z

Figure 4.9.: Necessary resolution in logarithmic cycle space

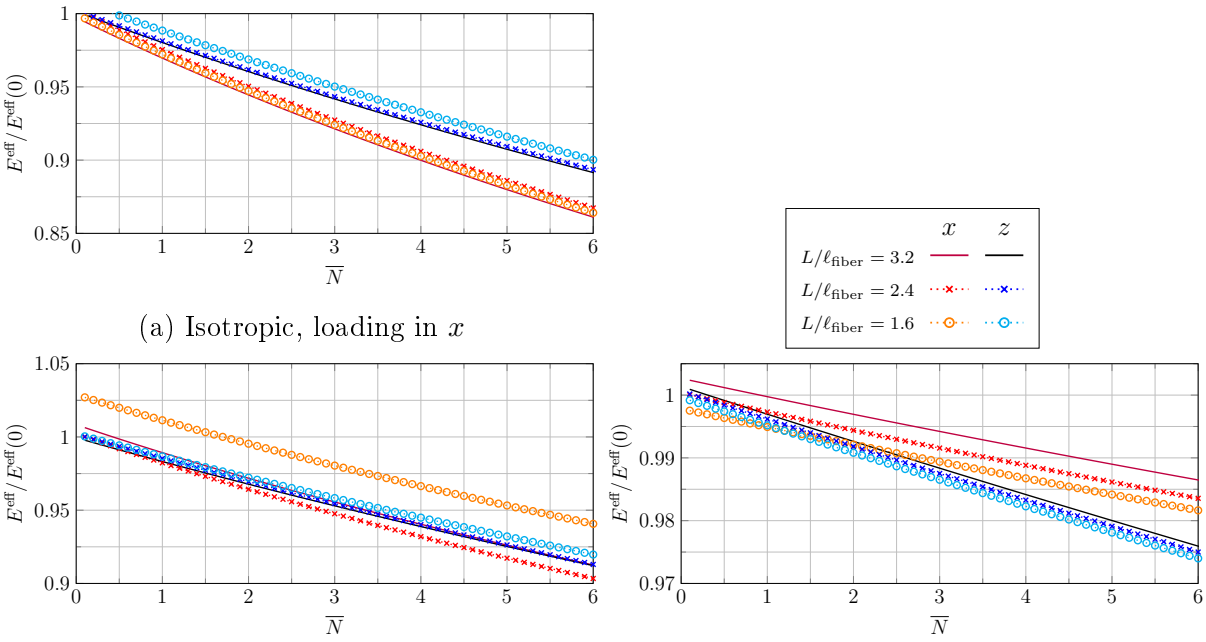

(a) Isotropic, loading in x

(b) Planar isotropic, loading in x

(c) Unidirectional, loading in x

Figure 4.10.: Dependence of the computational results on the size of the unit cell

1.0%. The most critical case is the planar-isotropic structure under loading in x-direction. In this case, the deviation of the predicted Young's modulus evolution in x-direction is 1%. This deviation is well within limits of engineering accuracy and we consider the 384^3 structure to be representative for the model at hand. For the remainder of the manuscript, we fix the size of the volume elements to be of an edge length of 2.4 fiber lengths.

Fields on the microscale

To gain some understanding of the local fields on the microscale, we discuss the evolution of the damage and the strain field for the isotropic case under loading in x-direction. We load the structure shown in Fig. 4.7(b) at a constant stress amplitude of $\sigma_{\text{max}} = 100$ MPa. The resulting damage and maximum principal strain fields in the x-y-plane are shown in Fig. 4.11. Taking a look at the damage evolution, we observer that, in the early stages, damage is initiated at the fiber tips. Subsequently, the damage spreads through the structure. At the last cycle shown in Fig. 4.11(c), damage evolved also close to fibers which are oriented perpendicular to the loading direction. The maximum reduction of the stiffness locally reached for the isotropic structure under a load amplitude of 100 MPa

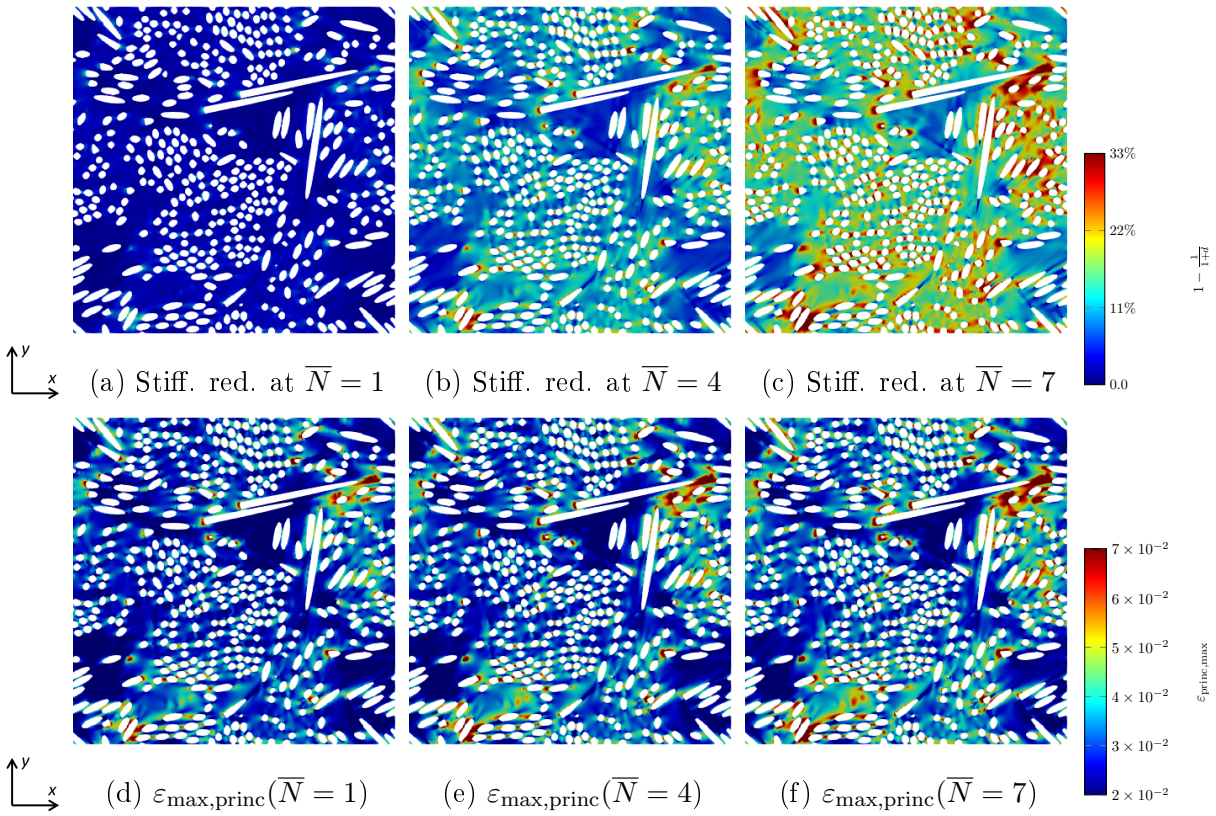

Figure 4.11.: Local stiffness reduction ($1-1/(1+D) \equiv d/(1+D)$, top) and maximum principal strain (bottom) on the isotropic structure under loading in x-direction

load case	$\overline{\boldsymbol{\sigma}}_{xx}^{\max}$	$\overline{\boldsymbol{\sigma}}_{yy}^{\max}$	$\overline{\boldsymbol{\sigma}}_{zz}^{\max}$	$\overline{\boldsymbol{\sigma}}_{yz}^{\max}$	$\overline{\boldsymbol{\sigma}}_{xz}^{\max}$	$\overline{\boldsymbol{\sigma}}_{xy}^{\max}$
# 1	100 MPa	0	0	0	0	0
# 2	0	100 MPa	0	0	0	0
# 3	0	0	100 MPa	0	0	0
# 4	0	0	0	100 MPa	0	0
# 5	0	0	0	0	100 MPa	0
# 6	0	0	0	0	0	100 MPa

Table 4.3.: Tensor components of the stress amplitude (in MPa) for precomputed load cases used for database generation

in x-direction is 33%. This corresponds to a damage value of $D = 0.5$. The loss of the homogenized Young's modulus of the complete RVE in load direction at this time step is 10% and thus well in the order of typical stiffness loss in short fiber reinforced polymers prior to failure [9]. Higher loading amplitudes lead to more pronounced damage.
The strain evolution, starting from cycle $N = 10$ ($\overline{N} = 1$) up to cycle $N = 10^7$ ($\overline{N} = 7$), is shown in the bottom row in terms of the maximum principal strain. The evolution of the strain closely corresponds to the damage field evolution. In particular, it does not show localization. As for the damage field, the strain increases mainly at the tips of fibers oriented in loading direction. However, there are no microcrack-like patterns evolving throughout the matrix. Rather, the damage effects only lead to increasingly large strains at these critical spots.

4.4.3. Reduced-order model

We investigate the capability of the reduced model to approximate the full-field solution in this section. For the sake of brevity, we use the isotropic, the planar isotropic and the unidirectional structure, shown in Fig. 4.7, for these studies. For each of the structures, we precomputed the load cases listed in Tab. 5.4. For assessing the accuracy of the reduced-order models, a strain-based error measure is introduced. For our stress driven simulations, the predicted effective (peak) strains of the full-field simulation $\overline{\boldsymbol{\varepsilon}}_{\max}$ and the reduced-order model $\overline{\boldsymbol{\varepsilon}}_{\max}^{\mathrm{rom}}$ are compared in terms of the error measure

$$e^{\mathrm{rom}} = \max_i \left(\frac{\left\| \overline{\boldsymbol{\varepsilon}}_{\max}(\overline{N}_i) - \overline{\boldsymbol{\varepsilon}}_{\max}^{\mathrm{rom}}(\overline{N}_i) \right\|}{\left\| \overline{\boldsymbol{\varepsilon}}_{\max}(\overline{N}_i) \right\|} \right). \tag{4.4.4}$$

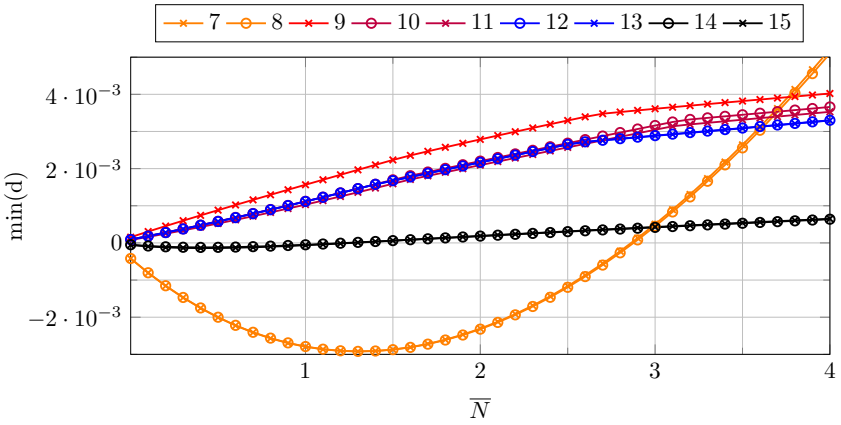

Figure 4.12.: Minimum value of the reconstructed damage field for the unidirectional structure under shear in the yz-plane for different numbers of incorporated modes M_σ

Mode selection

For selecting the modes of the reduced-order model, we investigated different strategies. In the end, the simplest strategy turned out to be the most powerful, and we shall report on it in the following.

Please recall that the continuous model discussed in section 4.2.1 is uniquely solvable (upon implicit discretization in cycle space) and is characterized by a damage variable which can only grow point-wise. In the mixed formulation and upon a Galerkin discretization, see section 4.3.1, these properties needed to be re-evaluated. It turned out that the mixed formulation is theoretically well-posed provided a lower bound D_- (strictly greater than $D = -1$) is imposed on the damage field. Indeed, under this assumption, the operator whose roots correspond to solutions of the discretized equations turns out to be strongly monotone, and classical monotone-operator theory implies the claim.

For the study at hand, we use classical proper orthogonal decomposition (POD) for extracting damage and stress modes from the precomputed load cases. We chose the number of stress and damage modes to be identical, and refer to this number briefly as the number of modes.

Please note that working with the lower bound D_- is only sufficient for obtaining a well-posed model, and may be unnecessary in practice. Indeed, imposing such a constraint a priori may induce significant computational overhead. Also, for our computational experiments, the reduced-order model could be solved rapidly and robustly even without additionally imposed constraints. The reasons behind this surprising behavior is studied

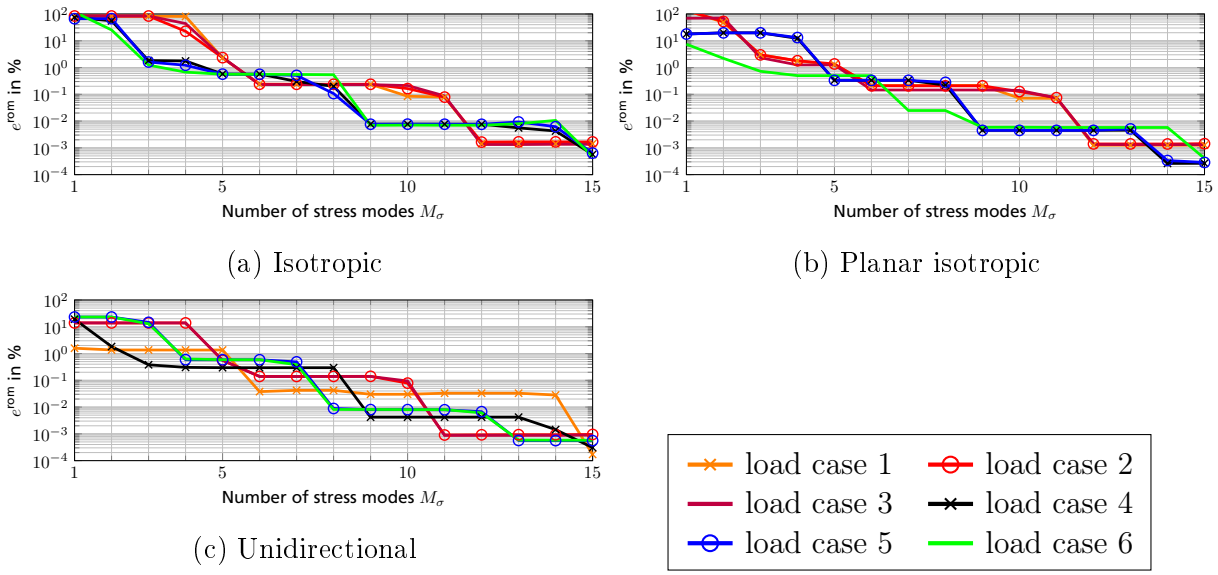

(a) Isotropic

(b) Planar isotropic

(c) Unidirectional

Figure 4.13.: Accuracy study for the database generated from ten snapshots per loading path

more closely in the following. For this purpose, we reconstruct the damage fields predicted by the reduced-order model by summing the mode coefficients multiplied by their pre-computed and stored damage modes at each step and extract the minimum damage-value from the corresponding full damage field.

The evolution of the minimum damage-value was computed for all load cases listed in Tab. 5.4. The most critical case in terms of the damage minimum for seven incorporated modes is the unidirectional structure under load case 4. The minimum damage-value evolution for this case is shown in Fig. 4.12 for different numbers of incorporated modes. For seven and eight modes, the minimum damage-value of the reconstructed damage field is $D = -2.92 \times 10^{-3}$. Albeit negative, this value is far from $D = -1$. By increasing the number of modes incorporated into the reduced-order model, the minimum damage-value increases. This does not come unexpected. Indeed, the reduced-order model approximates the full-field prediction with higher accuracy. The full-field prediction, on the other hand, satisfies the constraint $D \geq 0$ by construction, see section 4.2.1.

For 15 modes, the minimum damage-value is larger than $D = -3.5 \times 10^{-4}$ for all load cases listed in Tab. 5.4 and all considered microstructures. Using 15 modes thus appears sufficient to inherit the well-posedness and stability properties from the continuous model.

We continue with discussing the accuracy of the mode-selection procedure. In Fig. 4.13, the strain error (4.4.4) is shown vs. the number of incorporated modes for the isotropic, the planar isotropic and the unidirectional structure, respectively.

In general, the results of the reduced-order model agree well with the full-field predictions.

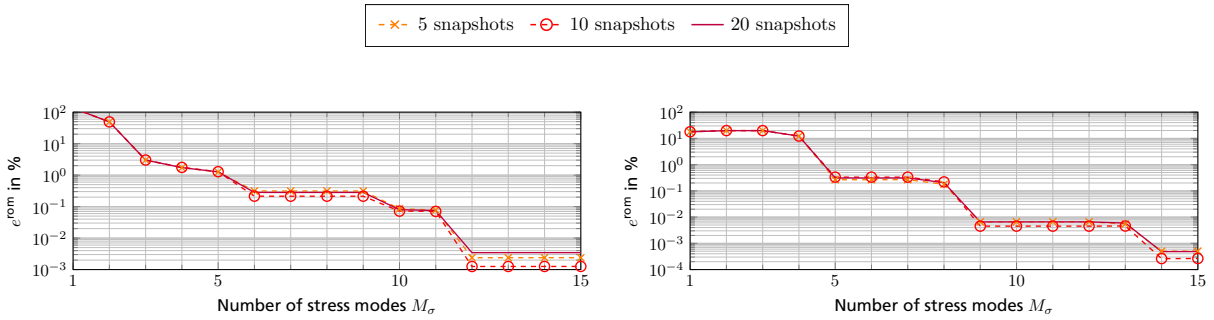

(a) Load case 1

(b) Load case 4

Figure 4.14.: Influence of the Number of Snapshots Per Loading path (NSPL) for the planar-isotropic structure (see Fig. 4.7(b))

Incorporating six modes into the reduced-order model already leads to a strain error below 1% for all load cases computed on the respective structures. Load cases with expected similar effective response, e.g., extension in x-direction, y-direction or z-direction for the isotropic structure (load cases 1, 2 and 3, respectively), show similar approximation behavior. This is remarkable, as we did not account for this symmetry explicitly in the mode-selection procedure.
We will use 15 POD-modes in the reduced-order model subsequently.

Number of snapshots per path

To identify stress and damage modes, we use proper orthogonal decomposition. Some care has to be taken concerning the number of snapshots used for each considered loading path. We discuss the necessary choice for the number of snapshots per loading path (NSPL) in this section.
We use equidistant sampling steps in the logarithmic cycle variable $\overline{N}$. For the sake of brevity, we only discuss the planar-isotropic case here. The other fiber orientations lead to similar qualitative and quantitative results. The effect of including a different number of snapshots is shown in Fig. 4.14. We observe that the capability of the reduced-order model to approximate the effective strain amplitude predicted by the full-field model does not strongly depend on the chosen number of snapshots. Indeed, the strain-amplitude error (4.4.4) is in the same order of magnitude at all number of modes in Fig. 4.14 regardless of the number of snapshots (NSPL). Even a model order reduction based on as few as three snapshots per load path appears to be reasonable. This appears to be a consequence of the non-localizing nature of the fatigue-damage model.

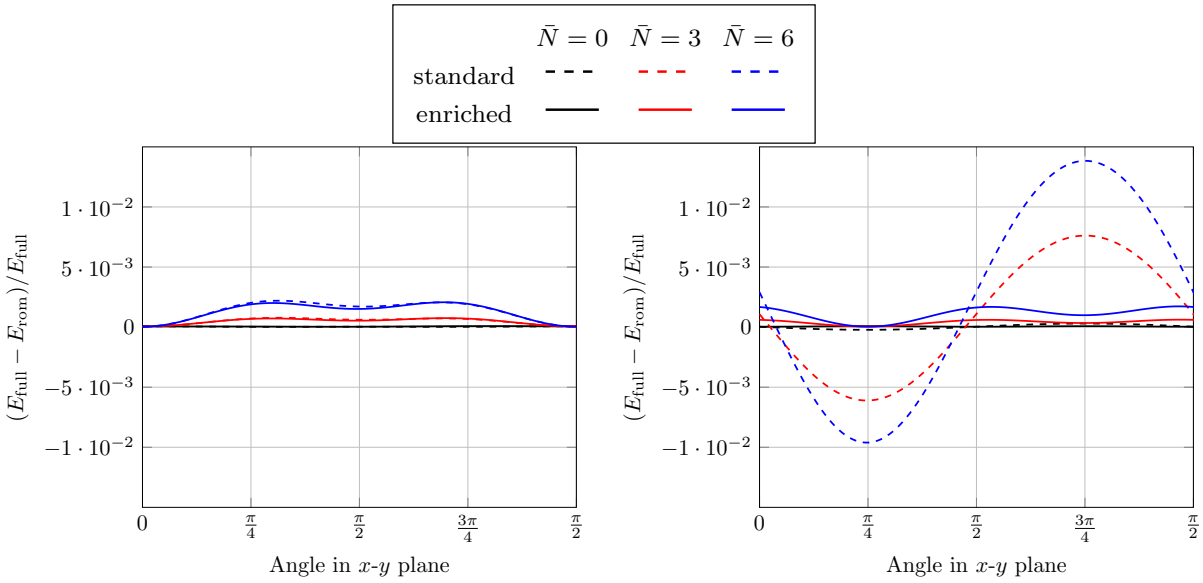

(a) Extension in x-direction

(b) Extension in 45°-direction

Figure 4.15.: Deviation of the direction-dependent Young's modulus from the full-field prediction in the x-y-plane for the planar-isotropic structure for different databases

However, if the number of snapshots is chosen too small, the number of extractable modes is limited. On the other hand, the achieved approximation quality is certainly limited by choosing too few modes. Therefore, we fix NSPL= 10. An extension to more snapshots does not seem necessary and is thus omitted for the sake of faster precomputations.

Necessary loading paths for database generation

In this section, we investigate the capabilities of the reduced-order model to predict the effective stiffness degradation for loading scenarios that were not accounted for in the database generation. More precisely, we discuss two variants: a change of the loading direction and a change of the loading amplitude. For the sake of brevity, we restrict to the planar-isotropic structure.

We start with the effect of changing the loading direction. We consider load cases of pure extension at the constant stress amplitude of $\overline{\boldsymbol{\sigma}}_{xx}^{\max} = 100$ MPa and stress ratio $R = 0$. The material parameters are chosen according to Tab. 4.1. First, we study loading in x-direction. Additionally we consider an extension at a 45° angle around the z-axis. Due to the symmetry of the planar-isotropic microstructure, both loading scenarios should

give rise to identical responses (up to a rotation).
We consider a database built upon the load cases listed in Tab. 5.4, referred to as standard database in the following. Note that the first load case is part of the database. The *enriched* database comprises, in addition to the load cases of the standard database, the 45°-rotated full-field prediction.
The results of the reduced-order models for these two load cases, both, for the standard database and the enriched database, are plotted in Fig. 4.15. The Young's modulus computed from the full-field prediction is referred to as E_{full} and the Young's modulus computed from the reduced-order model as E_{rom}. The error measure $(E_{\text{full}} - E_{\text{rom}})/E_{\text{full}}$ is plotted over a range of 180° in the x-y-plane, where 0° corresponds to the x-axis and 90° to the y-axis.
We observe that the first load case, extension in x-direction, leads to a negligible relative error of about 0.1%, both, for the standard and the enriched database. On the contrary, when considering the 45°-rotated load case, the standard database is not able to reproduce the load case with the same accuracy. At an angle of 135°, the Young's modulus at $\overline{N}$ predicted with the standard database deviates from the full-field prediction by a relative error of 1.4%. Yet, the induced error remains on an acceptable level.
When including the 45°-oriented extension load-case into the precomputations, the accuracy of the reduced-order model is increased. Both load cases, tension in x-direction and tension in 45° are predicted with similar accuracy in the order of 0.1%.
As a take-away message from these studies, we state that some caution has to be taken regarding a discretization of the space of possible loadings to select the modes from. Yet, the standard sampling with six load cases appears reasonable in terms of accuracy. To increase the accuracy, the sampling strategy could be extended in an adaptive way. For the work at hand, we fix the standard six load cases.
As a second step in studying the necessary precomputations, we investigate the effect of varying the loading amplitude. We restrict the computational examples to the planar-isotropic structure. Recall that precomputations with a peak stress $\overline{\boldsymbol{\sigma}}_{xx}^{\max} = 100$ MPa are used to generate the database, see Tab. 5.4. For this study, we multiply these load amplitudes by factors of 5 and 0.2, respectively. Simulations at a peak stress of $\overline{\boldsymbol{\sigma}}_{xx}^{\max} = 500$ MPa well exceed typical stress values in fatigue experiments and are only chosen here to test the capability of the numerical model to adapt to stress amplitudes higher than the training level. For the load cases with modified amplitudes, we compute the strain-amplitude error (4.4.4) by comparison of the full-field to the reduced-order model predictions. The results are shown in Tab. 4.4.
We observe that the load case with $\overline{\boldsymbol{\sigma}}_{xx}^{\max} = 20$ MPa, which is smaller than the training load case $\overline{\boldsymbol{\sigma}}_{xx}^{\max} = 100$ MPa included into the database, is predicted accurately with

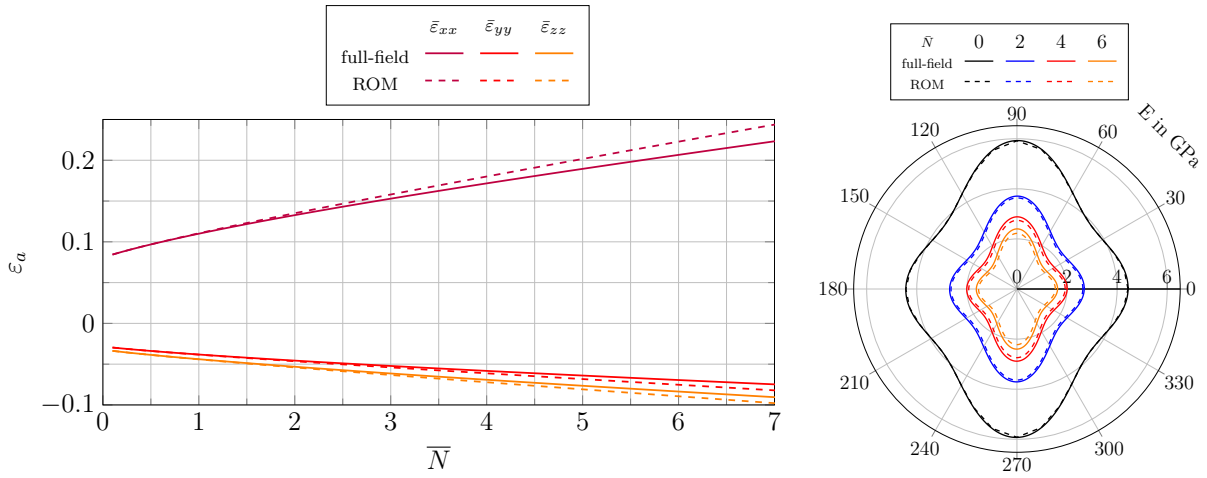

(a) Evolution of the effective strain amplitude under extension in x-direction

(b) Evolution of the effective stiffness under extension in x-direction

Figure 4.16.: Stiffness and strain results for planar-isotropic structure under 500 MPa loading: comparison of full-field predictions and reduced-order model

	Strain errors for loading in			
	$\overline{\boldsymbol{\sigma}}^{\max}_{xx}$	$\overline{\boldsymbol{\sigma}}^{\max}_{zz}$	$\overline{\boldsymbol{\sigma}}^{\max}_{yz}$	$\overline{\boldsymbol{\sigma}}^{\max}_{xy}$
20 MPa	1.1×10^{-5}	6.0×10^{-6}	1.3×10^{-6}	9.8×10^{-7}
100 MPa	1.3×10^{-5}	1.3×10^{-5}	2.6×10^{-6}	4.1×10^{-6}
500 MPa	9.2×10^{-2}	3.9×10^{-2}	2.9×10^{-3}	9.2×10^{-2}

Table 4.4.: Strain-amplitude errors (4.4.4) for changing loading amplitude

	Strain errors for loading in			
	$\overline{\boldsymbol{\sigma}}_{xx}^{\max}$	$\overline{\boldsymbol{\sigma}}_{zz}^{\max}$	$\overline{\boldsymbol{\sigma}}_{yz}^{\max}$	$\overline{\boldsymbol{\sigma}}_{xy}^{\max}$
20 MPa	2.9×10^{-5}	3.5×10^{-5}	4.1×10^{-5}	4.2×10^{-5}
100 MPa	1.4×10^{-3}	6.3×10^{-4}	7.1×10^{-4}	2.0×10^{-3}
500 MPa	1.1×10^{-1}	6.2×10^{-2}	8.6×10^{-3}	2.4×10^{-1}

Table 4.5.: Strain-amplitude errors (4.4.4) for changing loading amplitude, trained at 20MPa

strain-amplitude errors below 10^{-4}. For a higher amplitude at $\overline{\boldsymbol{\sigma}}^{\max} = 500$ MPa, the accuracy decreases significantly. We observe a maximum error of 9.23 % in load cases 1 and 6. In Fig. 4.16(a), the strain amplitudes computed by the full-field model and the reduced-order model for this load case are shown in more detail. Up to strains of 0.13 in loading direction, the deviation of the full-field strain curve to the reduced-order model predictions is small. Indeed, at $\overline{N} = 1.8$, where the full-field model predicts $\varepsilon_{a,xx} = 0.128$, the reduced-order model predicts $\varepsilon_{a,xx} = 0.130$, which is a relative deviation of 1.6%. For further increasing strain amplitudes, the deviation between the effective strain-amplitude curve of the full-field model and of the reduced-order model increases, as well. In addition to the strain amplitude, we investigate the evolution of the Young's modulus body. For load case 1, the Young's modulus body in the x-z-plane is plotted in Fig. 4.16(b). We observe that, even though the magnitude is not accurately met, the reduced-order model still predicts the shape of the Young's modulus body in accordance with the full-field solution, also at high cycle numbers.

Unexpectedly, despite being trained at 100 MPa, the database is most accurate for a stress amplitude of 20 MPa. To understand this effect more thoroughly, we trained a database with lower load amplitudes of 20 MPa and compare its accuracy to the standard database, trained at 100 MPa. We compare the errors produced by the 20 MPa database, see Tab. 4.5, to those of the standard database in Tab. 4.4. The most critical load case at an amplitude of 20 MPa can be reproduced with an accuracy of 2.9×10^{-5}, which has the same order of magnitude as the error produced by the 100-MPa database for the same load case of 1.1×10^{-5}. In contrast, the 100 MPa load cases treated by the 20-MPa database cannot be reproduced with the same accuracy as for the 100-MPa database. Indeed, the maximum error increases from 1.3×10^{-5} to 2.0×10^{-3}, which corresponds to a loss in accuracy by a factor of 154. The trend for even higher load amplitudes of 500 MPa is similar. This investigation reveals that the fatigue-damage evolution at lower stress amplitude is easier to approximate - as a result of the underlying physics - than

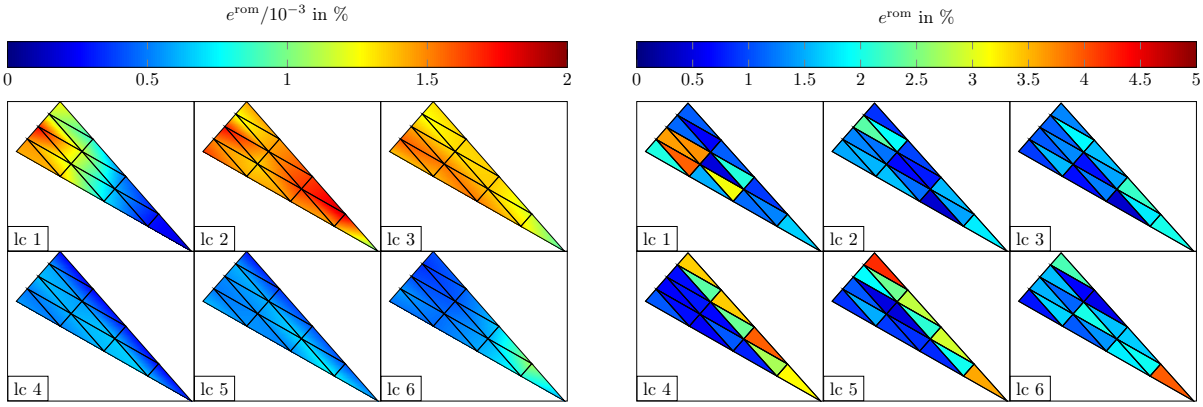

(a) Accuracy at nodes

(b) Accuracy at centroids

Figure 4.17.: Accuracy study on the fiber-orientation triangle: strain error (4.4.4) at pre-computed and interpolated structures

at higher stress amplitudes. This is the reason for the higher accuracy of the 100 MPa database for a stress amplitude of 20 MPa.
We conclude that the model may be safely used for computations where the strain evolution reaches strain levels of the training level or below, but some caution is advised when exceeding the pre-training levels. This effect is a consequence of the non-linearity of the model. It was with this insight at hand that we selected a training amplitude of 100 MPa, as the reasonable stress amplitudes of interest are covered in this way. Despite some deviations in the predicted effective strain amplitudes, the effective stiffness of the reduced-order model is predicted rather accurately.

Covering different fiber orientation states

With component-scale applications in mind, a variety of fiber-orientation states needs to be considered. Guided by the state of the art in injection-molding simulations [229], we consider a varying second-order fiber-orientation tensor [169] as the input for the generated microstructures. To create a database encompassing all possible second-order fiber-orientation tensors, we utilize the fiber-orientation interpolation procedure proposed by Köbler et al. [160]. Up to an orthogonal transformation, second-order fiber-orientation tensors may be parameterized by a two-dimensional triangle, corresponding to the two largest eigenvalues of the second-order fiber-orientation tensor. Based on a triangulation of this fiber-orientation triangle, a reduced-order model is identified for every node of this triangulation. Subsequently, the effective models are interpolated to the entire triangle. We refer to Köbler et al. [160] for details.

We discretize the fiber-orientation triangle by 15 nodes as shown in Fig. 4.17, resulting in 16 sub-triangles. For each of the 15 nodes, we generate microstructures and precompute all six load cases listed in Tab. 5.4 for these structures. These precomputations are then used to build a database via proper orthogonal decomposition, as described in section 4.4.3. In a first verification step, we compare the evolution of the strain amplitude predicted by the full-field computations on these 15 structures with the predictions of the reduced-order model by means of the error measure (4.4.4). In Fig. 4.17(a), this error measure is plotted at each of the nodes for the reference load cases (lc) , see Tab. 5.4. The accuracy on the precomputed structures is good for all microstructures and all considered load cases. The maximum observed strain-amplitude error is 1.8×10^{-4} for the structure with eigenvalues $\lambda_1 = 0.417$, $\lambda_2 = 0.417$ and $\lambda_3 = 0.167$ under extension in x-direction (load case 1). We observe the errors in the extension load cases to be higher than the errors in the shear cases. The accuracy using 15 modes is sufficient for the precomputed structures. Note that the choice of 15 modes arises from the study on the non-negativity of the damage field, see section 4.4.3. In terms of the accuracy choosing even fewer modes would be reasonable.

As a second verification step, we investigate the predictions of the model on fiber orientation states that have not been precomputed directly, but are interpolated from nearby precomputed states. For these structures within the faces of the discretized fiber-orientation triangle, as suggested by Köbler et al. [160], we compute the material response of the surrounding structures at the nodes of the discretized fiber-orientation triangle via the reduced-order model, and successively interpolate the effective stresses. This procedure increases the effort by a factor of three, both, in terms of CPU time and memory usage, as, for each Gauss point, three material laws have to be evaluated.

To assess the predictive capabilities of the interpolation procedure, we generated microstructures at the centroids of the 16 sub-triangles. The computed (full-field) effective strain-amplitude tensors serve as our reference. We compare these effective strain amplitudes to the effective strain amplitudes predicted by the reduced-order model via interpolation in terms of the error measure (4.4.4). In Fig. 4.17(b), we observe that the strain errors do not exceed 5 % in the maximum strain-amplitude error. Since nodal errors are found to be very small, the latter error is mainly caused by the interpolation procedure. For the remainder of this work, we will use the presented fiber-orientation triangulation.

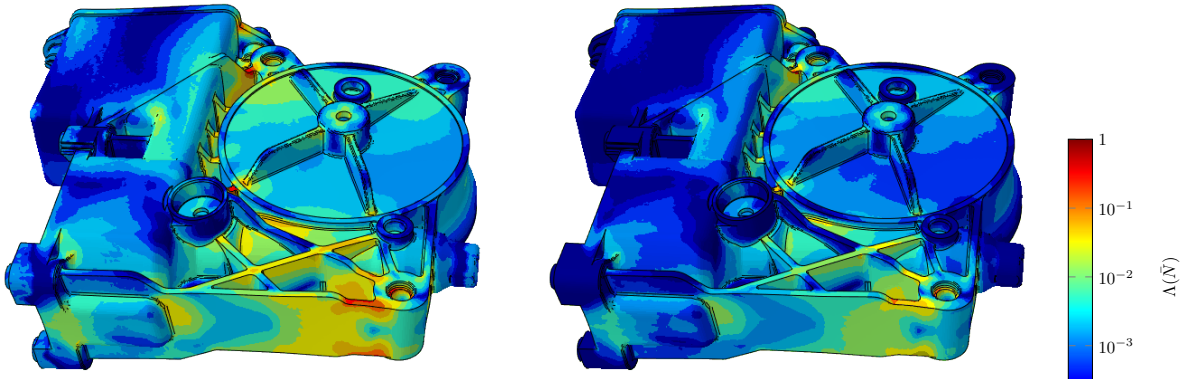

(a) Damage state for model in chapter 3 (b) Damage state for model in work at hand

Figure 4.18.: Relative degradation of the acoustic tensor (5.5.7) after 10^6 cycles

4.5. Component-scale simulations

We demonstrate the numerical capabilities of the presented model on component scale in terms of efficiency in both computational and memory usage by comparison to the approach of chapter 3. This models differs from the one presented in this work mainly in two aspects.

1. Non-local/local: The approach of chapter 3 introduces a damage-gradient term to avoid mesh-dependent results. The model proposed in this work is well-defined without an additional damage-gradient term.

2. Polynomial order: The highest polynomial order in the variables $(\boldsymbol{\sigma}, D)$ in equations (4.3.2) and (4.3.3) is two, whereas the approach of chapter 3 leads to polynomials of the order of three in $(\boldsymbol{\varepsilon}, D)$. Thus, less data needs to be processed at the Gauss point level for the former model.

In contrast to the approach presented in the work at hand, the model of chapter 3 permits localization, which makes the choice of the snapshots for proper orthogonal decomposition more difficult. Indeed, choosing an equidistant sampling method, in chapter 3, we incorporate 40 strain and 40 damage modes to reach acceptable accuracy. As discussed in section 4.4.3, we make use of only 15 stress and 15 damage modes to ensure that the damage field is accurately captured.
We chose to demonstrate the efficiency of the model at hand on the same component and load case as described in chapter 3: a short-fiber reinforced motor-housing subjected

	CPU time	max. memory usage	av. memory usage
quadratic damage (chapter 3)	12200 h	65.5 GB	47.4 GB
compliance based damage	712 h	39.0 GB	22.9 GB

Table 4.6.: Computational effort for the considered fatigue-damage models

to fatigue loading. For details on the fiber-orientation distribution inside the component, as well as on the load case, we refer to chapter 3. We use the simulation software ABAQUS [192] for computations on the macroscale. Both computations were performed on the same Linux cluster with 256 CPUs distributed on 16 nodes up to the cycle 10^6. Similar to the approach in chapter 3, we chose the determinant of the acoustic tensor A^{aco} as a quantitative measure for the material degradation and define

$$\Lambda(\overline{N}) = \max_{\|\mathbf{n}\|=1} \left[1 - \frac{\det A^{\mathrm{aco}}(\mathbf{n}, \mathbb{C}(\overline{N}))}{\det A^{\mathrm{aco}}(\mathbf{n}, \mathbb{C}(0))} \right], \tag{4.5.1}$$

where $\mathbf{n}$ denotes a unit-normal vector, to assess the current damage state in the macroscopic model. The damage state of the motor housing component after 10^6 cycles is shown in Fig. 4.5 for, both, the quadratic type damage model of chapter 3 (Fig. 4.18(a)) and the compliance-based damage model proposed in the work at hand (Fig. 4.18(b)). The regions of critical damage evolution, i.e., regions with a high relative decrease in the maximum of the acoustic tensor determinant, are found to be similar for both models.
The CPU time and the memory usage are shown in Tab. 4.6. Both, in terms of CPU time and memory usage, the efficiency of the model at hand is improved compared to the previous work. The CPU time of the compliance based damage model at hand leads to a speed up by a factor of 17 compared to the quadratic damage model of chapter 3. The memory usage is on average improved by 52% and the peak memory usage by 40%.
This gain has three main causes. For a start, a lower number of incorporated modes is used, which decreases the size of the system matrices. Secondly, the polynomial in the damage evolution and stress-strain relationship in terms of the internal variables is of lower order. Thirdly, in contrast to the approach in chapter 3, we use a local model and do not have to incorporate gradient terms. The last two factors decrease the number of system matrices which need to be precomputed and stored.

4.6. Conclusions

We considered the problem of fatigue-damage evolution in short-fiber reinforced polymer composites. In order to account for the influence of the fiber reinforcements, both, in terms of the fiber geometry and the fiber orientation, we proposed a multiscale model for the fatigue-damage evolution in the stable second phase. The principal object of interest for us is the anisotropic stiffness degradation of such composites when subjected to (high-cycle) fatigue loading. Indeed, the failure behavior of thermoplastic components under fatigue loading appears to be difficult to predict if the stiffness decrease under fatigue loading previous to failure is not accounted for.

Motivated by the stability of the second phase in the fatigue-damage evolution, we explored the recently introduced class of damage models based on the compliance tensor [207]. Indeed, the inherent convexity of the model class appears sufficient for representing the fatigue-damage phenomena of interest, and offer to alleviate the computational burden associated to damage models with gradient extension [211].

We showed that, despite its simplicity, the model matches our experimental results rather well, provided the initial damage occurring in the first few cycles is taken into consideration. The precise value of the initial damage requires further studies.

With upscaling in mind, we studied a mixed formulation of the incremental potential of the multiscale fatigue-damage model. In this formulation, the potential is a third-order polynomial in the mode coefficients, and thus lends itself naturally to an efficient model-order reduction. Surprisingly, we could show that this mixed formulation inherits well-posedness from the purely primal formulation by rewriting the mixed formulation in terms of a specific operator, which is strongly monotone under a natural condition on the damage field.

The multiscale fatigue-damage model was tested thoroughly, both as a full-field and as a reduced-order model. Due to the (strongly) convex nature of the model, emergence of effective properties via suitable representative volume elements [176] is guaranteed. Also, due to the precluded localization, the multiscale model is characterized by high computational efficiency, which could be demonstrated on component scale.

This chapter was mainly concerned with setting up the multiscale technology necessary to handle industrial-scale applications. As a next step, it appears imperative to account for the initial damage caused in the first few cycles by an appropriate modification of the model and to investigate the extension to R-values different from zero as well as the dependence on the loading frequency. Supplemented by an appropriate failure criterion on the macroscopic scale, the presented multiscale fatigue-damage model will be ready

for applications.

5. A space-time upscaling technique for modeling high-cycle fatigue-damage of short-fiber reinforced composites[1]

5.1. Introduction

In this chapter, we propose a fatigue-damage model for the matrix material in short-fiber reinforced polymers formulated in the time scale. This model may be regarded as an extension of the rate-independent convex damage model proposed by Görthofer et al. [207] to fatigue damage. Similar to approaches of chapter 3 and Jain et al. [217], we are interested in the stable stiffness degradation of the material observed prior to failure. In contrast to these models, we chose a formulation of the damage material law in time space rather than cycle space. Building upon the work of Paas et al. [230] and Peerlings [211], the proposed material evolution only increases damage under loading (in contrast to unloading). One of the main advantages of a damage model formulated in time-space is the consistent incorporation of changes in the loading path into the material-evolution equations. Indeed, changes in mean stress values or the wave form directly influence the material behavior. Their main disadvantage however is the possibly very large computational costs for computations in the high-cycle regime.
To combine the advantages of both approaches, we propose a cycle-jump technique building upon parametric loading curves. In fatigue experiments, the wave form of the loading path is known a priori. A parametrization of the wave form enables us to reformulate the time-scale model in cycle space and, subsequently, a logarithmic cycle space. As the

[1] Reproduced from: N. Magino, J. Köbler, H. Andrä, F. Welschinger, R. Müller, M. Schneider, "A space-time upscaling technique for modeling high-cycle fatigue-damage of short-fiber reinforced composites," *Composites Science and Technology*, vol. 222, pp. 109340, 2022.

mechanical experiments in the work at hand have a sinusoidal wave form, we discuss this case in detail.

We obtain related fatigue-damage models formulated in three time-like scales: time space, cycle space and *logarithmic* cycle space. We thoroughly discuss approximations and resulting regimes of applicability in section 5.3. In the high-cycle regime, the logarithmic cycles scale is applicable and allows for very large steps in cycle steps, reducing the computational effort significantly.

The obtained logarithmic cycle scale may be viewed as an extension of the compliance-based fatigue damage model [231] using an effective stress depending on the parametrized wave form. It thus extends the former model to computations at different mean stress values. Incidentally, this point of view enables us to make use of the model-order reduction technique based on a reformulation of the equations in terms of the stress proposed in a recent work of the authors [231]. We study the accuracy of model-order reduction technique for a commercial polyamide material.

Last but not least, we demonstrate the capability of the model to predict the stiffness degradation of a short-fiber reinforced polymer at different stress amplitudes, stress ratios, orientation states and geometries. Using only one material parameter, the fatigue damage evolution speed α, we can show that the material behavior of the composite under these various loading scenarios is predicted with reasonable accuracy sufficient for industrial applications.

5.2. The fatigue-damage model in time

We introduce a damage material based on a free energy density

$$w\left(\boldsymbol{\varepsilon}, D\right) = \frac{1}{2}\frac{1}{1+D}\,\boldsymbol{\varepsilon} : \mathbb{C}_0 : \boldsymbol{\varepsilon} \tag{5.2.1}$$

with a scalar damage variable $D \geq 0$, an undamaged stiffness tensor $\mathbb{C}_0$ and the strain tensor $\boldsymbol{\varepsilon}$. Using a damage variable and a suitable free energy potential is a rather typical strategy in continuum damage mechanics [232]. However, the form of the damage model is non-standard. It may be considered as an adaption of the damage model introduced by Görthofer et al. [207] to fatigue loading. The corresponding stress is derived from the energy density by

$$\boldsymbol{\sigma} \equiv \frac{\partial w}{\partial \boldsymbol{\varepsilon}}\left(\varepsilon, D\right) = \frac{1}{1+D}\,\mathbb{C}_0 : \boldsymbol{\varepsilon}. \tag{5.2.2}$$

The associated damage-driving force computes as

$$Y_D \equiv -\frac{\partial w}{\partial D}(\boldsymbol{\varepsilon}, D) = \frac{1}{2}\frac{1}{(1+D)^2}\,\boldsymbol{\varepsilon} : \mathbb{C}_0 : \boldsymbol{\varepsilon}. \tag{5.2.3}$$

Note that for a linearization of $1/(1+D)$ around the undamaged state, the stress strain relationship matches the Lemaitre model [233]. We may express the driving force Y_D as a function of the stress $\boldsymbol{\sigma}$ and the internal variable D

$$Y_D(\boldsymbol{\sigma}, D) = \frac{1}{2}\boldsymbol{\sigma} : \mathbb{S}_0 : \boldsymbol{\sigma} \tag{5.2.4}$$

with the compliance tensor $\mathbb{S}_0 = \mathbb{C}_0^{-1}$ of the undamaged state. Paas et al. [230] and Peerlings [211] introduced phenomenological models to capture the effects of fatigue damage. They proposed a damage evolution law where damage only increases under positive loading, i.e., whenever a carefully chosen equivalent strain measure $\varepsilon_{\mathrm{eq}}$ was increasing, i.e., the condition $\dot{\varepsilon}_{\mathrm{eq}} > 0$ holds. Suiker et al. [234] used a similar approach in the context of cyclic plasticity.
We follow this line of reasoning and consider the damage-driving force Y_D as an equivalent strain measure. More precisely, we define

$$\dot{D}(\boldsymbol{\varepsilon}, D, q) = \begin{cases} \alpha_q(q)\, Y_D(\boldsymbol{\varepsilon}, D), & \text{if } \dot{Y}_D(\boldsymbol{\varepsilon}, D) \geq 0, \\ 0, & \text{otherwise.} \end{cases} \tag{5.2.5}$$

Here, α_q denotes a (time-dependent) material parameter which governs the speed of damage evolution. Similar to Largeton et al. [235], who considered the effect of aging onto viscoelastic properties, we introduce a variable q to model the cycle dependence of the material parameter via the *empirical* relationship

$$\alpha_q(q) = \frac{4\alpha_{\mathrm{t}}}{q} \tag{5.2.6}$$

with a parameter $\alpha_{\mathrm{t}} > 0$. The variable q is assumed to grow at a constant rate

$$\dot{q} = K_{\mathrm{t}} \tag{5.2.7}$$

with some scalar parameter K_{t}. The evolution equation (5.2.7) for q can be integrated explicitly. For a fixed duration of a load cycle $T > 0$, we express the (global) time t as the superposition of a cycle-count variable $N \geq 0$ and a sub-cycle variable $\tau \in [0, 1)$

$$t = T\,(N + \tau). \tag{5.2.8}$$

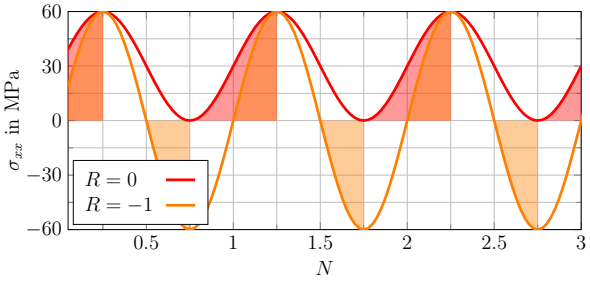

(a) Loading, $R = 0$

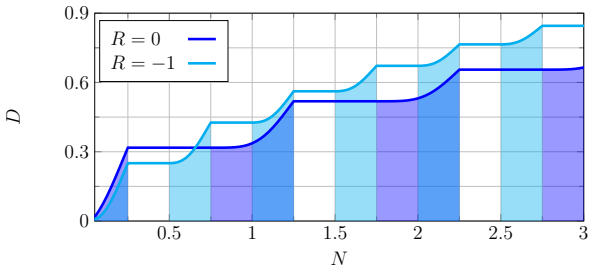

(b) Damage evolution, $R = -1$

Figure 5.1.: Damage evolution under cyclic loading of a homogeneous material

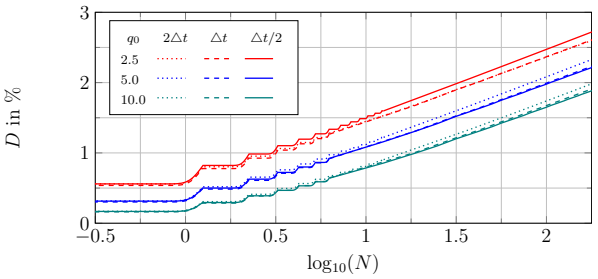

(a) Time-resolution study for the fatigue-damage model

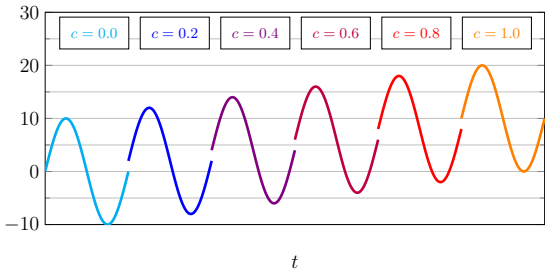

(b) Influence of shift parameter c on the wave form

Figure 5.2.: Time evolution under fatigue

For the initial condition $q(t = 0) = q_0$, we obtain the expression

$$q = q_0 + K_\mathrm{t}\, t \equiv q_0 + K\,(N + \tau) \tag{5.2.9}$$

in terms of the parameter $K = K_\mathrm{t} T$ for constant duration of a single load cycle T. The model at hand permits damage to grow only during loading. The latter is characterized by the condition $\dot{Y}_D > 0$. To demonstrate the behavior of the material model, we consider an exemplary isotropic matrix material with Young's modulus $E = 3.35$ GPa, Poisson's ratio $\nu = 0.4$ and material-model parameters $\alpha_t = 0.1$ 1/MPa, $K = 5.0$ as well as $q_0 = 5.0$. The material is subjected to a sinusoidal loading for uniaxial stress-driven tension in x-direction. The load curves are shown in Fig. 5.1(a) for two different stress ratios R, defined by $R = \sigma_{\min}/\sigma_{\max}$, namely $R = 0$ and $R = -1$. The peak stress in both cases is $\sigma_{\max} = 60$ MPa. The corresponding damage evolutions are shown in Fig. 5.1(b). Damage only increases for a positive loading rate $\dot{Y}_D \geq 0$. Comparing the different load cases after 3 load cycles in Fig. 5.1(b), we observe that for same maximum stress $\sigma_{\max}$, the damage evolution for a stress ratio of $R = -1$ is faster than for $R = 0$. We complete the discussion with several remarks:

For a start, the proposed model is thermodynamically consistent. Indeed, the dissipation for isothermal, small-strain systems [236, Chapter 5.3] computes as

$$\begin{aligned}\mathcal{D} \equiv \boldsymbol{\sigma} : \dot{\boldsymbol{\varepsilon}} - \dot{w} = \sigma : \dot{\boldsymbol{\varepsilon}} - \frac{\partial w(\boldsymbol{\varepsilon}, D)}{\partial D}\,\dot{D} - \frac{\partial w(\boldsymbol{\varepsilon}, D)}{\partial \boldsymbol{\varepsilon}} : \dot{\boldsymbol{\varepsilon}} \\ = \begin{cases} \alpha_q(q)\, Y_D(\boldsymbol{\varepsilon}, D)^2, & \text{if } \dot{Y}_D(\boldsymbol{\varepsilon}, D) \geq 0, \\ 0, & \text{otherwise.} \end{cases}\end{aligned} \tag{5.2.10}$$

This is always positive for

$$\alpha_q(q) = \frac{4\alpha_t}{q_0 + K(N + \tau)} \geq 0. \tag{5.2.11}$$

Thus, the dissipation $\mathcal{D}$ is non-negative, i.e., thermodynamic consistency holds. Secondly, the free energy of the material model is jointly convex in the variables $\boldsymbol{\varepsilon}$ and D. Thus, the model does not permit localization and allows to compute mesh-insensitive results without regularization methods pertinent in continuum damage models [237–239]. For a more in-depth discussion, we refer to Görthöfer et al. [207]. In the context of efficient simulation of cyclic loading, this comes with another advantage. In localizing fatigue models, cycle-jump techniques critically depend on an accurate adaptive step-size selection-strategy [198]. Non-localizing models are more robust and thus expected to be less sensitive w.r.t. the chosen cycle-jump size. Clearly, as damage localization is excluded, the applicability of the model is inherently limited to stable, non-localized damage corresponding to the range of stable stiffness degradation prior to failure under fatigue loading. A model permitting damage localization has been studied in chapter 3. Some advantages and disadvantages compared to non-local fatigue models have been discussed in chapter 4. In the context of non-localizing fatigue damage the damage model needs to be complemented by an appropriate criterion to predict failure. Moreover, the proposed model does not distinguish between tension and compression, but rather between loading and unloading. For similar models with tension-compression distinction, we refer to Ladevèze and co-workers [240, 241].

5.3. The fatigue-damage model in cycle space

For high cycle fatigue experiments, the number of fatigue cycles is typically in the range of $10^3 - 10^6$ cycles. Thus, the computational cost of a numerical model resolving each individual cycle can be huge. In this section we first study the necessary time step resolution of the model introduced in section 5.2. We then reformulate the model in cycle space and

logarithmic cycle space relying on approximations valid for the high cycle-regime for one Gaussian integration point. We demonstrate the capabilities of the model formulated in cycle space and logarithmic cycle space to use significantly larger steps. Subsequently, a combined time-scale and logarithmic cycle-scale approach is discussed that combines the accuracy of the time-scale model in the first few cycles with the computational efficiency of the logarithmic cycle space formulation at cycles exceeding 10^3. Last but not least, we discuss the assumptions necessary to extend the reformulation obtained from one Gauss-Point to a full field computation and compare the damage evolution for time-scale and reformulated models on a generic fiber structure.

First, we study the necessary number of time (scale) increments for the model formulated in time scale (described by equations (5.2.5) and (5.2.7))

$$\dot{D}(\boldsymbol{\varepsilon}, D, q) = \begin{cases} \alpha_q(q)\, Y_D(\boldsymbol{\varepsilon}, D), & \text{if } \dot{Y}_D(\boldsymbol{\varepsilon}, D) \geq 0, \\ 0, & \text{otherwise}, \end{cases} \tag{5.3.1}$$

$$\dot{q} = K, \tag{5.3.2}$$

with the initial conditions $D(t=0) = 0$ and $q(t=0) = q_0$.

We use the same material parameters for the matrix material as for Fig. 5.1. We consider a sinusoidal uniaxial tension loading with a peak stress of $\sigma_{\max} = 60$ MPa and a stress ratio of $R = 0$. We discretize the evolution equation (5.3.1) with a backward Euler scheme, and select a reference time step for the time-scale model of $\triangle t = T/80$.

In Fig. 5.2(a), the evolution of the damage variable D under the described loading conditions for a pure matrix material is shown for different step sizes. We consider the relative error measure

$$e^X_{\text{step}}(N) = 2\frac{\|D_X(N) - D_{\triangle/2}(N)\|}{\|D_X(N) + D_{\triangle/2}(N)\|} \tag{5.3.3}$$

to compare computations using different step sizes X to computations with the finest computed step $\triangle/2$. For $q_0 = 5.0$, the relative error for the time-scale model at $N = 10^3$ is $e^{\triangle}_{\text{step}} = 0.87\%$ for the reference time step and $e^{2\triangle}_{\text{step}} = 1.26\%$ for a time step twice the reference time step. The choice of a reference time step $\triangle t = T/80$ thus ensures the relative error to be below 1%. Thus, computing $N = 10^5$ cycles, a common cycle count for high-cycle fatigue, requires 8×10^6 time steps. This becomes prohibitive for complex microstructures or even heterogeneous materials.

We thus proceed by seeking a reformulation of the material equations in cycle and subsequently in logarithmic cycle space that allows for efficient computation at large cycle numbers. In experiments, the load path within one cycle is known a priori. We consider the most commonly used wave form in fatigue loading, the sinusoidal wave

[118, 242–245]. Knowing the wave form enables us to derive a model in cycle space from the time model discussed section 5.2 via integration. We assume a sinusoidal wave form

$$\boldsymbol{\sigma} = \left(\sin\left(\frac{2\pi}{T}t\right) + c\right)\boldsymbol{\sigma}_{\mathrm{a}} = \Big(\sin\left(2\pi\tau\right) + c\Big)\boldsymbol{\sigma}_{\mathrm{a}} \tag{5.3.4}$$

for a prescribed stress amplitude $\boldsymbol{\sigma}_a$. As depicted in Fig. 5.2(b) for a load amplitude of $\sigma_{\mathrm{a}} = 10$ MPa, the parameter c shifts the mean stress of the load path. The maximum stress during the cycle is defined at $\boldsymbol{\sigma}_{\max} = \boldsymbol{\sigma}_{\mathrm{a}}(c+1)$.
Plugging equation (5.3.4) into the damage evolution equation (5.2.5) yields

$$\begin{aligned} D(N+1) - D(N) &= \int_0^1 \dot{D}(T(N+\tau))\,\mathrm{d}\tau \\ &= \begin{cases} \int_0^1 \frac{4\alpha_{\mathrm{t}}}{q_0 + K(N+\tau)} Y_D \,\mathrm{d}\tau, & \text{if } -\Big(\sin\left(2\pi\tau\right) + c\Big)\cos\left(2\pi\tau\right) \geq 0, \\ 0, & \text{otherwise.} \end{cases} \end{aligned}$$

In the high cycle fatigue regime, the inequality $\tau \ll N + q_0/K$ holds. We thus use the approximation

$$q_0 + K(N+\tau) \approx q_0 + K\,N. \tag{5.3.5}$$

With these two approximations, we integrate the damage evolution under loading

$$\begin{aligned} & D(N+1) - D(N) && (5.3.6) \\ &\approx \frac{2\alpha_{\mathrm{t}}}{(q_0 + K\,N)}\boldsymbol{\sigma}_{\mathrm{a}} : \mathbb{S}_0 : \boldsymbol{\sigma}_{\mathrm{a}}\left(\left[\int_{\frac{1}{4}}^{\frac{1}{2}+\frac{\arcsin(c)}{2\pi}} + \int_{\frac{3}{4}}^{1-\frac{\arcsin(c)}{2\pi}}\right]\left(\sin\left(2\pi\tau\right) + c\right)^2 \mathrm{d}\tau\right) \\ &= \frac{\alpha_{\mathrm{t}}}{q_0 + K\,N}\,\boldsymbol{\sigma}_{\mathrm{a}} : \mathbb{S}_0 : \boldsymbol{\sigma}_{\mathrm{a}}\left(\frac{1}{2} + c^2\right). && (5.3.7) \end{aligned}$$

Treating the cycle variable N as a *continuous* variable, we are led to the approximation

$$\frac{\partial D}{\partial N}(N) \approx \frac{\alpha_{\mathrm{t}}}{q_0 + K\,N}\,\boldsymbol{\sigma}_{\mathrm{a}} : \mathbb{S}_0 : \boldsymbol{\sigma}_{\mathrm{a}}\left(\frac{1}{2} + c^2\right).$$

Then, at constant stress amplitude $\boldsymbol{\sigma}_a$ and for an initial condition $D(N=0) = 0$, we may further integrate over the cycles to arrive at an explicit expression in cycle space

$$D(N) \approx \frac{\alpha_{\mathrm{t}}}{K}\boldsymbol{\sigma}_{\mathrm{a}} : \mathbb{S}_0 : \boldsymbol{\sigma}_{\mathrm{a}}\left(\frac{1}{2} + c^2\right)\log\left(K\,N + q_0\right). \tag{5.3.8}$$

At high cycle counts $N > 10^3$ and for typical values of $q_0 \in (0, 10]$ and $K \in [1, 10]$, the assumption $q_0 + K\,N \approx K\,N$ is valid. We thus may further approximate

$$D(N) \approx \frac{\alpha_\mathrm{t}}{K} \boldsymbol{\sigma}_\mathrm{a} : \mathbb{S}_0 : \boldsymbol{\sigma}_\mathrm{a} \left(\frac{1}{2} + c^2 \right) \left(\log\left(N\right) + \log\left(K\right) \right). \tag{5.3.9}$$

For notational simplicity, we introduce the parameter $\alpha = \alpha_\mathrm{t} / \left(2K \log_{10}(e)\right)$ and rewrite the damage evolution

$$D(N) \approx 2\alpha\, \boldsymbol{\sigma}_\mathrm{a} : \mathbb{S}_0 : \boldsymbol{\sigma}_\mathrm{a} \left(\frac{1}{2} + c^2 \right) \left(\log_{10}(N) + \log_{10}(K) \right). \tag{5.3.10}$$

We arrive at the final expression

$$D' = 2\alpha\, \boldsymbol{\sigma}_\mathrm{a} : \mathbb{S}_0 : \boldsymbol{\sigma}_\mathrm{a} \left(\frac{1}{2} + c^2 \right), \tag{5.3.11}$$

where we replaced the approximation by an equality sign and denote by prime the derivative w.r.t. the logarithmic cycle count $\overline{N} = \log_{10} N$, $D' \equiv \partial D / \partial \overline{N}$. Please note that cyclic loading for load waves different from the sinusoidal wave can be treated similarly. The sinusoidal wave form is just the most commonly used in fatigue experiments on short-fiber reinforced polymers.
We derived approximate models in different time-like scales. To sum up, we obtained

1. an evolution equation in cycle space

$$\frac{\partial D}{\partial N} = \frac{\alpha_\mathrm{t}}{q_0 + K\,N} \boldsymbol{\sigma}_\mathrm{a} : \mathbb{S}_0 : \boldsymbol{\sigma}_\mathrm{a} \left(\frac{1}{2} + c^2 \right), \tag{5.3.12}$$

2. an evolution equation in *logarithmic* cycle space

$$\frac{\partial D}{\partial \overline{N}} \equiv 2\alpha\, \boldsymbol{\sigma}_\mathrm{a} : \mathbb{S}_0 : \boldsymbol{\sigma}_\mathrm{a} \left(\frac{1}{2} + c^2 \right). \tag{5.3.13}$$

We study the necessary resolution in cycle space for the models at hand. We discretize the above equations using a backward Euler scheme and use reference step sizes of $\triangle N = 1/8$ for the cycle model and increase the step size for the logarithmic model according to the relation $\triangle N = 2N$ dependent on the current cycle N. In Fig. 5.3, the evolution of the damage variable D is shown for pure tension loading with a stress ratio $R = 0$ and a stress amplitude of $\sigma_\mathrm{a} = 30$ MPa. In Fig. 5.3(a), we observe that the influence of the parameter q_0 is restricted to the first few cycles of the damage evolution. Indeed, after ten or more cycles ($\log_{10} > 1$), the slope of the damage evolution is almost independent of q_0. In Fig. 5.3(b), the damage evolution computed in logarithmic cycle space is shown. By the

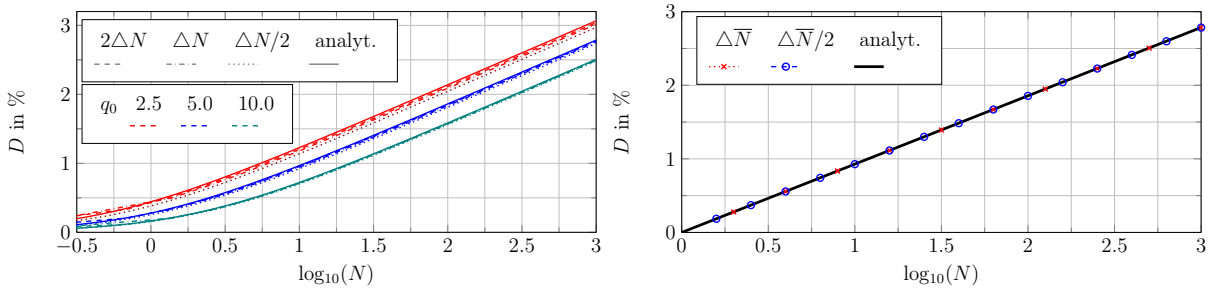

(a) Cycle space model

(b) Logarithmic cycle space model

Figure 5.3.: Resolution study in terms of necessary (logarithmic) cycles

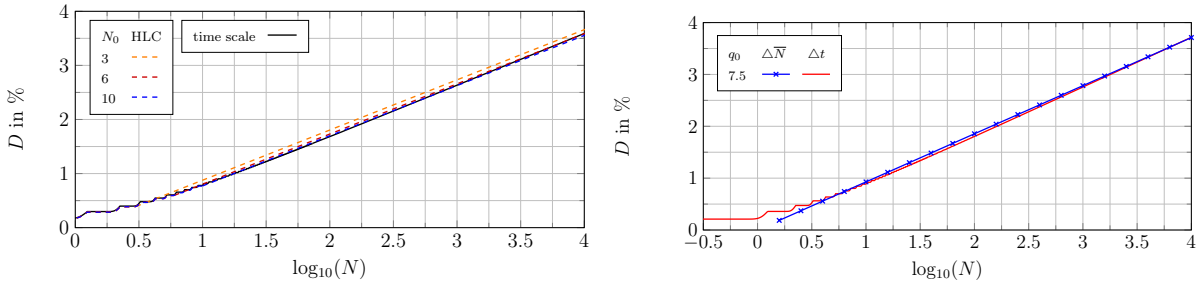

(a) HLC-approach using different numbers of cycles N_0 for initial time-scale based computation for $q_0 = 10.0$

(b) Damage for the time-scale model with $q_0 = 7.5$ and the logarithmic cycle-scale model with $D(\overline{N} = 0) = 0$

Figure 5.4.: Comparison of the damage evolution predicted by the time-scale, the HLC and the logarithmic cycle-scale approach

assumption $q_0 + KN \approx KN$, used in the derivation of the logarithmic model, the influence of a varying initial value of q_0 is neglected in the model formulated in logarithmic cycle space. Thus, the material evolution in the logarithmic cycle-scale model is independent of q_0.

We use the error measure (5.3.3) to quantify the deviations of the numerical computations depending on the resolution. At the cycle count $N = 10^3$, the relative error for the cycle space model with $q_0 = 5.0$ is $e^{\Delta}_{\text{step}} = 0.44\%$ and $e^{2\Delta}_{\text{step}} = 1.30\%$ for the reference and a time step twice the reference step, respectively. Thus, using the reference cycle step with $\triangle N = T/8$, the relative error is below 1%. When using the logarithmic cycle model, the reference time step $\triangle \overline{N} = 0.3 \log_{10} N$ is not constant in cycle space. Thus the gain in computational efficiency depends on the computed number of cycles. For high-cycle fatigue with a typical cycle number of $N = 10^5$, or $\overline{N} = 5$, respectively, the necessary number of cycle steps is $N^{\text{necess}}_{\triangle N} = 8 \times 10^5$. The number of necessary steps in logarithmic cycle space is 17. This is a speed-up by a factor of 4.7×10^5 or 4.7×10^4 in comparison

with the cycle-scale model and the time-scale model, respectively.
Even though the reformulation of the material model in logarithmic cycle scale comes with a significant computational speed up, the approximations made in the derivation of the evolution equations do not account for the material evolution in the first few cycles of the material under fatigue loading. As a remedy, consider an approach which combines the accuracy of the time-scale model with the computational efficiency of the model in logarithmic cycle space. In this combined approach, to which we will refer as Hybrid Log-Cycle model (HLC) in the following, the first few cycles N_0 are computed explicitly in time scale. The damage field at the last cycle computed in time scale is then used as the initial condition for the logarithmic cycle-scale model. Hence, the rapidly changing damage evolution behavior in the initial phase can be accounted for, while the computational efficiency remains reasonable at large cycles.
In Fig. 5.4(a), the HLC-approach is investigated for different cycle numbers computed in time scale N_0. Here, the parameter $q_0 = 10$ is chosen. For reference, the corresponding damage evolution computed in time scale is plotted in black. We observe that, for increasing number of computed cycles in time space N_0, the deviation between the HLC and the time-scale evolution becomes smaller. Indeed, while, for

Property	value	unit
Second order fiber-orientation tensor	$\begin{bmatrix} 0.77 & 0 & 0 \\ 0 & 0.21 & 0 \\ 0 & 0 & 0.02 \end{bmatrix}$	-
Fiber length	300	μm
Fiber diameter	13	μm
Voxel length	2.5	μm
Fiber-volume content	17.8	%
Size	128^3	-

Table 5.1.: Geometric properties of the generic fiber structure

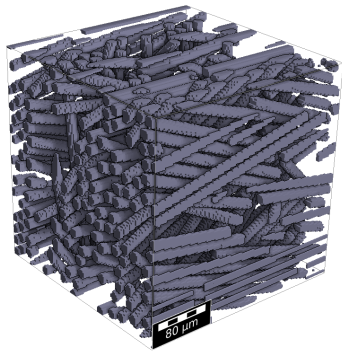

Figure 5.5.: Generic structure

$N_0 = 3$ and $N_0 = 6$, the deviations between the two approaches are still noticeably large, the deviation between HLC and time-scale model for $N_0 = 10$ is barely visible. For $N_0 = 10$, the deviations between the curves are reasonably small, i.e., the relative deviation at $N = 10^3$ is 0.46%.
Arguing in the opposite direction is also possible, i.e., we asked ourselves the question whether there are suitable material parameters, such that the model parametrized in time and the log-cycle model with $D(\overline{N} = 0) = 0$ are reasonably close. This can indeed be done, but involves some tinkering. For $q_0 = 6.5$, a suitable agreement can be reached, see Fig. 5.4(b). More precisely, we observe that the damage evolution of the two models is

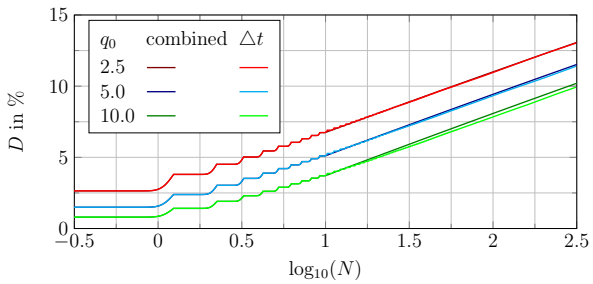

(a) Damage evolution for HLC-approach using $N_0 = 10$ at different values of q_0 vs. time-scale approach on generic structure

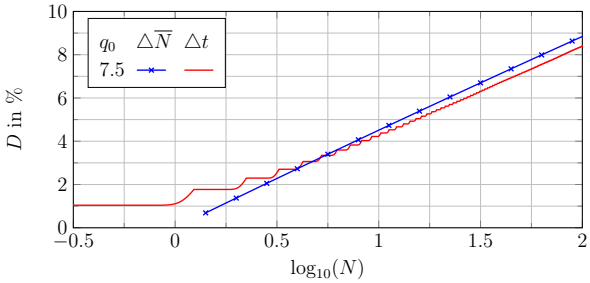

(b) Damage for the time-scale model with $q_0 = 7.5$ and the logarithmic cycle-scale model with $D(\overline{N} = 0) = 0$ for the generic structure

Figure 5.6.: Comparison of the damage evolution using time-scale, HLC and logarithmic cycle-scale approach for the generic structure

similar for cycles larger than 100. Indeed, the relative deviation of the damage value for both models at $\overline{N} = 2.5$ is 1.17%.

Last but not least, we study the model embedded in a multiscale framework, i.e., the effective strains emerging from a composite material with linear elastic fibers and a matrix material governed by the novel fatigue-damage model. Considering a microstructure, we assume that the stress field does not largely deteriorate during one loading cycle, i.e., that the change in the damage field during one cycle is small. If the structure is subjected to proportional loading within one cycle, i.e. $\sigma_{\mathrm{a}}(x,t) = \hat{\sigma}_{\mathrm{a}}(N,x)\bar{\sigma}_{\mathrm{a}}(\tau)$, the derivation of the Gauss-point equations can be extended to full field equations.

To study the emerging fields numerically, we make use of a "generic" fiber structure. The geometric properties of the microstructure are listed in Tab. 5.1. The structure is subjected to load-driven uniaxial sinusoidal tension with an amplitude of 60 MPa and a stress ratio of $R = 0$.

Similar to the pure matrix material, we compare the HLC and the time-scale computations for the generic structure in Fig. 5.6(a). Here, we chose $N_0 = 10$ for the HLC model. In Fig. 5.6(a), the maximum of the current damage field in the structure is plotted. The resulting deviation at $\overline{N} = 2.5$ is 0.28%, 0.96% and 2.62% for chosen $q_0 = 2.5$, $q_0 = 15.0$ and $q_0 = 10.0$, respectively.

In Fig. 5.6(b), we compare the evolution of the current maximum of the damage field in the generic structure for the time-scale model with $q_0 = 6.5$ to the logarithmic cycle-scale model with the initial condition $D(\overline{N} = 0) = 0$. Analogously to the computations on the pure matrix material, the deviation of the evolution damage is small, i.e., 1.55% at $\overline{N} = 2.5$.

To sum up, the formulation in logarithmic cycle space offers an extremely efficient way to compute the stiffness loss of a material subjected to stress ratios between -1 and 0. The N_0-dependent stiffness loss in the first few cycles can be accounted for by a combined time-cycle scale approach. For the remainder of the manuscript we chose to use $q_0 = 6.5$ instead, which corresponds to an initial condition $D(\overline{N} = 0) = 0$ as confirmed in the above numerical experiments. The load amplitude $\boldsymbol{\sigma}_a$ and maximum stress $\boldsymbol{\sigma}_{\max}$ enter the evolution equation via an effective stress

$$\boldsymbol{\sigma}_{\text{eff}} = \boldsymbol{\sigma}_{\text{a}}\sqrt{1+2c^2}, \tag{5.3.14}$$

where c is implicitly defined via $\boldsymbol{\sigma}_{\max} = (1+c)\boldsymbol{\sigma}_{\text{a}}$.
We conclude this section with a few remarks. For a start, the fatigue-damage model formulated in logarithmic cycle space resembles the model proposed in chapter 4, using the effective stress (5.3.14) instead of the maximum stress $\boldsymbol{\sigma}_{\max}$. In this work [231], the authors did not concern themselves with time-upscaling techniques but directly formulated the material model in the logarithmic time domain, motivated by experimental results shown in section 5.5.
With the time-scale formulation and the upscaling approach at hand, we are able to extend the model to different R-values in a straight-forward and consistent manner. Moreover, the model formulated in logarithmic cycle space, as discussed more thoroughly in chapter 4, can be viewed as generalized standard material (GSM) [17,246]. This perspective enables to recast the model in terms of an optimization problem.

5.4. Efficient computation of fiber-reinforced components

We are interested in the effective behavior of short-fiber reinforced composites. Consider a cubic cell $Y \subseteq \mathbb{R}^3$, on which a heterogeneous field of compliance tensors $Y \ni x \mapsto \mathbb{S}_0(x)$ and a characteristic function $\xi : Y \longrightarrow \{0,1\}$ are given. The latter describes the material distribution at every point $x \in Y$, i.e., $\xi^{-1}(1)$ is the domain of the matrix material and $\xi^{-1}(0)$ the domain of the fiber material.
We seek a displacement fluctuation field $u(x)$, a strain field $\boldsymbol{\varepsilon}(x)$, a stress field $\boldsymbol{\sigma}(x)$ and a damage field $D(x)$ solving the balance of linear momentum

$$\operatorname{div} \boldsymbol{\sigma}(\overline{N}) = 0, \tag{5.4.1}$$

where we suppress the dependence on x, the kinematic compatibility condition

$$\varepsilon(\overline{N}) = \left\langle \varepsilon(\overline{N}) \right\rangle_Y + \nabla^{\mathrm{s}} \mathbf{u}(\overline{N}), \tag{5.4.2}$$

the constitutive equation formulated in a stress-explicit manner

$$\boldsymbol{\varepsilon}(\overline{N}) = \xi(1 + D(\overline{N}))\, \mathbb{S}_0 : \boldsymbol{\sigma}(\overline{N}) + (1 - \xi)\, \mathbb{S}_0 : \boldsymbol{\sigma}(\overline{N}) \tag{5.4.3}$$

and the evolution of the internal variable $D(\overline{N})$

$$D' = \frac{\alpha}{2}\, \boldsymbol{\sigma}(\overline{N}) : \mathbb{S}_0 : \boldsymbol{\sigma}(\overline{N}), \tag{5.4.4}$$

prescribing an effective stress $\overline{\boldsymbol{\sigma}}_{\mathrm{eff}}(\overline{N})$

$$\langle \boldsymbol{\sigma} \rangle_Y (\overline{N}) = \overline{\boldsymbol{\sigma}}_{\mathrm{eff}}(\overline{N}) = \sqrt{\frac{1}{2} + c^2}\, \overline{\boldsymbol{\sigma}}_{\mathrm{a}}(\overline{N}), \tag{5.4.5}$$

where $\langle . \rangle_Y$ stands for averaging over the cell Y. $\boldsymbol{\Sigma}_{\mathrm{a}}$ refers to the stress amplitude tensor. Discretizing the time-like variable $\overline{N}$ recovers the (mixed) variational principle of chapter 4

$$S(\boldsymbol{\sigma}, D) \longrightarrow \min_{D \geq D_-} \max_{\substack{\operatorname{div} \boldsymbol{\sigma} = 0 \\ \langle \boldsymbol{\sigma} \rangle_Y = \overline{\boldsymbol{\sigma}}}}, \tag{5.4.6}$$

where we replaced the prescribed stress amplitude $\overline{\boldsymbol{\sigma}}$ in the previous formulation by the effective stress $\overline{\boldsymbol{\sigma}}_{\mathrm{eff}}$ in terms of the saddle-point function

$$S\left(\boldsymbol{\sigma}, D\right) = \left\langle -\xi \frac{(1+D)}{2}\, \boldsymbol{\sigma} : \mathbb{S}_0 : \boldsymbol{\sigma} + \xi \frac{1}{2\alpha \triangle \overline{N}} \left(D - D^n\right)^2 + (1-\xi) \frac{1}{2} \boldsymbol{\sigma} : \mathbb{S}_0 : \boldsymbol{\sigma} \right\rangle_Y \tag{5.4.7}$$

with $D^n = D(\overline{N}^n)$ at the previous time increment.

To compute the effective behavior of the material on component scale, we follow the model-order reduction strategy proposed in chapter 4. Indeed, to use the framework for arbitrary R-values, we only need to adjust the macroscopic effective stress $\overline{\boldsymbol{\sigma}}_{\mathrm{eff}}$ according to equation (5.3.11). In other words, a material database trained with a certain load amplitude and R-value can be used to compute the material behavior for different amplitudes and stress ratios by applying a modified effective stress to the material on the macroscale. As discussed in section 5.3, in some cases, like an arbitrary choice of N_0, the user might be interested in a combined time-cycle-scale approach. As stated in section 5.3, for the manuscript at hand, we will stick to the logarithmic cycle-scale model with $q_0 = 7.5$.

5.5. Comparison to experimental data

We demonstrate the capability of the model to reproduce the stiffness degradation in short-fiber reinforced components by comparing the model predictions to experimental data of reinforced PA polyamide 6.6.
First, we discuss the material characterization process and the experimental setup. Subsequently, we discuss the numerical material-characterization procedure. Finally, we compare numerical predictions and experimental results for the proposed model at different load scenarios, stress ratios and fiber orientations.

5.5.1. Experimental setup and parameter identification

Fatigue experiments for specimens with different fiber orientations, geometries, load amplitudes and stress ratios were performed.
The material is a commercial polyamide 6.6 reinforced by 35 wt% short E-glass fibers. The material properties of the constituents are listed in Tab. 5.2.

Property	Matrix	Fiber
Young's modulus	3.35 GPa	72.0 GPa
Poisson's ratio	0.38	0.22
Damage parameter α	0.1 1/MPa	–

Table 5.2.: Mechanical properties of the constituents

The specimens were milled from an injection-molded plate with dimensions $80 \times 80 \times 2\ \mathrm{mm}^3$. For more details about the injection-molding process, we refer to Hessman et al. [247, Fig. 1]. Depending on the orientation of the specimen length w.r.t. the injection direction of the thermoplastic material, we refer to the specimens as 0°-oriented and 90°-oriented [247]. Due to the injection-molding process, the specimens show a characteristic fiber structure forming layers of different local fiber orientations. To obtain the fiber-orientation distribution over the depth of the specimen, a control volume was cut from the center of the plate. Subsequently, the volume was characterized via X-ray microcomputed tomography (μCT) and the fiber-segmentation algorithm introduced by Hessman et al. [224].
We performed fatigue experiments on three different specimen geometries, shown in Fig. 5.7. The different geometries differ by the radius of the notch. The first specimen is devoid of notches. We refer to it as specimen A in the further discussion. Specimen B is a mildly notched specimen with a notch radius of 2 mm. The third geometry with a notch radius of 0.05 mm is the most sharply notched considered for the presented experiments.

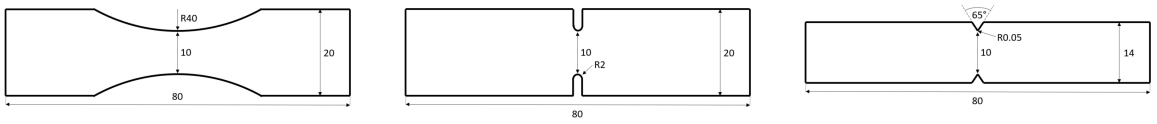

(a) Unnotched: specimen A (b) Mild notch: specimen B (c) Sharp notch: specimen C

Figure 5.7.: Test geometries subjected to cyclic loading

We refer to it as specimen C.

The specimens were subjected to sinusoidal stress-driven loadings at different amplitudes σ_a for the stress ratios $R = 0$ and $R = -1$. For stress ratios of $R = -1$, a buckling column was employed to avoid buckling of the specimens during fatigue testing. The strains were measured at the surface of the fatigue specimens, with an extensiometer of a reference length $l_0 = 20$ mm for all experiments with stress ratios values of $R = 0$ and an extensiometer of a reference length $l_0 = 5$ mm for all experiments with stress-ratio values of $R = -1$. The frequencies in the experiments ranged between $0.5 - 5$ Hz and were selected to ensure that the temperature changes at the specimen surfaces remain below 2 K.

We are interested in the loss of the dynamic stiffness of the material under fatigue loading. Thus, we recorded the maximum strain $\varepsilon_{\max}$ and the minimum strain $\varepsilon_{\min}$ for every (reported) cycle. The dynamic stiffness of the specimen is then calculated by

$$E_{\text{dyn}} = \frac{\sigma_{\max} - \sigma_{\min}}{\varepsilon_{\max} - \varepsilon_{\min}}. \tag{5.5.1}$$

The evolution of the dynamic Young's modulus for specimens oriented in 0°- as well as 90°-direction and for stress ratios of $R = 0$ is shown in Fig. 5.8. The experiments were conducted at different stress amplitudes σ_a. We observe that the dynamic stiffness of the specimen decreases over the load history. The higher the load amplitude applied to the specimen, the faster is the degradation process. They show a stable regime of stiffness degradation up to 10^3-10^6 cycles depending on the loading amplitude. Subsequent to this stable regime, the specimens enter a regime of unstable failure. This regime is characterized by massive fluctuations in the measured specimen as the strain extensiometer may be distorted and a steep decent in the stiffness. To gain a more thorough understanding of the available data, a linear function of the form

$$E_{\text{dyn}}(\overline{N}) = E^0_{\text{dyn}} - k\,\overline{N} \tag{5.5.2}$$

is used to model the data, where E^0_{dyn} represents the initial dynamic Young's modulus of the specimen at $\overline{N} = 0$ and the parameter k characterizes the speed of the stiffness degradation. For each individual stiffness evolution curve, the parameters of the model

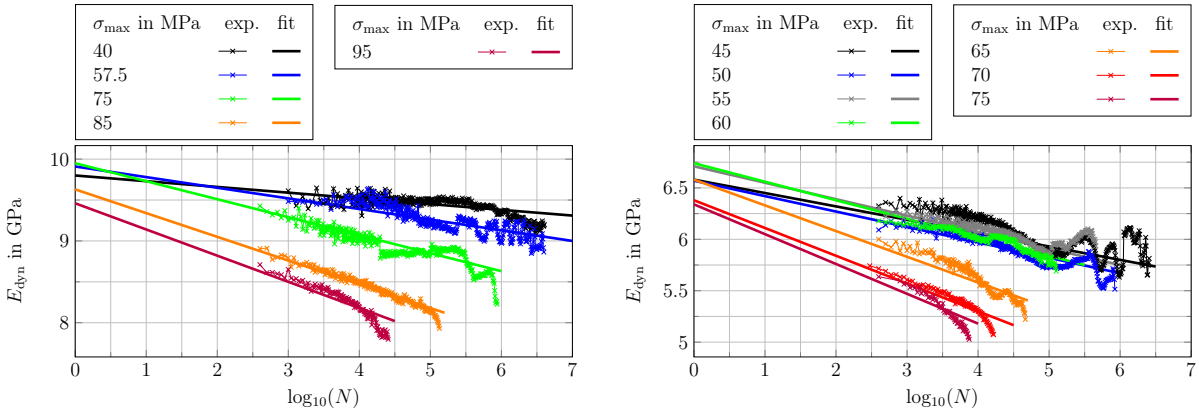

(a) Specimen 0°-oriented (b) Specimen 90°-oriented

Figure 5.8.: Evolution of the dynamic Young's modulus E_{dyn} for specimen A and $R = 0$, fitted to the model function $E_{\mathrm{dyn}}(\overline{N}) = E^0_{\mathrm{dyn}} - k\,\overline{N}$

function (5.5.2) were identified via linear regression. The resulting fits are displayed in Fig. 5.8. We observe a profound scattering of the initial Young's modulus E^0_{dyn}. For measurements on 90°-oriented specimens, this effect is even more pronounced than for the measurements of the 0°-oriented specimens, and is of the order of 5%.

The parameters k and E^0_{dyn} are plotted in Fig. 5.9. The initial stiffness E^0_{dyn} for 0°-oriented specimens scatters between 9.95 MPa and 9.46 MPa, which is a relative deviation of 5.2%. For the 90°-oriented specimens, the values of E^0_{dyn} lie between 6.74 MPa and 6.34 MPa, which is a relative deviation of 6.3%. The initial stiffness E_0 seems to decrease with the applied loading amplitude. There are several reasons for this rather surprising behavior. First, thermoplastics are well-known to be viscoelastic in nature. The experiments at different stress amplitudes are also performed at different frequencies. This is due to an optimization between time expense of the experiment and a restriction of the self-heating of the material. Thus higher amplitudes are driven with lower frequencies and their measured dynamic modulus appears to be higher. Another possible explanation is fiber breakage during the first loading cycle. However, the stiffness *decrease*, represented by the parameter k, seems to be fairly reproducible. Indeed, plotting k over the stress maximum $\sigma_{\max}$ for the 0°-specimens and 90°-oriented specimens in Fig. 5.9(b), k roughly follows a quadratic trend.

We conclude that there is a significant statistical scattering in the dynamic stiffness. This might be due to the underlying random microstructure obtained from the injection modeling. In particular the initial dynamic stiffness of the specimens shows significant variation. However, when focusing on the relative stiffness degradation, the decrease under fatigue-loading seems to be quite reproducible. In the work at hand, we do not concern

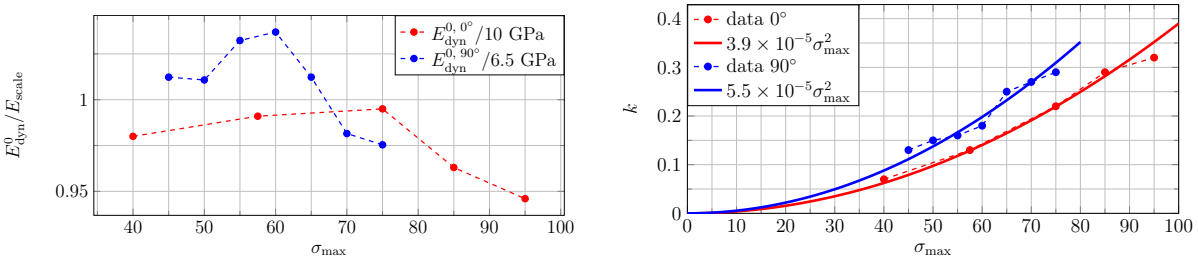

(a) Parameter E_0 (b) Parameter k

Figure 5.9.: Parameters obtained by fitting to the model function (5.5.2)

ourselves with the modeling of statistical fluctuations of the initial specimen stiffness. Rather, we focus on the fatigue-damage effects on the material. We thus normalize all experimental data with the use of the model function (5.5.2) and use the obtained data as our point of departure for fatigue-damage modeling.

To identify the material parameter α of the fatigue-damage model, the relative dynamic Young's modulus decrease of specimen A under loading with a stress ratio of $R = 0$ is used.

As shown in chapter 3 for a similar material model, the parameter α governing the damage evolution speed can be regarded as rescaling of the time scale

$$\frac{\mathrm{d}D}{\mathrm{d}\left(\rho\overline{N}\right)} = 2\frac{\alpha}{\rho}\boldsymbol{\sigma}_\mathrm{a} : \mathbb{S}_0 : \boldsymbol{\sigma}_\mathrm{a}\left(\frac{1}{2} + c^2\right). \tag{5.5.3}$$

For the identification of the material parameter α it is thus possible to compute a load case and adjust the damage evolution speed *afterwards* by rescaling the (pseudo) time $\overline{N}$. The results for an identified material parameter of $\alpha = 0.1$ 1/MPa are shown in Fig. 5.10. Note that only a single parameter for the matrix material is identified. Then, the material behavior of the composite material is fully identified.

The computed results for the composite material with different orientation states 0° and 90° show a good agreement with the experimental results. At different load amplitudes and material orientations, the degradation of the material in the steady fatigue-damage regime prior to failure can be reproduced.

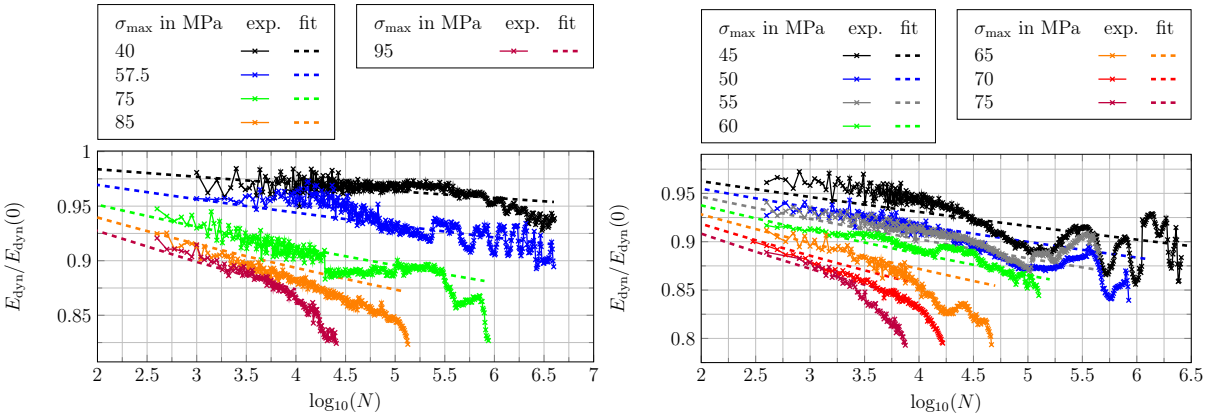

(a) Specimens 0°-oriented

(b) Specimens 90°-oriented

Figure 5.10.: Parameter identification for fatigue-damage model predictions using experimental data for $R = 0$ and specimen A with parameter $\alpha = 0.1$ 1/MPa

5.5.2. Numerical characterization of the material

To characterize the behavior of the short-fiber reinforced material we rely on computational homogenization. As discussed in section 5.4, we treat the matrix as a material undergoing damage. The short E-glass fibers are treated as an isotropic, purely elastic material.

With the fiber-orientation interpolation method [160] in mind, we solve the microscale problem discussed in section 5.4 using an FFT-based solution algorithm implemented in the software FeelMath [228] on a number of microstructures. The fiber structures are generated using the sequential addition and migration algorithm (SAM) [173] using the properties and spatial discretization listed in Tab. 5.3. We use the staggered grid discretization [54] in space and a nonlinear conjugate gradient method to reduce the strain residual suggested by Kabel et al. [249] below a tolerance of 10^{-5}. The framework of fiber-orientation interpolation [160] allows the engineer to fully characterize the material behavior of short-fiber reinforced composites with arbitrary fiber orientations using only a *finite* number of precomputations on the microstructures. The basic steps are the

Property	Value	Unit
Fiber length [248]	300	μm
Fiber diameter [248]	13	μm
Fiber aspect-ratio	23	-
Fiber-volume content	19.5	%
Minimum fiber distance	5	μm
Voxels per diameter	6.4	-
Cell length / Fiber length	2.6	

Table 5.3.: Properties of the generated microstructures

following.

1. Discretization of the space of possible fiber orientations $\{\mathcal{O}_i\}$.
2. Generation of fully-resolved fiber structures $\{Y_i\}$ for ever fiber-orientation $\{\mathcal{O}_i\}$.
3. Discretization of the space of possible load paths $\{\overline{\boldsymbol{\sigma}}_{\text{eff},j}\}$.
4. Precomputation of the material degradation on the fiber structures $\{Y_i\}$ under the load paths $\{\overline{\boldsymbol{\sigma}}_{\text{eff},j}\}$.
5. POD-analysis of the strain field paths for every structure Y_i and identification of system matrices for the reduced model for the fiber orientation $\mathcal{O}_i$.

The material behavior of an *arbitrary* microstructure characterized by its second-order fiber-orientation tensor [169] is then interpolated from three fiber orientations included in the set of precomputed structures which are closest to the unknown fiber-orientation state. For details we refer to Köbler et al. [160].

For this work, characterizing the PA6.6 material used in the experiments, we used the following parameters:

1. Equidistant triangulation of the fiber-orientation triangle with 15 fiber-orientation nodes as shown in Fig. 5.12(a).
2. Generation of the microstructures using the parameters given in Tab. 5.3.
3. Choice of six load cases: three pure extension (in x-, y- and z-direction, respectively) and three shear load cases (in the xy-, xz- and yz-planes, respectively) with a constant effective stress amplitude $\overline{\boldsymbol{\sigma}}_{\text{eff}}(\overline{N}) = 100$ MPa for $\overline{N} \in [0, 6]$.
4. Precomputation of the material degradation on the microstructures for the respective six load paths.
5. POD-analysis with ten snapshots per load path.

To quantify the accuracy of the used model-order reduction and interpolation strategy, we define a strain error measure

$$e^{\text{rom}} = \max_{N_i \in [0, N_{\text{steps}}]} \frac{\|\overline{\boldsymbol{\varepsilon}}_{\text{eff}}(\overline{N}_i) - \overline{\boldsymbol{\varepsilon}}^{\text{rom}}_{\text{eff}}(\overline{N}_i)\|}{\|\overline{\boldsymbol{\varepsilon}}_{\text{eff}}(\overline{N}_i)\|}, \tag{5.5.4}$$

where the number N_{steps} of considered load steps to compute the error is implicitly defined by

$$\|\overline{\boldsymbol{\varepsilon}}_{\text{eff}}(N_{\text{steps}})\| = 1.5\, \|\overline{\boldsymbol{\varepsilon}}_{\text{eff}}(0)\|. \tag{5.5.5}$$

Here, $\overline{\boldsymbol{\varepsilon}}_{\text{eff}}$ denotes the effective strain of the full-field solution and $\overline{\boldsymbol{\varepsilon}}^{\text{rom}}_{\text{eff}}$ refers to the effective strain of the reduced order model. The choice of this strain measure is motivated by the observation that the full field and the reduced order solution increasingly differ with increased cycle number, or damage respectively. In Fig. 5.11 the strain evolution of the full field solution for a fiber orientation tensor with eigenvalues $\lambda_1 = 0.903$, $\lambda_2 = 0.069$ to

its model order reduced (interpolated) evolution is shown. This case will be identified as the most critical one in terms of approximation in Fig. 5.12(b). The cycle at which the strain error is computed strongly influences the error magnitude. As fatigue experiments show that a stiffness decrease prior to fracture is in the order of a few ten percent, we consider the choice of (5.5.5), which roughly corresponds to a stiffness decrease of 33.3 %, to be sufficient.

We consider the load cases listed and labeled in Tab. 5.4. In the following, we use the error measure to quantify the errors introduced by the model-order reduction and by the fiber-orientation interpolation for these load cases.

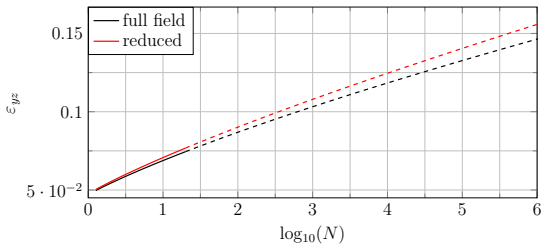

Figure 5.11.: Evolution of ε_{yz} in fiber structure with $\lambda_1 = 0.903$, $\lambda_2 = 0.069$ with $N < N_{\text{step}}$ (solid) and $N > N_{\text{step}}$ (dashed)

load case	$\overline{\boldsymbol{\sigma}}^{\text{eff}}_{xx}$	$\overline{\boldsymbol{\sigma}}^{\text{eff}}_{yy}$	$\overline{\boldsymbol{\sigma}}^{\text{eff}}_{zz}$	$\overline{\boldsymbol{\sigma}}^{\text{eff}}_{xy}$	$\overline{\boldsymbol{\sigma}}^{\text{eff}}_{xz}$	$\overline{\boldsymbol{\sigma}}^{\text{max}}_{yz}$
# 1	σ^{u}	0	0	0	0	0
# 2	0	σ^{u}	0	0	0	0
# 3	0	0	σ^{u}	0	0	0
# 4	0	0	0	σ^{u}	0	0
# 5	0	0	0	0	σ^{u}	0
# 6	0	0	0	0	0	σ^{u}

Table 5.4.: Tensor components of the effective stress for precomputed load cases used in the database generation with training amplitude $\sigma^{\text{u}} = 100$ MPa

First, we study the error introduced by the model-order reduction approach. In Fig. 5.12(a), the strain error measure is shown for every microstructure included in the training set (15 points of the fiber orientation triangle) and every training load case (lc) 1-6. For each of them, the strain error measure (5.5.4) is plotted for the reduced order model incorporating 15 strain and 15 damage modes. The error is well below 0.1% for all structures and load cases studied.

Secondly, we compare the predictions of the reduced order model interpolated to the centroids of the fiber orientation triangle to the full-field solution on microstructures directly generated and computed for the orientations at the elements' centroids. The arising error is a sum of errors due to the randomness of the statistical volume element, the model-order reduction and the interpolation approach. The error remains below 3% for all studied structures and load cases and is thus considered to be acceptable for the remainder of the manuscript.

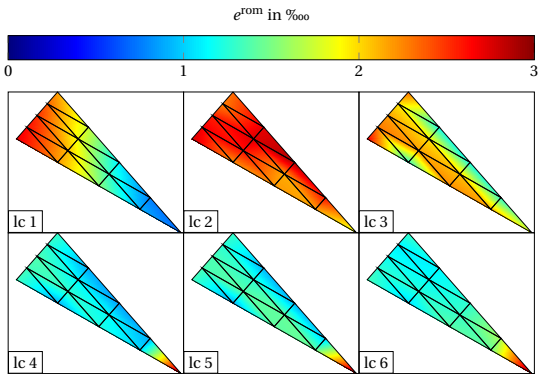

(a) Strain error (5.5.4) at precomputed microstructures

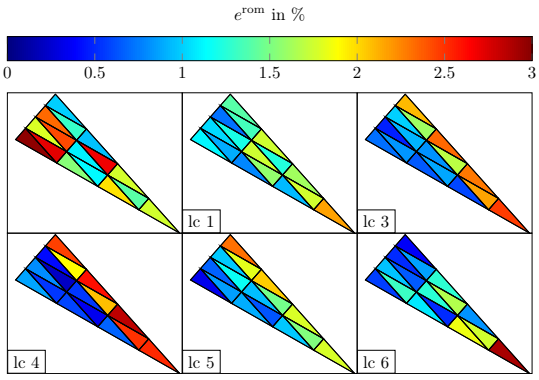

(b) Strain error (5.5.4) at interpolated microstructures

Figure 5.12.: Accuracy of model-order reduction and fiber interpolation for the considered load cases (lc)

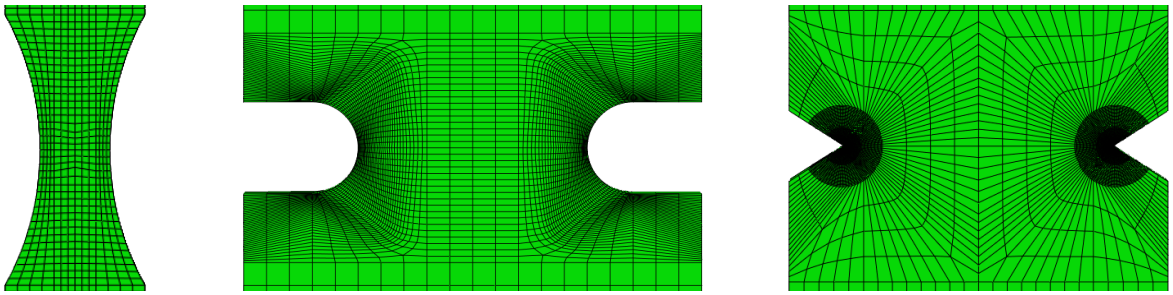

(a) Specimen A (b) Specimen B (c) Specimen C

Figure 5.13.: Reference discretization h

5.5.3. Comparison of numerical predictions to experimental data

To compute the fatigue damage in the specimens A-C (see Fig. 5.7), we use a finite element discretization with isoparametric, trilinear eight-node brick elements in space and an implicit Euler scheme for time integration. The layered fiber-orientation distribution in the specimens obtained from a μCT-scan analysis is used to determine the fiber-orientation distribution over the thickness of the specimens. We use a resolution of nine elements in thickness direction and assign an individual fiber-orientation according to the measurements to each of these layers.

The computations on the macroscale were performed with the commercial finite element software Abaqus [250]. To ensure accurate computations, we study the dependence of two computed properties on the mesh spacing. The specimen stiffness $E_{\text{spec}}(\overline{N})$ is computed as a function of the logarithmic cycle scale $\overline{N}$. Here, the contact points of the strain gauge u_0

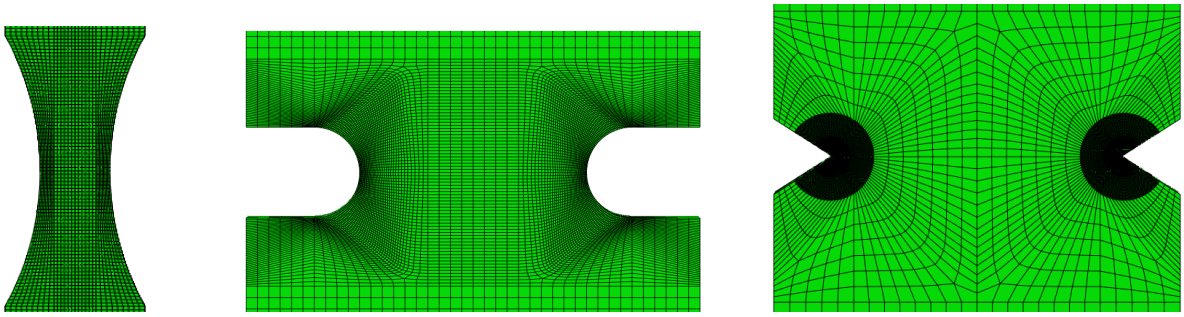

(a) Specimen A (b) Specimen B (c) Specimen C

Figure 5.14.: Refined discretization $h/2$

and u_1 with a reference length of l_0 in the experiments were chosen as measurement points for the displacement which determines the specimen stiffness

$$E_{\text{spec}} = l_0 \frac{F}{A_{\text{undef}}\,(u_0 - u_1)}, \tag{5.5.6}$$

where F is the extensional force and A_{undef} is the cross-sectional area of the undeformed specimen. Secondly, we define a fatigue-damage indicator Λ, which is a local quantity, depending implicitly on the geometry of the notch under consideration. This quantity is computed from the determinant of the acoustic tensor A^{aco} [169] via

$$\Lambda(\overline{N}) = \max_{\|\mathbf{n}\|=1} \left[1 - \frac{\det A^{\text{aco}}(\mathbf{n}, \mathbb{C}(\overline{N}))}{\det A^{\text{aco}}(\mathbf{n}, \mathbb{C}(0))}\right]. \tag{5.5.7}$$

We evaluate the fatigue-damage indicator $\Lambda(\overline{N})$ at the point of maximum damage and plot and study the evolution of this local property.

The reference meshes and the refined meshes of the three geometries are shown in Fig. 5.13 and Fig. 5.14, respectively. Notice, that the resulting element sizes in both meshes at the notch are smaller than the RVE. We chose the element size to accurately resolve the stress gradient. Thus, scale separation is presumingly violated and the averaged stiffness of the computed composite material may not be applicable. In fact, the exact position and orientation of a *single* fiber close to notch may influence the damage evolution of the specimen greatly. The model at hand can not account for these effects. However, we chose the element size to resolve the stress gradient at the notch.

Both, the specimen stiffness E_{spec} and the fatigue-damage indicator Λ in the notch root, are compared for both meshes in Fig 5.15. In the considered load cases, the location of maximal damaged point is not moving. Thus, the location at which the fatigue damage indicator Λ is plotted remains constant throughout the cycle evolution in Fig. 5.15(b). Note that under different loading conditions the point of maximum damage must not

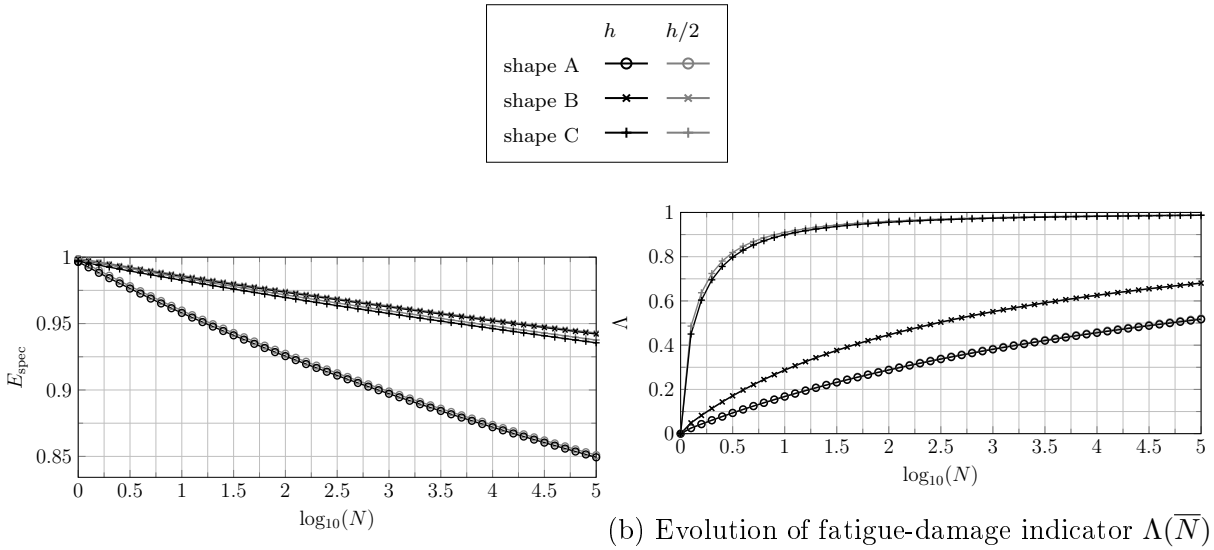

(a) Evolution of the specimen stiffness $E_{\text{spec}}(\overline{N})$

(b) Evolution of fatigue-damage indicator $\Lambda(\overline{N})$ in the notch root

Figure 5.15.: Resolution study for different specimens

necessarily remain at the same location due to stress redistribution. The specimens A, B, and C were subjected to an effective stress $\sigma_{\text{eff}} = F/A_{\text{undef}} = 82.3$ MPa, $\sigma_{\text{eff}} = 65.0$ MPa and $\sigma_{\text{eff}} = 52.0$ MPa, respectively. For all three specimens and both the integral quantity E_{spec} and the local field quantity Λ,
the deviations due to the different meshes are rather small. More specifically, using the relative error measures

$$e^{E}_{\text{rel}}(\overline{N}) = 2\frac{\|E^{h}_{\text{spec}} - E^{h/2}_{\text{spec}}\|}{\|E^{h}_{\text{spec}} + E^{h/2}_{\text{spec}}\|}, \tag{5.5.8}$$

$$e^{\Lambda}_{\text{rel}}(\overline{N}) = 2\frac{\|\Lambda^{h} - \Lambda^{h/2}\|}{\|\Lambda^{h} + \Lambda^{h/2}\|}, \tag{5.5.9}$$

Specimen	error in stiffness	error in Λ
A	0.19 %	0.73 %
B	0.09 %	0.39 %
C	0.27 %	0.17 %

Table 5.5.: Relative errors of the resolution study at $\overline{N} = 5$

the deviations at $\overline{N} = 5$ for the specimen stiffness E_{spec} and the fatigue-damage indicator Λ in the notch root are given in Tab. 5.5. All of the relative errors are well below 1%. Thus, the coarser mesh of the two is fixed for the remainder of the script.
To gain a deeper understanding of the emerging damage fields, the fatigue indicator Λ is plotted in Fig. 5.16. We consider the 0°-oriented specimens subjected to effective stresses $\sigma_{\text{eff}} = 82.3$ MPa, $\sigma_{\text{eff}} = 65.0$ MPa and $\sigma_{\text{eff}} = 52.0$ MPa for specimen A, B and C, respectively, at $\overline{N} = 5$. With increasing sharpness of the notch, the damage values at the notch increase as well. In contrast, the center of the specimen shows little damage. This observation does not come unexpected, as the stress peak in the notch drives the damage field via the evolution equation $\dot{D} = \alpha\, \boldsymbol{\sigma} : \mathbb{S}_0 : \boldsymbol{\sigma}$.
Due to the layered fiber-structure in the specimens, the fatigue-damage evolves non-uniformly over the specimen depth. In Fig. 5.17 the fatigue-damage is plotted for the

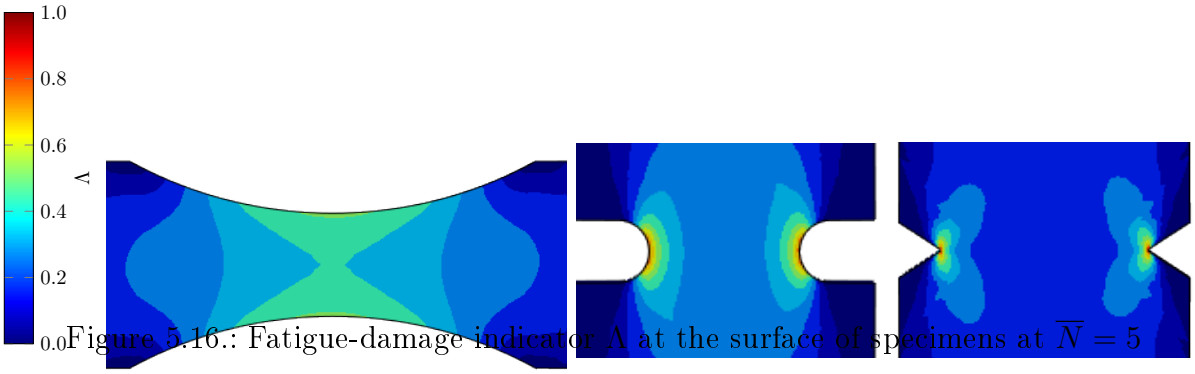

Figure 5.16.: Fatigue-damage indicator Λ at the surface of specimens at $\overline{N} = 5$

(a) Specimen A (b) Specimen B (c) Specimen C

0°- and 90°-oriented specimen A. The loading cases are 47.5 MPa, $R = 0$ and 37.5 MPa, $R = 0$ at $N = 10^7$, respectively. We observe, that the maximum fatigue-damage in the 0°-oriented specimens can be found in the surface layer, while the maximum fatigue-damage in the 90°-specimen is predicted in the center layer. This is due to the underlying microstructure: the maximum fatigue damage is predicted in the fiber layer, in which the most fibers are oriented in the loading direction. In the 0°-oriented specimen, the fibers in the approximately uniform outer fiber layers point in loading direction. In the 90°-oriented specimen these fibers point in the direction perpendicular to the loading direction. Thus for 90°-oriented specimens the appoximately isotropic center layer is the layer with the most fibers pointing in loading direction.

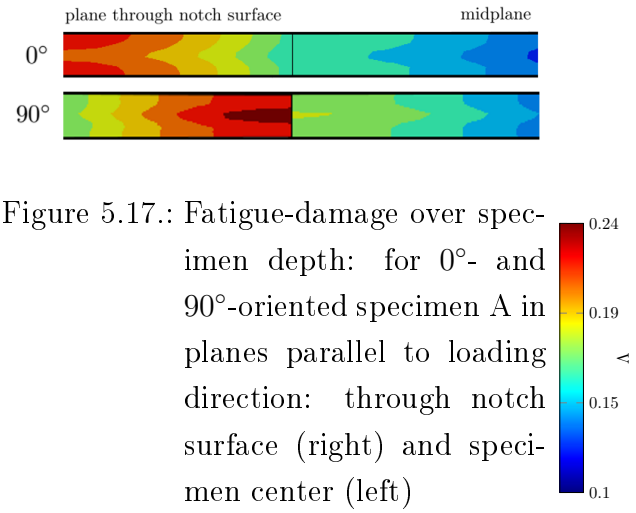

Figure 5.17.: Fatigue-damage over specimen depth: for 0°- and 90°-oriented specimen A in planes parallel to loading direction: through notch surface (right) and specimen center (left)

After these prestudies, we turn our attention to comparing the model predictions to experimental data. We first discuss the results for stress ratios of $R = -1$ for the unnotched specimen A. Experimental data and numerical predictions for specimens with fiber orientations of 0° and 90° are plotted in Fig. 5.18. For the 0°-oriented specimens shown in Fig. 5.18(a), we observe a long and stable degradation phase of the material, which is roughly linear in logarithmic cycle space. For increasing loading amplitudes, i.e, for amplitudes $\sigma_{\max}$ larger than 72 MPa, we additionally observe a secondary fatigue-damage process with a more rapid decrease in the dynamic stiffness. This regime might be due to localizing fatigue cracks in the matrix, which we do not account for in the damage model at hand. The slope of the curve prior to this localizing regime is reproduced by the fatigue-damage model quite accurately. Recall that we did

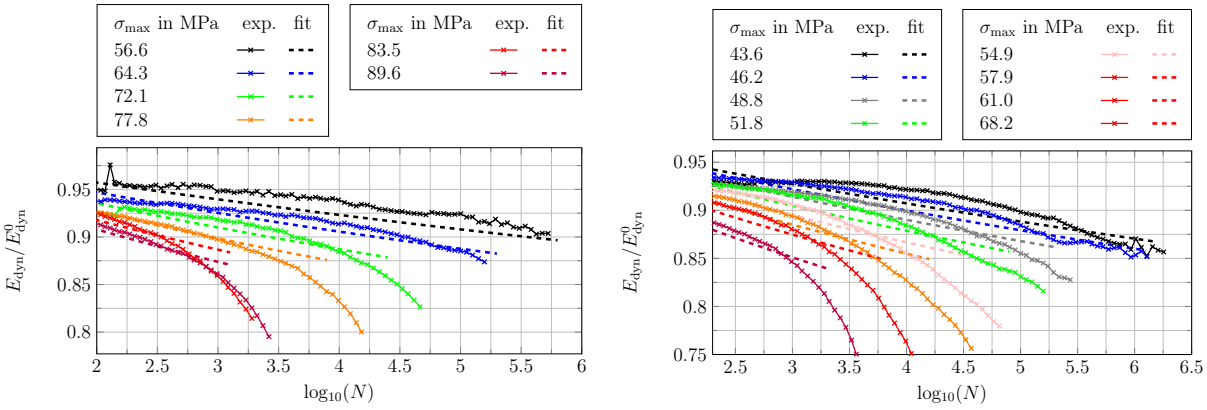

(a) 0°-oriented specimen

(b) 90°-oriented specimen

Figure 5.18.: Comparison of computational and experimental results for $R = -1$ and specimen A

not use the experimental data at $R = -1$ to identify material parameters, but rather solely rely on experimental data for $R = 0$ for parameter identification.

For the 90°-oriented specimen, see Fig. 5.18(b), the non-linearity of the degradation curve increases. Yet, the fatigue-damage model is able to reproduce the stress-amplitude dependency in the stiffness degradation $\overline{N} = 0.5$ prior to failure.

We proceed with the discussion of experimental and numerical predictions for specimen B, shown in Fig. 5.19. The stiffness degradation of the material under loadings with a stress ratio of $R = 0$ are less nonlinear in the experiments than the stiffness degradation of specimens under loadings with a stress ratio of $R = -1$, where some curves tend towards a quadratic degradation when approaching a regime close to failure. This observation is in accordance with the data from specimen A. The experiments for $R = 0$ and $R = -1$ were conducted on different machines. $R = 0$ experiments ran on an Hähnchen system, whereas $R = -1$ ran on a Schenk system. This circumstance might also be one reason for the differences in the measurements. However, when focusing on the fatigue-damage regime with a linear slope, the simple damage model captures the dependence on the orientation quite accurately. The largest deviations of the numerical predictions from the experimental data is found for experiments with $R = -1$ using 90°-oriented specimens at low stress amplitudes, shown in Fig. 5.19(d). In this setting, the experimental curves show a strongly non-linear behavior, which the numerical model does not reproduce. Yet, assuming that reproducing the linear trend in the data is of primary interest, the slope of the fatigue-damage model seems to be reasonable.

Finally, we compare experimental and computational predictions for the sharply notched specimen C in Fig. 5.20. The stiffness degradation for this specimen is in the range of

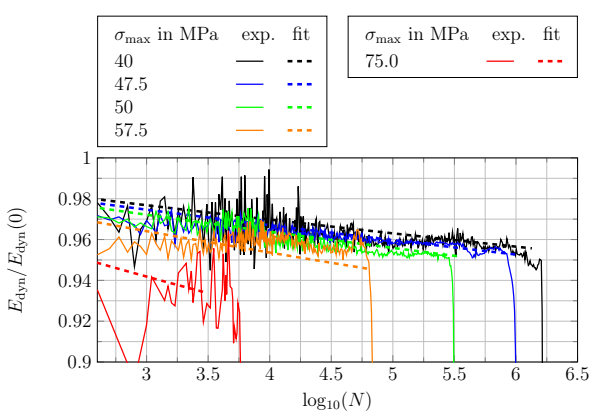

(a) 0°-oriented specimen, $R = 0$

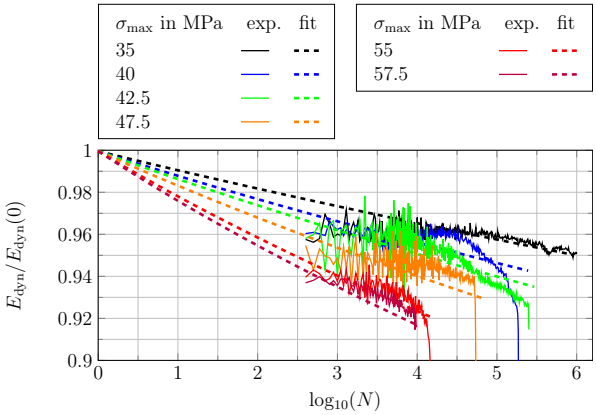

(b) 90°-oriented specimen, $R = 0$

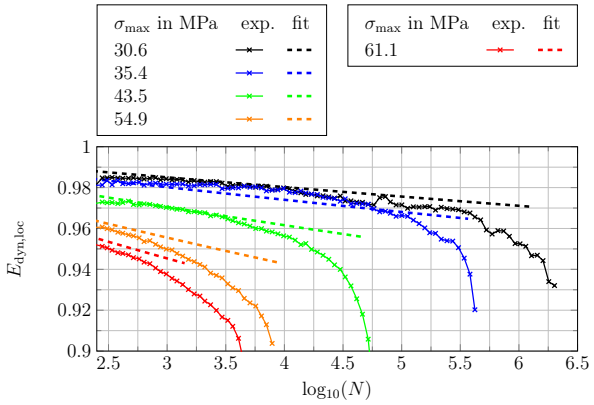

(c) 0°-oriented specimen, $R = -1$

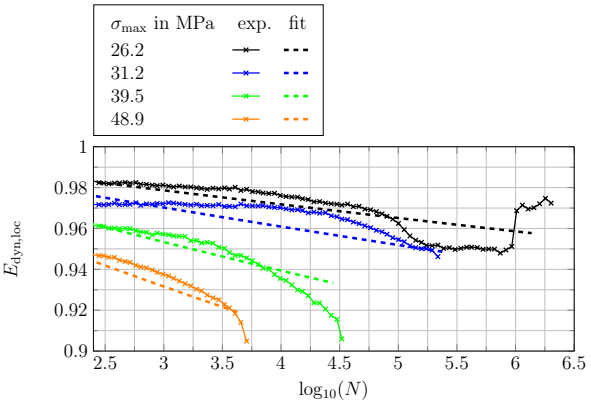

(d) 90°-oriented specimen, $R = -1$

Figure 5.19.: Comparison of computational and experimental results for specimen B

5%, which is half of the stiffness degradation observed in specimen B and about a quarter of the degradation observed in specimen A. This comes as no surprise, as the stress in the sharply notched specimen C is highly localized around the notch root. The majority of the part remains largely unaffected by fatigue damage. The overall stiffness degradation is thus smaller, yet noticeable. The linear fatigue-damage regime depending on R-value, orientation and stress amplitude is reproduced by the computational model with acceptable accuracy. The largest deviation observed when comparing experimental and numerical predictions for specimens C is found in the 0°-oriented, $R = -1$-stress valued experiment with a maximum stress $\sigma_{\max}$ of 54.4 MPa. The stiffness loss in the experiment at $\overline{N} = 2.5$ is 5.17%, while a stiffness loss of 3.78% is predicted, which is a relative error of 19.5%. All other load cases studied, prior to localization and failure, remain well below this deviation.

We conclude that the presented fatigue model is able to predict the stiffness loss in unnotched, mildly and sharply notched specimens subjected to stress amplitudes leading to fracture within the high cycle regime (10^3-10^6 cycles). The respective bearable load capacity depends on stress amplitude, stress ratio and orientation. Since the stress amplitude enters the damage evolution quadratically and is thus rather sensitive to its value, an extrapolation to other stress amplitudes should be handled with caution.

5.6. Conclusions

We proposed a special fatigue-damage model for the matrix material in short-fiber reinforced polymers formulated in time scale. This formulation enabled us to study the effect of fatigue damage during the first few cycles in detail. The proposed fatigue damage model is rather sensitive to the choice of parameters in the first few cycles, corresponding to the observation in experimental data that the dynamic modulus in the first few cycles scatters for different measurements. However, both material model and experimental data proved to be rather stable regarding the stiffness decrease in the high cycle regime.

To enable efficient computations in the high cycle regime, we proposed a cycle-jump technique building upon parametric loading curves. The parametrization of the loading curve enabled us to reformulate the model in terms of a cycle-scale and a logarithmic cycle-scale variable, respectively. Thus, the influence of load amplitude and mean stress can be consistently accounted for, while the computational efficiency is drastically increased compared to a pure time-scale based approach. The time-scale and cycle-scale models were

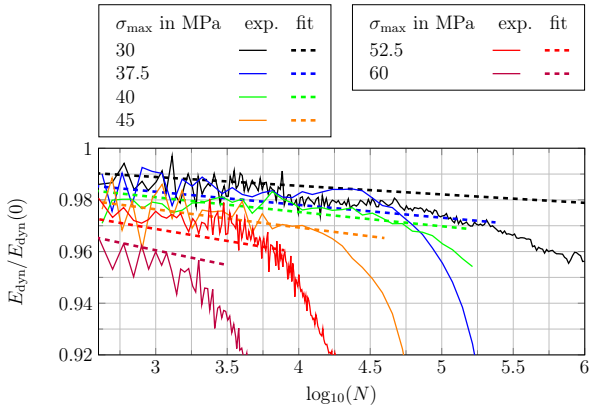

(a) 0°-oriented specimen, $R = 0$

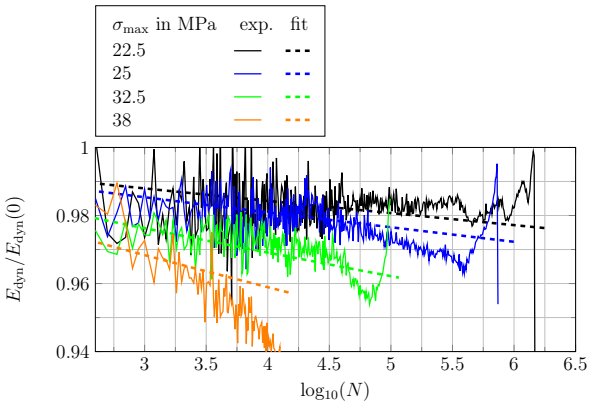

(b) 90°-oriented specimen, $R = 0$

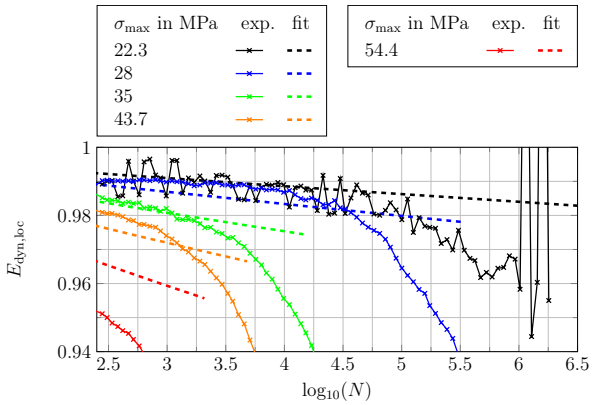

(c) 0°-oriented specimen, $R = -1$

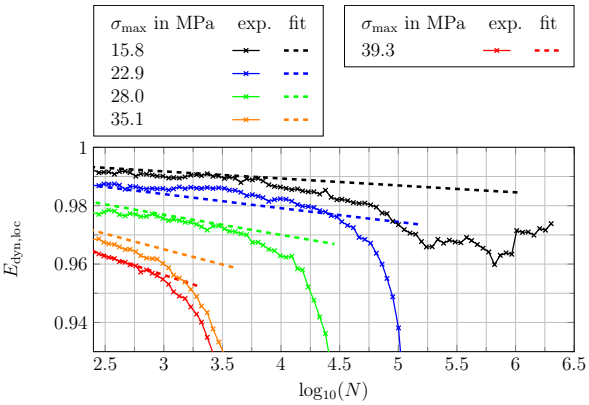

(d) 90°-oriented specimen, $R = -1$

Figure 5.20.: Comparison of computational and experimental results for specimen C

studied and compared thoroughly. A combined time and cycle-scale approach (HLC) is suggested to combine the accuracy of the time-scale model in the first few cycles with the computational efficiency of the cycle-scale model in the high cycle regime.
Subsequently, the method was applied to model the fatigue damage behavior of a short-fiber reinforced polyamide. The material evolution was studied for different stress amplitudes, stress ratios, orientations and geometries. Using the data from 0°-oriented and 90°-oriented specimens for stress ratios of $R = 0$ to calibrate the material parameter α, the material behavior at different orientations, stress ratios and geometries can be predicted with reasonable accuracy.
In subsequent work, the investigation of a failure criterion remains an open question. Additionally, the scattering of the initial dynamic stiffness should be investigated more thoroughly. With a suitable failure criterion at hand, combined with the statistical influence of the initial stiffness, the prediction of Wöhler curves for short-fiber reinforced components is possible.

6. Accounting for viscoelastic effects in a multiscale fatigue model for the degradation of the dynamic stiffness of short-fiber reinforced thermoplastics[1]

6.1. Introduction

In contrast to metals, polymer-based materials exhibit stiffness degradation under fatigue loading. This observation is the starting point of many damage materials in the fatigue literature [218, 251, 252]. They aim to model the material's degradation under cyclic loading based on measurements of the dynamic stiffness. At the same time, it is well-accepted in material science that polymers are viscoelastic in nature [253]. Thus, the observed dynamic stiffness of polymer-based materials depends on the loading frequency [103, 254]. In this chapter, we extend existing computational multiscale approaches for elastic fatigue-damage to viscoelasticity. We choose a linear viscoelastic material model and study its influence on the dynamic stiffness under cyclic loading conditions. Subsequently, we incorporate the most relevant effect, i.e., the frequency dependence at high cycles, into a fatigue-damage material model.

In section 6.2, we start by a systematical investigation of the influence of viscoelasticity on the dynamic modulus and its evolution in experiments. Under cyclic loading, we observe that the material reaches an asymptotic periodic orbit within a fairly low number

[1] Reproduced from: N. Magino, J. Köbler, H. Andrä, F. Welschinger, R. Müller, M. Schneider, "Accounting for viscoelastic effects in a multiscale fatigue model for the degradation of the dynamic stiffness of short-fiber reinforced thermoplastics," *Computational Mechanics*, vol. 71, pp. 493–515, 2023.

of cycles. Subsequently, we introduce a linear viscoelastic material model to describe the observed effects. For a linear viscoelastic material, the shape of the hysteresis curve at high cycles depends on the applied frequency, but does not evolve further. In contrast, fatigue-damage evolves at all stages of high-cycle fatigue. We thus propose to treat the two effects separately and utilize a two-step analysis of the current dynamic stiffness that is both accurate *and* efficient. In a first step, we discuss how to compute the dynamic stiffness for the periodic orbit, i.e., the asymptotic dynamic stiffness of the undamaged material (section 6.3). In a second step, we integrate the obtained fixed-point stiffness into a cycle-based fatigue-damage model (section 6.4).
In section 6.3, we discuss an elastic model with complex-valued stiffness [255, 256] to compute the periodic orbit for cyclic loading of viscoelastic materials. We show that for components consisting of linear elastic materials and just *one* viscoelastic constituent with a small phase shift, a *real-valued* scheme is sufficient to approximate the materials dynamic stiffness. Thus, for short-fiber reinforced thermoplastics with elastic fibers, a real-valued scheme is applicable.
In section 6.4, based on the derived real-valued elastic scheme, we propose an approach to integrate the frequency-dependence of the dynamic stiffness into existing fatigue-damage models. The method modifies the undamaged stiffness according to the current applied frequency. Apart from a simple precomputation of the effective matrix properties dependent on the current frequency, there is no need for any increase in the computational effort when going from an elastic-damage to a viscoelastic-damage model. We demonstrate the capability of the model to reproduce experimental results in a validation step.

6.2. On the dynamic modulus

6.2.1. In fatigue experiments

Polymer materials degrade under cyclic loading. To characterize the evolving fatigue damage in experiments, multiple quantities may be monitored. Apart from self-heating [257, 258], the most common approach is an analysis of the strain-stress hysteresis at the current cycle. As scalar measures of the hysteresis curves, stiffness measures are widely used in literature. They may be chosen in different ways, e.g., the slope of the curve close to the point of reversal. One of the most common choices is the dynamic modulus, defined

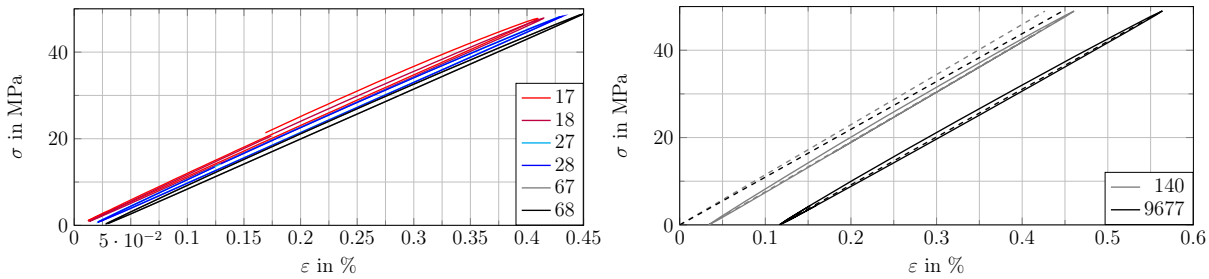

(a) Stress-strain curve at cycles 17, 18, 27, 28, 67 and 68

(b) Stress-strain curve at cycles 140 and 9677

Figure 6.1.: Evolution of the hysteresis of short-fiber reinforced PBT under fatigue loading

by

$$E_{\mathtt{dyn}} = \frac{\sigma_{\mathtt{max}} - \sigma_{\mathtt{min}}}{\varepsilon_{\mathtt{max}} - \varepsilon_{\mathtt{min}}}, \tag{6.2.1}$$

where $\sigma_{\mathtt{max}}$ and $\sigma_{\mathtt{min}}$ are the maximum and minimum stress level reached within the current hysteresis cycle, respectively. With $\varepsilon_{\mathtt{max}}$ and $\varepsilon_{\mathtt{min}}$, we refer to the maximum and minimum strain level within the same cycle. To understand the evolution of this quantity in polymer-based materials, we first investigate the evolution of the stress-strain hysteresis, which serves as the basis for the evaluation of the dynamic stiffness in experiments. Therefore, we subject a short-fiber reinforced PBT specimen to cyclic loading at constant stress amplitude and a stress ratio of $R = 0$, where

$$R = \frac{\sigma_{\mathtt{max}}}{\sigma_{\mathtt{min}}}. \tag{6.2.2}$$

The hysteresis curves and their evolution in the experiment are shown in Fig. 6.1. For the evolution of the hysteresis under fatigue loading, we observe two main effects: a shift of the hysteresis to larger strain values (creep) and a rotation of the hysteresis in the stress plane (damage).

The shift effect is especially pronounced in the first few cycles: in Fig. 6.1(a), we observe a visible shift of the hysteresis between cycle number 17 and 18. For higher cycle numbers, e.g., cycle number 27 and 28, the shift is barely noticeable. Additionally, we observe that the shift from 17 to 27 is of similar magnitude as the shift from 27 to 67 cycles. Thus, the shift effect decreases with increasing number of cycles.

The second observation is a rotation of the hysteresis. In Fig. 6.1(b), the hysteresis curves at cycle 140 and 9677 are compared. The dashed lines in gray and black indicate the slope of the two hysteresis curves. To simplify a comparison on a visual basis, we shifted both curves to zero. We observe that the slope of the hysteresis loops decreased under fatigue loading, i.e., the hysteresis loop was rotated clock-wise.

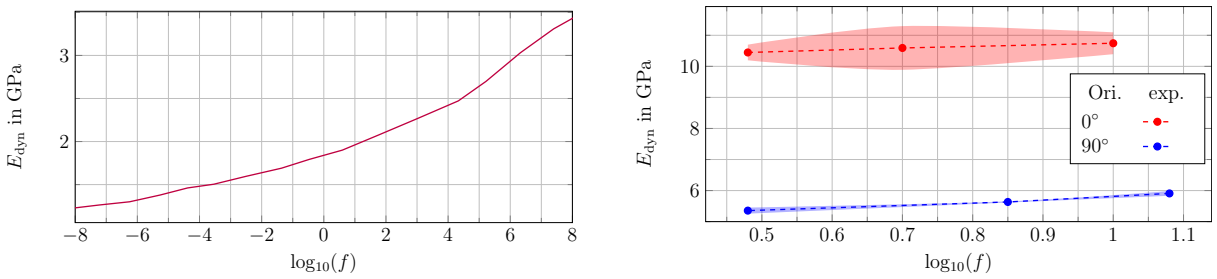

(a) PBT with 20 w.% glass-fiber reinforcements [254]

(b) Dynamic modulus at first few cycles in fatigue experiments

Figure 6.2.: Frequency dependence of short-fiber reinforced PBT

Another effect which we observe in fatigue experiments on short-fiber reinforced PBT is its frequency dependence. To realize the fatigue experiments in the shortest possible time, experiments at different loading amplitudes are often performed at different frequencies [121, 259] to avoid self-heating of the material at high loading amplitudes. The choice of a different frequency also influences the measured dynamic modulus. Goméz et al. [254] published experiments on short-fiber reinforced PBT, in which they characterized the dynamic stiffness at different frequencies. The dynamic modulus of PBT with 20 weight-% of reinforcements at 50.2° C is shown in Fig. 6.2(a). A clear increase of the material's dynamic modulus with increasing frequency is observed. Similarly, for short-fiber reinforced PBT at room temperature, we observe a dependence of the dynamic modulus on the loading frequency in fatigue experiments, see Fig. 6.2(b). The specimens used for fatigue testing were cut from injection molded plates parallel (0°) and perpendicular (90°) to the flow direction of the mold. For each of the load cases listed in Tab. 6.1, three specimens were tested. The semi-transparent bands around the data plotted in Fig. 6.2(b) mark the standard deviation of the experimental results. We observe, both for the 0°-oriented and the 90°-oriented specimens, that the load cases at higher frequencies exhibit a higher dynamic modulus. This is in accordance with the results from Gomez et al. [254].

Orientation	stress maximum	frequency
0°	60.0 MPa	10 Hz
	65.0 MPa	5 Hz
	70.0 MPa	3 Hz
90°	38.4 MPa	12 Hz
	42.8 MPa	7 Hz
	49.0 MPa	3 Hz

Table 6.1.: Realized load cases

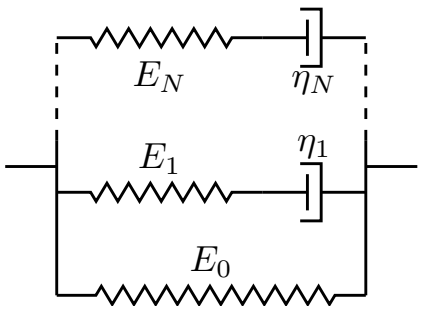

Figure 6.3.: Rheological model with N parallel Maxwell elements

The evaluated dynamic modulus is affected by all of the observed effects, i.e., shift of the strain hysteresis to higher strain values, rotation and frequency dependence. The effects originate from two material properties: viscoelasticity and damage. Viscoelastic behavior of the material is observed in the shift (creep) of the stress-strain hysteresis to higher strain values as well as the frequency dependence of dynamics modulus. Damage behavior is reflected in the clock-wise rotation of the stress-strain hysteresis with increasing load cycle. We investigate the consequences of a continuum mechanical model for linear viscoelasticity on the evaluated dynamic modulus in section 6.2.2.

6.2.2. In viscoelastic materials

To investigate the effect of a linear viscoelastic material model on the measured dynamic modulus, we assume that the material follows the behavior of a generalized Maxwell model [260, 261]. Its rheological model is schematically shown in Fig. 6.3.
The set of internal variables in this model consists of N viscoelastic strains $\boldsymbol{\varepsilon}^{\mathrm{v},j}$. In the context of generalized standard materials [17, 246], the generalized Maxwell model is defined via the free energy density

$$w\left(\boldsymbol{\varepsilon}, \boldsymbol{\varepsilon}^{\mathrm{v},1}, \ldots, \boldsymbol{\varepsilon}^{\mathrm{v},N}\right) = \frac{1}{2}\boldsymbol{\varepsilon} : \mathbb{C}_0 : \boldsymbol{\varepsilon} + \sum_{j=1}^{N} \frac{1}{2}\left(\boldsymbol{\varepsilon} - \boldsymbol{\varepsilon}^{\mathrm{v},j}\right) : \mathbb{C}_j : \left(\boldsymbol{\varepsilon} - \boldsymbol{\varepsilon}^{\mathrm{v},j}\right), \tag{6.2.3}$$

where $\mathbb{C}_j$ denotes the stiffness of the j-th Maxwell element, and the dissipation potential

$$\phi\left(\dot{\boldsymbol{\varepsilon}}^{\mathrm{v}}\right) = \frac{1}{2}\sum_{j=1}^{N} \dot{\boldsymbol{\varepsilon}}^{\mathrm{v},j} : \mathbb{D}_j : \dot{\boldsymbol{\varepsilon}}^{\mathrm{v},j}. \tag{6.2.4}$$

Here, $\mathbb{D}_j$ refers to the viscosity tensor of the j-th Maxwell element. We assume that both the stiffnesses and the viscosities are isotropic and their Poisson's ratios coincide in every element. Then, for a given function

$$\mathbb{K}(x) = \frac{x}{(1+x)\,(1-2\,x)}\,\mathbb{I}\otimes\mathbb{I} + \frac{x}{(1+x)}\,I^s \tag{6.2.5}$$

and a Young's modulus E_j, viscosity η_j and Poisson's ratio ν_j in every Maxwell element, we define the viscosity tensor

$$\mathbb{D}_j = \eta_j\,\mathbb{K}(\nu_j) \tag{6.2.6}$$

and the stiffness tensor

$$\mathbb{C}_j = E_j\,\mathbb{K}(\nu_j) \tag{6.2.7}$$

where $\mathbb{I}$ is the second-order identity tensor and I^s denotes the symmetric part of the fourth-order identity tensor. Additionally, we assume that

$$\nu_j = \nu \quad \text{for all } j \in \{0,\dots,N\}. \tag{6.2.8}$$

For concise notation, we define the time constant τ_j and its inverse β_j given by

$$\tau_j = \frac{\eta_j}{E_j} \quad \text{and} \quad \beta_j = \frac{E_j}{\eta_j} \tag{6.2.9}$$

for every Maxwell element.

To understand the evolution of the dynamic modulus for a generalized Maxwell model, we first investigate the one-dimensional case. We choose to use an example with $N = 1$ and the material constants $E_0 = 1$ GPa, $E_1 = 10$ GPa and $\eta_1 = 1$ GPa·s. We subject the material to loading at a constant stress amplitude of $\sigma_a = 30$ MPa, a stress ratio of $R = 0$ and a frequency of $f = 1$ Hz. The results are shown in Fig. 6.4. In the evolution of the stress-strain curve in Fig. 6.4(a), a shift of the hysteresis curve to higher strains is visible. As observed in the experiments discussed in section 6.2.1, the largest shift manifests in the first cycle and the magnitude of the shift decreases steadily with the number of cycles. When evaluating the dynamic modulus at every cycle, see Fig. 6.4(b), we observe a strong increase within the first few cycles. For cycles larger than ten, the material response reaches a steady state, i.e., the dynamic modulus approaches an asymptotic value. This observation is independent of the applied load amplitude and stress ratio. Indeed, in Fig. 6.5(a), we show the material subjected to cyclic extension at different stress amplitudes. We observe that the stress-strain curve approaches a periodic orbit, i.e., the difference between the hysteresis curves of two subsequent cycles become

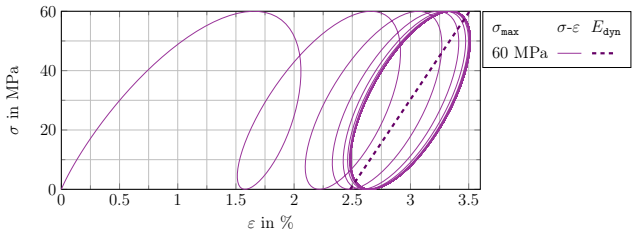

(a) Stress-strain evolution and dynamic modulus $E_{\mathtt{dyn}}$ at the sixth cycle

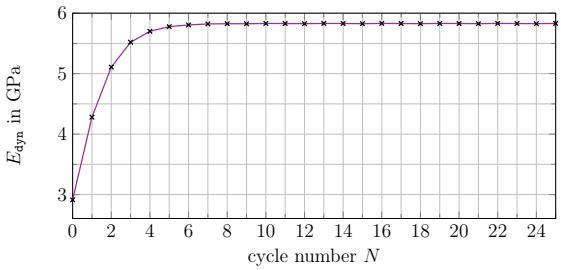

(b) Dynamic modulus evolution

Figure 6.4.: Evolution of stress-strain curve and dynamic modulus for a generalized Maxwell model (see Fig. 6.3)

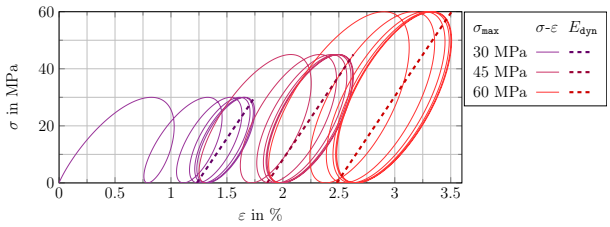

(a) Different load amplitudes

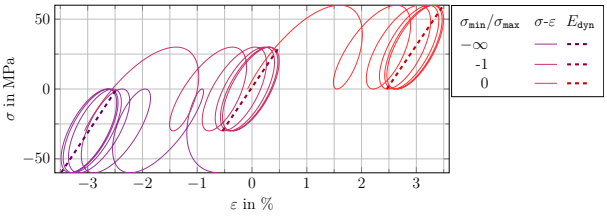

(b) Different load amplitudes

Figure 6.5.: Stress-strain curve at different load amplitudes ans stress ratios compared to the dynamic modulus $E_{\mathtt{dyn}}$ at the sixth cycle

smaller with every cycle. In the sixth cycle, we compare the dynamic modulus marked by the dashed line in the plots at every stress amplitude. We observe that the slope of the dashed line, i.e., the dynamic modulus, is independent of the applied stress amplitude.
Moreover, we plot stress-strain curves at different stress ratios R in Fig. 6.5(b). Similar to the hysteresis evolution under different load amplitudes, the hysteresis loops converge to periodic orbits, and the evaluated dynamic modulus in the sixth cycle is independent of the applied stress ratio.
In contrast to stress amplitude and stress ratio, the steady state reached for a viscoelastic material is not independent of the applied frequency. In Fig. 6.6, the material is subjected to cyclic loading at different frequencies. In Fig. 6.6(a), the stress-strain curves of the material for the first four cycles are plotted. The hysteresis evolves around a center point in the stress-strain diagram which is independent of the frequency. However, the shape of the hysteresis and, in particular, its symmetry axis, depends strongly on the frequency. The dynamic moduli are plotted in Fig. 6.6(b). They reflect the rotation of the symmetry axis of the hysteresis curve at different frequencies. The modulus values rapidly converge to an asymptotic value. The reached asymptotic value depends on the

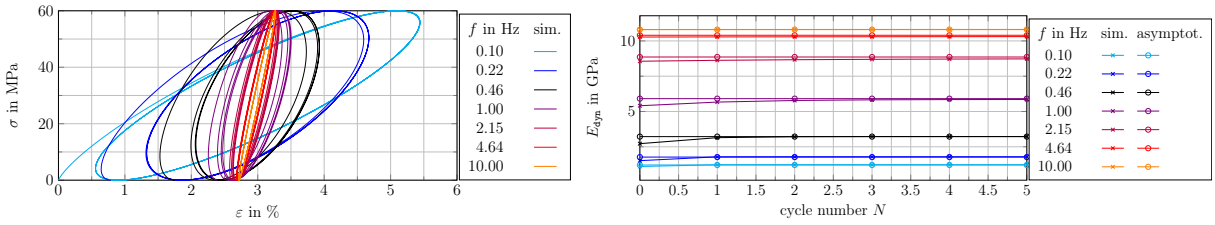

(a) Stress-strain curves

(b) Evolution of the dynamic modulus

Figure 6.6.: Linear viscoelastic material at different frequencies

frequency.

6.3. Modeling the long-term cyclic response of SFRPs

6.3.1. Material model

The constitutive behavior of heterogeneous materials is strongly influenced by the properties of the underlying microstructure. For short-fiber reinforced materials, these microstructures are characterized by the fiber orientation [262, 263], the fiber volume content [254] and the aspect ratio [264, 265] of the fiber inclusions. Thus, accurate material models need to account for the characteristics of the underlying microstructure. Due to the inherent anisotropy, characterizing ad-hoc phenomenological material models requires an expensive experimental program, in particular for long-term loading. In contrast, computational multiscale methods offer a possibility to derive the macroscopic material model from the material behavior of the constituents by computational means. Indeed, characterizing the individual phases typically comes with a reduced experimental effort. We thus chose to model the material behavior of the constituents, i.e., matrix and fiber, and to derive the macroscopic material behavior by micromechanics.

We consider a cubic cell $Y \subseteq \mathbb{R}^3$, together with spatially varying positive definite stiffness tensors $\mathbb{C}_m(x)$ for $m \in \{0, \dots, N\}$, and the coefficients $\beta_j(x)$ with $j \in \{1, \dots, N\}$ are given at every microscopic point $x \in Y$. We seek the strain fields $\boldsymbol{\varepsilon}$ and $\boldsymbol{\varepsilon}^{\mathrm{v},j}$, the stress

field $\boldsymbol{\sigma}$ and the displacement fluctuation field $\mathbf{u}$ satisfying

$$\operatorname{div} \boldsymbol{\sigma} = 0 \quad \text{in } Y, \tag{6.3.1}$$

$$\boldsymbol{\sigma} = \mathbb{C}_0 : \boldsymbol{\varepsilon} + \sum_{j=1}^{N} \mathbb{C}_j : \left(\boldsymbol{\varepsilon} - \boldsymbol{\varepsilon}^{\mathrm{v},j}\right) \quad \text{in } Y, \tag{6.3.2}$$

$$\dot{\boldsymbol{\varepsilon}}^{\mathrm{v},j} = \beta_j \left(\boldsymbol{\varepsilon} - \boldsymbol{\varepsilon}^{\mathrm{v},j}\right) \quad \text{in } Y, \tag{6.3.3}$$

$$\boldsymbol{\varepsilon} = \langle \boldsymbol{\varepsilon} \rangle_Y + \nabla^s \mathbf{u} \quad \text{in } Y, \tag{6.3.4}$$

together with the initial and boundary conditions

$$\mathbf{u} \text{ periodic} \quad \text{on } \partial Y, \tag{6.3.5}$$

$$\boldsymbol{\sigma} \cdot \mathbf{n} \text{ anti-periodic} \quad \text{on } \partial Y, \tag{6.3.6}$$

$$\boldsymbol{\varepsilon}^{\mathrm{v},j}\,(t=0) = 0 \quad \text{on } \partial Y, \tag{6.3.7}$$

$$\overline{\boldsymbol{\sigma}}(t) = \langle \boldsymbol{\sigma}(t) \rangle_Y\,, \tag{6.3.8}$$

for a prescribed macroscopic stress loading $\overline{\boldsymbol{\sigma}}(t)$. Here, $j \in \{1, \ldots, N\}$ indicates the Maxwell element, where N denotes the number of viscoelastic units in the generalized Maxwell chains, see Fig. 6.3. In formulas (6.3.1)-(6.3.6), we suppress the dependence of the fields on $x \in Y$ and the time t for simplicity of notation.
For later use, we record that the differential form of the constitutive law (6.3.2) and (6.3.3) can be equivalently represented in integral form [266]

$$\boldsymbol{\sigma}(x,t) = \int_0^t \mathbb{C}(x, t-u) : \frac{\partial \boldsymbol{\varepsilon}(x,u)}{\partial u} \mathrm{d}u \tag{6.3.9}$$

with the material function

$$\mathbb{C}(x,t) = \mathbb{C}_0(x) + \sum_{j=1}^{N} \mathbb{C}_j(x) \exp\left(-\beta_j t\right). \tag{6.3.10}$$

6.3.2. Choice of parameters

Similar to Krairi et al. [8], to identify matrix material parameters valid for the composite's material behavior, we consider tensile tests at different strain-rates. For short-fiber reinforced PBT, Mortazavian and Fatemi [267] reported on such experiments. However, these authors did not characterize the fiber orientations within the specimen. We assume the fiber orientation inside the injection molded specimen to be layered with the fiber orientation tensor components shown in Fig. 6.7(a), as suggested by the analysis of CT-scans of similar materials [224, 268–271]. We use a commercial PBT with 35 weight-% of

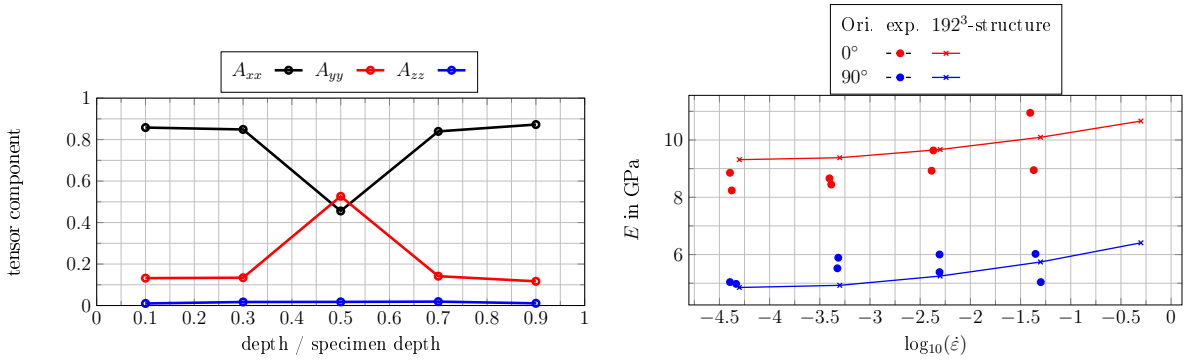

(a) Layered fiber structure

(b) Strain rate dependent modulus of layered fiber structure

Figure 6.7.: Young's modulus of the layered fiber structure at different strain rates compared to experimental data [267]

fiber inclusions and a respective fiber volume content of 17.8% [272]. The aspect ratio of the fibers is set to 29, see, e.g., Hessman et al. [224] for an analysis of typical aspect ratios.

Element i	$E_i^{\mathtt{matr}}$ in MPa	$\tau_i^{\mathtt{matr}}$ in s	$\nu_i^{\mathtt{matr}}$	$E_i^{\mathtt{fiber}}$ in GPa	$\nu_i^{\mathtt{fiber}}$
0	2475.0	-	0.4	72	0.22
1	582.4	2.4×10^{-3}	0.4		
2	429.9	2.4×10^{-2}	0.4		
3	316.2	2.2×10^{-1}	0.4		
4	233.0	1.9	0.4		

Table 6.2.: Identified material parameters for Maxwell element number i of PBT matrix and glass fibers

Based on the strain-rate dependent experiments on the composite, we obtained the moduli E_j and relaxation time constants $\tau_j = 1/\beta_j$ given in Tab. 6.2. In Fig. 6.7, the experimental results published by Mortazavian [267] are compared to viscoelastic computations on the layered fiber structure using the identified parameters. We observe that for both the 0°-oriented specimen and the 90°-oriented specimen, the computational prediction of the material modulus matches the experimental data rather well. Thus, the dependence on both strain rate and orientation is well-reproduced by the linear viscoelastic model with material parameters given in Tab. 6.2.

6.3.3. Dynamic stiffness of linear viscoelastic composites for long-term cyclic loading

We are interested in the long-term response of the viscoelastic composite subjected to a periodic excitation. Thus, we consider a periodic loading $\overline{\boldsymbol{\sigma}}(t)$ of the system (6.3.1)-(6.3.6) and seek solutions which are periodic in time with a period $T = 2\pi/\omega$. The system (6.3.1)-(6.3.6) possesses a unique solution, and we are concerned with obtaining computationally feasible approximations. For this purpose, we expand the total strain and the viscoelastic strain fields

$$\boldsymbol{\varepsilon}(x,t) = \sum_{k\in\mathbb{Z}} \hat{\boldsymbol{\varepsilon}}_k(x)\, \exp\left(\omega i\, kt\right) \tag{6.3.11}$$

$$\boldsymbol{\varepsilon}^{\mathrm{v},j}(x,t) = \sum_{k\in\mathbb{Z}} \hat{\boldsymbol{\varepsilon}}_k^{\mathrm{v},j}(x) \exp\left(\omega i\, kt\right) \tag{6.3.12}$$

into Fourier series w.r.t. the time variable.
For the time derivative, we obtain

$$\dot{\boldsymbol{\varepsilon}}^{\mathrm{v},j}(x,t) = \sum_{\omega\in\mathbb{Z}} \omega i\, k\hat{\boldsymbol{\varepsilon}}^{\mathrm{v},j}(x) \exp\left(\omega i\, kt\right). \tag{6.3.13}$$

The evolution equations (6.3.3) for the viscoelastic strains can be reassembled as

$$\omega i\, k\hat{\boldsymbol{\varepsilon}}^{\mathrm{v},j}(x) = \beta_j(x)\left(\hat{\boldsymbol{\varepsilon}}(x) - \hat{\boldsymbol{\varepsilon}}_k^{\mathrm{v},j}(x)\right) \quad \text{for all } k \in \mathbb{Z}. \tag{6.3.14}$$

As differential equations in real space get transformed to algebraic equations in Fourier space, we may solve for the fields $\hat{\boldsymbol{\varepsilon}}_k^{\mathrm{v},j}(x)$ explicitly

$$\hat{\boldsymbol{\varepsilon}}_k^{\mathrm{v},j}(x) = \frac{\beta_j(x)}{\beta_j(x) + \omega i\, k}\, \hat{\boldsymbol{\varepsilon}}(x). \tag{6.3.15}$$

With this formula at hand, we may recast the constitutive law (6.3.2) in a form reminiscent of linear elasticity, but with complex coefficients

$$\begin{aligned} \hat{\boldsymbol{\sigma}}_k(x) &= \mathbb{C}_0(x) : \hat{\boldsymbol{\varepsilon}}_k(x) + \sum_{j=1}^{N} \mathbb{C}_j(x) : \left(\hat{\boldsymbol{\varepsilon}}_k(x) - \hat{\boldsymbol{\varepsilon}}_k^{\mathrm{v},j}(x)\right) \\ &= \left[\mathbb{C}_0(x) + \sum_{j=1}^{N} \left(\frac{\omega i\, k}{\beta_j(x) + \omega i\, k}\right) \mathbb{C}_j(x)\right] : \hat{\boldsymbol{\varepsilon}}_k(x). \end{aligned} \tag{6.3.16}$$

Inserting the material law into the balance equation (6.3.1) yields

$$0 = \operatorname{div}\, \left(\left[\mathbb{C}_0(x) + \sum_{j=1}^{N} \left(\frac{\omega i\, k}{\beta_j(x) + \omega i\, k}\right) \mathbb{C}_j(x)\right] : \left[\hat{\overline{\boldsymbol{\varepsilon}}}_k + \nabla^s \hat{\mathbf{u}}_k(x)\right]\right). \tag{6.3.17}$$

Suppose that the tensor fields $\mathbb{C}_j$ are positive definite. Then, provided the Fourier coefficients $\hat{\overline{\boldsymbol{\sigma}}}_k$ of the macroscopic stress loading are contained in a specific subset $\mathcal{F}$ of the integers, i.e.,

$$\hat{\overline{\boldsymbol{\sigma}}}_k = 0 \quad \text{for} \quad k \notin \mathcal{F}, \tag{6.3.18}$$

we conclude

$$\hat{\mathbf{u}}_k(x) = 0 \quad \text{for} \quad k \notin \mathcal{F}. \tag{6.3.19}$$

Put differently, the displacement fluctuation field is then supported on this reduced set $\mathcal{F}$ of Fourier frequencies, as well.

We obtained a *complex*-valued elastic model [255] for the viscoelastic material's asymptotic periodic orbit. Typically, fiber reinforced polymer materials comprise just one viscoelastic constituent, the matrix, and one type of elastic inclusions, the fibers. We will discuss this special case in the following and derive a *real*-valued approximation for the dynamic stiffness of such materials.

To simplify further discussion, we assume a stress-driven sinusoidal load in the form

$$\overline{\boldsymbol{\sigma}}(t) = \overline{\boldsymbol{\sigma}}_{\mathtt{a}} \cos(\omega t) \tag{6.3.20}$$

with a stress-tensor valued "amplitude" $\overline{\boldsymbol{\sigma}}_{\mathtt{a}}$.

With the help of the expressions for the cosine and the sine in terms of the exponential function

$$\cos y = \frac{e^{iy} + e^{-iy}}{2} \quad \text{and} \quad \sin y = \frac{e^{iy} - e^{-iy}}{2i}, \quad y \in \mathbb{R}, \tag{6.3.21}$$

this loading may be written in the form

$$\overline{\boldsymbol{\sigma}}(t) = \frac{\overline{\boldsymbol{\sigma}}_{\mathtt{a}}}{2} e^{i\omega t} + \frac{\overline{\boldsymbol{\sigma}}_{\mathtt{a}}}{2} e^{-i\omega t}. \tag{6.3.22}$$

Thus, the Fourier coefficients compute as

$$\hat{\overline{\boldsymbol{\sigma}}}_1 = \frac{\overline{\boldsymbol{\sigma}}_{\mathtt{a}}}{2}, \quad \hat{\overline{\boldsymbol{\sigma}}}_{-1} = \frac{\overline{\boldsymbol{\sigma}}_{\mathtt{a}}}{2} \quad \text{and} \quad \hat{\overline{\boldsymbol{\sigma}}}_k = 0 \quad \text{for} \quad k \neq \pm 1. \tag{6.3.23}$$

By the previous argument (6.3.19), we thus seek a strain field $\boldsymbol{\varepsilon}$ supported only on the ± 1 Fourier frequencies. As we look for a real solution, it is actually more convenient to seek *real-valued* fields $\boldsymbol{\varepsilon}_c, \boldsymbol{\varepsilon}_s : Y \to \mathrm{Sym}(3)$, s.t. the representations

$$\hat{\boldsymbol{\varepsilon}}_{\pm 1} = \frac{1}{2} \left(\boldsymbol{\varepsilon}_c \pm i \, \boldsymbol{\varepsilon}_s \right). \tag{6.3.24}$$

are valid. We will also use a similar representation for the local stress fields

$$\hat{\boldsymbol{\sigma}}_{\pm 1} = \frac{1}{2}\left(\boldsymbol{\sigma}_c \mp i\,\boldsymbol{\sigma}_s\right). \tag{6.3.25}$$

In the fiber material, the linear elastic constitutive law (6.3.16) gives

$$\boldsymbol{\sigma}_{\mathtt{c}} = \mathbb{C}_{\mathtt{f}} : \boldsymbol{\varepsilon}_c^{\mathtt{f}} \quad \text{and} \quad \boldsymbol{\sigma}_{\mathtt{s}} = \mathbb{C}_{\mathtt{f}} : \boldsymbol{\varepsilon}_s^{\mathtt{f}}, \tag{6.3.26}$$

where $\mathbb{C}_{\mathtt{f}}$ denotes the elastic stiffness tensor of the fiber material. For the linear viscoelastic matrix material, we restrict to the case of an equal Poisson's ratio ν in all N elements of the Maxwell model. Then, the constitutive equation (6.3.16) can be rewritten as

$$\hat{\boldsymbol{\sigma}}_k(x) = \left[E_0(x) + \sum_{j=1}^{N}\left(\frac{\omega i\, k}{\beta_j(x) + \omega i\, k}\right) E_j(x)\right] \mathbb{K}(\nu) : \hat{\boldsymbol{\varepsilon}}_k(x) \tag{6.3.27}$$

within the linear viscoelastic matrix. With the abbreviations

$$r = E_0 + \sum_{j=1}^{N}\left(\frac{\omega^2}{\beta_j^2 + \omega^2}\right) E_j \quad \text{and} \quad q = \sum_{j=1}^{N} \frac{\beta_j\,\omega}{\beta_j^2 + \omega^2} E_j, \tag{6.3.28}$$

we deduce the strain-explicit representation

$$\begin{aligned} \boldsymbol{\varepsilon}_c^{\mathtt{m}} &= \frac{r}{r^2+q^2}\,\mathbb{K}(\nu)^{-1} : \boldsymbol{\sigma}_{\mathtt{c}} - \frac{q}{r^2+q^2}\,\mathbb{K}(\nu)^{-1} : \boldsymbol{\sigma}_{\mathtt{s}}, \\ \boldsymbol{\varepsilon}_s^{\mathtt{m}} &= \frac{q}{r^2+q^2}\,\mathbb{K}(\nu)^{-1} : \boldsymbol{\sigma}_{\mathtt{c}} + \frac{r}{r^2+q^2}\,\mathbb{K}(\nu)^{-1} : \boldsymbol{\sigma}_{\mathtt{s}}, \end{aligned} \tag{6.3.29}$$

see Appendix A.3 for details.
Defining the local compliance matrices

$$\mathbb{S}_c = \begin{cases} \mathbb{S}_{\mathtt{f}}, & \text{in fiber} \\ \frac{r}{r^2+q^2}\,\mathbb{K}(\nu)^{-1}, & \text{in matrix,} \end{cases} \quad \text{and} \quad \mathbb{S}_s = \begin{cases} 0, & \text{in fiber} \\ \frac{q}{r^2+q^2}\,\mathbb{K}(\nu)^{-1}, & \text{in matrix,} \end{cases} \tag{6.3.30}$$

where $\mathbb{S}_{\mathtt{f}} = \mathbb{C}_{\mathtt{f}}^{-1}$ denotes the compliance tensor of the fiber material, we may succinctly write

$$\begin{aligned} \boldsymbol{\varepsilon}_c &= \mathbb{S}_c : \boldsymbol{\sigma}_{\mathtt{c}} - \mathbb{S}_s : \boldsymbol{\sigma}_{\mathtt{s}} \\ \boldsymbol{\varepsilon}_s &= \mathbb{S}_s : \boldsymbol{\sigma}_{\mathtt{c}} + \mathbb{S}_c : \boldsymbol{\sigma}_{\mathtt{s}}. \end{aligned} \tag{6.3.31}$$

Upon spatial averaging, we deduce the expressions

$$\overline{\boldsymbol{\varepsilon}}_c = \mathbb{S}_c^{\mathtt{eff}} : \overline{\boldsymbol{\sigma}}_{\mathtt{c}} - \mathbb{S}_s^{\mathtt{eff}} : \overline{\boldsymbol{\sigma}}_{\mathtt{s}} \tag{6.3.32}$$

$$\overline{\boldsymbol{\varepsilon}}_s = \mathbb{S}_s^{\mathtt{eff}} : \overline{\boldsymbol{\sigma}}_{\mathtt{c}} + \mathbb{S}_c^{\mathtt{eff}} : \overline{\boldsymbol{\sigma}}_{\mathtt{s}}. \tag{6.3.33}$$

Using the prescribed conditions

$$\overline{\boldsymbol{\sigma}}_c = \overline{\boldsymbol{\sigma}}_a \quad \text{and} \quad \overline{\boldsymbol{\sigma}}_s = 0, \tag{6.3.34}$$

we conclude

$$\overline{\boldsymbol{\varepsilon}}(t) = \mathbb{S}_c^{\mathtt{eff}} : \overline{\boldsymbol{\sigma}}_a \cos(\omega t) + \mathbb{S}_s^{\mathtt{eff}} : \overline{\boldsymbol{\sigma}}_a \sin(\omega t). \tag{6.3.35}$$

Thus, to determine the evolution of the macroscopic strain under the loading (6.3.20), the two compliance tensors $\mathbb{S}_c^{\mathtt{eff}}$ and $\mathbb{S}_s^{\mathtt{eff}}$ need to be determined via computational homogenization. Due to the tensorial nature of the strain and the stress tensor, the convenient splitting of a superimposed cosine and sine wave in terms of a shift angle and an amplitude, well-known in the scalar case, is not available in this general setting. However, it appears plausible - at least in the case $q/r \ll 1$ - that we may approximate the effective response 6.3.35 by an effective model with shift-angle-amplitude form

$$\overline{\boldsymbol{\varepsilon}}(t) = \overline{\boldsymbol{\varepsilon}}_a C \cos\left(\omega t - \delta\right). \tag{6.3.36}$$

where C is a scalar and the corresponding sine-cosine form is

$$\overline{\boldsymbol{\varepsilon}}(t) = \overline{\boldsymbol{\varepsilon}}_a \left(A \cos(\omega t) + B \sin(\omega t)\right). \tag{6.3.37}$$

Then, the relations

$$\tan(\delta) = \frac{B}{A} \quad \text{and} \quad C^2 = A^2 + B^2 \tag{6.3.38}$$

hold. To approach this problem in a systematic manner, we use approximations of the local compliance tensors (6.3.30) that lead to a homogenized response of the appropriate form (6.3.36). Subsequently, we will use computational experiments to determine which approximation is appropriate.
We consider three approximations of this stress-strain relation for small phase shifts in the viscoelastic material, i.e., for $q/r \ll 1$.

1. Matrix-dominated approximation **MA**: For small fraction q/r, we consider the approximation

$$\mathbb{S}_s^{\mathtt{MA}} = \begin{cases} 0, & \text{in fiber} \\ \frac{q}{r^2+q^2}\, \mathbb{K}(\nu)^{-1}, & \text{in matrix,} \end{cases} \approx \begin{cases} \frac{q}{r}\, \mathbb{C}_{\mathtt{f}}^{-1}, & \text{in fiber} \\ \frac{q}{r^2+q^2}\, \mathbb{K}(\nu)^{-1}, & \text{in matrix.} \end{cases} \tag{6.3.39}$$

   We write the approximated stress-strain relation as

$$\overline{\boldsymbol{\varepsilon}}(t) \approx \langle \mathbb{S}_c : \overline{\boldsymbol{\sigma}}_a \rangle_Y \cos\left(\omega t\right) + \frac{q}{r} \langle \mathbb{S}_c : \overline{\boldsymbol{\sigma}}_a \rangle_Y \sin(\omega t) \tag{6.3.40}$$

$$= \langle \mathbb{S}_c : \overline{\boldsymbol{\sigma}}_a \rangle_Y \left(\cos\left(\omega t\right) + \frac{q}{r} \sin(\omega t)\right) \tag{6.3.41}$$

We define the approximated dynamic compliance as

$$\overline{\mathbb{S}}^{\mathtt{MA}}_{\mathtt{dyn}} = \langle \mathbb{S}_c \cos(\delta_{\mathtt{matr}}) + \mathbb{S}_s \sin(\delta_{\mathtt{matr}}) \rangle_Y \tag{6.3.42}$$

$$= \left\langle \begin{cases} \cos(\delta_{\mathtt{matrix}})\, \mathbb{C}_{\mathtt{f}}^{-1}, & \text{in fiber} \\ \cos(\delta_{\mathtt{matrix}})\, \frac{r}{r^2+q^2}\, \mathbb{K}(\nu)^{-1} + \sin(\delta_{\mathtt{matrix}})\, \frac{q}{r^2+q^2}\, \mathbb{K}(\nu)^{-1}, & \text{in matrix,} \end{cases} \right\rangle_Y . \tag{6.3.43}$$

Using the shift-angle-amplitude form (6.3.36), we finally obtain

$$\overline{\mathbb{S}}^{\mathtt{MA}}_{\mathtt{dyn}} = \left\langle \begin{cases} \cos(\delta_{\mathtt{matrix}})\, \mathbb{C}_{\mathtt{f}}^{-1}, & \text{in fiber} \\ \frac{1}{\sqrt{r^2+q^2}}\, \mathbb{K}(\nu)^{-1}, & \text{in matrix,} \end{cases} \right\rangle_Y . \tag{6.3.44}$$

2. Fiber-dominated shift approximation **FA:** For small fraction q/r, we consider the approximation

$$\mathbb{S}_s^{\mathtt{FA}} = \begin{cases} 0, & \text{in fiber} \\ \frac{q}{r^2+q^2}\, \mathbb{K}(\nu)^{-1}, & \text{in matrix,} \end{cases} \approx \begin{cases} 0, & \text{in fiber} \\ 0, & \text{in matrix} \end{cases} \tag{6.3.45}$$

leading to the approximation of the stress-strain relation

$$\overline{\boldsymbol{\varepsilon}}(t) \approx \langle \mathbb{S}_c : \overline{\boldsymbol{\sigma}}_a \rangle_Y \cos(\omega t). \tag{6.3.46}$$

The maximum effective strain is obtained at

$$t = 0. \tag{6.3.47}$$

We define

$$\delta_{\mathtt{fiber}} = 0 \tag{6.3.48}$$

and the approximated dynamic compliance as

$$\overline{\mathbb{S}}^{\mathtt{FA}}_{\mathtt{dyn}} = \langle \mathbb{S}_c \cos(\delta_{\mathtt{fiber}}) + \mathbb{S}_s \sin(\delta_{\mathtt{fiber}}) \mathbb{S}_0^{\mathtt{eff}} \rangle_Y \tag{6.3.49}$$

$$= \left\langle \begin{cases} \mathbb{C}_{\mathtt{f}}^{-1}, & \text{in fiber} \\ \mathbb{K}(\nu)^{-1} \frac{r}{r^2+q^2}, & \text{in matrix,} \end{cases} \right\rangle_Y . \tag{6.3.50}$$

3. Limit shift approximation **LA**: In the limit case of a neat matrix material or a neat fiber material under cyclic loading, the above approximations violate the expected phase shift of the homogenized material. Indeed, using MA, we obtain

$$\mathbb{C}_{\mathtt{dyn}} = \frac{1}{\cos \delta_{\mathtt{matrix}}}\, \mathbb{C}_{\mathtt{f}} \neq \mathbb{C}_{\mathtt{f}} \tag{6.3.51}$$

for neat fiber material. For FA, we obtain

$$\mathbb{C}_{\mathtt{dyn}} = \frac{r^2+q^2}{r}\,\mathbb{K}(\nu) \neq \sqrt{r^2+q^2}\,\mathbb{K}(\nu) \tag{6.3.52}$$

for neat matrix material. To circumvent this, we propose to use a combination of the above approximations

$$\overline{\mathbb{S}}^{\mathtt{LA}}_{\mathtt{dyn}} = \left\langle \begin{cases} \mathbb{S}_f, & \text{in fiber} \\ \frac{1}{\sqrt{r^2+q^2}}\,\mathbb{K}(\nu)^{-1}, & \text{in matrix,} \end{cases} \right\rangle_Y . \tag{6.3.53}$$

The three approaches MA, FA, and LA are compared to full linear viscoelastic computations (LVE) in a numerical study in section 6.3.4.
With the dynamic stiffness of the viscoelastic material and the elastic stiffness of the inclusions at hand, we may approximate the dynamic stiffness of the composite material based on *elastic* computations. We will refer to this approach as *surrogate elastic computation (SEC)* approach in the remainder of the manuscript. For convenience of the reader, we summarize the necessary computational steps in the following box.

Summary of the surrogate elastic computation (SEC) approach

Assumptions:

- *single* isotropic viscoelastic material, reinforced by elastic fibers
- Poisson's ratio ν equal in all stiffnesses and viscosities of the viscoelastic material

Input: elastic stiffness $\mathbb{C}_{\mathtt{f}}$; viscoelastic properties of the matrix E_i, β_i for all $i \in \{1, \dots, N\}$; Poisson's ratio ν; angular frequency ω of the loading

Computation:

1. Evaluate the dynamic material constants of the viscoelastic material

$$r \leftarrow E_0 + \sum_{j=1}^{N} \frac{\omega^2 E_j}{\omega^2 + \beta_j^2} \tag{6.3.54}$$

$$q \leftarrow \sum_{j=1}^{N} \frac{\omega E_j \beta_j}{\omega^2 + \beta_i^2} \tag{6.3.55}$$

2. Choose an approximation approach (MA, FA or LA) and compute the dynamic stiffness of the viscoelastic material

$$E_{\mathtt{dyn}} \leftarrow \begin{cases} \sqrt{r^2 + q^2}, & \text{for MA or LA} \\ \frac{r^2+q^2}{r}, & \text{for FA,} \end{cases} \tag{6.3.56}$$

3. Compute the isotropic stiffness $\mathbb{C}_{\mathtt{dyn}}^{\mathtt{matr}} = \mathbb{C}\left(E_{\mathtt{dyn}}, \nu\right)$ for the matrix material (see equation (6.2.7))

4. Compute the dynamic stiffness of the fiber material

$$\mathbb{C}_{\mathtt{dyn}}^{\mathtt{fibr}} \leftarrow \begin{cases} \mathbb{C}_f, & \text{for FA or LA} \\ \mathbb{C}_f \frac{1}{\cos \delta_{\mathtt{matr}}}, & \text{for MA,} \end{cases} \tag{6.3.57}$$

with

$$\delta_{\mathtt{matr}} \leftarrow \tan^{-1}\left(\frac{q}{r}\right). \tag{6.3.58}$$

5. Compute the homogenized elastic stiffness of the microstructure with the stiffness field

$$\mathbb{C}(x) = \begin{cases} \mathbb{C}_{\mathtt{dyn}}^{\mathtt{fibr}}, & \text{in the fiber,} \\ \mathbb{C}_{\mathtt{dyn}}^{\mathtt{matr}}, & \text{in the matrix.} \end{cases} \tag{6.3.59}$$

6.3.4. Computational investigations of the dynamic stiffness of SFRPs

In this section, we validate the derivations of the previous sections. Indeed, in section 6.3.3, we showed that we may approximate the dynamic stiffness with an efficient scheme. Instead of computing the material response of a viscoelastic material subjected to cyclic loading, we may compute a single "elastic" stiffness.

To verify the accuracy of the approximation, we choose a simple microstructure with fibers of aspect ratio ten, shown in Fig. 6.8(a). To compare the effect of the shift approximations MA, FA and LA. A viscoelastic material with large phase shift $\delta_{\mathtt{matrix}}$ at the applied loading frequency is chosen. We subject the material to stress-driven cyclic loading with a stress amplitude of σ_a =15 MPa and a frequency of 3 Hz. To keep the numerical effort at a minimum, only one Maxwell element for the matrix material model is used. Its material parameters are E_0 =1 GPa, E_1 =10 GPa and ν =0.4. We study the material behavior for two different viscosities, η_1=160 GPa·s leading to a phase shift of $\delta_{\mathtt{matrix}}$=57.6° at the applied load frequency and η_1=25 GPa·s leading to a phase shift of $\delta_{\mathtt{matrix}}$=27.4°, respectively. We vary the Young's modulus of the fiber material between $10^1 - 10^7$ MPa, its Poisson ratio is set to ν =0.22.

For the linear viscoelastic computation (LVE), we evaluate the strain of the homogenized material $\overline{\boldsymbol{\varepsilon}}(t)$ and identify the maximum $\overline{\boldsymbol{\varepsilon}}^{\mathtt{max}}_{xx}$ and minimum value $\overline{\boldsymbol{\varepsilon}}^{\mathtt{min}}_{xx}$ in each cycle N. When the difference $\triangle\boldsymbol{\varepsilon}_{xx}(N) = \overline{\boldsymbol{\varepsilon}}^{\mathtt{max}}_{xx}(N) - \overline{\boldsymbol{\varepsilon}}^{\mathtt{min}}_{xx}(N)$ reaches a steady state in N, we evaluate the dynamic modulus in x-direction

$$E^{x}_{\mathtt{dyn,LVE}} = \frac{2\sigma^{\mathtt{a}}_{xx}}{\triangle\boldsymbol{\varepsilon}_{xx}} \tag{6.3.60}$$

of the linear viscoelastic material (LVE). In Fig. 6.8, the predicted dynamic moduli are compared to the SEC model, using the three different approximation approaches MA, FA and LA. For a large phase shift, shown in Fig. 6.8(b), the FA overestimates the dynamic stiffness of the composite material significantly. Both MA and LA approximate the composite behavior comparatively well. In the region of typical stiffness contrast between matrix and fiber, i.e., for $\log_{10}(E_{\mathtt{fiber}}/\mathrm{GPa}) = 10^4 - 10^5$, the LA model matches the composite behavior more accurately than MA.

For smaller phase shifts, the deviation between the models decreases. Comparing the predicted dynamic moduli in Fig. 6.8(c) for a smaller phase shift to the moduli in Fig. 6.8(b), the deviation between MA and LA is barely visible. Both models approximate the linear viscoelastic model with reasonable accuracy.

To summarize, the deviations from the full computation using the LVE model are smaller

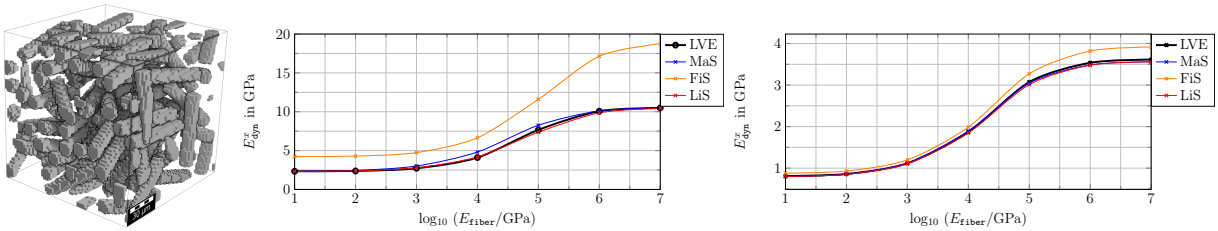

(a) Test structure (b) Fiber structure with $\delta_{\mathtt{matrx}} = 56.4°$ (c) Fiber structure with $\delta_{\mathtt{matrx}} = 27.4°$

Figure 6.8.: Comparison of different approximation approaches to the linear viscoelastic model (LVE)

for the LA than for the FA and the MA approach. Thus, we fix the LA approach to study the material behavior in the remainder of the manuscript.

With these insights at hand, we return to the industrial fiber-reinforced PBT. The material parameters of the matrix are chosen as described in section 6.3.2 and the fiber inclusions are modeled as an isotropic linear elastic material with the Young's modulus $E = 72$ GPa and the Poisson's ratio $\nu = 0.22$. The fiber structure is layered, with the fiber orientations in each layer chosen according to the structure plotted in Fig. 6.7(a) and its realization shown in Fig. 6.14.

The results for excitation of the fiber structure in 0°- and 90°-direction are shown in Fig. 6.9. The hysteresis loops plotted are the result of the linear viscoelastic computation. Here, for each load case the fifth hysteresis loop is shown. For better visualization, each of the hysteresis loops is shifted by some strain value ε_0. For the 0°-direction, the strain at the first time step of the plotted loop starts at 0%, 0.1% and 0.2% for the computations at 3 Hz, 5 Hz and 10 Hz, respectively. For the 90°-direction, the strain at the first time step of the plotted loop starts at 0%, 0.2% and 0.4% for the computations at 3 Hz, 7 Hz and 12 Hz, respectively. The dashed lines represent the Young's moduli computed by the SEC model in the respective direction. In Fig. 6.9(a), different stress amplitudes at a frequency of 10 Hz are shown. The hysteresis loops are shown in blue, green and red. As discussed in section 6.2.2 for the one-dimensional case, we observe that the dynamic stiffness of the composite material is independent of the load amplitude. In Fig. 6.9(b), the hysteresis curves for excitation in 0°-direction of the fiber structure are shown for different frequencies. The colored dashed lines, which represent the dynamic stiffness of each hysteresis loop computed by the SEC model, are shifted to higher strain values for better comparison. With increasing frequency, the dynamic stiffness increases. In Fig. 6.9(c), the hysteresis curves and their dynamic stiffness is shown for the 90°-direction. The SEC model represents the dynamic stiffness of the linear viscoelastic computations quite well. To study the approximation of the viscoelastic model quantitatively, the axial dynamic

stiffness

$$E_x^{\mathtt{visco}} = \frac{\sigma_{xx}^{\mathtt{max}} - \sigma_{xx}^{\mathtt{min}}}{\varepsilon_{xx}^{\mathtt{max}} - \varepsilon_{xx}^{\mathtt{min}}}, \tag{6.3.61}$$

obtained from both models is shown in Fig. 6.10. We observe that the SEC model represents the dynamic properties of the material model in this fifth cycle very well. The deviation between the stiffness computed by the time resolved viscoelastic model and the simplified SEC model is well below 1%.

To get an idea of the speed up obtained by using the SEC model instead of the viscoelastic computation, we computed one load cycles discretized by 40 time steps for the viscoelastic model on the layered fiber structure. The number of Maxwell elements is 4 and we used the FeelMath-solver [228] on 8 nodes. The resulting runtime is approximately 2.4h. In contrast, a single elastic time step on the same fiber structure takes approximately 2min on the same hardware. To obtain the material stiffness, we need to compute six load cases both in the SEC and the viscoelastic model. It is necessary to compute a few cycles to reach the periodic orbit. Assuming that six cycles are enough to reach the fixed point using the viscoelastic model, we get a speed-up factor of about 432.

Additionally, the SEC algorithm highly increases the memory efficiency of the computation. For a viscoelastic material with 4 Maxwell elements, i.e., 4 internal strain fields, we need to store 24 scalar fields. On the other hand, the SEC computation does not need any additional internal variables. Taking a microstructure discretized by 256^3 voxels as an example, storing one scalar field of double precision values takes 0.125 GB in memory. Thus, we can reduce the memory use by 3 GB in comparison with the viscoelastic material model.

6.3.5. Influence of fiber volume content and fiber orientation

To get further insights into the influence of viscoelastic properties of the polymer matrix onto the cyclic behavior of the composite material, we study the dependence of the material behavior on the fiber volume content and the fiber orientation.

Goméz et al. [254] studied the influence of the fiber volume content on the dynamic properties of short-fiber reinforced PBT at elevated temperatures by experiments. We use their experimental results as a reference for the trends observed in numerical predictions obtained by the SEC model.

Goméz et al. [254] measured the frequency-dependent material properties of PBT at 50.2°C. In Fig. 6.11, the dependence of the storage modulus of PBT on the frequency is shown in black. To reproduce this behavior by a linear viscoelastic material model,

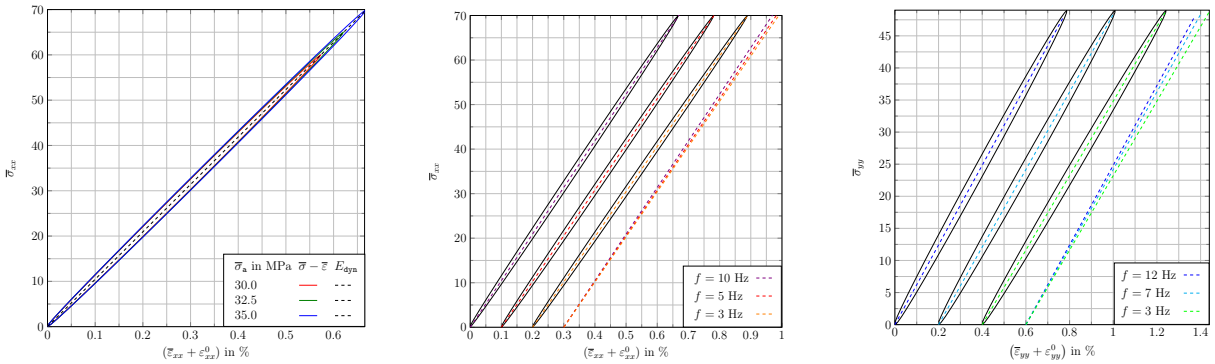

(a) Excitation in 0°-direction at different load amplitudes at 10 Hz

(b) Excitation in 0°-direction at different frequencies

(c) Excitation in 90°-direction at different frequencies

Figure 6.9.: Linear viscoelastic (LVE) model vs. SEC model on the layered fiber structure shifted by a strain value ε^0 for better comparison

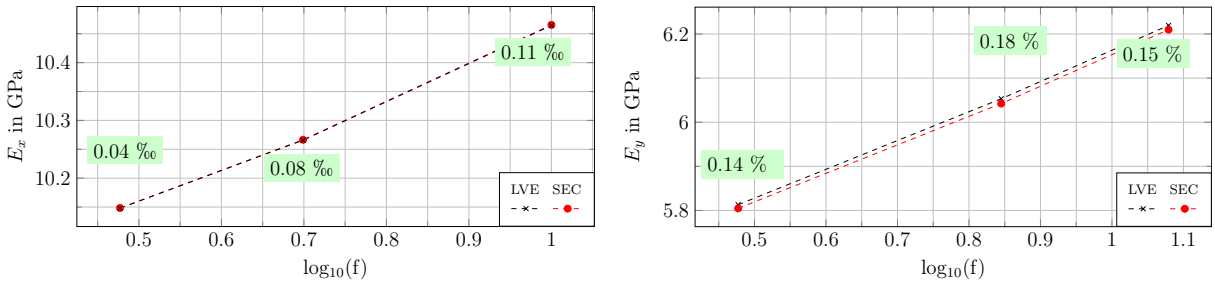

(a) Excitation in 0°-direction

(b) Excitation in 90°-direction

Figure 6.10.: Linear viscoelastic (LVE) vs. SEC model on the layered fiber structure

we chose to use 15 Maxwell elements, about one for each decade in the measured frequency range. The parameter identification proceeds with an algorithm similar to the one described in Woldekidan [273]. The obtained moduli E_j and relaxation time constants $\tau_j = 1/\beta_j$ are given in Tab. 6.3. The Poisson's ratio of all elements is set to $\nu = 0.4$ for all further computations, as commonly identified for PBT. The resulting fit of the material behavior is shown by the red line in Fig. 6.11. We observe that the material behavior can be represented accurately by the viscoelastic model. The dynamic modulus is mainly governed by the storage modulus as the phase shift in the material behavior is not pronounced.

Element i	$E_i^{\mathtt{matr}}$ in MPa	$\tau_i^{\mathtt{matr}}$ in s	$\nu_i^{\mathtt{matr}}$	$E_i^{\mathtt{fiber}}$ in GPa	$\nu_i^{\mathtt{fiber}}$
0	300.7	-	0.4	72	0.22
1	173.6	2.3×10^{-8}	0.4		
2	166.8	2.4×10^{-7}	0.4		
3	179.4	2.2×10^{-6}	0.4		
4	175.7	1.9×10^{-5}	0.4		
5	155.0	1.7×10^{-4}	0.4		
6	126.0	1.6×10^{-3}	0.4		
7	97.0	1.4×10^{-2}	0.4		
8	71.7	1.3×10^{-1}	0.4		
9	52.7	1.2×10^{0}	0.4		
10	38.8	1.2×10^{1}	0.4		
11	29.9	1.1×10^{2}	0.4		
12	24.0	1.0×10^{3}	0.4		
13	20.1	9.4×10^{3}	0.4		
14	17.5	8.8×10^{4}	0.4		
15	18.6	9.2×10^{5}	0.4		

Table 6.3.: Identified material parameters for Maxwell element number i of PBT matrix and glass fibers

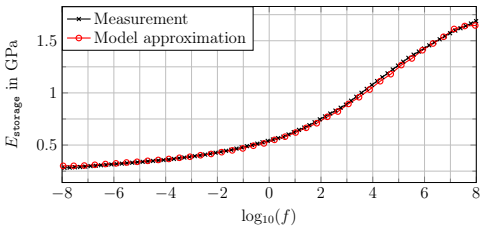

Figure 6.11.: Storage modulus

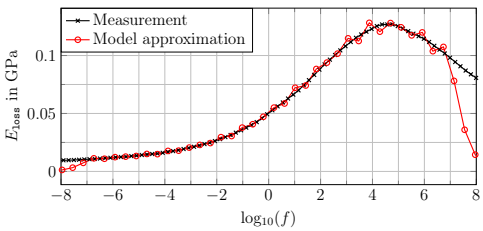

Figure 6.12.: Loss modulus

Goméz et al. [254] did not report on the fiber orientation inside the experimental specimens. In the present study, we use fiber structures with the eigenvalues of $\lambda_1 = 0.5$ and $\lambda_2 = 0.3$ in their second-order Advani-Tucker fiber orientation tensor [169]. Higher order momenta are recovered by the exact closure approximation [274]. We compare fiber structures with 0%, 12% and 29% fiber volume content. For the fiber structures of 12%

and 29% fiber volume content, two realizations are generated. The first has a volume edge-length $L_{\texttt{vol}}$ of 1.32 fiber lengths $\ell_{\texttt{fiber}}$, i.e., we use a volume-fiber length ratio of $L_{\texttt{vol}}/\ell_{\texttt{fiber}} = 1.32$. In the second structure this ratio is increased to $L_{\texttt{vol}}/\ell_{\texttt{fiber}} = 1.77$. The number of voxels per fiber diameter is thereby kept constant (6.4 voxels per fiber diameter). The fiber structures with a ratio of $L_{\texttt{vol}}/\ell_{\texttt{fiber}} = 1.77$ and with 12% and 29% fiber volume content are shown in Fig. 6.13, visualized with GeoDict[2]. The structures were generated using the Sequential Addition and Migration (SAM) algorithm [173].
In Fig. 6.13, the dependence of the dynamic modulus of the composite material on the frequency is shown. The increase in fiber volume content is reflected in a shift of the dynamic modulus to higher values. The slope of the curve is slightly increased, i.e., higher frequencies show a stronger influence on the composite than on the plain matrix material. These computational observations agree well with experimental observations reported by Goméz [254].

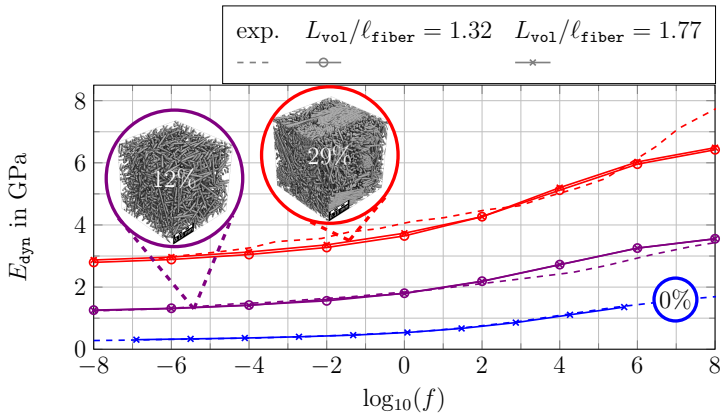

Figure 6.13.: Frequency dependent dynamic modulus for different fiber volume contents

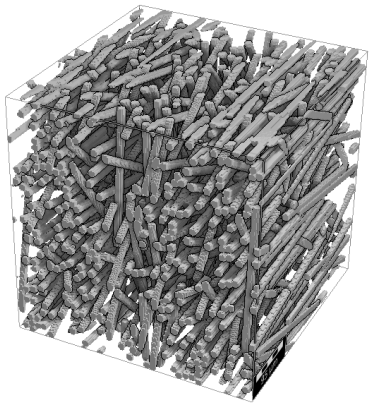

Figure 6.14.: Realization of the layered fiber structure

We further study the influence of the fiber orientation on the viscoelastic material behavior in the periodic orbit. In Fig. 6.15, the dependence of the composite's dynamic stiffness on the frequency is shown for three fiber structures with different fiber orientations. Each of the fiber structures is subjected to stress-driven extension in x-direction. The reinforcements in the direction of loading lead to a stiffening of the composite material. Thus, the uni-directional fiber structure shows the highest dynamic modulus in x-direction, as all fibers point in loading direction, followed by the planar-isotropic and the isotropic fiber structure. Higher frequencies lead to a higher dynamic modulus of the matrix and thus the

[2]Math2Market GmbH, http://www.geodict.de

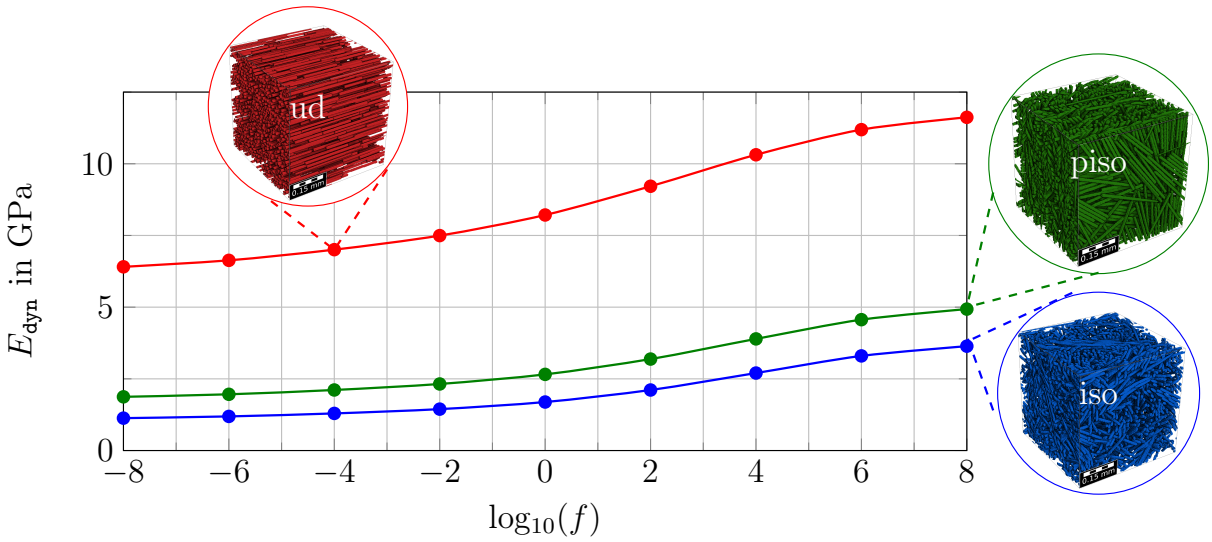

Figure 6.15.: Influence of fiber orientation on dynamic stiffness for isotropic (iso), planar-isotropic (piso) and uni-directional (ud) fiber structures

composite. This effect becomes apparent for all three structures. The increase of the composite dynamic stiffness with increasing frequencies is most pronounced for the isotropic structure, as the matrix behavior is more dominant in this case.

6.4. A fatigue-damage model for the dynamic stiffness in SFRPs

6.4.1. Material model

In polymer-based materials under fatigue loading, we observe a steady degradation of the mechanical behavior over a range of thousands or millions of cycles. This degradation is observable in a decrease of the measured dynamic stiffness. On the other hand, short-term effects of viscoelastic nature can significantly influence the measured stiffness, as discussed for linear viscoelastic materials in the previous section 6.3. As both of this effects, damage and viscoelasticity, manifest at different time scales, we chose to decouple these effects and model them in two subsequent steps. First, we compute the dynamic stiffness of the viscoelastic material at high cycles, i.e, we evaluate the function $\mathbb{C}_{\mathtt{dyn}}(f)$ using the SEC model discussed in section 6.3. Secondly, we use the evaluated long-term viscoelastic dynamic stiffness to model the evolution of the dynamic stiffness with a fatigue-damage

model. In principle, this approach is independent of the chosen damage model, i.e., the engineer is free to choose a proper damage variable D and to design an appropriate damage-evolution law $\mathrm{d}D/\mathrm{d}N = f(\varepsilon, D, \ldots)$ to suit the material behavior.
We demonstrate the effects of the proposed ansatz on a recently published compliance-based model [231] in the following. The *elastic* compliance-based material law is defined based on the free energy density

$$w(\boldsymbol{\varepsilon}, D) = \frac{1}{2}\frac{1}{1+D}\,\boldsymbol{\varepsilon} : \mathbb{C}_0 : \boldsymbol{\varepsilon}. \tag{6.4.1}$$

with the elastic stiffness tensor $\mathbb{C}_0$, the strain *amplitude* tensor $\boldsymbol{\varepsilon}$ and a scalar damage variable $D \in [0, \infty)$, and the dissipation potential

$$\phi(D') = \frac{1}{2\alpha}(D')^2. \tag{6.4.2}$$

The damage evolution, directly formulated in logarithmic cycle space $D' \equiv \mathrm{d}(D)/\mathrm{d}(\log_{10} N)$ is governed by the damage speed parameter α. We refer to chapter 4 for a detailed discussion of the model. We introduce $\overline{N} = \log_{10} N$ as short-hand notation for the variable in logarithmic cycle space. To account for the frequency-dependent long-term behavior of the viscoelastic matrix material, we replace the elastic stiffness with the dynamic stiffness $\mathbb{C}_{\mathtt{dyn}}$. This yields

$$w(\boldsymbol{\varepsilon}, D) = \frac{1}{2}\frac{1}{1+D}\,\boldsymbol{\varepsilon} : \mathbb{C}_{\mathtt{dyn}}(f) : \boldsymbol{\varepsilon}. \tag{6.4.3}$$

The modification effects both the stress-strain relation

$$\boldsymbol{\sigma} = \frac{1}{1+D}\,\mathbb{C}_{\mathtt{dyn}}(f) : \boldsymbol{\varepsilon}, \tag{6.4.4}$$

where $\boldsymbol{\sigma}$ is the stress amplitude tensor in the current cycle, and the damage evolution equation

$$D' = \alpha\frac{1}{2}\,\boldsymbol{\sigma} : (\mathbb{C}_{\mathtt{dyn}}(f))^{-1} : \boldsymbol{\sigma}, \tag{6.4.5}$$

i.e., the damage evolution is governed by the load amplitude *and* the frequency. Experimental studies revealed that damage evolution inside the polymer matrix and the resulting stiffness degradation of the composite material is indeed influenced by the load amplitude [243, 275, 276]. Moreover, a recent study of Imaddahen et al. [277] reports that the fatigue process in short-glass fiber reinforced polypropylene depends on the strain rate or frequency. They observed an improvement of the fatigue strength at higher frequencies, i.e., a higher number of bearable load cycles at higher frequencies. As a possible explanation for this result they refer to the static experiments of Fitoussi et al. [278] where the

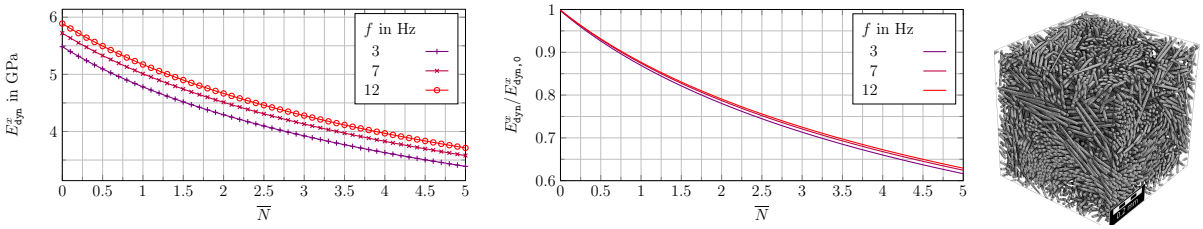

(a) Absolute degradation over the logarithmic cycle space $\overline{N}$

(b) Relative degradation over the logarithmic cycle space $\overline{N}$

(c) Isotropic fiber structure

Figure 6.16.: Influence of frequency on stiffness degradation

authors showed that damage effects at high strain rates are delayed in polymer composites. This observation suggests that the damage evolution in thermoplastic materials is reduced by an increase in frequency.

To uncover the influence of an increased frequency in the proposed model (6.4.2)-(6.4.3), we study the influence of the frequency on the stiffness degradation in simulations. In Fig. 6.16, the degradation of the dynamic Young's modulus in x-direction $E^x_{\mathtt{dyn}}$ is shown for the structure with isotropic fiber orientation shown in Fig. 6.16(c) and stress-driven uniaxial extension of the material with a load amplitude of 50 MPa. The material parameters are listed in Tab. 6.2. The stiffness of the material increases with increasing frequency. Thus, the evolution of the dynamic modulus is shifted to higher values for higher frequencies. Plotting the relative evolution of the Young's modulus, we observe that higher frequencies lead to slower degradation. Higher frequencies lead to a slower degradation. This in accordance with the experimental observations of Imaddahen et al. [277].

6.4.2. Experiments vs. computational predictions

To validate the viscoelastic damage model discussed in section 6.4.1, we performed fatigue experiments at different load amplitudes and frequencies. The experiments were done on specimen geometries as shown in Fig. 6.17(a). The geometries were cut from an injection-molded plate. The layered fiber orientation structure inside the plate, which evolves due to the injection process, was characterized by µCT-scans and is shown in Fig. 6.17(b). For the scans, a small volume at the center of the injection molded plate was cut out. Subsequently, the fiber orientation in nine layers subdivided over the thickness of the plate was analyzed, see Hessman et al. [224] for more details on the method. We investigate two types of specimens, 0°-oriented and 90°-oriented. By 0°-oriented, we refer

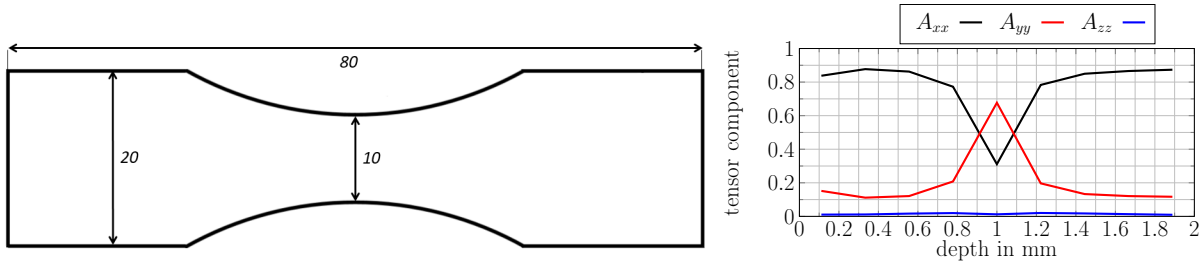

(a) Geometry of specimens with thickness of 2mm

(b) Fiber orientation

Figure 6.17.: Geometry and fiber structure of test specimen

to specimens that were cut from the plate in the direction of the mold injection and in which the resulting fiber orientation is thus mainly oriented in the loading direction. By 90°-oriented specimens, we mean specimens that were cut transverse to the mold injection direction. The specimens were subjected to cyclic loading with stress ratios $R = 0$. The different load cases are listed in Tab. 6.1. To get an estimate for the scattering of the measurements, each load case was conducted three times.

For the computational predictions, we use the (visco)elastic material properties of the matrix and fiber listed in Tab. 6.2. For the damage evolution in the matrix material, a straightforward parameter-identification strategy, see chapter 3, led to the parameter $\alpha = 0.18$ 1/MPa. Subsequently, the reduced order model was trained for the frequencies of interest. For the macroscopic specimen, we considered a layered fiber structure resolving nine layers, see Fig. 6.17(b). For more details about the computational procedure on component scale, the model order reduction and the setup of the simulation on the component level in the finite-element solver Abaqus [192], we refer to chapter 4.

In Fig. 6.18, we compare the resulting stiffness evolution in the component simulations to the experimental measurements. Both the measured and the predicted dynamic stiffness increase with increasing frequency. An increase of the frequency by several Hz results in an increase of the dynamic stiffness by several hundred MPa. The computational predictions of this increase match the experimental values quite well, both qualitatively and quantitatively. The scattering of the measurements of 0°-oriented specimens is significantly higher than for the 90°-specimens. For 0°, the initial predicted dynamic stiffness matches the measured mean value and the predicted degradation is within the experimental scattering up to the last decade of the experiment. For the 90°-oriented specimen the dynamic stiffness within the first few hundred is overestimated by the computational predictions. Yet, for cycle numbers exceeding 100, the deviation between computational predictions and experimental measurements is acceptable.

The applied damage model does not account for localization effects by construction and

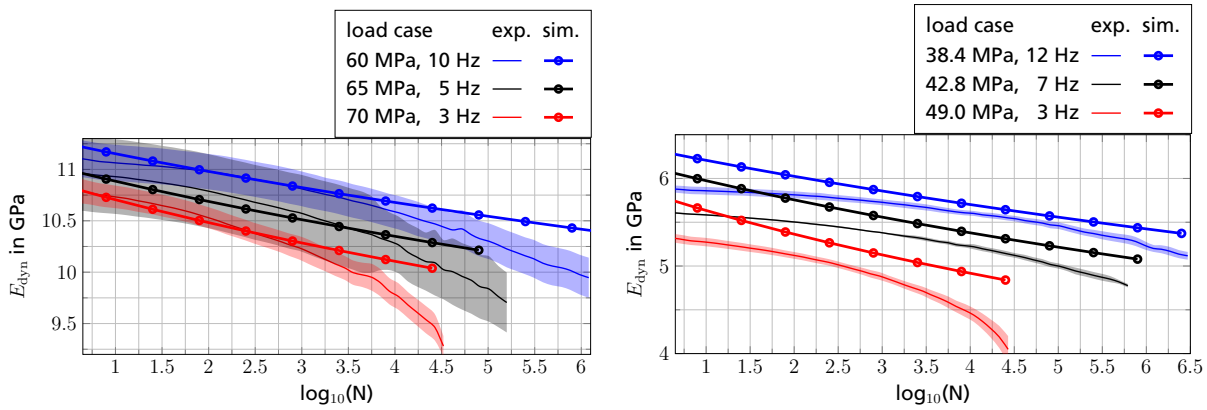

(a) 0°-oriented (b) 90°-oriented

Figure 6.18.: Stiffness degradation: simulation vs. experiment

is therefore unable to represent a negative second derivative in the stiffness degradation. Rather, we focus on the reproduction of the approximately linear trends in the stable stiffness degradation, see chapter 4 and 5. The damage processes leading to the stiffness degradation within the last decade of the fatigue process are most likely already localized. To improve predictions in this regime, a localizing damage model needs to be applied.

6.5. Conclusion

In this chapter, the dynamic stiffness of short-fiber reinforced composite materials under high-cycle fatigue loading at different stress amplitudes and frequencies was studied. Experiments reveal a frequency dependence that is not typically accounted for in contemporary existing elastic fatigue damage models. To accurately predict the dynamic stiffness in fatigue experiments, this dependence needs to be accounted for.
We restrict ourselves to linear viscoelastic material model for the thermoplastic matrix. At high stress levels locally occurring in the composite material, this is an approximation. Yet, we are able to reproduce the composite material behavior at a range of strain-rates already with this simple material model, see section 6.3.2. For cyclic loading of linear viscoelastic materials, a frequency dependent relation between the stress and strain amplitudes at the steady-state is known. We use this relation to approximate the dynamic stiffness of a short-fiber reinforced polymer with equal Poisson's ratios in every Maxwell element valid for small phase shifts. The effective dynamic stiffness may be determined as an elastic effective stiffness (SEC) and is shown to be rather accurate for short-fiber

reinforced PBT, see section 6.3.4. The proposed algorithm is both memory and time efficient.

We validated the approach using experiments of short-fiber reinforced PBT at different load amplitudes, frequencies and fiber orientations. The model is able to predict the frequency dependence in the dynamic stiffness degradation. Additionally, the trend of a slower damage evolution at higher frequencies is reproduced, as the the damage evolution equation is governed by the dynamic stiffness.

To calibrate the model, we need to identify the viscoelastic material parameters of the matrix (see section 6.3.2) from strain-rate experiments on the composite and the damage parameter α from a single fatigue experiment for the matrix. The experimental expense is thus significantly reduced in comparison to a multitude of fatigue measurements.

It remains to propose an interpolation approach for the frequency dependent material behavior in the reduced order model. For the computations on the microstructure, it is straightforward to account for a change in frequency by adjusting $\mathbb{C}_{\mathtt{dyn}}(f)$ to the new frequency. However, for the reduced order model, a database for every frequency of interest has to be trained and the macroscopic computation is run at a constant prescribed frequency. To account for a frequency change, the reduced order model thus needs further development.

Additional effects that are of interest in short-fiber reinforced components include temperature dependence. Since polymers are known to show interchangeable properties in frequency and temperature change, it would be interesting to investigate an extension to temperature dependency.

7. Conclusion

The main result of this work is the development of a multiscale material model for the fatigue degradation of the dynamic stiffness in SFRTs. Two classes of damage models for the matrix degradation have been developed and integrated in a data-driven model order reduction framework that enables an efficient computation of fatigue degradation at the macroscale.

The first class of fatigue damage model discussed in chapter 3 is very similar to classical continuum damage [129, 206] and phase-field models [133, 204, 205], formulated directly in cycle space. The model is able to capture localization at the microscale and directly suitable for Galerkin-type model order reduction technique. Upon localization, the existence of a representative volume element (RVE) is lost and consistent homogenization is no longer applicable. Thus, the computation up to highly localized damage fields is at most valid on the microscale. Nevertheless, this allows the exploration of localized damage evolution in SFRT in a detailed level. For moderate stiffness degeneration and non-localized damage fields, the model order reduction scheme enables an efficient computation of the anisotropic stiffness evolution on component scale.

The second class of fatigue damage model is introduced in chapter 4. It can be regarded as the an extension of the convex rate-independent damage model proposed by Görthofer et al. [207] to fatigue. It precludes localization a priori and does not require a regularization strategy. However, due to the hyperbolic structure of the strain energy potential, the model order reduction technique used in chapter 3 is no longer applicable. Thus, a new model order reduction strategy has been developed. It has been shown to capture the microscale behavior rather well at significantly decreased computational costs as the model proposed in chapter 3. Therefore, to model the stiffness degradation within a multiscale framework, fatigue damage models of convex type are preferable. However, when localization is of interest, one needs to resort to the class of classical damage models.

The fatigue damage models discussed in chapter 3 and 4 have been directly formulated in (logarithmic) cycle space as a pseudo-time scale. This approach enables an efficient computation of high cycle fatigue, however it lacks an physical understanding for the load-dependent damage evolution in time. When applying different load wave forms or

stress ratios, the effect on the damage evolution had remained an open question. Thus, we proposed a fatigue damage model directly formulated in time space in chapter 5. It preserves the convex structure which is shown to be advantageous for an application within the multiscale framework (see chapter 4). Building upon the work of Paas et al. [230] and Peerlings et al. [211], damage evolution is only permitted under loading and precluded under unloading. This approach enables the prediction of fatigue damage evolution under arbitrary loading. An approximation of the fatigue damage evolution in (logarithmic) cycle space has been recovered for sinusoidal loadings. The model has been applied to the stiffness degradation of short-fiber reinforced polyamid specimens with different fiber orientations, notch geometries and stress ratios and has shown to be in good agreement with the experimental measurements. However, as the model precludes localization by definition, the third and final stage of stiffness degradation can not be captured. How to model this stage of evolution consistently within a multiscale framework is out of the scope of this work.

The models discussed in chapter 3-5 neglect viscoelastic effect for the sake of simplicity. However, short-fiber reinforced materials are well-known to be viscoelastic in nature. In chapter 6, we turn our attention to viscoelastic effects in experimental measurements of PBT-based materials and their consequences for the measured dynamic stiffness. We propose to use a linear-viscoelastic material model for the matrix to capture the relevant processes. For high-cycle loading at constant stress or strain amplitude, the linear-viscoelastic material reinforced by elastic inclusions is shown to reach a steady cycle. This cyclic fixed point is the point of departure for our investigation of the dynamic stiffness properties of the composite material. We propose a simple approximation valid for materials with rather small phase shifts to identify the dynamic stiffness at the fixed point via a single elastic computation. This enables us to integrate the, now frequency dependent, viscoelastic dynamic stiffness into the proposed multiscale framework. We demonstrated that the model captures the stiffness degradation in PBT-based SFRT rather well. We integrated the viscoelastic effects into the compliance based fatigue damage model. As the viscoelastic effects are reflected only in a modified undamaged dynamic stiffness of the material, the approach can easily be transferred to other fatigue damage models formulated in cycle space, see, e.g., chapter 3.

In the present work, a complete framework – from microstructure simulation to component prediction – to model fatigue damage under different loading conditions has been set up and validated by experimental results. A suitable failure criterion on the macroscale within the proposed framework remains an open question. This is mainly due to the fact that transfering failure processes from microscale to macroscale within the context of homogenization is a rather difficult task. Failure at every scale is interpreted differently:

the formation of cracks is already considered as failure on the microstructural level, while from a macroscopic view point, failure only begins when cracks through larger parts of the specimen begin to evolve. However, in many engineering components, the prediction of the complete fracture is not the goal. Rather, engineers are interested in the evolution of the not yet critical fatigue damage, to exchange the component after a stiffness loss of several (ten) percent. For these components, the proposed framework is ready for application.

The material model for the fiber adopted is the simplest choice one can think of: linear-elastic. Yet, in many experiments on short-fiber reinforced materials also fiber breakage has been observed under certain loading conditions. The incorporation of a fiber failure model and its influence on the degradation of the composite remain to be investigated. As this failure mode is of highly localized nature, an incorporation to multiscale models based on snapshot-informed model order reduction seems to be a tedious task. Possibly, alternative surrogate models need to be developed.

Furthermore, thermal effects have not been investigated in this work. For many polymers, the time-temperature superposition principle holds. Thus, it might be interesting to integrate thermal dependencies in a similar fashion as the frequency dependency discussed in chapter 6. Similarly, the effect of creep needs to be further investigated. The material modeling in the work at hand solely focuses on the prediction of the *dynamic* stiffness of the material, where creep naturally is excluded. Yet, SFRT are well known to exhibit creep under fatigue loading with non-zero mean stress.

Last but not least, the material equations developed are solely motivated on phenomenological observations. As they are not motivated by material scientific considerations, their scope of applicability is limited to the previously regime, e.g., one needs to carefully revalidate the material model if one moves away from the validated range of stress ratios between 0 and -1.

A. Appendix

A.1. Derivation of the saddle-point problem

We wish to establish the equivalence of minimizing the Ortiz-Stainier potential (4.2.20)

$$F\left(\overline{\boldsymbol{\varepsilon}}, \mathbf{u}, D\right) = \left\langle \frac{1}{2\left(1+D\right)} \left(\overline{\boldsymbol{\varepsilon}} + \nabla^s \mathbf{u}\right) : \mathbb{C} : \left(\overline{\boldsymbol{\varepsilon}} + \nabla^s \mathbf{u}\right) + \frac{1}{2\alpha \triangle \overline{N}} \left(D - D^n\right)^2 \right\rangle_Y - \overline{\boldsymbol{\varepsilon}} : \overline{\boldsymbol{\sigma}} \tag{A.1.1}$$

and the variational principle (4.3.4)

$$S\left(\boldsymbol{\sigma}, D\right) \equiv \left\langle -\frac{1+D}{2} \boldsymbol{\sigma} : \mathbb{S} : \boldsymbol{\sigma} + \frac{1}{2\alpha \triangle \overline{N}} \left(D - D^n\right)^2 \right\rangle_Y \longrightarrow \min_{D} \max_{\substack{\operatorname{div} \boldsymbol{\sigma} = 0 \\ \langle \boldsymbol{\sigma} \rangle_Y = \overline{\boldsymbol{\sigma}}}} \tag{A.1.2}$$

in terms of the relationship (4.3.2)

$$\boldsymbol{\varepsilon} = \left(1+D\right) \mathbb{S} : \boldsymbol{\sigma}. \tag{A.1.3}$$

This appendix provides a derivation based on convex duality. More precisely, suppose a convex function $f : X \to \mathbb{R}$ is given on a Banach space X. Let $f^* : X' \to \mathbb{R}$ be its Legendre transform

$$f^*(y) = \sup_{x \in X} \langle x, y \rangle - f(x), \tag{A.1.4}$$

where $\langle \cdot, \cdot \rangle$ denotes the natural pairing $\langle \cdot, \cdot \rangle : X \times X' \to \mathbb{R}$. Suppose that a closed subspace $U \subseteq X$ is given, and let $U^* \subseteq X^*$ be its annihilator

$$U^* = \{ y \in X^* \mid \langle y, x \rangle = 0 \quad \text{for all} \quad x \in U \}. \tag{A.1.5}$$

Then, according to convex duality [279, Thm. 31.4], the identity

$$\min_{x \in U} f(x) = - \min_{y \in U^*} f^*(y) \tag{A.1.6}$$

holds. For the problem at hand, we consider the space X to consist of square-integrable strain (or stress) fields on the unit cell Y, and we consider the objective function

$$f(\boldsymbol{\varepsilon}) = \left\langle \frac{1}{2\left(1+D\right)} \boldsymbol{\varepsilon} : \mathbb{C} : \boldsymbol{\varepsilon} + \frac{1}{2\alpha \triangle \overline{N}} \left(D - D^n\right)^2 \right\rangle_Y - \langle \varepsilon \rangle_Y : \boldsymbol{\sigma}, \tag{A.1.7}$$

treating the damage variable D as a parameter, and work on the subspace of kinematically compatible strains

$$U = \{\boldsymbol{\varepsilon} \in X \,|\, \boldsymbol{\varepsilon} = \overline{\boldsymbol{\varepsilon}} + \nabla^s \mathbf{u} \text{ for some } \overline{\boldsymbol{\varepsilon}} \text{ and } \mathbf{u}\}\,. \tag{A.1.8}$$

The Legendre transform of the function (A.1.7) computes as

$$f^*(\tau) = \left\langle \frac{(1+D)}{2}\, (\overline{\boldsymbol{\sigma}} + \tau) : \mathbb{S} : (\overline{\boldsymbol{\sigma}} + \tau) - \frac{1}{2\alpha \triangle \overline{N}} \left(D - D^n\right)^2 \right\rangle_Y \tag{A.1.9}$$

in terms of the compliance $\mathbb{S} = \mathbb{C}^{-1}$. Indeed, the Legendre dual (A.1.4) is defined in terms of a maximization principle

$$f^*(\tau) = \sup_{\boldsymbol{\varepsilon} \in X} \langle \tau : \boldsymbol{\varepsilon} \rangle_Y - \left\langle \frac{1}{2}\, \boldsymbol{\varepsilon} : \tilde{\mathbb{C}} : \boldsymbol{\varepsilon} + \frac{1}{2\alpha \triangle \overline{N}} \left(D - D^n\right)^2 \right\rangle_Y + \langle \boldsymbol{\varepsilon} \rangle_Y : \overline{\boldsymbol{\varepsilon}}, \tag{A.1.10}$$

whose critical points $\boldsymbol{\varepsilon} \in X$ satisfy

$$\tau - \tilde{\mathbb{C}} : \boldsymbol{\varepsilon} + \overline{\boldsymbol{\sigma}} = 0, \text{ i.e., } \quad \boldsymbol{\varepsilon} = \tilde{\mathbb{S}} : (\overline{\boldsymbol{\sigma}} + \tau)\,. \tag{A.1.11}$$

Here, we set

$$\tilde{\mathbb{C}} = \frac{1}{1+D}\, \mathbb{C} \quad \text{and} \quad \tilde{\mathbb{S}} = (1+D)\, \mathbb{S} \tag{A.1.12}$$

for notational brevity. Inserting the explicit expression for the strain field $\boldsymbol{\varepsilon}$ into the definition (A.1.10) yields

$$\begin{aligned} f^*(\tau) &= \left\langle \tau : \tilde{\mathbb{S}} : (\overline{\boldsymbol{\sigma}} + \tau) \right\rangle_Y - \left\langle \frac{1}{2}\, (\overline{\boldsymbol{\sigma}} + \tau) : \tilde{\mathbb{S}} : (\overline{\boldsymbol{\sigma}} + \tau) + \frac{1}{2\alpha \triangle \overline{N}} \left(D - D^n\right)^2 \right\rangle_Y + \\ &\quad \left\langle \overline{\boldsymbol{\sigma}} : \tilde{\mathbb{S}} : (\overline{\boldsymbol{\sigma}} + \tau) \right\rangle_Y \\ &= \left\langle (\overline{\boldsymbol{\sigma}} + \tau) : \tilde{\mathbb{S}} : (\overline{\boldsymbol{\sigma}} + \tau) \right\rangle_Y - \left\langle \frac{1}{2}\, (\overline{\boldsymbol{\sigma}} + \tau) : \tilde{\mathbb{S}} : (\overline{\boldsymbol{\sigma}} + \tau) + \frac{1}{2\alpha \triangle \overline{N}} \left(D - D^n\right)^2 \right\rangle_Y \\ &= \left\langle \frac{1}{2}\, (\overline{\boldsymbol{\sigma}} + \tau) : \tilde{\mathbb{S}} : (\overline{\boldsymbol{\sigma}} + \tau) - \frac{1}{2\alpha \triangle \overline{N}} \left(D - D^n\right)^2 \right\rangle_Y, \end{aligned} \tag{A.1.13}$$

i.e., the representation (A.1.9) emerges. To complete the picture, we note that the orthogonal complement[1] U^* takes the form

$$U^* = \{\tau \in X \,|\, \langle \tau \rangle_Y = 0 \text{ and } \operatorname{div} \tau = 0\}\,, \tag{A.1.14}$$

[1] As we are working in a Hilbert space, we may canonically identify the dual space with the primal Hilbert space, and exchange the annihilator by the orthogonal complement, both in view of Riesz' representation theorem.

i.e., it consists of equilibrium stress fluctuations. Combined with the expression (A.1.10), we conclude by convex duality (A.1.6) that we may transform

$$\begin{aligned}
&\min_{\overline{\boldsymbol{\varepsilon}},\mathbf{u}} \left\langle \frac{1}{2\,(1+D)}\,(\overline{\boldsymbol{\varepsilon}}+\nabla^s\mathbf{u}):\mathbb{C}:(\overline{\boldsymbol{\varepsilon}}+\nabla^s\mathbf{u})+\frac{1}{2\alpha\triangle\overline{N}}\,(D-D^n)^2\right\rangle_Y - \overline{\boldsymbol{\varepsilon}}:\overline{\boldsymbol{\sigma}}\\
=&-\min_{\substack{\operatorname{div}\,\tau=0\\ \langle\tau\rangle_Y=0}} \left\langle \frac{(1+D)}{2}\,(\overline{\boldsymbol{\sigma}}+\tau):\mathbb{S}:(\overline{\boldsymbol{\sigma}}+\tau)-\frac{1}{2\alpha\triangle\overline{N}}\,(D-D^n)^2\right\rangle_Y\\
=&-\min_{\substack{\operatorname{div}\,\boldsymbol{\sigma}=0\\ \langle\boldsymbol{\sigma}\rangle_Y=\overline{\boldsymbol{\sigma}}}} \left\langle \frac{(1+D)}{2}\,\boldsymbol{\sigma}:\mathbb{S}:\boldsymbol{\sigma}-\frac{1}{2\alpha\triangle\overline{N}}\,(D-D^n)^2\right\rangle_Y\\
=&\max_{\substack{\operatorname{div}\,\boldsymbol{\sigma}=0\\ \langle\boldsymbol{\sigma}\rangle_Y=\overline{\boldsymbol{\sigma}}}} \left\langle -\frac{(1+D)}{2}\,\boldsymbol{\sigma}:\mathbb{S}:\boldsymbol{\sigma}+\frac{1}{2\alpha\triangle\overline{N}}\,(D-D^n)^2\right\rangle_Y,
\end{aligned} \tag{A.1.15}$$

where we introduced the total stress field $\sigma=\Sigma+\tau$. Moreover, the identification (A.1.11) turns into

$$\boldsymbol{\varepsilon}=(1+D)\,\mathbb{S}:\boldsymbol{\sigma}. \tag{A.1.16}$$

Last but not least, we further minimize over the damage field to conclude

$$\begin{aligned}
&\min_{\overline{\boldsymbol{\varepsilon}},\mathbf{u},D} \left\langle \frac{1}{2\,(1+D)}\,(\overline{\boldsymbol{\varepsilon}}+\nabla^s\mathbf{u}):\mathbb{C}:(\overline{\boldsymbol{\varepsilon}}+\nabla^s\mathbf{u})+\frac{1}{2\alpha\triangle\overline{N}}\,(D-D^n)^2\right\rangle_Y - \overline{\boldsymbol{\varepsilon}}:\overline{\boldsymbol{\sigma}}\\
=&\min_{D}\max_{\substack{\operatorname{div}\,\boldsymbol{\sigma}=0\\ \langle\boldsymbol{\sigma}\rangle_Y=\overline{\boldsymbol{\sigma}}}} \left\langle -\frac{(1+D)}{2}\,\boldsymbol{\sigma}:\mathbb{S}:\boldsymbol{\sigma}+\frac{1}{2\alpha\triangle\overline{N}}\,(D-D^n)^2\right\rangle_Y,
\end{aligned} \tag{A.1.17}$$

what was to be shown.

A.2. Monotonicity of the operator $\mathcal{A}_M$

In this appendix, we wish to derive the identity (4.3.18)

$$\begin{aligned}
&\left\langle \mathcal{A}_M(\vec{\sigma}^\beta,\vec{D}^\beta)-\mathcal{A}_M(\vec{\sigma}^\gamma,\vec{D}^\gamma),(\vec{\sigma}^\beta,\vec{D}^\beta)-(\vec{\sigma}^\gamma,\vec{D}^\gamma)\right\rangle_M\\
=&\left\langle \frac{2+D^\beta+D^\gamma}{2}(\sigma^\beta-\sigma^\gamma):\mathbb{S}:(\sigma^\beta-\sigma^\gamma)+\frac{1}{\alpha\triangle\overline{N}}\,(D^\beta-D^\gamma)^2\right\rangle_Y.
\end{aligned} \tag{A.2.1}$$

For fixed compliance tensor $\mathbb{S}$ and $D^n,\bar{\alpha}\in\mathbb{R}$, we investigate the operator

$$\mathcal{A}:\operatorname{Sym}(m)\times\mathbb{R}\to\operatorname{Sym}(m)\times\mathbb{R},\quad (\sigma,D)\mapsto\left((1+D)\,\mathbb{S}:\sigma,\bar{\alpha}^{-1}(D-D^n)-\frac{1}{2}\sigma:\mathbb{S}:\sigma\right) \tag{A.2.2}$$

For any $(\sigma^\beta, D^\beta), (\sigma^\gamma, D^\gamma) \in \mathrm{Sym}(m) \times \mathbb{R}_{\geq 0}$, we observe

$$\begin{aligned}
&\left[\mathcal{A}(\sigma^\beta, D^\beta) - \mathcal{A}(\sigma^\gamma, D^\gamma)\right](\sigma^\beta - \sigma^\gamma, d^\beta - D^\gamma) \\
&= \left[(1 + D^\beta)\,\mathbb{S} : \sigma^\beta - (1 + D^\gamma)\,\mathbb{S} : \sigma^\gamma\right] : (\sigma^\beta - \sigma^\gamma) \\
&+ \bar{\alpha}^{-1}(D^\beta - D^\gamma)^2 - \frac{1}{2}(\sigma^\beta : \mathbb{S} : \sigma^\beta - \sigma^\gamma : \mathbb{S} : \sigma^\gamma)(D^\beta - D^\gamma).
\end{aligned} \tag{A.2.3}$$

Introducing the short-hand notation $\tilde{D}^\kappa = 1 + D^\kappa$, $\kappa \in \{\beta, \gamma\}$, we transform

$$\begin{aligned}
&\left[\tilde{D}^\beta\,\mathbb{S} : \sigma^\beta - \tilde{D}^\gamma\,\mathbb{S} : \sigma^\gamma\right] : (\sigma^\beta - \sigma^\gamma) - \frac{1}{2}(\sigma^\beta : \mathbb{S} : \sigma^\beta - \sigma^\gamma : \mathbb{S} : \sigma^\gamma)(\tilde{D}^\beta - \tilde{D}^\gamma) \\
= \;& \tilde{D}^\beta\,\sigma^\beta : \mathbb{S} : \sigma^\beta - (\tilde{D}^\beta + \tilde{D}^\gamma)\,\sigma^\beta : \mathbb{S} : \sigma^\gamma + \tilde{D}^\gamma\,\sigma^\gamma : \mathbb{S} : \sigma^\gamma \\
& - \frac{1}{2}(\tilde{D}^\beta\sigma^\beta : \mathbb{S} : \sigma^\beta - \tilde{D}^\beta\sigma^\gamma : \mathbb{S} : \sigma^\gamma - \tilde{D}^\gamma\sigma^\beta : \mathbb{S} : \sigma^\beta + \tilde{D}^\gamma\sigma^\gamma : \mathbb{S} : \sigma^\gamma) \\
= \;& \frac{1}{2}\tilde{D}^\beta\,\sigma^\beta : \mathbb{S} : \sigma^\beta - (\tilde{D}^\beta + \tilde{D}^\gamma)\,\sigma^\beta : \mathbb{S} : \sigma^\gamma + \frac{1}{2}\tilde{D}^\gamma\,\sigma^\gamma : \mathbb{S} : \sigma^\gamma + \frac{1}{2}(\tilde{D}^\beta\sigma^\gamma : \mathbb{S} : \sigma^\gamma \\
& + \tilde{D}^\gamma\sigma^\beta : \mathbb{S} : \sigma^\beta) \\
= \;& \frac{1}{2}(\tilde{D}^\beta + \tilde{D}^\gamma)\,(\sigma^\beta : \mathbb{S} : \sigma^\beta - 2\,\sigma^\beta : \mathbb{S} : \sigma^\gamma + \sigma^\gamma : \mathbb{S} : \sigma^\gamma) \\
= \;& \frac{\tilde{D}^\beta + \tilde{D}^\gamma}{2}\,(\sigma^\beta - \sigma^\gamma) : \mathbb{S} : (\sigma^\beta - \sigma^\gamma).
\end{aligned} \tag{A.2.4}$$

Inserting this result back into the original formula, we obtain

$$\left[\mathcal{A}(\sigma^\beta, D^\beta) - \mathcal{A}(\sigma^\gamma, D^\gamma)\right](\sigma^\beta - \sigma^\gamma, D^\beta - D^\gamma) \tag{A.2.5}$$

$$= \frac{2 + D^\beta + D^\gamma}{2}\,(\sigma^\beta - \sigma^\gamma) : \mathbb{S} : (\sigma^\beta - \sigma^\gamma) + \bar{\alpha}^{-1}(D^\beta - D^\gamma)^2. \tag{A.2.6}$$

Regarding $\mathbb{C}$, $\bar{\alpha} = \alpha \triangle \overline{N}$ and D^n as dependent on $x \in Y$, averaging the latter identity proves the formula (A.2.1), as claimed.

A.3. Coefficients for the stress-strain evolution

We derive the strain coefficients $\boldsymbol{\varepsilon}_c$ and $\boldsymbol{\varepsilon}_s$ for the sinusoidal loading (6.3.20). As shown in section 6.3.3, the stress in Fourier space is given by

$$\hat{\boldsymbol{\sigma}}_{\pm 1} = \frac{1}{2}\,(\boldsymbol{\sigma}_{\mathsf{c}} \mp i\boldsymbol{\sigma}_{\mathsf{s}})\,, \tag{A.3.1}$$

$$\hat{\boldsymbol{\sigma}}_k = 0 \quad \text{for all } k \notin \{-1, 1\}. \tag{A.3.2}$$

The constitutive equation (6.3.27) then reduces to

$$\frac{1}{2}\left(\boldsymbol{\sigma}_{\mathtt{c}} - i\boldsymbol{\sigma}_{\mathtt{s}}\right) = \left(E_0 + \sum_{j=1}^{N} \frac{\omega i}{\beta_j + \omega i} E_j\right) \mathbb{K}(\nu) : \boldsymbol{\varepsilon}_1, \tag{A.3.3}$$

$$\frac{1}{2}\left(\boldsymbol{\sigma}_{\mathtt{c}} + i\boldsymbol{\sigma}_{\mathtt{s}}\right) = \left(E_0 - \sum_{j=1}^{N} \frac{\omega i}{\beta_j - \omega i} E_j\right) \mathbb{K}(\nu) : \boldsymbol{\varepsilon}_{-1}. \tag{A.3.4}$$

With the abbreviations (6.3.28), we write

$$\frac{1}{2}\left(\boldsymbol{\sigma}_{\mathtt{c}} - i\boldsymbol{\sigma}_{\mathtt{s}}\right) = (r + qi)\, \mathbb{K}(\nu) : \boldsymbol{\varepsilon}_1, \tag{A.3.5}$$

$$\frac{1}{2}\left(\boldsymbol{\sigma}_{\mathtt{c}} + i\boldsymbol{\sigma}_{\mathtt{s}}\right) = (r - qi)\, \mathbb{K}(\nu) : \boldsymbol{\varepsilon}_{-1}. \tag{A.3.6}$$

or, rather,

$$\boldsymbol{\varepsilon}_1 = \frac{1}{2}\left(\frac{1}{r + qi}\mathbb{K}(\nu)^{-1} : \boldsymbol{\sigma}_c - \frac{i}{r + qi}\mathbb{K}(\nu)^{-1} : \boldsymbol{\sigma}_s\right), \tag{A.3.7}$$

$$\boldsymbol{\varepsilon}_{-1} = \frac{1}{2}\left(\frac{1}{r - qi}\mathbb{K}(\nu)^{-1} : \boldsymbol{\sigma}_c + \frac{i}{r - qi}\mathbb{K}(\nu)^{-1} : \boldsymbol{\sigma}_s\right). \tag{A.3.8}$$

We obtain the stress-strain relation

$$\boldsymbol{\varepsilon} = \boldsymbol{\varepsilon}_{-1} \exp(-i\omega t) + \boldsymbol{\varepsilon}_1 \exp(i\omega t) \tag{A.3.9}$$

$$= \frac{1}{2}\left(\frac{1}{r - qi}\exp(-i\omega t) + \frac{1}{r + qi}\exp(i\omega t)\right) \mathbb{K}(\nu)^{-1} : \boldsymbol{\sigma}_{\mathtt{c}} \tag{A.3.10}$$

$$+ \frac{1}{2}\left(\frac{i}{r - qi}\exp(-i\omega t) - \frac{i}{r + qi}\exp(i\omega t)\right) \mathbb{K}(\nu)^{-1} : \boldsymbol{\sigma}_{\mathtt{s}} \tag{A.3.11}$$

$$= \frac{1}{2}\left(\frac{r + qi}{r^2 + q^2}\exp(-i\omega t) + \frac{r - qi}{r^2 + q^2}\exp(i\omega t)\right) \mathbb{K}(\nu)^{-1} : \boldsymbol{\sigma}_{\mathtt{c}} \tag{A.3.12}$$

$$+ \frac{1}{2}\left(\frac{ri - q}{r^2 + q^2}\exp(-i\omega t) - \frac{ri + q}{r^2 + q^2}\exp(i\omega t)\right) \mathbb{K}(\nu)^{-1} : \boldsymbol{\sigma}_{\mathtt{s}} \tag{A.3.13}$$

$$= \left(\frac{r}{r^2 + q^2}\cos(\omega t) + \frac{q}{r^2 + q^2}\sin(\omega t)\right) \mathbb{K}(\nu)^{-1} : \boldsymbol{\sigma}_{\mathtt{c}} \tag{A.3.14}$$

$$+ \left(\frac{-q}{r^2 + q^2}\cos(\omega t) + \frac{r}{r^2 + q^2}\sin(\omega t)\right) \mathbb{K}(\nu)^{-1} : \boldsymbol{\sigma}_{\mathtt{s}}. \tag{A.3.15}$$

Thus, the coefficients $\boldsymbol{\varepsilon}_c$ and $\boldsymbol{\varepsilon}_s$ in front of the cosine function and the sine function, respectively, reassemble to the desired expression

$$\boldsymbol{\varepsilon}_c^{\mathtt{m}} = \frac{r}{r^2 + q^2}\, \mathbb{K}(\nu)^{-1} : \boldsymbol{\sigma}_{\mathtt{c}} - \frac{q}{r^2 + q^2}\, \mathbb{K}(\nu)^{-1} : \boldsymbol{\sigma}_{\mathtt{s}}, \tag{A.3.16}$$

$$\boldsymbol{\varepsilon}_s^{\mathtt{m}} = \frac{q}{r^2 + q^2}\, \mathbb{K}(\nu)^{-1} : \boldsymbol{\sigma}_{\mathtt{c}} + \frac{r}{r^2 + q^2}\, \mathbb{K}(\nu)^{-1} : \boldsymbol{\sigma}_{\mathtt{s}}. \tag{A.3.17}$$

B. List of Publications

Journal papers

- J. Köbler, N. Magino, H. Andrä, F. Welschinger, R. Müller, M. Schneider, "A computational multi-scale model for the stiffness degradation of short-fiber reinforced plastics subjected to fatigue loading," *Computer Methods in Applied Mechanics and Engineering*, vol. 373, pp. 113522, 2021.
- N. Magino, J. Köbler, H. Andrä, F. Welschinger, R. Müller, M. Schneider, "A multiscale high-cycle fatigue-damage model for the stiffness degradation of fiber-reinforced materials based on a mixed variational framework," *Computer Methods in Applied Mechanics and Engineering*, vol. 388, pp. 114198, 2022.
- N. Magino, J. Köbler, H. Andrä, F. Welschinger, R. Müller, M. Schneider, "A space-time upscaling technique for modeling high-cycle fatigue-damage of short-fiber reinforced composites," *Composites Science and Technology*, vol. 222, pp. 109340, 2022.
- N. Magino, J. Köbler, H. Andrä, F. Welschinger, R. Müller, M. Schneider, "Accounting for viscoelastic effects in a multiscale fatigue model for the degradation of the dynamic stiffness of short-fiber reinforced thermoplastics," *Computational Mechanics*, vol. 71, pp. 493–515, 2023.

Conference proceedings

- N. Magino, J. Köbler, H. Andrä, R. Müller, F. Welschinger, "A multi-scale fatigue-damage model for fiber-reinforced polymers," *PAMM*, vol. 20, no. 1, 2021.

- N. Magino, J. Köbler, H. Andrä, F. Welschinger, R. Müller, M. Schneider, "A Multiscale Fatigue Model for the Degradation of Fiber-Reinforced Materials," Large-Scale Scientific Computing, 13th International Conference, 2022.

Bibliography

[1] M. F. Ashby, *Materials Selection in Mechanical Design*. Oxford: Elsevier, 2011.

[2] "Short Fiber Thermoplastic Market: Trends, Opportunities and Competitive Analysis." https://www.lucintel.com/short-fiber-thermoplastics-market.aspx?RepId=RPT2154.

[3] E. Chebbi, J. Mars, M. Wali, and F. Dammak, "Fatigue Behavior of Short Glass Fiber Reinforced Polyamide 66: Experimental Study and Fatigue Damage Modelling," *Periodica Polytechnica Mechanical Engineering*, vol. 60, no. 4, pp. 247–255, 2016.

[4] L. G. Moretto Lise, *Investigation of damage evolution due to cyclic mechanical loads and load/frequency spectra-effects in short-fibre-reinforced thermoplastics*. PhD thesis, Universidad Federale De Santa Catarina, 2020.

[5] H. Nouri, F. Meraghni, and P. Lory, "Fatigue damage model for injection-molded short glass fibre reinforced thermoplastics," *International Journal of Fatigue*, vol. 31, no. 5, pp. 934–942, 2009.

[6] W. Van Paepegem and J. Degrieck, "A new coupled approach of residual stiffness and strength for fatigue of fibre-reinforced composites," *International Journal of Fatigue*, vol. 24, pp. 747–762, 2002.

[7] S. Kammoun, I. Doghri, L. Brassart, and L. Delannay, "Micromechanical modeling of the progressive failure in short glass–fiber reinforced thermoplastics – First Pseudo-Grain Damage model," *Composites Part A: Applied Science and Manufacturing*, vol. 73, pp. 166–175, 2015.

[8] A. Krairi, I. Doghri, and G. Robert, "Multiscale high cycle fatigue models for neat and short fiber reinforced thermoplastic polymers," *International Journal of Fatigue*, vol. 92, no. 1, pp. 179–192, 2016.

[9] A. Jain, J. M. Veas, S. Straesser, W. van Paepegem, I. Verpoest, and S. V. Lomov, "The Master SN curve approach – A hybrid multi-scale fatigue simulation of short fiber reinforced composites," *Composites Part A: Applied Science and Manufacturing*, vol. 91, pp. 510–518, 2016.

[10] H. Moulinec and P. Suquet, "A numerical method for computing the overall response of nonlinear composites with complex microstructure," *Computational Methods in Applied Mechanical Engineering*, vol. 157, pp. 69–94, 1998.

[11] M. Schneider, "A review of nonlinear FFT-based computational homogenization methods," *Acta Mechanica*, vol. 232, pp. 2051–2100, 2021.

[12] J. Köbler, *Effziente Multiskalen-Methode für Viskoelastizität und Ermüdung von kurzfaserverstärkten Polymeren*. PhD thesis, TU Kaiserslautern, 2022.

[13] P. Haupt, *Continuum Mechanics and Theory of Materials*. Berlin Heidelberg: Springer, 2000.

[14] G. A. Holzapfel, *Nonlinear Solid Mechanics: A Continuum Approach for Engineering*. New York: John Wiley & Sons, 2000.

[15] M. Šilavý, *The Mechanics and Thermodynamics of Continuous Media*. Berlin Heidelberg: Springer, 1997.

[16] I.-S. Liu, *Continuum Mechanics*. Berlin Heidelberg: Springer, 2002.

[17] B. Halphen and Q. S. Nguyen, "Sur les matériaux standards généralisés," *Journal de mécanique*, vol. 14, no. 1, pp. 39–63, 1975.

[18] P. Germain, Q. S. Nguyen, and P. Suquet, "Continuum Thermodynamics," *Journal of Applied Mechanics*, vol. 105, pp. 1010–1020, 1983.

[19] W. Voigt, *Lehrbuch der Kristallphysik: (mit Ausschluß der Kristalloptik)*. Springer Fachmedien Wiesbaden GmbH, 1966.

[20] A. Reuss, "Berechnung der Fließgrenze von Mischkristallen auf Grund der Plastizitätsbedingung für Einkristalle.," *ZAMM - Journal of Applied Mathematics and Mechanics / Zeitschrift für Angewandte Mathematik und Mechanik*, vol. 9, no. 1, pp. 49–58, 1929.

[21] Z. Hashin and S. Shtrikman, "A variational approach to the theory of elastic behaviour of multiphase materials," *Journal of the Mechanics and Physics of Solids*, vol. 11, pp. 127–140, 1963.

[22] I. M. Gitman, H. Askes, and L. Sluys, "Representative volume size as a macroscopic length scale parameter," *5th international conference on fracture mechanics of concrete and concrete structures*, pp. 483–491, 2004.

[23] I. M. Gitman, H. Askes, L. Sluys, and O. Lloberas-Valls, "The concept of Representative Volume for elastic, hardening and softening materials," *XXXII International Summer School-Conference Advance problems in Mechanics*, pp. 180–184, 2004.

[24] P. Suquet, "Elements of Homogenization for Inelastic Solid Mechanics," in *Homogenization Techniques for Composite Media* (E. Sanchez-Palancia and A. Zaoui, eds.), ch. 4, pp. 193–278, New York: Springer, 1985.

[25] R. Hill, "Elastic properties of reinforced solids: some theoretical principles," *Journal of the Mechanics and Physics of Solids*, vol. 11, no. 5, pp. 357–372, 1963.

[26] P. Suquet, "Local and Global Aspects in the Mathematical Theory of Plasticity," in *Plasticity Today: Modelling, Methods and Application* (A. Sawczuk and G. Bianchi, eds.), ch. 16, pp. 279–310, London: Elsevier, 1987.

[27] J. Eshelby, "The determination of the elastic field of an ellipsoidal inclusion, and related problems," *Proceedings of the Royal Society of London. Series A. Mathematical and Physical Sciences*, vol. 241, no. 1226, pp. 376–396, 1957.

[28] A. Zaoui, "Continuum micromechanics: survey.," *Journal of Engineering Mechanics - ASCE, American Society of Civil Engineers*, vol. 128, no. 8, pp. 808–816, 2002.

[29] E. Kröner, "Berechnung der elastischen Konstanten des Vielkristalls aus den Konstanten des Einkristalls," *Zeitschrift für Physik*, vol. 151, no. 4, pp. 504–518, 1958.

[30] R. Hill, "A self-consistent mechanics of composite materials," *Journal of the Mechanics and Physics of Solids*, vol. 13, no. 4, pp. 213–222, 1965.

[31] B. Budiansky, "On the elastic moduli of some heterogeneous materials," *Journal of the Mechanics and Physics of Solids*, vol. 13, no. 4, pp. 223–227, 1965.

[32] T. Mori and K. Tanaka, "Average stress in matrix and average elastic energy of materials with misfitting inclusions," *Acta Metallurgica*, vol. 21, no. 5, pp. 571–574, 1973.

[33] Y. Benveniste, "A new approach to the application of Mori-Tanaka's theory in composite materials," *Mechanics of Materials*, vol. 6, no. 2, pp. 147–157, 1987.

[34] A. N. Norris, "A differential schema for the effective moduli of composites," *Mechanics of Materials*, vol. 4, pp. 1–16, 1985.

[35] R. W. Zimmermann, "Elastic moduli of a solid containing spherical inclusions," *Mechanics of Materials*, vol. 12, pp. 17–24, 1991.

[36] D. Gross and T. Seelig, *Bruchmechanik*. Berlin: Springer Berlin Heidelberg, 2011.

[37] B. Klusemann, H. J. Böhm, and B. Svendsen, "Homogenization methods for multi-phase elastic composites with non-elliptical reinforcements: Comparisons and benchmarks," *European Journal of Mechanics A / Solids*, vol. 34, pp. 21–37, 2012.

[38] K. Matouš, M. G. D. Geers, V. G. Kouznetsova, and A. Gillman, "A review of predictive nonlinear theories for multiscale modeling of heterogeneous materials," *Journal of Computational Physics*, vol. 330, pp. 192–220, 2017.

[39] S. Staub, H. Andrä, M. Kabel, and T. Zangenmeister, "Multi-Scale Simulation of Viscoelastic Fiber-Reinforced Composites," *Technische Mechanik*, vol. 32, no. 1, pp. 70–83, 2012.

[40] I. Schmidt, "Numerical homogenisation of an elasto-plastic model-material with large elastic strains: macroscopic yield surfaces and the eulerian normality rule," *Computational Mechanics*, vol. 48, no. 5, pp. 579–590, 2011.

[41] F. Feyel, "Multiscale FE2 elastoviscoplastic analysis of composite structures," *Computational Material Science*, vol. 16, pp. 344–354, 1999.

[42] F. Feyel, "Multiscale non linear FE 2 analysis of composite structures : Fiber size effects," *Le Journal de Physique IV*, vol. 11, pp. 195–202, 2001.

[43] F. Feyel, "A multilevel finite element method (FE2) to describe the response of highly non-linear structures using generalized continua," *Computer Methods in Applied Mechanics and Engineering*, vol. 192, no. 28-30, pp. 3233–3244, 2003.

[44] V. Kouznetsova, W. A. M. Brekelmans, and F. P. T. Baaijens, "An approach to micro-macro modeling of heterogeneous materials," *Computational Mechanics*, vol. 27, pp. 37–48, 2001.

[45] J. Fish and Q. Yu, "Computational mechanics of fatigue and life predictions for composite materials and structures," *Computer Methods in Applied Mechanics and Engineering*, vol. 191, pp. 4827–4849, 2002.

[46] L. Tikarrouchine, A. Benaarbia, G. Chatzigeorgia, and F. Meraghni, "Micromechanical modeling of the progressive failure in short glass–fiber reinforced thermoplastics – first pseudo-grain damage model," *Composite Structures*, vol. 255, p. 112926, 2021.

[47] P. Arbenz, C. Flaig, and Kellenberger, "Bone structure analysis on multiple GPGPUs," *Journal of Parallel and Distributed Computing*, vol. 74, pp. 2941–2950, 2014.

[48] H. Moulinec and P. Suquet, "A fast numerical method for computing the linear and nonlinear mechanical properties of composites," *Comptes Rendus de l'Académie des Sciences. Série II*, vol. 318, no. 11, pp. 1417–1423, 1994.

[49] J. Spahn, H. Andrä, M. Kabel, and R. Müller, "A multiscale approach for modeling progressive damage of composite materials using fast fourier transforms," *Computer Methods in Applied Mechanics and Engineering*, vol. 268, pp. 871–883, 2014.

[50] J. Kochmann, S. Wulfinghoff, L. Ehle, J. Mayer, B. Svendsen, and S. Reese, "Efficient and accurate two-scale FE-FFT-based prediction of the effective material behavior of elasto-viscoplastic polycrystals," *Computational Mechanics*, vol. 61, pp. 751–764, 2018.

[51] G. Panasenko, *Multi-scale modelling for structures and composites*. Dordrecht Norwell: Springer, 2005.

[52] "Fastest Fourier Transform in the West (FFTW)." http://fftw.org/.

[53] F. Willot, "Fourier-based schemes for computing the mechanical response of composites with accurate local fields," *Comptes Rendus Mécanique*, vol. 343, no. 3, pp. 232–245, 2015.

[54] M. Schneider, F. Ospald, and M. Kabel, "Computational homogenization of elasticity on a staggered grid," *International Journal for Numerical Methods in Engineering*, vol. 105, no. 9, pp. 693–720, 2016.

[55] O. C. Zienkiewitz, R. L. Taylor, and J. Z. Zhu, *The Finite Element Method: Its Basis and Fundamentals*. Burlington: Elsevier Butterworth-Heinemann, 1967.

[56] J. Fish and T. Belytschko, *A First Course in Finite Elements*. West Sussex: John Wiley and Sons, 1967.

[57] P. Brenner, S. Grivet-Talocia, A. Quarteroni, G. Rozza, S. W., and L. M. Silveira, *Model Order Reduction – Volume 1: System- and Data-Driven Methods and Algorithms*. Berlin / Boston: de Gruyter, 2020.

[58] M. Gubisch and S. Volkwein, *Proper Orthogonal Decomposition for Linear-Quadratic Optimal Control*, pp. 3–63. Philadelphia: SIAM, 2017.

[59] R. Pinnau, *Model Reduction via Proper Orthogonal Decomposition*, pp. 95–109. Berlin, Heidelberg: Springer Berlin Heidelberg, 2008.

[60] Y. Maday and A. T. Patera, *Reduced basis methods*, pp. 139–179. Berlin /Boston: de Gruyter, 2020.

[61] F. Chinesta, A. Ammar, and et al., "An overview of the proper generalized decomposition with applications in computational rheology," *Journal of Non-Newtonian Fluid Mechanics*, vol. 166, pp. 578–592, 2011.

[62] F. Chinesta, P. Ladevèze, and E. Cueto, "A Short Review on Model Order Reduction Based on Proper Generalized Decomposition," *Archives of Computational Methods in Engineering*, vol. 18, pp. 395–404, 2011.

[63] G. J. Dvorak, "Transformation Field Analysis of Inelastic Composite Materials," *Proceedings: Mathematical and Physical Sciences*, vol. 437, no. 1900, pp. 311–327, 1992.

[64] G. J. Dvorak and J. Zhang, "Transformation field analysis of damage evolution in composite materials," *Journal of the Mechanics and Physics of Solids*, vol. 49, pp. 2517–2541, 2001.

[65] J. C. Michel and P. Suquet, "Nonuniform transformation field analysis," *International Journal of Solids and Structures*, vol. 40, no. 25, pp. 6937–6955, 2003.

[66] S. Roussette, J. C. Michel, and P. Suquet, "Nonuniform transformation field analysis of elastic–viscoplastic composites," *Composites Science and Technology*, vol. 69, pp. 22–27, 2009.

[67] F. Fritzen and M. Leuschner, "Reduced basis hybrid computational homogenization based on a mixed incremental formulation," *Computer Methods in Applied Mechanics and Engineering*, vol. 260, pp. 143–154, 2013.

[68] Z. Liu, M. A. Bessa, and W. K. Liu, "Self-consistent clustering analysis: An efficient multi-scale scheme for inelastic heterogeneous materials," *Computer Methods in Applied Mechanics*, vol. 306, pp. 319–341, 2016.

[69] M. Schneider, "On the mathematical foundations of the self-consistent clustering analysis for non-linear materials at small strains," *Comput. Meth. Appl. Mech. Eng.*, vol. 354, pp. 783–801, 2019.

[70] B. P. Ferreira, F. M. Andrade Pires, and M. A. Bessa, "Adaptive clustering-based reduced-order modeling framework: Fast and accurate modeling of localized history-dependent phenomena," *arXiv*, 2021.

[71] C. Yu, O. L. Kafka, and W. K. Liu, "Multiresolution clustering analysis for efficient modeling of hierarchical material systems," *Computational Mechanics*, vol. 67, pp. 1239–1306, 2021.

[72] M. Barrault, Y. Maday, N. C. Nguyen, and A. Patera, "An 'empirical interpolation' method: application to efficient reduced-basis discretization of partial differential equations," *Numerical Analysis*, vol. 339, pp. 667–672, 2004.

[73] S. Chaturantabut and D. C. Sorensen, "Nonlinear Model Reduction via Discrete Empirical Interpolation," *SIAM Journal on Scientific Computing*, vol. 39, no. 5, pp. 2737–2764, 2010.

[74] C. Farhat, T. Chapman, and P. Avery, "Structure-preserving, stability, and accuracy properties of the energy-conserving sampling and weighting method for the hyper reduction of nonlinear finite element dynamic models," *International Journal for Numerical Methods in Engineering*, vol. 102, no. 5, pp. 1077–1110, 2015.

[75] J. A. Hernández, M. A. Caicedo, and A. Ferrer, "Dimensional hyper-reduction of nonlinear finite element models via empirical cubature," *Computer Methods in Applied Mechanics and Engineering*, vol. 313, pp. 687–722, 2017.

[76] R. A. van Tuijl, J. J. C. Remmers, and M. G. D. Geers, "Integration efficiency for model reduction in micro-mechanical analyses," *Computational Mechanics*, vol. 62, pp. 151–169, 2018.

[77] P. Li and L. Pileggi, "Compact reduced-order modeling of weakly nonlinear analog and rf circuits," *IEEE Transactions on computer-aided design of integrated circuits and systems*, vol. 23, no. 2, pp. 184–2013, 2005.

[78] J. R. Phillips, "Projection-based approaches for model reduction of weakly nonlinear, time-varying systems," *IEEE Transactions on computer-aided design of integrated circuits and systems*, vol. 22, no. 2, pp. 171–187, 2003.

[79] J.-C. Michel and P. Suquet, "A model-reduction approach in micromechanics of materials preserving the variational structure of constitutive relations," *Journal of the Mechanics and Physics of Solids*, vol. 90, pp. 254–285, 2016.

[80] J.-C. Michel and P. Suquet, "A model-reduction approach to the micromechanical analysis of polycristalline material," *Computational Mechanics*, vol. 57, no. 3, pp. 483–508, 2016.

[81] M. Milano and P. Koumoutsakos, "Neural Network Modeling for Near Wall Turbulent Flow," *Journal of Computational Physics*, vol. 182, pp. 1–26, 2002.

[82] K. Kashima, "Nonlinear model reduction by deep autoencoder of noise response data," *IEEE 55th conference on decision and control (CDC)*, pp. 5750–5755, 2016.

[83] W. Ge and V. L. Tagarielli, "A computational framework to establish data-driven constitutive models for time- or path-dependent heterogeneous solids," *Scientific Reports*, vol. 11, p. 15916, 2021.

[84] K. Bhattacharya, B. Liu, A. M. Stuart, and M. Trautner, "Learning Markovian Homogenized Models in Viscoelasticity," *arXiv*, 2022.

[85] F. Regazzoni, M. Salvador, L. Dede, and A. Quarteroni, "A machine learning method for real-time numerical simulations of cardiac electromechanics," *Computer Methods in Applied Mechanics and Engineering*, vol. 393, p. 114825, 2022.

[86] D. Balzani, D. Brands, J. Schröder, and C. Carstensen, "Sensitivity analysis of statistical measures for the reconstruction of microstructures based on the minimization of generalized least-square functionals," *Technische Mechanik*, vol. 30, pp. 297–315, 2010.

[87] L. Scheunemann, D. Balzani, D. Brands, and J. Schröder, "Design of 3D statistically similar Representative Volume Elements based on Minkowski functionals," *Mechanics of Materials*, vol. 90, pp. 185–201, 2015.

[88] Z. Liu and C. T. Wu, "Exploring the 3D architectures of deep material network in data-driven multiscale mechanics," *Journal of the Mechanics and Physics of Solids*, vol. 127, pp. 20–46, 2019.

[89] Z. Liu, C. T. Wu, and M. Koishi, "A deep material network for multiscale topology learning and accelerated nonlinear modeling of heterogeneous materials," *Computer Methods in Applied Mechanics and Engineering*, vol. 345, pp. 1138–1168, 2019.

[90] S. Gajek, M. Schneider, and T. Böhlke, "On the micromechanics of deep material networks," *Journal of the Mathematics and Physics of Solids*, vol. 142, p. 103984, 2020.

[91] A. Hassan, N. A. Rahman, and R. Yahya, "Moisture Absorption Effect on Thermal, Dynamic Mechanical and Mechanical Properties of Injection-Molded Short Glass-Fiber/Polyamide 6,6 Composites," *Fibers and Polymers*, vol. 13, pp. 899–906, 2012.

[92] M. F. Arif, F. Meraghni, and et al., "In situ damage mechanisms investigation of PA66/GF30 composite: Effect of relative humidity," *Composites Part B: Engineering*, vol. 58, pp. 487–495, 2014.

[93] S. Felder, N. A. Vu, S. Reese, and J.-W. Simon, "Experimental and numerical investigation of the material behavior of semi-crystalline polyamide 6," *Technische Mechanik*, vol. 40, pp. 22–30, 2019.

[94] S. Felder, N. A. Vu, S. Reese, and J.-W. Simon, "Modeling the effect of temperature and degree of crystallinity on the mechanical response of polyamide 6," *Mechanics of Materials*, vol. 148, p. 103476, 2020.

[95] N. Jia and V. A. Kagan, "Effects of Time and Temperature on the Tension-Tension Fatigue Behavior of Short Fiber Reinforced Polyamides," *Polymer Composites*, vol. 19, pp. 408–414, 1998.

[96] J. D. Ferry, *Viscoelastic properties of polymers*. New York: John Wiley and Sons, 1980.

[97] M. L. Williams, R. F. Landel, and J. D. Ferry, "The temperature dependence of relaxation mechanisms in amorphous polymers and other glass-forming liquids," *Journal of the American Chemical Society*, vol. 77, pp. 3701–3707, 1955.

[98] D. Zhao, S. Ge, E. Senses, P. Akcora, J. Jestin, and S. K. Kumar, "Role of filler shape and connectivity on the viscoelastic behavior in polymer nanocomposites," *Macromulecules*, vol. 48, pp. 5433–5438, 2015.

[99] J.-L. Yang, Z. Zhang, A. K. Schlarb, and K. Friedrich, "On the characterization of tensile creep resistance of polyamide 66 nanocomposites. Part I. Experimental results and general discussions," *Polymer*, vol. 47, pp. 2791–2801, 2006.

[100] M. A. A. Saidi, A. Hassan, M. U. Wahit, L. J. Choy, and H. Anuar, "Thermal, dynamic mechanical analysis and mechanical properties of polybutylene terephthalate/polyethylene terephthalate blends," *Jurnal Teknologi*, vol. 82, pp. 73–83, 2020.

[101] K. Breuer, M. Schöneich, and M. Stommel, "Viscoelasticity of short fiber composites in the time domain: from three-phases micromechanics to finite element analyses," *Continuum Mechanics and Thermodynamics*, vol. 31, pp. 363–372, 2019.

[102] D. O. Obada, L. S. Kuburi, M. Dauda, S. Umaru, D. Dodoo-Arhin, M. B. Balogun, I. Iliyasu, and M. J. Iorpenda, "Effect of variation in frequencies on the viscoelastic properties of coir and coconut husk powder reinforced polymer composites," *Journal of King Saud University – Engineering Sciences*, vol. 32, pp. 148–157, 2020.

[103] D. Abdo, A. Gleadall, and V. V. Silberschmidt, "Damage and damping of short-glass-fibre-reinforced PBT composites under dynamic conditions: Effect of matrix behaviour," *Composite Structures*, vol. 226, p. 111286, 2019.

[104] H. Andä, D. Dobrovolski, K. Schladitz, S. Staub, and R. Müller, *Multi-scale Simulation of Composite Materials*, pp. 31–56. Heidelberg Berlin: Springer, 2019.

[105] J. L. Thomason, "The influence of fibre properties of the performance of glass-fibre-reinforced polyamide 6,6," *Composite Science and Technology*, vol. 59, pp. 2315–2328, 1999.

[106] G. Meneghetti, M. Ricotta, and et al., "An hysteresis energy-based synthesis of fully reversed axial fatigue behaviour of different polypropylene composites," *Composites Part B: Engineering*, vol. 65, pp. 17–25, 2014.

[107] A. K. Head, "The mechanism of fatigue of metals," *Physics of Solids*, vol. 1, no. 2, pp. 134–141, 1953.

[108] M. N. Riddell, G. P. Koo, and J. L. O'Toole, "Fatigue mechanisms of thermoplastics," *Polymer Engineering and Science*, pp. 363–368, 1966.

[109] L. Laiarinandrasana, T. F. Morgeneyer, H. Proudhorn, F. Nguyen, and E. Maire, "Effect of Multiaxial Stress State on Morphology and Spatial Distribution of Voids in Deformed Semicrystalline Polymer Assessed by X-ray Tomography," *Macromolecules*, vol. 52, pp. 4658–4668, 2012.

[110] H. Rolland, N. Saintier, I. Raphael, N. Lenoir, A. King, and G. Robert, "Fatigue damage mechanisms of short fiber reinforced PA66 as observed by in-situ synchrotron X-ray microtomography," *Composites Part B: Engineering*, vol. 143, pp. 217–229, 2018.

[111] E. Mouraglia-Seignobos, D. R. Long, L. Odoni, L. Vanel, P. Sotta, and C. Rochas, "Physical Mechanisms of Fatigue in Neat Polyamid 6,6," *Macromolecules*, vol. 47, pp. 3880–3894, 2014.

[112] C. Fusco, L. Vanel, and R. L. Long, "Long-time damage under creep experiments in disordered materials: Transition from exponential to logarithmic fracture dynamics," *The European Physical Journal E*, vol. 36, no. 34, 2013.

[113] H. B. H. Hamouda, L. Laiarinandrasana, and R. Piques, "A local approach to creep fracture by slow crack growth in an MDPE: Damage modelling," *International Journal of Pressure Vessels and Piping*, vol. 86, pp. 228–238, 2009.

[114] I. Raphael, N. Saintier, G. Robert, G. Béga, and L. Laiarinandrasana, "On the role of the spherulitic microstructure in fatigue damage of pure polymer and glass-fiber reinforced semi-crystalline polyamid 6.6," *International Journal of Fatigue*, vol. 126, pp. 44–54, 2019.

[115] F. Cosmi and A. Bernasconi, "Micro-CT investigation on fatigue damage evolution in short fibre reinforced polymers," *Composites Science and Technology*, vol. 79, pp. 70–76, 2013.

[116] H. Rolland, N. Saintier, N. Lenoir, A. King, and G. Robert, "Fatigue mechanisms description in short glass fibre reinforced thermoplastic by microtomographic observations," *Procedia Structural Integrity*, vol. 2, pp. 301–308, 2016.

[117] E. Belmonte, M. De Monte, C. Hoffmann, and M. Quaresimin, "Damage mechanisms in a short glass fiber reinforced polyamide under fatigue loading," *International Journal of Fatigue*, vol. 94, no. 1, pp. 145–157, 2017.

[118] M. F. Arif, F. Meraghni, and et al., "Multiscale fatigue damage characterization in short glass fiber reinforced polyamide-66," *Composites Part B: Engineering*, vol. 61, pp. 55–65, 2014.

[119] N. Sato, T. Kurauchi, S. Sato, and O. Kamigaito, "Microfailure behaviour of randomly dispersed short fibre reinforced thermoplastic composites obtained by direct SEM observation," *Journal of Materials Science*, vol. 26, pp. 3891–3893, 1991.

[120] J. Brunbauer, A. Mösenbacher, C. Guster, and G. Pinter, "Fundamental influences on quasistatic and cyclic material behavior of short glass fiber reinforced polyamide illustrated on microscopic scale," *Journal of Applied Polymer Science*, vol. 131, p. 40842, 2014.

[121] M. De Monte, E. Moosbrugger, and M. Quaresimin, "Influence of temperature and thickness on the off-axis behaviour of short glass fibre reinforced polyamide 6.6 cyclic loading," *Composites Part A: Applied Science and Manufacturing*, vol. 42, no. 10, pp. 1368–1379, 2010.

[122] R. E. Lavengood and Gulbransen, "The effect of aspect ratio on the fatigue life of short boron fiber reinforced composites," *Polymer Science and Engineering*, vol. 9, no. 5, pp. 365–369, 1969.

[123] S. Mortazavian and A. Fatemi, "Fatigue behavior and modeling of short fiber reinforced polymer composites: A literature review," *International Journal of Fatigue*, vol. 70, pp. 297–321, 2015.

[124] A. Wöhler, "Über die Festigkeits-Versuche mit Eisen und Stahl," *Zeitschrift für Bauwesen*, vol. 20, pp. 73–106, 1870.

[125] A. A. Griffith, "The phenomena of rupture and flow in solids," *Philosophical Transactions of the Royal Society of London*, pp. 163–198, 1921.

[126] P. C. Paris, M. P. Gomez, and W. E. Anderson, "A Rational Analytic Theory of Fatigue," *The Trend of Engineering*, pp. 9–14, 1961.

[127] I. H. Sahputra and A. T. Echtermeyer, "Molecular dynamics simulations of strain-controlled fatigue behaviour of amorphous polyethylene," *Journal of Polymer Research*, vol. 21, no. 11, 2014.

[128] I. H. Sahputra and A. T. Echtermeyer, "Creep-Fatigue Relationship in Polymer: Molecular Dynamics Simulations Approach," *Macromolecular Theory and Simulations*, vol. 24, no. 1, pp. 65–73, 2015.

[129] L. M. Kachanov, "Rupture Time Under Creep Conditions," *International Journal of Fracture*, vol. 97, pp. 6–18, 1999.

[130] G. A. Francfort and J.-J. Marigo, "Revisiting brittle fracture as an energy minimization problem," *Journal of Mechanics Physics of Solids*, vol. 46, pp. 1319–1342, 1998.

[131] B. Bourdin, "Numerical implementation of the variational formulation for quasi-static brittle fracture," *Interfaces and Free Boundaries*, vol. 9, pp. 411–430, 2007.

[132] C. Miehe, F. Welschinger, and M. Hofacker, "Thermodynamically consistent phase-field models of fracture: Variational principles and multi-field FE implementations," *International Journal for Numerical Methods in Engineering*, vol. 83, no. 10, pp. 1273–1311, 2010.

[133] C. Miehe, M. Hofacker, and F. Welschinger, "A phase field model for rate-independent crack propagation: Robust algorithmic implementation based on operator splits," *Computational Methods in Applied Mechanical Engineering*, vol. 199, pp. 2765–2778, 2010.

[134] J. Lemaitre, "A Continuous Damage Mechanics Model for Ductile Fracture," *Journal of Engineering Materials and Technology*, vol. 107, no. 1, pp. 83–89, 1985.

[135] J. Lemaitre, *A Course on Damage Mechanics*. Berlin: Springer, 1996.

[136] A. L. Gurson, *Continuum Theory of ductile rupture by void nucleation and growth: part I - yield criteria and flow rules for porous ductile media*. Providence: Brown University, 1975.

[137] P. Carrara, M. Ambati, R. Alessi, and L. De Lorenzis, "A framework to model the fatigue behavior of brittle materials based on a variational phase-field approach," *Computer Methods in Applied Mechanics and Engineering*, vol. 361, p. 112731, 2020.

[138] R. Alessi, S. Vidoli, and L. De Lorenzis, "A phenomenological approach to fatigue with a variational phase-field model: The one-dimensional case," *Engineering Fracture Mechanics*, vol. 190, pp. 53–73, 2018.

[139] M. Seiler, T. Linse, P. Hantschke, and M. Kästner, "An efficient phase-field model for fatigue fracture in ductile materials," *Engineering Fracture Mechanics*, vol. 224, p. 106807, 2020.

[140] A. Zago and G. S. Springer, "Fatigue lives of short fiber reinforced thermoplastics parts," *Journal of Reinforced Plastics Composites*, vol. 20, pp. 606–620, 2001.

[141] A. Zago and G. Springer, "Constant Amplitude Fatigue of Short Glass and Carbon Fiber Reinforced Thermoplastics," *Journal of Reinforced Plastics and Composites*, vol. 20, no. 7, pp. 564–595, 2001.

[142] B. Klimkeit, S. Castagnet, Y. Nadot, A. El Habib, G. Benoit, S. Bergamo, C. Dumas, and S. Achard, "Fatigue damage mechanisms in short fiber reinforced pbt+pet gf30," *Materials Science and Engineering: A*, vol. 528, pp. 1577–1588, 2011.

[143] B. Klimkeit, Y. Nadot, S. Castagnet, C. Nadot-Martin, C. Dumas, S. Bergamo, M. Sonsino, and A. Büter, "Multiaxial fatigue life assessment for reinforced polymers," *International Journal of Fatigue*, vol. 33, pp. 766–780, 2011.

[144] N. Fouchier, C. Nadot-Martin, E. Conrado, A. Bernasconi, and S. Castagnet, "Fatigue life assessment of a Short Fibre Reinforced Thermoplastic at high temperature using a Through Process Modelling in a viscoelastic framework," *International Journal of Fatigue*, vol. 124, pp. 236–244, 2019.

[145] F. Meraghni, H. Nouri, N. Bourgeois, C. Czarnota, and P. Lory, "Parameters identification of fatigue damage model for short glass fiber reinforced polyamide (PA6-GF30) using digital image correlation," *Procedia Engineering*, vol. 10, pp. 2110–2116, 2011.

[146] A. Launay, M. H. Maitournam, Y. Marco, and I. Raoult, "Multiaxial fatigue models for short glass fibre reinforced polyamide. Part I: Nonlinear anisotropic constitutive behavior for cyclic response," *International Journal of Fatigue*, vol. 47, pp. 382–389, 2013.

[147] A. Launay, M. H. Maitournam, Y. Marco, and I. Raoult, "Multiaxial fatigue models for short glass fibre reinforced polyamide. Part II: Fatigue life estimation," *International Journal of Fatigue*, vol. 47, pp. 390–406, 2013.

[148] L. Leveuf, L. Navrátil, V. Le Saux, Y. Marco, J. Olhagaray, and S. Leclercq, "Constitutive equations for the cyclic behaviour of short carbon fibre-reinforced thermoplastics and identification on a uniaxial database," *Continuum Mechanics and Thermodynamics*, vol. 32, no. 2, pp. 403–420, 2020.

[149] S. Teichtmeister, D. Kienle, F. Aldakheel, and M.-A. Keip, "Phase field modeling of fracture in anisotropic brittle solids," *International Journal of Non-Linear Mechanics*, vol. 97, pp. 1–21, 2017.

[150] M. Schneider, "An FFT-based method for computing weighted minimal surfaces in microstructures with applications to the computational homogenization of brittle fracture," *International Journal for Numerical Methods in Engineering*, vol. 121, no. 7, pp. 1367–1387, 2020.

[151] T. Guennouni, "Sur une méthode de calcul de structures soumises à des chargements cycliques: l'homogénéisation en temps," *Modélisation Mathématique et Analyse Numérique*, vol. 22, pp. 417–455, 1988.

[152] S. Haouala and I. Doghri, "Modeling and algorithms for two-scale time homogenization of viscoelastic-viscoplastic solids under large number of cycles," *International Journal of Plasticity*, vol. 70, pp. 98–125, 2015.

[153] R. de Borst, J. Pamin, R. H. J. Peerlings, and L. J. Sluys, "On gradient-enhanced damage and plasticity models for failure in quasi-brittle and frictional materials," *Computational Mechanics*, vol. 17, pp. 130–141, 1995.

[154] B. Svendsen, "Continuum Thermodynamic and Rate Variational Formulation of Models for Extended Continua," in *Advances in Extended and Multifield Theories for Continua* (B. Markert, ed.), (Berlin), pp. 1–18, Springer, 2011.

[155] B. Bourdin, G. A. Francfort, and J.-J. Marigo, "Numerical experiments in revisited brittle fracture," *Journal of the Mechanics and Physics of Solids*, vol. 48, pp. 797–826, 2000.

[156] A. Schlüter, A. Willenbücher, C. Kuhn, and R. Müller, "Phase field approximation of dynamic brittle fracture," *Computational Mechanics*, vol. 54, no. 5, pp. 1–21, 2014.

[157] F. Ernesti, M. Schneider, and T. Böhlke, "Fast implicit solvers for phase-field fracture problems on heterogeneous microstructures," *Computer Methods in Applied Mechanics and Engineering*, vol. 363, p. 112793, 2020.

[158] S. Wulfinghoff, M. Fassin, and S. Reese, "A damage growth criterion for anisotropic damage models motivated from micromechanics," *International Journal of Solids and Structures*, vol. 121, pp. 21–32, 2017.

[159] P. Ponte Castañeda and P. Suquet, "Nonlinear Composites," *Advances in Applied Mechanics*, vol. 34, pp. 171–302, 2017.

[160] J. Köbler, M. Schneider, F. Ospald, H. Andrä, and R. Müller, "Fiber orientation interpolation for the multiscale analysis of short fiber reinforced composite parts," *Computational Mechanics*, vol. 61, no. 6, pp. 729–750, 2018.

[161] C. Dorn and M. Schneider, "Lippmann-Schwinger solvers for the explicit jump discretization for thermal computational homogenization problems," *International Journal for Numerical Methods in Engineering*, vol. 118, no. 11, pp. 631–653, 2019.

[162] S. Burke, C. Ortmer, and E. Sueli, "An Adaptive Finite Element Approximation Of a Generalized Ambrosio–Tortorelli Functional," *Mathematical Models and Methods in Applied Sciences*, vol. 23, no. 09, pp. 1663–1697, 2013.

[163] J. Zeman, J. Vondřejc, J. Novak, and I. Marek, "Accelerating a FFT-based solver for numerical homogenization of periodic media by conjugate gradients," *Journal of Computational Physics*, vol. 229, no. 21, pp. 8065–8071, 2010.

[164] S. Brisard and L. Dormieux, "FFT-based methods for the mechanics of composites: A general variational framework," *Computational Materials Science*, vol. 49, no. 3, pp. 663–671, 2010.

[165] S. Brisard and L. Dormieux, "Combining Galerkin approximation techniques with the principle of Hashin and Shtrikman to derive a new FFT-based numerical method for the homogenization of composites," *Computer Methods in Applied Mechanics and Engineering*, vol. 217 - 220, pp. 197 – 212, 2012.

[166] M. Kabel, S. Fliegener, and M. Schneider, "Mixed boundary conditions for FFT-based homogenization at finite strains," *Computational Mechanics*, vol. 57, no. 2, pp. 193–210, 2016.

[167] G. H. Golub and C. F. Van Loan, *Matrix Computations*. Johns Hopkins University Press, 3rd ed., 1996.

[168] J. Bezanson, A. Edelman, S. Karpinski, and V. B. Shah, "Julia: A Fresh Approach to Numerical Computing," *SIAM Review*, vol. 59, no. 1, pp. 65–98, 2017.

[169] S. G. Advani and C. L. Tucker, "The Use of Tensors to Describe and Predict Fiber Orientation in Short Fiber Composites," *Journal of Rheology*, vol. 31, no. 8, pp. 751–784, 1987.

[170] V. Müller and T. Böhlke, "Prediction of effective elastic properties of fiber reinforced composites using fiber orientation tensors," *Composites Science and Technology*, vol. 130, pp. 36–45, 2016.

[171] P. Kennedy and R. Zheng, *Flow Analysis of Injection Molds*. Hanser Verlag, 2nd ed., 2003.

[172] "GeoDict." Math2Market GmbH, `http://www.geodict.de`, Kaiserslautern, Germany. Accessed: 2020-06-09.

[173] M. Schneider, "The Sequential Addition and Migration method to generate representative volume elements for the homogenization of short fiber reinforced plastics," *Computational Mechanics*, vol. 59, pp. 247–263, 2017.

[174] V. Müller, M. Kabel, H. Andrä, and T. Böhlke, "Homogenization of linear elastic properties of short fiber reinforced composites – A comparison of mean field and voxel-based methods," *International Journal of Solids and Structures*, vol. 67–68, pp. 56–70, 2015.

[175] T. Böhlke and C. Brüggemann, "Graphical representation of the generalized Hooke's law," *Technische Mechanik*, vol. 21, no. 2, pp. 145–158, 2001.

[176] T. Kanit, S. Forst, I. Galliet, V. Mounoury, and D. Jeulin, "Determination of the size of the representative volume element for random composites: statistical and numerical approach," *International Journal of Solids and Structures*, vol. 40, pp. 3647–3679, 2003.

[177] I. M. Gitman, H. Askes, and L. Sluys, "Representative volume: Existence and size determination," *Engineering Fracture Mechanics*, vol. 74, pp. 2518–2534, 2007.

[178] M. Schneider, "A dynamical view of nonlinear conjugate gradient methods with applications to FFT-based computational micromechanics," *Computational Mechanics*, vol. 66, pp. 239–257, 2020.

[179] J. Carmeliet, "Optimal estimation of gradient damage parameters from localization phenomena in quasi-brittle materials," *Mechanics of Cohesive-frictional Materials*, vol. 4, no. 1, pp. 1–16, 1999.

[180] M. Geers, R. de Borst, W. Brekelmans, and R. Peerlings, "Validation and internal length scale determination for a gradient damage model: application to short glass-fibre-reinforced polypropylene," *International Journal of Solids and Structures*, vol. 36, no. 17, pp. 2557 – 2583, 1999.

[181] K. Pham, H. Amor, J.-J. Marigo, and C. Maurini, "Gradient Damage Models and Their Use to Approximate Brittle Fracture," *International Journal of Damage Mechanics*, vol. 20, no. 4, pp. 618–652, 2011.

[182] C. Kuhn and R. Müller, "Simulation of size effects by a phase field model for fracture," *Theoretical and Applied Mechanics Letters*, vol. 4, no. 5, p. 051008, 2014.

[183] J. Crank and P. Nicolson, "A practical method for numerical evaluation of solutions of partial differential equations of the heat conduction type," *Mathematical Proceedings of the Cambridge Philosophical Society*, vol. 43, no. 1, pp. 50–67, 1947.

[184] G. W. Milton, *The Theory of Composites*. Cambridge: Cambridge University Press, 2002.

[185] R. Pietrogrande, *Multiscale modeling of short fiber-reinforced thermoplastics under fatigue loading*. PhD thesis, University of Padova, 2018.

[186] J. Michel and P. Suquet, "Computational analysis of nonlinear composite structures using the nonuniform transformation field analysis," *Computer Methods in Applied Mechanics and Engineering*, vol. 193, pp. 5477–5502, 2004.

[187] J.-C. Michel and P. Suquet, "A model-reduction approach in micromechanics of materials preserving the variational structure of constitutive relations," *Journal of the Mechanics and Physics of Solids*, vol. 90, pp. 254–285, 2016.

[188] J. Mujica, *Complex Analysis in Banach Spaces*. Dover Books on Mathematics, Mineola (NY): Dover Publications, 2010.

[189] J.-C. Michel and P. Suquet, "Effective potentials in nonlinear polycrystals and quadrature formulae," *Proceedings of the Royal Society A*, vol. 473, p. 20170213, 2017.

[190] K. Carlberg and C. Farhat, "A low-cost, goal-oriented 'compact proper orthogonal decomposition' bases for model reduction of static systems," *International Journal for Numerical Methods in Engineering*, vol. 86, pp. 381–402, 2011.

[191] D. Niedziela, U. Strautins, V. Hosdez, A. Kech, and A. Latz, "Improved multiscale fiber orientation modeling in injection molding of short fiber reinforced thermoplastics: simulation and experiment," *Int. J. Multiphys. Special Edition: Multiphys. Simul. Adv. Methods Ind. Eng.*, pp. 357–366, 2011.

[192] "Abaqus/Standard." Dassault Systèmes Simulia https://www.3ds.com/products-services/simulia/products/abaqus/.

[193] A. Latz, U. Strautins, and D. Niedziela, "Comparative numerical study of two concentrated fiber suspension models," *Journal of Non-Newtonian Fluid Mechanics*, vol. 165, no. 13–14, pp. 764–781, 2010.

[194] "FLUID Simulation Software for Complex Fluids." Fraunhofer ITWM, `https://www.itwm.fraunhofer.de/en/departments/sms/products-services/fluid-simulation-software-complex-fluids.html`, Kaiserslautern, Germany. Accessed: 2020-06-10.

[195] F. Folgar and C. Tucker, "Orientation behavior of fibers in concentrated suspensions," *Journal of Reinforced Plastics and Composites*, vol. 3, pp. 98–119, 2007.

[196] B. E. Verweyst and C. L. Tucker, "Fiber Suspensions in Complex Geometries: Flow/Orientation Coupling," *The Canadian Journal of Chemical Engineering*, vol. 80, no. 6, pp. 1093–1106, 2002.

[197] D. Cojocaru and A. M. Karlsson, "A simple numerical method of cycle jumps for cyclically loaded structures," *International Journal of Fatigue*, vol. 28, no. 3, pp. 1677–1689, 2006.

[198] C. Lüders, M. Sinapius, and D. Krause, "Adaptive cycle jump and limits of degradation in micromechanical fatigue simulations of fibre-reinforced plastics," *International Journal of Damage Mechanics*, vol. 28, no. 10, 2019.

[199] G. Puel and D. Aubry, "Material fatigue simulation using a periodic time-homogenisation method," *Revue Européenne de Mécanique Numérique*, vol. 21, no. 3-6, pp. 312–324, 2012.

[200] F. Fritzen and M. Hassani, "Space–time model order reduction for nonlinear viscoelastic systems subjected to long-term loading," *Meccanica*, vol. 53, p. 1333–1355, 2018.

[201] H. Amor, J.-J. Marigo, and C. Maurini, "Regularization formulation of the variational brittle fracture with unilateral contact: Numerical experiments," *Journal of the Mechanics and Physics of Solids*, vol. 57, no. 8, pp. 1209–1229, 2009.

[202] C. Kuhn, *Numerical and analytical investigation of a phase field model for fracture.* PhD thesis, TU Kaiserslautern, 2013.

[203] Z. Liu, C. T. Wu, and M. Koishi, "A deep material network for multiscale topology learning and accelerated nonlinear modeling of heterogeneous materials," *Computer Methods in Applied Mechanics and Engineering*, vol. 345, pp. 1138 – 1168, 2019.

[204] C. Kuhn and R. Müller, "A continuum phase field model for fracture," *Engineering Fracture Mechanics*, vol. 77, no. 18, pp. 3625–3634, 2010.

[205] M. Ambati, T. Gerasimov, and L. De Lorenzis, "A review on phase-field models of brittle fracture and a new fast hybrid formulation," *Computational Mechanics*, vol. 55, pp. 383–405, 2015.

[206] L. M. Kachanov, "Time of the rupture process under creep conditions," *Izvestiya Akademii Nauk SSSR. Otdelenie Tekhnicheskikh Nauk. Mekhanika i Mashinostroenie*, vol. 8, pp. 26–31, 1958.

[207] J. Görthofer, M. Schneider, A. Hrymak, and T. Böhlke, "A convex anisotropic damage model based on the compliance tensor," *International Journal of Damage Mechanics*, vol. 31, no. 1, pp. 43–86, 2022.

[208] S. Govindjee, "Anisotropic modelling and numerical simulation of brittle damage in concrete," *International Journal for Numerical Methods in Engineering*, vol. 38, pp. 3611–3633, 1995.

[209] S. Wulfinghoff, M. Fassin, and S. Reese, "A damage growth criterion for anisotropic damage models motivated from micromechanics," *International Journal of Solids and Structures*, vol. 121, pp. 21–32, 2017.

[210] R. Vignjevic, N. Djordjevic, T. De Vuyst, and S. Gemkow, "Modelling of strain softening materials based on equivalent damage force," *Computer Methods in Applied Mechanics and Engineering*, vol. 335, pp. 52–68, 2018.

[211] R. H. J. Peerlings, W. A. M. Brekelmans, and et al., "Gradient-enhanced damage modelling of high-cycle fatigue," *International Journal for Numerical Methods in Engineering*, vol. 49, pp. 1547–1569, 2000.

[212] S. Forest and E. Lorentz, "Localization phenomena and regularization methods," in *Local Approach to Fracture* (J. Besson, ed.), (Paris), pp. 311–373, Ecole des Mines de Paris/Les Presses, 2004.

[213] A. Mielke, T. Roubicek, and J. Zeman, "Complete damage in elastic and viscoelastic media and its energetics," *Computational Methods in Applied Mechanical Engineering*, vol. 199, pp. 1242–1253, 2010.

[214] B. Bourdin, G. A. Francfort, and J.-J. Margio, "The Variational Approach to Fracture," *Journal of Elasticity*, vol. 91, pp. 5–148, 2008.

[215] C. Gu, "Qlmor: A projection-based nonlinear model order reduction approach using quadratic-linear representation of nonlinear systems," *IEEE Transactions on Computer-Aided Design of Integrated Circuits and Systems*, vol. 30, pp. 1307–1320, 2011.

[216] Q. S. Nguyen, *Stability and Nonlinear Solid Mechanics*. New York: Wiley, 2000.

[217] A. Jain, W. van Paepegem, I. Verpoest, and S. V. Lomov, "A feasibility study of the Master SN curve approach for short fiber reinforced composites," *International Journal of Fatigue*, vol. 91, pp. 264–274, 2016.

[218] J. Köbler, N. Magino, H. Andrä, F. Welschinger, R. Müller, and M. Schneider, "A computational multi-scale model for the stiffness degradation of short-fiber reinforced plastics subjected to fatigue loading," *Computer Methods in Applied Mechanics and Engineering*, vol. 373, p. 113522, 2021.

[219] M. Ortiz and L. Stainier, "The variational formulation of viscoplastic constitutive updates," *Computer Methods in Applied Mechanical Engineering*, vol. 171, pp. 419–444, 1999.

[220] C. Miehe, "Strain-driven homogenization of inelastic microstructures and composites based on an incremental variational formulation," *International Journal for Numerical Methods in Engineering*, vol. 55, pp. 1285–1322, 2002.

[221] N. Bakhvalov and G. Panasenko, *Homogenisation: Averaging Processes in Periodic Media.* Netherland: Springer, 1989.

[222] R. Herzog, C. Meyer, and G. Wachsmuth, "Integrability of displacement and stresses in linear and nonlinear elasticity with mixed boundary conditions," *Journal of Mathematical Analysis and Applications*, vol. 382, no. 2, pp. 802–813, 2011.

[223] F. Becker, *Entwicklung einer Beschreibungsmethodik für das mechanische Verhalten unverstärkter Thermoplaste bei hohen Deformationsgeschwindigkeiten.* PhD thesis, Martin-Luther-Universität Halle-Wittenberg, 1976.

[224] P. A. Hessman, T. Riedel, F. Welschinger, K. Hornberger, and T. Böhlke, "Microstructural analysis of short glass fiber reinforced thermoplastics based on x-ray micro-computed tomography," *Composites Science and Technology*, vol. 183, p. 107752, 2019.

[225] H. H. Bauschke and P. L. Combettes, *Convex Analysis and Monotone Operator Theory in Hilbert Spaces.* CMS Books in Mathematics, Springer, 2nd ed., 2017.

[226] L. Fick, Y. Maday, A. P. Patera, and T. Taddei, "A stabilized POD model for turbulent flows over arange of Reynolds numbers: optimal parametersampling and constrained projection," *Journal of Computational Physics*, vol. 371, pp. 214–243, 2018.

[227] M. Kabel, T. Böhlke, and M. Schneider, "Efficient fixed point and Newton–Krylov solvers for FFT-based homogenization of elasticity at large deformations," *Computational Mechanics*, vol. 54, pp. 1497–1514, 2014.

[228] FeelMath, "FeelMath." Fraunhofer Institute for Industrial Mathematics http://www.itwm.fraunhofer.de/en/fraunhofer-itwm.html, Kaiserslautern, Germany, 2017.

[229] F. Wittemann, R. Maertens, L. Kärger, and F. Henning, "Injection molding simulation of short fiber reinforced thermosets with anisotropic and non-Newtonian flow behavior," *Composites Part A: Applied Science and Manufacturing*, vol. 124, p. 105476, 2019.

[230] M. H. J. W. Paas, P. J. G. Schreurs, and W. A. M. Brekelmans, "A continuum approach to brittle and fatigue damage: theory and numerical procedures," *International Journal of Solids and Structures*, vol. 30, pp. 579–599, 1993.

[231] N. Magino, J. Köbler, and et al., "A multiscale high-cycle fatigue-damage model for the stiffness degradation of fiber-reinforced materials based on a mixed variational framework," *Computer Methods in Applied Mechanics and Engineering*, vol. 388, p. 114198, 2022.

[232] J. L. Chaboche, "Continuum damage mechanics: Present state and future trends," *Nuclear Engineering and Design*, vol. 105, pp. 19–33, 1987.

[233] J. Lemaitre and R. Desmorat, *Engineering Damage Mechanics – Ductile, Creep, Fatigue and Brittle Failures.* Berlin Heidelberg: Springer, 2005.

[234] A. S. J. Suiker and R. de Borst, "A numerical model for the cyclic deterioration of railway tracks," *International Journal of Numerical Methods in Engineering*, vol. 57, pp. 441–470, 2003.

[235] R. Largenton, J.-C. Michel, and P. Suquet, "Extension of the Nonuniform Transformation Field Analysis to linear viscoelastic composites in the presence of aging and swelling," *Mechanics of Material*, vol. 73, pp. 76–100, 2014.

[236] H. Altenbach, *Kontinuumsmechanik – Einführung in die materialunabhängigen und materialabängigen Gleichungen.* Berlin Heidelberg: Springer, 2015.

[237] M. Fremond and B. Nedjar, "Damage, gradient of damage, and principle of virtual power," *International Journal of Solids and Structures*, vol. 33, pp. 1083–1103, 1996.

[238] R. H. J. Peerlings, R. de Borst, W. A. M. Brekelmans, J. H. P. de Vree, and I. Spee, "Some observations on localisation in non-local and gradient damage models," *European Journal of Mechanics. A, Solids*, vol. 15, pp. 937–953, 1996.

[239] R. H. J. Peerlings, R. de Borst, W. A. M. Brekelmans, and M. G. D. Geers, "Gradient–enhanced damage modelling of concrete fracture," *Mechanics of cohesive-frictional materials*, vol. 3, pp. 323–342, 1998.

[240] P. Ladevèze, "An anisotropic damage theory with unilateral effects: Application to laminates and to three- and four-dimensional composites," in *Continuum Damage Mechanics of Materials and Structures* (O. Allix and F. Hild, eds.), pp. 205–233, Oxford: Elsevier Science, 2002.

[241] P. Ladevèze, A. Gasser, and O. Allix, "Damage Mechanisms Modeling for Ceramic Composites," *Journal of Engineering Materials and Technology*, vol. 116, pp. 331–336, 1994.

[242] J. Schijve, *Fatigue under Variable-Amplitude Loading*, pp. 295–328. Dordrecht: Springer Netherlands, 2009.

[243] P. R. Vieira, E. M. L. Carvalho, and et al., "Experimental fatigue behavior of pultruded glass fibre reinforced polymer composite materials," *Composites Part B: Engineering*, vol. 146, pp. 69–75, 2018.

[244] M. Kawai, H. Takeuchi, and et al., "Effects of temperature and stress ratio on fatigue life of injection molded short carbon fiber-reinforced polyamide composite," *Composites Part A: Applied Science and Manufacturing*, vol. 98, pp. 9–24, 2017.

[245] P. B. S. Bailey and M. Highman, "Application of strain-controlled fatigue testing methods to polymer matrix composites," *Procedia Structural Integrity*, vol. 2, pp. 128–135, 2016.

[246] Q. S. Nguyen, *Stability and Nonlinear Solid Mechanics*. New York: Wiley, 2000.

[247] P. A. Hessman, F. Welschinger, and et al., "On mean field homogenization schemes for short fiber reinforced composites: Unified formulation, application and benchmark," *International Journal of Solids and Structures*, vol. 230-231, p. 111141, 2021.

[248] Z. Mouti, K. Westwood, and et al., "Finite Element Analysis of Glass Fiber-Reinforced Polyamide Engine Oil Pan Subjected to Localized Low Velocity Impact from Flying Projectiles," *Steel Research International*, vol. 83, no. 10, pp. 957–963, 2012.

[249] M. Kabel, T. Böhlke, and M. Schneider, "Efficient fixed point and Newton–Krylov solvers for FFT-based homogenization of elasticity at large deformations," *Computational Mechanics*, vol. 54, no. 6, pp. 1497–1514, 2014.

[250] "Abaqus/Standard." Dassault Systèmes Simulia https://www.3ds.com/products-services/simulia/products/abaqus/. Accessed: 2021-10-19.

[251] A. Djebli, M. Bendouba, and et al., "ExperimentalAnalysis andDamageModeling of High-Density Polyethylene under Fatigue Loading," *Acta Mech Solida Sinica*, vol. 29, no. 2, pp. 133–144, 2016.

[252] E. Chebbi, J. Mars, and et al., "A new cumulative fatigue damage model for short glass fiber-reinforced polyamide 66," in *Design and Modeling of Mechanical Systems—III* (M. Haddar, F. Chaari, A. Benamara, M. Chouchane, C. Karra, and N. Aifaoui, eds.), pp. 227–234, Cham: Springer, 2018.

[253] H. F. Brinson and L. C. Brinson, *Polymer Engineering Science and Viscoelasticity - An Introduction*. New York: Springer, 2008.

[254] C. Gómez, J. Mira, F. J. Carrión-Vilches, and F. Cavas, "Dynamic Moduli of Polybutylene Terephthalate Glass Fiber Reinforced in High-Temperature Environments," *Materials*, vol. 14, p. 483, 2021.

[255] G. Milton, "On characterizing the set of possible effective tensors of composites: The variational method and the translation method," *Communications on Pure and Applied Mathematics*, vol. 43, pp. 63–125, 1990.

[256] A. V. Cherkaev and L. V. Gibiansky, "Variational principles for complex conductivity, viscoelasticity, and similar problems in media with complex moduli," *Journal of Mathematical Physics*, vol. 35, pp. 127–145, 1993.

[257] G. La Rosa and A. Risitano, "Thermographic methodology for rapid determination of the fatigue limit of materials and mechanical components," *International Journal of Fatigue*, vol. 22, pp. 65–73, 2000.

[258] V. Crupi, E. Giglielmino, G. Risitano, and F. Tavilla, "Experimental analyses of SFRP material under static and fatigue loading by means of thermographic and DIC techniques," *Composites Part B: Engineering*, vol. 77, pp. 268–277, 2015.

[259] N. Magino, J. Köbler, H. Andrä, F. Welschinger, R. Müller, and M. Schneider, "A space-time upscaling technique for modeling high-cycle fatigue-damage of short-fiber reinforced composites," *Composites Science and Technology*, vol. 233, p. 109340, 2022.

[260] J. C. Maxwell, "On the dynamical theory of gases," *Philosophical Transactions of the Royal Society of London*, pp. 49–88, 1867.

[261] A. Wiechert, "Gesetze der elastischen Nachwirkung für constante Temperatur," *Annalen der Physik*, vol. 286, no. 10, pp. 335–348, 1893.

[262] M. Kawai and T. Taniguchi, "Off-axis fatigue behavior of plain weave carbon/epoxy fabric laminates at room and high temperatures and its mechanical modeling," *Composites Part A: Applied Science and Manufacturing*, vol. 37, pp. 243–256, 2006.

[263] M. de Monte, *Multiaxial fatigue behaviour of short fibre reinforced thermoplastics*. PhD thesis, Università di Bologna, 2008.

[264] S.-R. Ryu and D.-J. Lee, "Effects of Fiber Aspect Ratio, Fiber Content, and Bonding Agent on Tensile and Tear Properties of Short-Fiber Reinforced Rubber," *KSME International Journal*, vol. 14, pp. 35–43, 2001.

[265] Z.-M. Huang, C.-C. Zhang, and Y.-D. Xue, "Stiffness prediction of short fiber reinforced composites," *International Journal of Mechanical Sciences*, vol. 161-162, p. 105068, 2019.

[266] N. W. Tschoegl, *The phenomenological theory of linear viscoelastic behavior*. Berlin, Heidelberg: Spinger, 1989.

[267] S. Mortazavian and A. Fatemi, "Tensile behavior and modeling of short fiber-reinforced polymer composites including temperature and strain rate effects," *Journal of Thermoplastic Composites*, vol. 30, pp. 1414–1437, 2017.

[268] S. Toll and P.-O. Andersson, "Microstructure of Long- and Short-Fiber Reinforced Injection Molded Polyamide," *Polymer Composites*, vol. 14, no. 2, pp. 116–125, 1993.

[269] G. J. von Bradsky, R. S. Bailey, A. J. Cervenka, H. G. Zachmann, and P. S. Allan, "Characterisation of finite length composites: Part IV-Structural studies on injection moulded composites," *International Union of Pure and Applied Chemistry*, vol. 69, no. 12, pp. 2523–2539, 1997.

[270] T. B. Nguyen Thi, M. Morioka, A. Yokoyama, S. Hamanaka, K. Yamashita, and C. Nonomura, "Measurement of fiber orientation distribution in injection-moldedshort-glass-fiber composites using X-ray computed tomography," *Journal of Materials Processing Technology*, vol. 219, pp. 1–9, 2015.

[271] S. Pei, K. Wang, J. Li, Y. Li, D. Zeng, X. Su, X. Xiao, and H. Yang, "Mechanical Properties Prediction of Injection Molded Short/Long Carbon Fiber Reinforced

Polymer Composites Using Micro X-Ray Computed Tomography," *Composites Part A: Applied Science and Manufacturing*, vol. 130, p. 105732, 2020.

[272] Z. A. Mohad Ishak and N. C. Lim, "Effect of moisture absorption on the tensile properties of short glass fiber reinforced poly(butylene terephthalate)," *Polymer Engineering Science*, vol. 34, no. 22, pp. 1645–1655, 1994.

[273] M. F. Woldekidan, *Response Modelling of Bitumen, Bituminous Mastic and Mortar*. PhD thesis, Technische Universiteit Delft, 2011.

[274] S. Montgomery-Smith, W. He, D. A. Jack, and D. E. Smith, "Exact tensor closures for the three-dimensional Jeffery's equation," *Journal of Fluid Mechanics*, vol. 680, pp. 321–335, 8 2011.

[275] K. C. Dao and D. J. Dicken, "Fatigue failure mechanisms in polymers," *Polymer Engineering and Science*, vol. 27, no. 4, pp. 271–276, 1987.

[276] A. J. Lesser, "Changes in mechanical behavior during fatigue of semicrystalline thermoplastics," *Journal of Applied Polymer Science*, vol. 58, no. 5, pp. 869–879, 1995.

[277] M. A. Imaddahen, M. Shirinbayan, H. Ayari, M. Foucard, A. Tcharkhtchi, and J. Fitoussi, "Multi-scale analysis of short glass fiber-reinforced polypropylene under monotonic and fatigue loading," *Polymer Composites*, vol. 41, pp. 4649–4662, 2020.

[278] J. Fitoussi, F. Meraghni, Z. Jendli, G. Hug, and D. Baptiste, "Experimental methodology for high strain-rates tensile behaviour analysis of polymer matrix composites," *Composite Science and Technology*, vol. 65, pp. 2174–2188, 2005.

[279] R. T. Rockafellar, *Convex Analysis*. Princeton: Princeton University Press, 1970.